



Probing complex organic heritage materials with X-ray Raman scattering

Rafaella Georgiou

► To cite this version:

Rafaella Georgiou. Probing complex organic heritage materials with X-ray Raman scattering. Physics [physics]. Université Paris-Saclay, 2021. English. NNT : 2021UPAST076 . tel-03506928

HAL Id: tel-03506928

<https://theses.hal.science/tel-03506928>

Submitted on 3 Jan 2022

HAL is a multi-disciplinary open access archive for the deposit and dissemination of scientific research documents, whether they are published or not. The documents may come from teaching and research institutions in France or abroad, or from public or private research centers.

L'archive ouverte pluridisciplinaire **HAL**, est destinée au dépôt et à la diffusion de documents scientifiques de niveau recherche, publiés ou non, émanant des établissements d'enseignement et de recherche français ou étrangers, des laboratoires publics ou privés.

Sonder les matériaux organiques
patrimoniaux complexes par
diffusion Raman de rayons X

*Probing complex organic heritage materials
with x-ray Raman scattering*

Thèse de doctorat de l'université Paris-Saclay

École doctorale n° 573, Interfaces : approches
interdisciplinaires, fondements, applications et innovation
(Interfaces)

Spécialité de doctorat : Physique

Unité de recherche : Université Paris-Saclay, CNRS, UVSQ, Institut
photonique d'analyse non-destructive européen
des matériaux anciens, 91192, Saint-Aubin, France

Référent : Université de Versailles Saint-Quentin-en-Yvelines

**Thèse présentée et soutenue à Paris-Saclay,
le 01/07/2021, par**

Rafaella GEORGIU

Composition du jury :

| | |
|--|---------------------------|
| Joanne Xie Professeure des universités, ENS Paris-Saclay, PPSM, Gif-sur-Yvette, France | Présidente |
| Simo Huotari Professeur, Department of Physics, Université d'Helsinki | Rapporteur & Examineur |
| Caroline Tokarski Professeure, Université de Bordeaux | Rapporteur & Examinatrice |
| Karim Benzerara Directeur de Recherche CNRS, Institut de Minéralogie, de Physique des Matériaux et de Cosmochimie, Paris | Examineur |
| Ilaria Bonaduce Associate Professor, Department of Chemistry, University of Pisa | Examinatrice |
| Marie-Angélique Languille Ingénieure de recherche CNRS, Centre de recherche sur la conservation, Paris | Examinatrice |

Direction de la thèse :

| | |
|--|--------------|
| Loïc Bertrand Chercheur, PPSM, Gif-sur-Yvette, France et Université Paris-Saclay | Directeur |
| Rueff Jean-Pascal Directeur de Recherche, Synchrotron SOLEIL, Gif-sur-Yvette, France | Co-encadrant |

Titre : Sonder les matériaux organiques patrimoniaux complexes par diffusion Raman de rayons X

Mots clés : Imagerie 3D | Spectroscopie XRS | Fossiles organiques | Exsudats de plantes | Pigments organiques | Patrimoine culturel et naturel

Résumé : Les moyens analytiques permettant d'évaluer la composition organique d'échantillons complexes sont limités et précieux pour les sciences du patrimoine. Ce travail explore le potentiel de la diffusion Raman de rayons X (XRS) comme approche non invasive pour étudier des matériaux paléontologiques, archéologiques et artistiques. Nous optimisons la méthodologie XRS requise pour l'étude d'échantillons complexes, comprenant des spécimens paléontologiques organiques et une collection d'exsudats végétaux à valeur patrimoniale, et explorons sa capacité à accéder aux différents niveaux d'information recherchés. La spectroscopie XRS est employée pour étudier des échantillons organiques anciens en 3D sur des dimensions millimétriques, de façon non invasive, pour déterminer les signatures organiques et retracer leur évolution dans le temps. En exploitant la tomographie directe basée sur le contraste des signaux chimiques, nous introduisons l'imagerie Raman des rayons X en 3D (XRI) dans le domaine du patrimoine naturel. La collecte successive d'images XRI tomographiques d'un spécimen exceptionnellement préservé, un insecte ancien de 53 millions d'années piégé dans l'ambre, permet d'évaluer la distribution spatiale des vestiges biologiques. Les résultats soulignent l'importance d'une imagerie de spéciation des spécimens à l'échelle de l'objet, afin de comprendre la biochimie, l'évolution moléculaire et les interactions entre organisme et milieu de dépôt. L'imagerie chimique tridimensionnelle apparaît essentielle à la compréhension de matériaux hétérogènes du patrimoine chimiquement altérés qui, ont subi des processus de diagenèse et de vieillissement au fil du temps. Nous démontrons que la spectroscopie XRS à haute résolution spectrale offre une nouvelle voie d'analyse de matériaux organiques

du patrimoine culturel. Nous examinons une collection historique d'exsudats de plantes australiennes utilisées par les peuples aborigènes depuis des milliers d'années. L'analyse détaillée de la signature spectrale des transitions électroniques à partir des niveaux de cœur des atomes de carbone et d'oxygène permet d'identifier les liaisons chimiques et de comparer des sécrétions végétales appartenant à des classes chimiques distinctes (terpénoïdes, polysaccharides, composés phénoliques et aromatiques). Nous démontrons par une analyse statistique que la caractérisation et la discrimination directe des composés organiques complexes est atteinte par spectroscopie XRS, avec une bonne sensibilité et de manière non invasive. Des approches statistiques ont été développées pour traiter les données tridimensionnelles XRI et décomposer les spectres obtenus. Nous montrons que la microscopie à transmission des rayons X en balayage (acronyme anglais : STXM), dans la gamme des rayons X mous, complète les approches XRI quand la limite spatiale de ces dernières est atteinte. Nous avons analysé des pigments organiques documentés dans le manuscrit de De Mayern par STXM. Les images à l'échelle nanométrique fournissent de nouvelles informations sur la chimie du carbone de ces pigments et démontrent leur complexité chimique qui ne peut être abordée qu'à cette résolution spatiale. En conclusion, les résultats illustrent la valeur des méthodes XRS en tant que sonde spectroscopique et d'imagerie non invasive in situ de la spéciation des éléments légers dans les matériaux du patrimoine. Avec ce travail, nous fournissons une nouvelle perspective de l'exploitation de données XRS applicable à un grand nombre de systèmes organiques, hétérogènes et chimiquement complexes, et nous discutons des défis restant à surmonter et des perspectives futures de ces approches.

Title: Probing complex organic heritage materials with x-ray Raman scattering

Keywords: 3D x-ray imaging | x-ray Raman spectroscopy | Organic fossils | Plant exudates | Organic pigments | Cultural and natural heritage

Abstract: The analytical means to assess the organic composition of complex samples are limited and precious for heritage studies. The work unfolds the potentials of x-ray Raman scattering (XRS) as a non-invasive probe for the study of paleontological, archaeological and art materials. We optimize the XRS methodology required for the study of complex samples, including organic paleontological specimens and a collection of plant exudates of heritage value, and explore its ability to access the different levels of information sought. XRS is employed as a bulk, non-invasive, 3D imaging probe to study ancient organic samples to determine organic signatures and trace their evolution through time. Taking advantage of the direct tomography technique based on chemical bond contrast, we introduce 3D x-ray Raman imaging (XRI) in the field of natural heritage studies. The successive collection of XRS carbon K-edge tomographic images of an exceptionally preserved specimen, a 53 million-year old insect entrapped in amber, provides a means to assess the spatial distribution of biological remnants. The results point to the importance of characterization of paleontological specimens through imaging at the scale of the object, to understand the specimens biochemistry, molecular evolution, and interactions between the organism and the depositional setting. Three-dimensional chemical imaging appears essential for understanding chemically altered heterogeneous heritage materials that have undergone diagenesis and aging processes over time. We demonstrate that high energy resolution XRS

spectroscopy provides a new perception in the analysis of organic cultural heritage materials. We examine a historical collection of Australian plant exudates which assembles natural products used by Aboriginal peoples for thousands of years. Detailed analysis of the spectral signatures of core electron transitions in the carbon and oxygen atoms, allows us to identify chemical bonds and inter-compare plant secretions belonging to distinct chemical classes (terpenoids, polysaccharides, phenolic and aromatic compounds). We exemplify via statistical analysis that characterization and discrimination of the complex organic compounds is attained using XRS in a non-invasive manner. Additional statistical approaches have been developed to process the three-dimensional XRS imaging data and to decompose the obtained XRS spectra. We show that scanning transmission x-ray microscopy (STXM), in the soft x-ray range, complements XRS approach when its spatial limit is reached. We have analyzed organic dark-coloured pigments documented in De Mayern's manuscript by STXM. The nanoscale images provide new insights on the carbon chemistry of these pigments and demonstrate their chemical complexity that can only be addressed at the nanometric spatial resolution. In conclusion, the results exemplify the value of XRS as an in-situ non-invasive spectroscopic and imaging probe of light elements in heritage materials. Through this work we provide a new viewpoint for exploitation of XRS data in a wide range of organic, heterogeneous, and chemically complex systems, and discuss its remaining challenges and future perspectives.

Acknowledgments

This manuscript is the outcome of several years of research work that could not be carried out without the time, energy and expertise of a multidisciplinary team.

I would like to express my gratitude to Mr. Loïc BERTRAND, researcher at Université Paris-Saclay and École normale supérieure for his role as the thesis director and his help and guidance throughout these years of research. I am particularly grateful for all the help given by Mr. Jean-Pascal RUEFF, researcher at synchrotron SOLEIL and co-director of the thesis.

This work owes a lot to Mr. Uwe BERGMANN, professor at the University of Wisconsin-Madison whose friendly help, advice and support were of great help to me. Without his encouragement, this thesis would not have materialized.

I warmly thank the members of the jury for having accepted to evaluate my work and to participate in the examination: Mr. Simo HUOTARI, professor at the Department of Physics of University of Helsinki, Mrs. Caroline TOKARSKI, professor at the Université de Bordeaux, Mr. Karim BENZERARA, researcher at the Institut de Minéralogie, de Physique des Matériaux et de Cosmochimie, Mrs. Ilaria BONADUCE, associate professor at the Department of Chemistry of University of Pisa, Mrs. Marie-Angélique LANGUILLE, Researcher at the Centre de recherche sur la conservation, and Mrs. Joanne XIE, professor at École normale supérieure.

The conception of the project benefited from the opinions, suggestions, help and expertise of several scientists, whom I would like to thank: Mr. Serge COHEN, researcher at IPANEMA, Mr. Christoph SAHLE, scientist at ESRF, Mr. Dimosthenis SOKARAS, scientist at SSRL, Mr. Sylvain BERNARD, researcher at the Institut de Minéralogie, de Physique des Matériaux et de Cosmochimie, Mrs. Rachel POPELCA-FILCOFF, professor at the University of Melbourne, Mrs. Victoria BELTRAN, post-doctoral researcher at University of Antwerp, Mr. Pierre GUERIAU, post-doctoral researcher at University of Lausanne, Mr. Alessandro MIRONE, researcher at ESRF, Mr. Stefan STANESCU, scientist at SOLEIL, and Mrs. Leila SAUVAGE, paper conservator and scientist at the Rijksmuseum.

I would like to underline the constant support from the IPANEMA team, which made the completion of this work easier: Many thanks to Marie GODET, Clémence IACONNI, Tulin OKBINOGLU, Selwin HAGERAATS, Sam WEBB, Sebastian SCHÖDER, Marouane BEN JEL-

LOUL, Mathieu THOURY, Anne-Fleur BARFUSS, Bénédicte CHARBONNEL and in particular Giulia FRANCESCHIN, Maëva L'HERONDE and Regina OPRANDI, whom have been constantly supportive and encouraging.

Finally, George, you may see the concretisation of this work as the result of your continuous support and trust. Starting from my studies in Physics until today you have been selflessly present without questioning any of my choices. Doubtlesly, this work is dedicated to you.

Contents

| | |
|--|----------|
| Introduction | 1 |
| References | 3 |
| 1 X-ray Raman scattering: A hard x-ray probe of complex organic systems | 6 |
| 1.1 Introduction | 6 |
| 1.1.1 Nomenclature | 9 |
| 1.1.2 Published reviews and books | 9 |
| 1.2 A brief historical perspective | 9 |
| 1.3 Principles of XRS | 11 |
| 1.3.1 Momentum transfer dependence | 11 |
| 1.3.1.1 Low momentum transfer | 13 |
| 1.3.1.2 Higher momentum transfer | 14 |
| 1.3.2 Compton scattering | 14 |
| 1.3.3 XRS core electron excitations | 15 |
| 1.3.3.1 Hybridization of carbon | 15 |
| 1.3.3.2 Carbon molecular bonding | 17 |
| 1.3.4 XRS simulations | 19 |
| 1.3.5 Complementarity, advantages and limits over x-ray absorption spec- | |
| troscopy | 26 |
| 1.4 Experimental section | 27 |
| 1.4.1 Energy resolution | 29 |
| 1.4.1.1 Monochromators | 32 |
| 1.4.1.2 Crystal analyzers | 32 |
| 1.4.2 <i>Signal-to-noise</i> ratio | 33 |
| 1.4.3 Optimization of <i>signal-to-background</i> ratio | 34 |
| 1.4.3.1 Contribution from Compton scattering | 35 |
| 1.4.3.2 Background arising from the sample environment | 35 |
| 1.4.4 XRS 3D Imaging | 37 |

CONTENTS

| | | |
|---------|---|-----------|
| 1.4.4.1 | Spatial resolution | 38 |
| 1.5 | XRS of complex organic systems | 39 |
| 1.5.1 | Analyzing mixtures of compounds | 39 |
| 1.5.1.1 | Polycyclic aromatic hydrocarbons in crude oils | 39 |
| 1.5.1.2 | Polycyclic aromatic hydrocarbon model compounds | 40 |
| 1.5.1.3 | Natural-occurring organic systems | 41 |
| 1.5.1.4 | Biomass-derived pyrolysis and hydrothermal carbon | 46 |
| 1.5.1.5 | Lithium-ion battery electrolyte solutions | 46 |
| 1.5.2 | Looking for minor features | 49 |
| 1.5.2.1 | Paleontological organic specimens | 49 |
| 1.5.2.2 | Heteroatoms-containing PAHs | 49 |
| 1.5.3 | Resolving spatially heterogeneous systems | 51 |
| 1.5.3.1 | First examples of 3D imaging | 51 |
| 1.5.3.2 | Time-resolved XRS studies of chemical reactions | 54 |
| 1.6 | Current challenges | 56 |
| | References | 56 |
| 2 | Disentangling the chemistry of Australian plant exudates from a unique historical collection | 75 |
| 2.1 | Introduction | 75 |
| 2.2 | Results | 79 |
| 2.2.1 | Main spectroscopic properties of plant exudates | 79 |
| 2.2.1.1 | <i>Xanthorrhoea</i> resins | 79 |
| 2.2.1.2 | <i>Callitris</i> resins | 80 |
| 2.2.1.3 | <i>Eucalyptus</i> kino | 81 |
| 2.2.1.4 | <i>Acacia</i> gums | 82 |
| 2.3 | Discussion | 86 |
| 2.3.1 | X-ray Raman spectroscopy as an unconventional complement to lab-based techniques | 86 |
| 2.3.2 | Classification of compounds into chemical classes | 88 |
| 2.3.3 | Cultural uses and limitation of extant data | 91 |

CONTENTS

| | | |
|----------|--|------------|
| 2.4 | Conclusions | 91 |
| 2.5 | Materials and methods | 92 |
| 2.5.1 | Materials | 92 |
| 2.5.2 | XRS spectroscopy | 93 |
| 2.5.3 | FTIR spectroscopy | 94 |
| 2.5.4 | XRS data reduction | 94 |
| 2.5.5 | Statistical testing of XRS data classification | 95 |
| | References | 96 |
| 3 | Carbon speciation in organic fossils using 2D to 3D x-ray Raman multispectral imaging | 104 |
| 3.1 | Introduction | 104 |
| 3.2 | Results and discussion | 106 |
| 3.2.1 | Micro-scale 2D imaging of carbon on centimetric Carboniferous plants | 107 |
| 3.2.2 | Revisiting the 3D preservation of insect in amber | 110 |
| 3.3 | Conclusions and implications | 117 |
| 3.4 | Materials and methods | 118 |
| 3.4.1 | Paleontological samples | 118 |
| 3.4.2 | X-ray Raman-based spectral imaging | 119 |
| 3.4.3 | 3D reconstruction of the XRI data | 120 |
| 3.4.4 | Statistical processing of the 3D XRI data | 120 |
| | References | 120 |
| 4 | Nanoscale characterization of organic dark-coloured pigments | 125 |
| 4.1 | Introduction | 125 |
| 4.2 | Materials and methods | 128 |
| 4.2.1 | Materials | 128 |
| 4.2.2 | Scanning transmission x-ray microscopy | 129 |
| 4.2.2.1 | Sample preparation | 132 |
| 4.2.2.2 | Data processing | 132 |
| 4.2.3 | X-ray Raman scattering spectroscopy | 133 |
| 4.3 | Results | 133 |

CONTENTS

| | | |
|---------|--|------------|
| 4.3.1 | Hierarchical clustering of STXM nanoscale images | 133 |
| 4.3.2 | Charred date pits sample | 134 |
| 4.3.3 | Charred peach stone sample | 135 |
| 4.3.4 | Sticklac black sample | 139 |
| 4.3.5 | Bone black sample | 139 |
| 4.3.6 | Candle fume black sample | 141 |
| 4.3.7 | Bister samples | 144 |
| 4.3.8 | Carbon black sample | 144 |
| 4.3.9 | Vine black sample | 146 |
| 4.4 | Discussion | 147 |
| 4.4.1 | Nano-scale heterogeneity of the dark-coloured organic pigments . . . | 147 |
| 4.4.2 | The importance of the precursor material and manufacture process in the pigment's final chemistry | 147 |
| 4.4.3 | Comparison of soft-XAS and XRS carbon K-edge spectra | 150 |
| | References | 154 |
| | Conclusions and Perspectives | 160 |
| | A Supplementary information for Chapter 2 | 162 |
| A.1 | Materials and Methods | 162 |
| A.1.1 | Materials | 162 |
| A.1.2 | XRS spectroscopy | 162 |
| A.1.3 | FT-IR spectroscopy | 163 |
| A.1.3.1 | <i>Xanthorrhoea</i> resins | 163 |
| A.1.3.2 | <i>Callitris</i> resins | 164 |
| A.1.3.3 | <i>Eucalyptus</i> kino | 164 |
| A.1.3.4 | <i>Acacia</i> gums | 164 |
| A.1.4 | ICP-MS | 165 |
| A.1.5 | XRS data reduction | 165 |
| | References | 173 |

CONTENTS

| | | |
|----------|--|------------|
| B | Supplementary information for Chapter 4 | 175 |
| B.1 | Mayerne Manuscript: " <i>Pictoria, sculptoria et quae subalternarum artium</i> " . . . | 175 |
| | References | 184 |
| C | Three XRS-dedicated beamlines | 185 |
| C.1 | ESRF ID20 | 185 |
| C.2 | SSRL 6-2b | 186 |
| C.3 | SOLEIL GALAXIES | 188 |
| | References | 189 |
| D | Scientific dissemination and synchrotron experiments | 190 |
| D.1 | Scientific dissemination | 190 |
| D.1.1 | Publications | 190 |
| D.1.2 | Conferences | 190 |
| D.2 | Synchrotron experiments | 191 |
| E | Résumé de thèse | 193 |
| | List of Figures | 194 |
| | List of Tables | 197 |
| | Acronyms | 198 |

Introduction

Disentangling the chemistry of ubiquitous carbon-based compounds in ancient and art materials, although challenging, is an essential source of information in many natural and cultural heritage studies [1]. Heritage materials are chemically complex systems consisting of mixtures of differing chemical groups, including combinations of organic and inorganic phases present at different relative abundance. Often, they are characterized by multi-scale heterogeneity due to spatial variations of the chemical composition. Through the years, heritage materials have undergone ageing process or diagenesis which results in partial or complete alteration of their original chemistry. Spectroscopic (i.e. highly sensitive) and imaging approaches employed for their chemical characterization shed light on their original or altered chemistry, the undergone ageing processes or diagenesis, and their curation history.

Numerous techniques have been developed to probe carbon speciation in complex systems. Invasive approaches, based on separation techniques, have been long used for the detailed identification of organics in heritage samples, yet, the information extracted from a selected sampling area cannot address the spatial chemical complexity. Non-invasive alternatives, in particular Fourier transform infrared spectroscopy (FT-IR), optical Raman microspectroscopy, time-of-flight secondary ion mass spectrometry (ToF-SIMS), x-ray photoelectron spectroscopy (XPS), x-ray absorption spectroscopy (XAS), electron energy loss spectroscopy (EELS) are employed to characterize complex organic materials and to probe speciation of light elements, either through point analysis or imaging [2–8]. Although powerful and non-destructive, the main limitation of these techniques is the superficial information depth which imposes requirements on sample preparation and environment constraints. X-ray Raman scattering (XRS) comprises a complementary hard x-ray bulk probe of light elements (millimeters), and overcomes specific limitations of these techniques.

This thesis set out to investigate the potentials of XRS as a non-invasive, imaging and spectroscopic tool for the study of paleontological, archaeological and art materials by exploring three directions: the chemical complexity, the mixing of phases, or spatial heterogeneity. XRS is a non-resonant inelastic scattering process of hard x-rays which can probe chemical information in complex organic systems, including heritage samples [9, 10]. Using hard x-rays,

XRS provides speciation information primarily to light elements, such as carbon, whose binding energy falls in the soft x-ray region. In the XRS process, an incident photon of typical energy in the 6–15 keV range is inelastically scattered and part of its energy is transferred to excite inner shell electrons into unoccupied states [11]. This methodology enables the measurement to be done in a non-invasive way, in air, and provides information not compromised by surface contamination while ensuring that the dominant signal contribution is from the bulk of the probed material [12]. In 1967, the theoretical work of Mizuno and Ohmura established the connection between XRS and XAS [13], while the pioneer experimental work of Suzuki showed explicitly the first x-ray Raman spectra [14]. XRS is now available with the advent of extremely bright synchrotron sources [15–17]. XRS possesses the sensitivity of XAS to the chemical environment of the absorbing atom and provides information on its chemical bonding and oxidation state [18]. In addition, the scattering of hard x-ray photons by core electrons can lead to high momentum transfer which enhances the multipolar contributions compared to conventional XANES and enlarge speciation sensitivity [19]. XRS is therefore a promising alternative of soft XAS techniques – including scanning transmission x-ray microscopy (STXM) – for the study of electronic and physico-chemical properties of materials.

In *Chapter 1*, we present the fundamentals of XRS required to use the technique and discuss the main parameters of the experimental set-ups to optimize spectral and spatial resolution while maximizing signal-to-noise ratio. We critically review example applications that target on analysis of organic systems, the identification of minor spectral features and the spatially discrimination in heterogeneous systems.

Through the analysis of chemically complex samples, including organic paleontological specimens and plant exudates of heritage value, we examine the different levels of information that XRS can provide while optimizing the methodology for each system. Detailed analysis of the XRS spectral signatures of core electron transitions in the carbon and oxygen atoms, allows us to identify chemical bonds and intercompare organic-rich heritage materials. In *Chapter 2*, we report the fine spectroscopic study of well-preserved native Australian plant exudates, assembled a century ago by plant naturalists. We employ XRS to characterize the molecular compositions of well-preserved, native Australian plant exudates (*Xanthorrhoea*, *Callitris*, *Eucalyptus* and *Acacia*) from a historic collection. XRS and FT-IR provide detailed chemical information about these complex natural materials, allowing a broader understanding of their

terpenoid, aromatic, phenolic and polysaccharide compounds and subsequent chemical classification. The fundamental understanding of the chemistry of these native Australian plant exudates is the first step for their future identification in complex heritage objects.

The experimental work presented here provides one of the first investigations into how three-dimensional chemical imaging appears essential for addressing chemical complexity of altered heterogeneous heritage materials that have undergone diagenesis and aging processes over time. In *Chapter 3*, we introduce 3D x-ray Raman scattering imaging (XRI) in the field of natural heritage studies. Taking advantage of the direct tomography technique based on chemical bond contrast, we collect XRS carbon K-edge tomographic images of an exceptionally preserved specimen, a 53 million-year old ancient insect entrapped in amber, and assess the spatial distribution of organic remnants which enhance our understanding of the specimen's biochemistry, molecular evolution, and interactions between the organism and the depositional setting.

When the limit of XRS spatial resolution is reached, STXM is employed as an alternative probe for the investigation of nanocomplex organic heritage materials. In *Chapter 4*, we show how nanoscale chemical characterization provided new insights into the carbon chemistry of organic dark-coloured pigments. STXM demonstrates the complexity of artistic pigments based on carbon that cannot be addressed at the micrometric spatial resolution achieved via XRS. The nanoscale chemical heterogeneity observed in the analyzed pigments indicates a non-homogeneous distribution of organic phases, possibly a result of varied chemical transformations of the precursor materials. Statistical approaches employed for the exploitation of the XRS and STXM data facilitated the extraction of valuable information of the chemically complex organic systems studied.

Lastly, we discuss the existing challenges and the applications' perspectives of this powerful technique for complex organic systems.

References

- [1] Richard P Evershed. "Organic residue analysis in archaeology: the archaeological biomarker revolution". In: *Archaeometry* 50.6 (2008), pp. 895–924.

- [2] Francesca Casadio, Céline Daher, and Ludovic Bellot-Gurlet. “Raman spectroscopy of cultural heritage materials: overview of applications and new frontiers in instrumentation, sampling modalities, and data processing”. In: *Analytical Chemistry for Cultural Heritage* (2017), pp. 161–211.
- [3] Silvia Prati et al. “New frontiers in application of FTIR microscopy for characterization of cultural heritage materials”. In: *Topics in Current Chemistry* 374.3 (2016), p. 26.
- [4] Vincent Mazel et al. “Identification of ritual blood in African artifacts using TOF-SIMS and synchrotron radiation microspectroscopies”. In: *Analytical chemistry* 79.24 (2007), pp. 9253–9260.
- [5] Scott A Sandford et al. “Organics captured from comet 81P/Wild 2 by the Stardust spacecraft”. In: *Science* 314.5806 (2006), pp. 1720–1724.
- [6] Ann Newman and Robert Wenslow. “Solid-state Characterization Techniques”. In: *Pharmaceutical Crystals: Science and Engineering* (2018), pp. 89–121.
- [7] Simon R Kelemen et al. “Direct characterization of kerogen by X-ray and solid-state ^{13}C nuclear magnetic resonance methods”. In: *Energy & Fuels* 21.3 (2007), pp. 1548–1561.
- [8] Sylvie Derenne and Thanh Thuy Nguyen Tu. “Characterizing the molecular structure of organic matter from natural environments: An analytical challenge”. In: *Comptes Rendus Geoscience* 346.3-4 (2014), pp. 53–63.
- [9] Simo Huotari et al. “Direct tomography with chemical-bond contrast”. In: *Nature Materials* 10.7 (2011), pp. 489–493.
- [10] Rafaella Georgiou et al. “Carbon speciation in organic fossils using 2D to 3D x-ray Raman multispectral imaging”. In: *Science advances* 5.8 (2019), eaaw5019.
- [11] Winfried Schülke. “Non-resonant inelastic X-ray scattering: Regime of core-electron excitations (X-ray Raman scattering)”. In: *Electron Dynamics by Inelastic X-Ray Scattering*. New York: Oxford University Press, 2007, pp. 186–236.
- [12] Pierre Gueriau et al. “Noninvasive Synchrotron-Based X-ray Raman Scattering Discriminates Carbonaceous Compounds in Ancient and Historical Materials”. In: *Analytical Chemistry* 89.20 (2017), pp. 10819–10826.

- [13] Yukio Mizuno and Yoshihiro Ohmura. “Theory of X-ray Raman scattering”. In: *Journal of the Physical Society of Japan* 22.2 (1967), pp. 445–449.
- [14] Tadasu Suzuki. “X-ray Raman scattering experiment. I”. In: *Journal of the Physical Society of Japan* 22.5 (1967), pp. 1139–1150.
- [15] Simo Huotari et al. “A large-solid-angle X-ray Raman scattering spectrometer at ID20 of the European Synchrotron Radiation Facility”. In: *Journal of Synchrotron Radiation* 24.2 (2017), pp. 521–530.
- [16] Dimosthenis Sokaras et al. “A high resolution and large solid angle x-ray Raman spectroscopy end-station at the Stanford Synchrotron Radiation Lightsource”. In: *Review of Scientific Instruments* 83.4 (2012), p. 043112.
- [17] Jean-Pascal Rueff et al. “The GALAXIES beamline at the SOLEIL synchrotron: inelastic X-ray scattering and photoelectron spectroscopy in the hard X-ray range”. In: *Journal of synchrotron radiation* 22.1 (2015), pp. 175–179.
- [18] Joachim Stöhr. *NEXAFS spectroscopy*. Vol. 25. Springer Science & Business Media, 2013.
- [19] Michael Krisch and Francesco Sette. “X-ray Raman scattering from low Z materials”. In: *Surface Review and Letters* 9.02 (2002), pp. 969–976.

X-ray Raman scattering: A hard x-ray probe of complex organic systems

This chapter provides a review of the characterization of organic systems via x-ray Raman scattering (XRS) and a step-by-step guidance for its application. We present the fundamentals of XRS required to use the technique and discuss the main parameters of the experimental set-ups to optimize spectral and spatial resolution while maximizing signal-to-background ratio. We review applications that target the analysis of mixtures of compounds, the identification of minor spectral features and the spatial discrimination in heterogeneous systems. We discuss the recent development of the direct tomography technique, which utilizes the XRS process as a contrast mechanism for assessing the 3D spatially resolved carbon chemistry of complex organic materials. We conclude by exposing the current limitations of the technique.

1.1 Introduction

Deciphering the chemical nature and properties of complex organic systems is of paramount importance for a vast corpus of studies: from characterization of prebiotic organic systems to understand biomolecules' synthesis and the pathway to living systems [1], to the study of natural organic solids that play a major role in the global carbon cycle [2, 3], and the synthesis of new organic carbon forms [4]. The abundance and variety of organic compounds can be explained by carbon's ability to form hybridized orbitals [5] (Table 1.1). Organic species vary from simple diatomic (e.g. CN, CO, C₂, etc) and polyatomic (e.g. CH₂, CH₄, C₂H₂, HCN, CH₃OH, etc) molecules to complex molecular structures (e.g. polycyclic aromatic hydrocarbons, carbohydrates, terpenoids, steroids, flavonoids, fullerenes, epoxy compounds, etc) of synthetic or natural origin [6]. Determining the molecular composition and chemistry in complex organic systems is challenging due to multi-scale heterogeneity (i.e. spatial variations in the chemical composition), difference in relative abundance of individual components (e.g. organic phases

may be present as a minor component), and complexity of chemical composition (consisting of differing chemical groups) in the volume probed.

Historically, the strategy has been either to decompose the solids thermally before separating, identifying and quantifying the generated liquids and gases, or to employ selective chemical fragmentations, derivatizations, cleavages or ionizations before analyses [7–9]. Yet, incomplete decomposition and poorly constrained chemical transformations occurring during such procedures have long been responsible for inaccuracies. Additionally, such approaches, only yield information extracted from a selected sampling area without addressing spatial chemical complexity and require the destruction of the sample. Various non-invasive techniques, including FT-IR, Raman spectroscopy, nuclear magnetic resonance (NMR), ToF-SIMS, XPS, XAS and EELS, are widely employed to characterize the structure of complex organic materials via point analysis and imaging. These techniques are used to probe the speciation and relative quantity of carbon, nitrogen, oxygen and sulfur [10–16]. The advantage of these noninvasive techniques is that unaltered, solid samples can be analyzed, without their decomposition and destruction. Yet each of these techniques has limitations, and carbon speciation remains challenging due to a multitude of experimental constraints including sample preparation, sample environment, probe depth and sensitivity, and spatial resolution. In this review, we show how the XRS approach provides a powerful complement to these well-established technique for characterizing the speciation of light elements in complex organic materials.

X-ray absorption near edge structure (XANES) at the carbon K-edge, can be applied in complex organic systems to elucidate the local carbon bonding environment [17, 18]. Soft x-ray synchrotron-based techniques have been employed to collect carbon K-edge XANES data in diverse organic materials with spatial resolution down to the nanometric scale [19]. Despite the broad use, the short penetration depth of soft x-rays (few hundred nanometers) in the carbon K-edge range (280–320 eV) imposes restrictions on the sample preparation (e.g. thin focused ion beam (FIB) sectioning) and environment (e.g. vacuum, low-Z environment).

X-ray Raman scattering is a hard x-ray non-resonant inelastic scattering process, in which an incident photon is scattered and part of its energy is transferred to excite inner shell electrons into unoccupied states [20]. As such, XRS can probe low-energy absorption edges whose binding energy falls into the soft x-ray region while exciting in the hard x-ray regime. XRS possesses the sensitivity of x-ray absorption spectroscopy (XAS) to the chemical environment

of the absorbing atom and provides information on its chemical bonding and oxidation state. Using hard x-ray photons, XRS can overcome the limitations of low energy probes in terms of the sample environment or surface sensitivity related to the short penetration depth of soft x-rays or electrons. XRS is therefore a promising alternative of soft XAS techniques – including STXM and transmission x-ray microscopy (TXM) – for the study of electronic and physico-chemical properties of organic materials. Furthermore, XRS can probe transition symmetries which are non-accessible by XAS, providing an additional knob for investigating materials' properties.

The last two decades have seen the rapid development of XRS-based research for the study of low-energy edge transitions for a variety of organic materials [21–27], liquid systems [28–32] including water-based systems [33–49], gases [50–52] and crystals [28, 53–66]. XRS has been also employed to access transitions beyond the dipole limit (i.e. multipole transitions) in light elements [67–71], lanthanides [72–75], and actinides [76–80]. Following the pioneering work by Mao et al. [81], a considerable amount of work has been published on the use of XRS for in-situ characterization of materials under high pressure, in which the samples are enclosed by diamond anvil cells and a gasket material. The goal of high pressure XRS studies is to probe variations in the bonding characteristics, orbital hybridization, oxidation state and spin state to understand the local atomic structure and/or the changes of electronic structure of the materials under study. High pressure XRS experiments have focused on the study of various edges including the He K-edge [36], the Li K-edge [82], the B K-edge [83–86], the C K-edge [81, 87–91], the N K-edge [92–95], the O K-edge [34, 35, 37, 38, 41–43, 56, 84, 91, 96–103], the Ca L-edge [104], the Si L-edge [58, 105], the Fe L- [64, 106] and M-edges [57, 64, 107], the V M-edge [108] and the Ba N-edge [37]. Comprehensive reviews on high pressure XRS studies were provided by Rueff and Shukla [109], Lee, Eng, and Mao [104], Sternemann and Wilke [110]. XRS has been employed for in-situ time-resolved studies of chemical reactions under well-defined thermodynamic conditions aiming to understand the reaction pathways [24, 32, 111–114]. More recently, XRS studies have focused on the study of lithium compounds linked with the emerging interest in lithium-based batteries and/or energy materials in general [60, 115–121].

Building on the vastly expanded potential and its broad interest, we review here the use of XRS as a probe for organic materials. We focus on complex organic systems, which present

multi-scale heterogeneity due to chemical composition spatial variations, difference in relative abundance of their individual components (e.g. organic phases present as a minor component), or complex chemical composition (consisting of differing chemical groups) in the volume probed. We present the fundamentals of XRS and explain the main parameters of the experimental set-ups to optimize spectral and spatial resolution while maximizing signal-to-noise and signal-to-background ratio. We provide a step-by-step guidance for the characterization of organic systems for readers without extensive knowledge of XRS. Finally, we review example state-of-the-art applications that target on analysis of the mixtures of compounds, identification of minor features in samples and resolving spatially heterogeneous systems.

1.1.1 Nomenclature

X-ray Raman scattering (XRS) spectroscopy is one flavor of the non resonant branch of inelastic x-ray scattering (IXS) techniques. In the literature, x-ray Raman scattering is alternatively often referred to as non-resonant inelastic x-ray scattering (NRIXS) or shorter NIXS from core electrons. Throughout this thesis we will use the term x-ray Raman scattering.

1.1.2 Published reviews and books

This review is complementary, and will not cover topics addressed in previous reviews, particularly high-pressure XRS applications [104, 109, 110]. It will provide the main theoretical background useful for the use of the techniques in chemistry but it does not aim at substituting extensive reviews on inelastic x-ray scattering theory [122–124]. A detailed overview of the theoretical background of the XRS process is given in chapters 3 and 6 of the ‘Electron dynamics by inelastic x-ray scattering’ book by W. Schülke [20].

1.2 A brief historical perspective

* Adapted from Bergmann, Glatzel, and Cramer [125].

Although the theoretical basis for light scattering had been provided by Smekal [126] in 1923 researchers paid particular attention once inelastic scattering was proven by Raman [127]. Immediately after the observation of photons’ inelastic scattering in the optical region in 1928, Raman suggested the presence of analogous phenomena in the x-ray regime [127] and re-

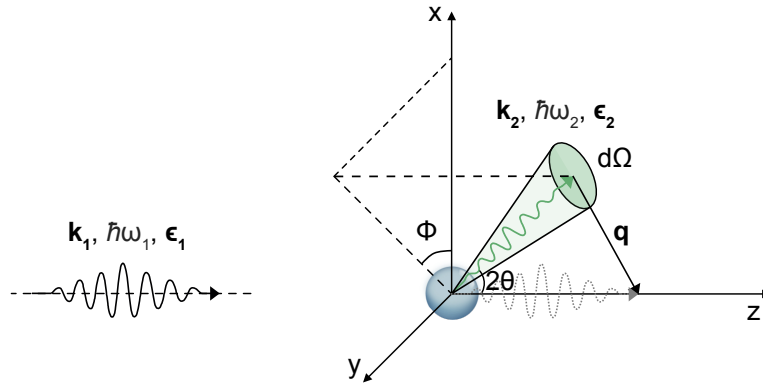


Figure 1.1: Schematic diagram of the inelastic scattering process. The incident photon, characterized by wave vector \mathbf{k}_1 , energy $\hbar\omega_1$, and polarization vector ϵ_1 , is inelastically scattered and part of its energy excites a core electron into an unoccupied state while the excess of energy and momentum is released with a scattered photon characterized by wave vector \mathbf{k}_2 , energy $\hbar\omega_2$, polarization vector ϵ_2 and momentum transfer \mathbf{q} .

searchers started hunting for the proof. Already in the same year, using a Mo x-ray tube and a block of graphite as a scattering element, Davis and Mitchel claimed to have observed a carbon K line corresponding to an energy loss of 279 eV [128]; however, the results were not reproducible [129, 130]. Finally, Ehrenberg assigned the feature observed by Davis and Mitchel to a $L\beta$ fluorescence signal of contamination of the sample by uranium. In a letter to Compton in 1936, Sommerfeld referred to the experiments by Ray [131] and suggested the presence of Raman lines due to the interaction of Röntgen rays with thin layers of carbon. Sommerfeld interpreted the presence of discrete lines in the spectrum as residues of the K electron contribution to the Compton band, composed by scattered photons exciting but not ionizing the scattering atom [132]. Das Gupta reported the observation of the effect several times in the 50s [133–136] and suggested the name “Smekal–Raman modified x-ray scattering” [134]. Finally, in 1967, the theoretical work of Mizuno and Ohmura [137] established the connection between x-ray Raman scattering and x-ray absorption spectroscopy, while the pioneer experimental work of Suzuki [138] explicitly showed the first x-ray Raman spectra.

1.3 Principles of XRS

The underlying kinematics of the inelastic x-ray scattering process is shown in Figure 1.1. An incident photon characterized by an energy $\hbar\omega_1$, a wave vector \mathbf{k}_1 and a polarization vector ϵ_1 , excites a core electron to an unoccupied state while the excess of energy and momentum is released with a scattered photon characterized by an energy $\hbar\omega_2$, a wave vector \mathbf{k}_2 and a polarization vector ϵ_2 . During the scattering process, the energy $\hbar\omega \equiv \hbar(\omega_1 - \omega_2)$ and the momentum $\hbar\mathbf{q} \equiv \hbar(\mathbf{k}_1 - \mathbf{k}_2)$ are transferred to the target electrons. Prior to the interaction with the photon, the target electrons are characterized by a state vector $|i\rangle$ and energy E_i . After the interaction, the electrons are left in a state $|f\rangle$ with energy E_f (Figure 1.3). Energy conservation requires:

$$\hbar\omega = E_i - E_f. \quad (1.1)$$

The transferred momentum is expressed as a function of the scattering angle θ by

$$q^2 = \|\mathbf{q}\|^2 = k_1^2 + k_2^2 - 2k_1k_2 \cos(2\theta). \quad (1.2)$$

For x-rays, $k_1 \approx k_2$ so that

$$q \approx 2k_1 \sin \theta \quad (1.3)$$

thus the momentum transfer depends uniquely on the scattering angle and the incoming wavelength λ since

$$k = \frac{2\pi}{\lambda}. \quad (1.4)$$

1.3.1 Momentum transfer dependence

The conceptual basis of inelastic x-ray scattering originate from a Kramers–Heisenberg formula, derived from a perturbation treatment using the interaction Hamiltonian describing the interaction between the incident electromagnetic field and the scattering electron system.

The Hamiltonian \mathcal{H} can be written down into two terms, the non-interacting term \mathcal{H}_o and the interaction Hamiltonian term \mathcal{H}_i :

$$\mathcal{H} = \mathcal{H}_o + \mathcal{H}_i. \quad (1.5)$$

The term \mathcal{H}_o describes the non-interacting electron system and is equal to

$$\mathcal{H}_o = \sum_j \frac{1}{2m} \mathbf{p}_j^2 + \sum_{jj'} V(r_{jj'}) \quad (1.6)$$

where $V(r)$ is the scalar potential of the electron system and \mathbf{p} is the momentum operator. The sum j, j' is over all the electrons of the scattering system.

The term \mathcal{H}_i describes the interaction between the electrons and the incident electromagnetic field and is equal to

$$\mathcal{H}_i = \sum_j \frac{e^2}{2mc^2} \mathbf{A}^2(\mathbf{r}_j) - \frac{e}{mc} \mathbf{A}(\mathbf{r}_j) \cdot \mathbf{p}_j \quad (1.7)$$

where $\mathbf{A}(\mathbf{r})$ is the operator of the vector potential of the interacting electromagnetic field at the electron position \mathbf{r} . The sum j is over all the electrons of the scattering system described by their momentum \mathbf{p}_j and their position \mathbf{r}_j .

The double differential scattering cross section (DDSCS), is calculated from the interaction Hamiltonian \mathcal{H}_i via Fermi's golden rule in the sudden approximation. In non-resonant XRS experiments, the incident x-ray photon energy is far away from any electron binding energy of the system and thus the \mathbf{A}^2 term of the electron-photon interaction Hamiltonian dominates. The measured quantity, described by the double differential scattering cross-section can be written as

$$\frac{d^2\sigma}{d\Omega d\omega_2} = \left(\frac{d\sigma}{d\Omega} \right)_{\text{Th}} S(\mathbf{q}, \omega). \quad (1.8)$$

The term $\left(\frac{d\sigma}{d\Omega} \right)_{\text{Th}}$ represents the Thomson differential scattering cross section which describes the photon-electron coupling strength, and is equal to

$$\left(\frac{d\sigma}{d\Omega} \right)_{\text{Th}} = r_0^2 \left(\frac{\omega_2}{\omega_1} \right) |\boldsymbol{\epsilon}_1 \cdot \boldsymbol{\epsilon}_2^*|^2 \quad (1.9)$$

where r_0 is the classical electron radius

$$r_0 = \frac{e^2}{mc^2}. \quad (1.10)$$

The dynamic structure factor $S(\mathbf{q}, \omega)$, condenses all the information about the scattering

many-body electron system that can be obtained by non-resonant XRS.

$$S(\mathbf{q}, \omega) = \sum_f \left| \langle f | \sum_j e^{(-i\mathbf{q} \cdot \mathbf{r}_j)} | i \rangle \right|^2 \delta(E_i - E_f + \hbar\omega). \quad (1.11)$$

Substituting in Eq. 1.8 the dynamical structure factor $S(\mathbf{q}, \omega)$ the non-resonant XRS scattering differential cross-section is

$$\frac{d^2\sigma}{d\Omega d\omega_2} = \left(\frac{d\sigma}{d\Omega} \right)_{\text{Th}} \sum_f \left| \langle f | \sum_j e^{(-i\mathbf{q} \cdot \mathbf{r}_j)} | i \rangle \right|^2 \delta(E_i - E_f + \hbar\omega) \quad (1.12)$$

in a system of electrons in position \mathbf{r}_j . In this form, the XRS cross-section is equivalent to an absorption cross-section with $e^{i\mathbf{q} \cdot \mathbf{r}}$ playing the role of transition operator. In the limit of small $|\mathbf{q}|$, $e^{i\mathbf{q} \cdot \mathbf{r}}$ can be expanded in a Taylor series as

$$e^{i\mathbf{q} \cdot \mathbf{r}} \approx 1 + i\mathbf{q} \cdot \mathbf{r} - \frac{(\mathbf{q} \cdot \mathbf{r})^2}{2} + \dots \quad (1.13)$$

1.3.1.1 Low momentum transfer

In the case of low momentum transfer \mathbf{q} , the second term $\mathbf{q} \cdot \mathbf{r}$ dominates. The constant term ($e^{i\mathbf{q} \cdot \mathbf{r}} \approx 1$) does not contribute to the cross-section given that the initial and final states are orthogonal ($\langle f | i \rangle = 0$). As shown by Mizuno and Ohmura [137], when the dipole approximation $\mathbf{q} \cdot \mathbf{r} \ll 1$ is fulfilled, the dynamic structure factor $S(\mathbf{q}, \omega)$ for a given core electron j can be written as

$$\frac{d^2\sigma}{d\Omega d\omega_2} \rightarrow \sum_f \mathbf{q}^2 |\langle i | \mathbf{r} | f \rangle|^2 \delta(E_i - E_f + \hbar\omega) \quad (1.14)$$

and the XRS process becomes proportional to the photoabsorption cross-section. In XAS, the conventional absorption transition operator $(\boldsymbol{\epsilon} \cdot \mathbf{r})e^{(i\mathbf{k} \cdot \mathbf{r})}$ simplifies into $\boldsymbol{\epsilon} \cdot \mathbf{r}$ in the dipolar approximation in which we set $e^{(i\mathbf{k} \cdot \mathbf{r})} \approx 1$ assuming that the orbital radius \mathbf{r} is much smaller than the wavelength k^{-1} of the absorbed radiation. The term $\boldsymbol{\epsilon} \cdot \mathbf{r}$ in XAS can be compared to the term $\mathbf{q} \cdot \mathbf{r}$ in XRS, where the momentum transfer \mathbf{q} plays the role of the polarization vector $\boldsymbol{\epsilon}$. As the momentum transfer \mathbf{q} is increasing, the dipole approximation is insufficient and it is recommended to expand $e^{(i\mathbf{k} \cdot \mathbf{r})}$ in spherical harmonics [73].

1.3.1.2 Higher momentum transfer

XRS can access non-dipole transitions if it reaches the range where $\mathbf{q} \cdot \mathbf{r} \geq 1$ [139]. The term $\mathbf{q} \cdot \mathbf{r}$ depends on the photons' incident energy and the scattering angle thus the dipole approximation ($\mathbf{q} \cdot \mathbf{r} < 1$) is not valid for all geometries. Given a constant incident energy, XRS enables dipole forbidden transitions by increasing the scattering angle θ thus increasing the transferred momentum $q \approx 2k_1 \sin \theta$ (Figure 1.9). Measurements at different q 's yield access to the entire unoccupied density of states [140].

1.3.2 Compton scattering

When the reciprocal momentum transfer q^{-1} is small (i.e. for very large q) compared to the mean orbital radius (r_c) of the absorbing atom, the scattering takes place within the impulse approximation where single-particle properties of the system are probed. The impulse approximation theory assumes that the electrons of the target can be treated as single particles when the energy and momentum of the incident x-rays are large compared to the characteristic energy E_0 (i.e. binding energy for inner shell states, Fermi energy for valence electrons) and momentum of the bound state [141, 142]. This branch of inelastic x-ray scattering is called Compton scattering and it provides access to single particles' momenta, i.e. the electron momentum distribution of the system, given that $qr_c \gg 1$ and $\hbar\omega \gg E_0$ [20].

Basic kinematics of Compton scattering

The basic kinematics of Compton scattering is shown in Figure 1.2.

The conservation of energy requires

$$\hbar\omega_1 + m_e c^2 = \hbar\omega_2 + \sqrt{p_e^2 c^2 + m_e^2 c^4} \quad (1.15)$$

where $\hbar\omega_1$ and $\hbar\omega_2$ is the energy of the incident x-ray photon and of the scattered photon respectively, $m_e c^2$ is the rest mass energy of the target electron and the term $\sqrt{p_e^2 c^2 + m_e^2 c^4}$ corresponds to the energy of the recoil electron expressed in terms of its momentum p_e (Figure 1.15).

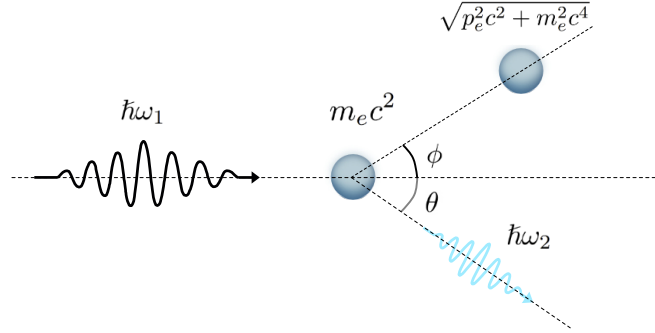


Figure 1.2: Basic kinematics of Compton scattering

The conservation of the momentum requires

$$p_e^2 c^2 = (\hbar\omega_1)^2 + (\hbar\omega_2)^2 - 2\hbar^2\omega_1\omega_2 \cos \theta. \quad (1.16)$$

The two expressions of the energy and momentum conservation (Equations 1.15 and 1.16) can be equated to give the Compton wavelength shift $\Delta\lambda_C = \lambda_f - \lambda_i$, where λ_i and λ_f are the incident and scattered wavelengths

$$\Delta\lambda_C = \frac{h}{m_e c} (1 - \cos \theta). \quad (1.17)$$

This corresponds to an energy shift ΔE_C which strongly depends on the incident energy E_i and the scattering angle θ :

$$\Delta E_C = E_i \left(\frac{E_f}{m_e c^2} \right) (1 - \cos \theta) \quad (1.18)$$

where E_f is the scattered photon energy.

1.3.3 XRS core electron excitations

1.3.3.1 Hybridization of carbon

The carbon electron configuration in the ground state is $1s^2 2s^2 2p^2$. The four valence electrons of carbon $2s^2 2p^2$ allow the formation of covalent bonds with numerous other elements, such as hydrogen, nitrogen, oxygen, sulphur. The formation of organic molecules, their geometry

and molecular bonding is often explained through the concept of orbital hybridization. Hybridized orbitals occur through a linear superposition of carbon atomic orbitals $2s$ and $2p_{x,y,z}$, in different proportions, before the creation of molecular orbitals.

Carbon hybridization occurs in three types (Table 1.1) [5, 143]:

(i) the sp^3 hybridization of carbon is a result of the $2s$ orbital with the $2p_x$ and the $2p_z$ mixing, in two combinations:

$$\Psi_1 = \sqrt{\frac{1}{4}}2s + \sqrt{\frac{1}{2}}(-2p_x) + \sqrt{\frac{1}{4}}(-2p_z) \quad (1.19)$$

$$\Psi_2 = \sqrt{\frac{1}{4}}2s + \sqrt{\frac{1}{2}}(2p_x) + \sqrt{\frac{1}{4}}(-2p_z) \quad (1.20)$$

to create a pair of sp^3 hybrid orbitals and the mixing of $2s$ orbital with the $2p_y$ and the $2p_z$, in two combinations:

$$\Psi_3 = \sqrt{\frac{1}{4}}2s + \sqrt{\frac{1}{2}}(-2p_y) + \sqrt{\frac{1}{4}}(2p_z) \quad (1.21)$$

$$\Psi_4 = \sqrt{\frac{1}{4}}2s + \sqrt{\frac{1}{2}}(2p_y) + \sqrt{\frac{1}{4}}(2p_z) \quad (1.22)$$

to create another pair of sp^3 hybrid orbitals. In total, four sp^3 tetrahedral hybrid orbitals are formed.

(ii) The sp^2 hybridization of carbon is the result of mixing the $2s$ orbital with the $2p_x$ and $2p_z$, in two combinations:

$$\Psi_1 = \sqrt{\frac{1}{3}}2s + \sqrt{\frac{1}{2}}(-2p_x) + \sqrt{\frac{1}{6}}(2p_z) \quad (1.23)$$

$$\Psi_2 = \sqrt{\frac{1}{3}}2s + \sqrt{\frac{1}{2}}(2p_x) + \sqrt{\frac{1}{6}}(2p_z) \quad (1.24)$$

to form a pair of sp^2 hybrid orbitals and the mixing of the $2s$ orbital with the $2p_z$

$$\Psi_3 = \sqrt{\frac{1}{3}}2s + \sqrt{\frac{2}{3}}(-2p_z) \quad (1.25)$$

to form the third hybrid orbital. In total, three sp^2 planar hybrid orbitals are formed and one perpendicular $2p_y$ orbital remains unaffected.

(iii) The sp hybridization of carbon is the result of mixing the $2s$ orbital with the $2p_x$, in the two possible orientations:

$$\Psi_1 = \sqrt{\frac{1}{2}}2s + \sqrt{\frac{1}{2}}(-2p_x) \quad (1.26)$$

$$\Psi_2 = \sqrt{\frac{1}{2}}2s + \sqrt{\frac{1}{2}}(2p_x) \quad (1.27)$$

to form a pair of linear sp hybrid orbitals, leaving the two perpendicular $2p_z$ and $2p_y$ orbitals unaffected.

1.3.3.2 Carbon molecular bonding

Carbon atoms are involved in the formation of two bonds: the π and σ . The overlap of two atomic orbitals (hybridized or unhybridized) gives rise to two molecular orbitals (MO): a bonding orbital (i.e. π or σ) with energy lower than the atomic orbitals and an antibonding orbital (i.e. π^* or σ^*) with higher energy. The higher energy antibonding orbital is empty in the ground state. The σ bond is formed by the overlap of orbitals where the center of the electron density are on the common axis to the two nuclei. For example, for the formation of C–H bond, the carbon sp^3 orbital interacts with the hydrogen $1s$ orbital to form the σ_{CH} bonding orbital and the empty in the ground state, σ_{CH}^* antibonding orbital. A π bond is formed by the overlap of adjacent p atomic orbitals whose axes are parallel. The formation of a double bond, as in alkenes (e.g. $CH_2=CH_2$), is a result of a combination of a σ and a π bond. A triple bond, as in alkynes (e.g. $H-C\equiv C-H$) is formed by the combination of two π and one σ bond. The excitation of a core electron into a π^* or a σ^* orbital, due to interaction with a photon, is referred to as a $1s-\sigma^*$ or $1s-\pi^*$ transition and the energy required for the transition can be characteristic of the molecule under study (Table 1.2, 1.3, and Figure 1.4, 1.5).

Within the limits of the dipole approximation, XRS provides access to core-level excitation spectra of low- Z materials, comparable with absorption edges accessible by soft x-rays absorption spectroscopy. Similarly to XAS, in XRS spectroscopy, we observe the transitions of core electrons to bound unoccupied states (i.e. “pre-edge” transitions) (Figure 1.3). In isolated

| Hybridization | Examples | Molecular orbitals |
|---------------|---|--|
| sp^3 | Alkanes (e.g. CH_4) | 4 sp^3 tetrahedral orbitals |
| sp^2 | Alkenes (e.g. C_2H_4) | 3 planar sp^2 orbitals and 1 perpendicular p orbital ($2p_z$) |
| f sp | Alkynes (e.g. C_2H_2) | 2 linear sp orbitals and 2 perpendicular p orbitals ($2p_{y,z}$) |

Table 1.1: Hybridization of carbon orbitals [5]. Carbon hybridization occurs in three types: the sp^3 , sp^2 , and sp hybridization.

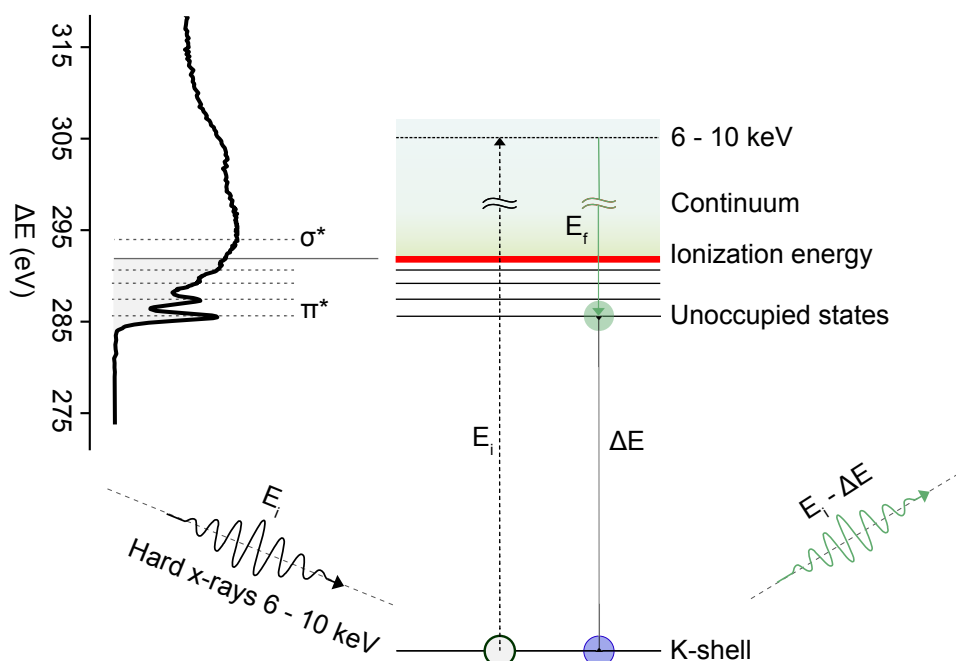


Figure 1.3: X-ray Raman scattering induced transitions of core electron.

molecules, the highest occupied and lowest unoccupied states are often referred to as “highest occupied molecular orbital (HOMO)” and “lowest unoccupied molecular orbital (LUMO)”, respectively. Thanks to the sensitivity to the molecular orbitals, the spectral features close to the absorption edge are related to the chemical environment of the absorbing atom and provide information on its chemical bonding and oxidation state.

A database of inner shell excitation spectra, gathering a large number of carbon and oxygen K-edges spectra of gas phase atoms and molecules recorded by EELS is provided by Hitchcock and Mancini [144] (Figures 1.4,1.5). STXM carbon K-edge spectra of reference compounds are also provided by Solomon et al. [145] and Le Guillou et al. [146].

1.3.4 XRS simulations

Calculations of the spectra of materials (solids, molecules or liquids) are possible using several codes, which can take into account the q dependence and non-dipolar effects. The computing scheme differs depending on the type of final state involved the XRS process. One electron calculations implemented at ERKALE [158], FEFF [140], FDMNES [71], StoBe deMon [159, 160] or Quantum ESPRESSO [161–163] will work well for delocalized final state such as for the carbon

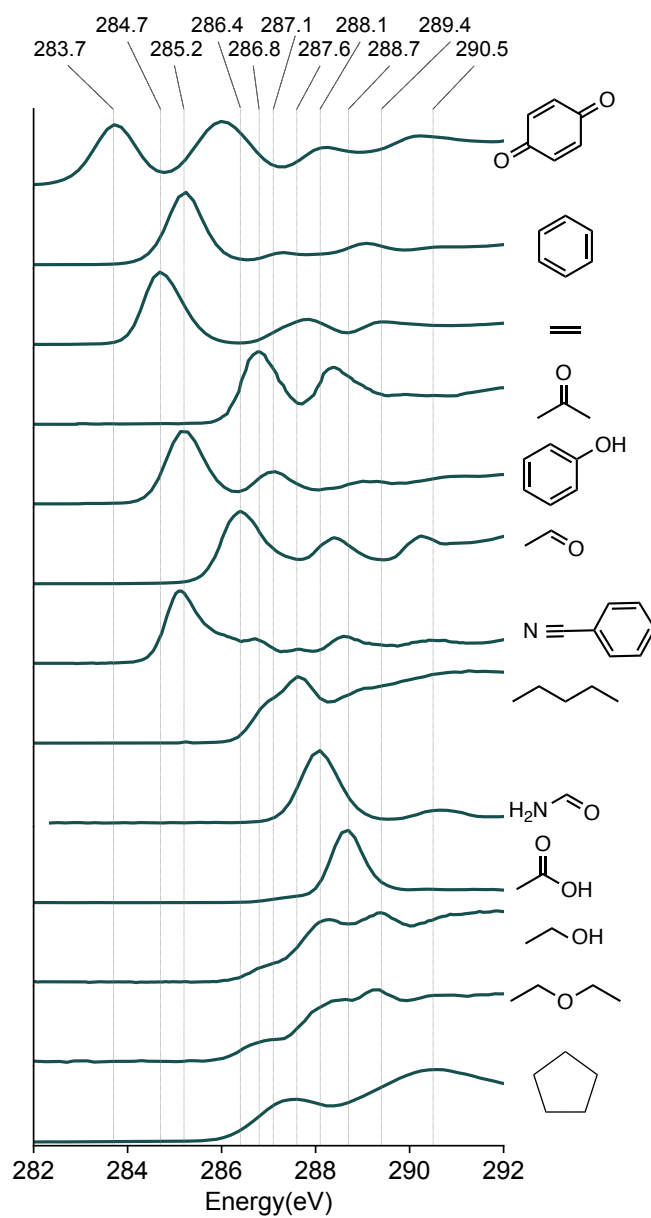


Figure 1.4: Carbon core excitation reference spectra of gas phase molecules recorded by EELS. Data: Hitchcock and Mancini database [144].

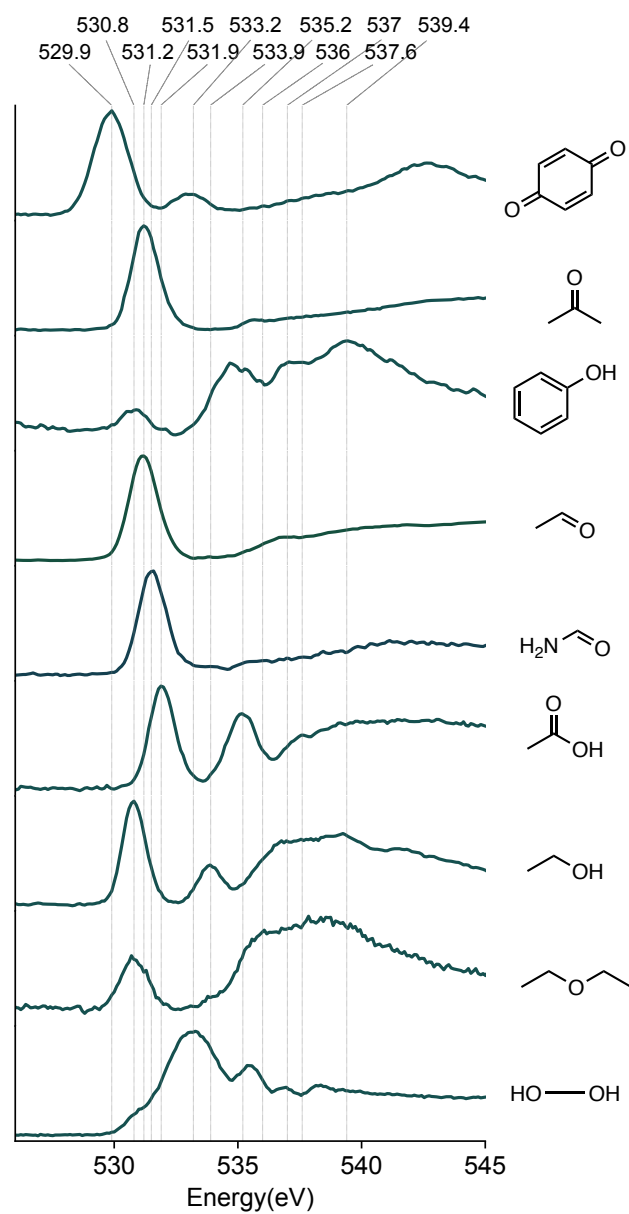


Figure 1.5: Oxygen core excitation reference spectra of gas phase molecules recorded by EELS. Data: Hitchcock and Mancini database [144].

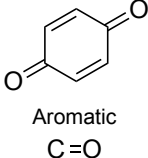
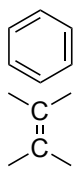
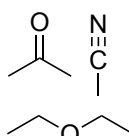
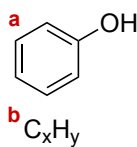
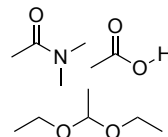
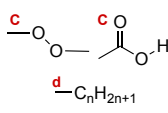
| | Assignment | Energy (eV) | Transitions |
|---|---|-------------|--|
|  | Aromatic carbonyl (C=O) and/or quinone [147] | 283–284.5 | 1s– π^* |
|  | Aromatic and/or olefinic carbon [146] | 285.2–285.6 | 1s– π^* |
|  | Ketones ($R_2C=O$)/ nitriles ($C\equiv N$)[146]/ ethers ($R-O-R'$)[148] | 286–287 | 1s– π^* |
|  | Phenols ($Ar-OH$) (287–287.3 eV) [149]/ aliphatics (C_xH_y) (287.3–288 eV) [146] | 287–288 | ^a 1s– π^* ^b 1s–3p/ σ^* |
|  | Amides ($R-C(=O)-N(R',R'')$)/ carboxyl ($-C(=O)OH$)/ acetal carbon ($R_2C(OR')_2$, $R'\neq H$)[146] | 288.3–288.8 | 1s– π^* |
| R–OH | Alcohols ($R-OH$) [150] | 289–289.6 | 1s–3p/ σ^* |
|  | Additional 1s– π^* transitions of carboxylic or peroxide groups/ alkyl carbon [150, 151] | 290–290.9 | ^c 1s– π^* ^d 1s–4p |
| – | Graphitic materials display an exciton at 291.5 eV which reflects the electron delocalization over several aromatic units [151] | 291.5 | 1s– σ^* |

Table 1.2: Characteristic core electron transitions at the carbon K-edge of simple molecules.

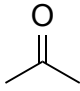
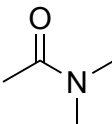
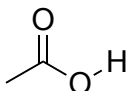
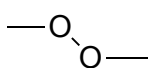
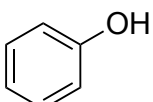
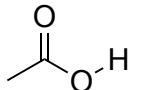
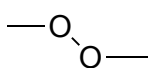
| | Assignment | Energy (eV) | Transitions |
|---|--|-------------|----------------|
|  | Ketones ($R_2C=O$ (531.3 eV)[152]/ | 530.8–531.6 | 1s- π^* |
|  | Amides $R-C(=O)-N(R',R'')$ (531.5 eV)[153] | | |
|  | Carboxyls ($-C(=O)OH$)[154] | 531.9–532.3 | 1s- π^* |
|  | Peroxides ($ROOR$) [155] | 533–533.5 | 1s- σ^* |
| $R-OH$ | Alcohols ($R-OH$) [156] | 533.9–534.7 | 1s- σ^* |
|  | Phenols ($Ar-OH$) [157]/ | 535.2–535.7 | 1s- π^* |
|  | carboxyls ($-(C=O)OH$) [154] | | |
|  | Excitations to Rydberg MO's (Peroxides ($ROOR$) [155]) | 536.3–537 | 1s-3s |
| $R-O-O-R$ $R-OH$ | Peroxides ($ROOR$) [155]/ Alcohols($R-OH$) [156] | 537–538.5 | 1s- σ^* |

Table 1.3: Characteristic core electron transitions at the oxygen K-edge of simple molecules.

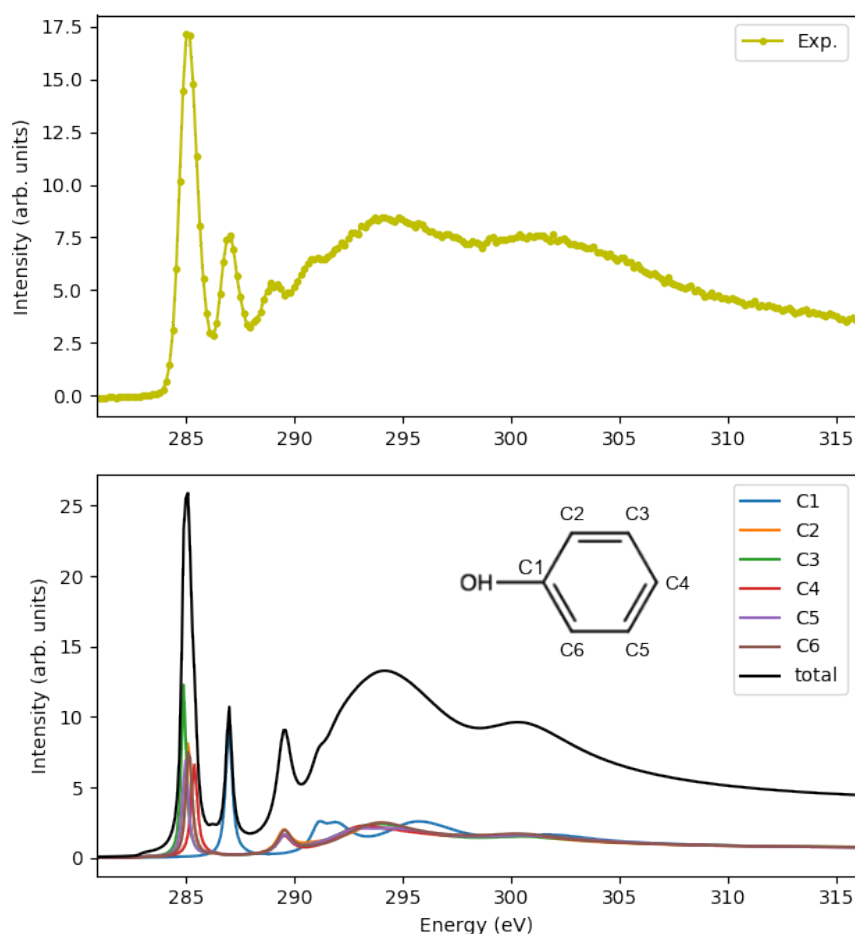


Figure 1.6: Calculation of phenol molecule XRS spectrum. Experimental carbon K-edge XAS spectrum in phenol molecule [from Francis and Hitchcock [168]] (circles) and corresponding computed XRS spectrum (lines) at $q = 1 \text{ \AA}$. The C's refer to the different carbon atoms as labeled in the inset.

K-edge. An illustration of such approaches is given in Figure 1.6 and 1.7. OCEAN implements a two-particle code which considers more exactly the interactions between the core hole and the excited electron. The XRS spectra are calculated by solving the Bethe-Salpeter equation [164, 165]. Finally, localized multiplets' features require atomic like multi-electrons codes such as Cowan's code [166] or Quanty [167]. All these codes offer XRS dedicated modules.

As an illustration, we have computed the XRS spectrum in the phenol molecule by FDMNES using a cluster of 4 \AA radius, at $q = 1 \text{ \AA}$, here compared to EELS data. The results are shown in Figure 1.6. The calculations provides a realistic description of the XRS spectra including multiple scattering effects, even though spectral differences remain. Interestingly, the spectral contributions of all atoms present in the considered atomic cluster can be singled out. In phenol, this spectral decomposition indicates that the main resonance at 285 eV comes

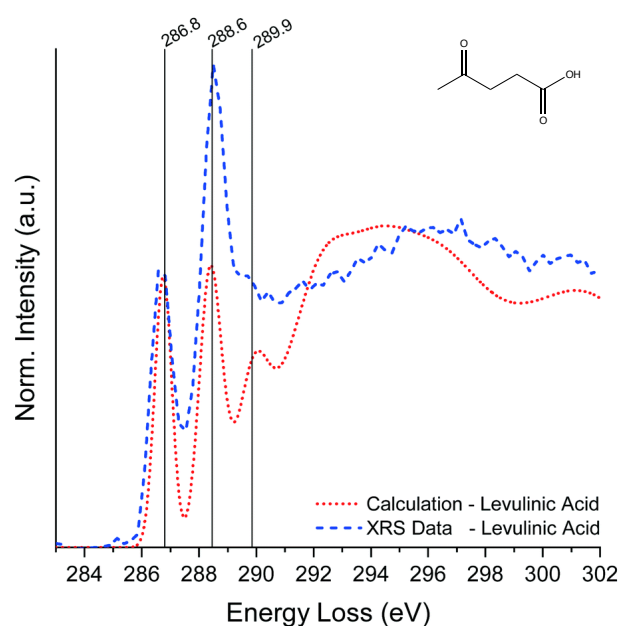


Figure 1.7: Density functional theory (DFT) calculation of levulinic acid XRS spectrum. Experimental carbon K-edge XRS spectrum (blue) and computed XRS spectrum (red) of levulinic acid. Higgins et al. [27] performed DFT calculations (ERKALE software) to compute the theoretical XRS spectrum, at momentum transfer $q=4.5 \text{ \AA}^{-1}$ (average experimental value). The experimental core electron transitions are matching with the calculation, however the experimental intensity is not well predicted. Source: Reproduced from Higgins et al. [27].

from the aromatic carbons while the 287 eV feature originates from the hydroxyl group (C1 atom). The same atom also contributes to the spectral weight at higher energy around 292 eV. This departs from the simplistic view which relates one single characteristic resonance energy to a given chemical group e.g. carboxyl. Thus, calculations can be an efficient aid to interpret the XRS data.

1.3.5 Complementarity, advantages and limits over x-ray absorption spectroscopy

While the most commonly used x-ray methods to study low-Z elements are conventional XAS techniques using soft x-rays, there are certain samples and sample conditions, where the application of more penetrating hard x-rays is advantageous and in some cases critical. XRS offers this capability and can be performed *in-situ* and *in-operando* (e.g. using a chemical reaction cell), under ambient conditions (atmospheric pressure, regular humidity and room temperature), under extreme conditions (e.g. using a furnace or diamond anvil cell) and in its natural phase (solid, liquid, or gas). As hard x-rays penetrate deep into the sample, it does not have to be surface-cleaned or diluted (to avoid saturation in fluorescence yield-detected XAS). XRS thus overcomes several difficulties related to the soft x-ray probe of conventional low-Z XAS techniques, where the samples have to be either specifically prepared or altered, often in an invasive manner, or studied in a vacuum chamber. For example, scanning transmission x-ray microscopy (STXM) requires ultra thin sections, (thickness lower than the attenuation length of the soft x-rays) usually prepared via ultramicrotomy or FIB techniques, which may be risky to the sample. XRS spectral shape is not affected by self-absorption processes, contrary to soft x-rays studies in which spectral saturation can be observed due to self-absorption. While the bulk sensitivity of the hard x-ray probe has practical advantages, by averaging the signal over a larger volume, XRS is not sensitive to spatially resolve nanoscale heterogeneity.

Both XRS and STXM spectroscopy are affected by angular dependence. As an example, for highly oriented pyrolytic graphite (HOPG) the intensity of π^* transitions is minimized when the angle of incidence (α) between the synchrotron beam and the *c*-axis of HOPG is $\alpha = 0$, while the intensity of σ^* transitions is maximized [169] (Figure 1.10 B). However, performing bulk XRS measurements provides a statistically significant assessment of carbon speciation compared to soft-XAS experiments. Collecting a spectrum of highly oriented systems (e.g. non-powder graphitic-species) through STXM is challenging due to the polarization-

dependence of core transitions, although it can be achieved through control of the polarization of the incident beam.

Contrary to XAS, XRS measurements may yield access to the unoccupied density of states beyond the dipole limit [170] when the momentum transfer of the scattered photon, q , is large [139] (see subsection 1.3.1.2). This can lead to new spectral features that can be exploited for gaining chemical information of enhanced imaging contrast.

The main limitation of XRS is the small cross-section of the non-resonant inelastic scattering process (on the order of few barns), which is orders of magnitudes lower than the probability of photo-absorption process (Mbarns) (Figure 1.8). A successful XRS experiment thus requires a high flux, monochromatic incident beam and a large solid-angle detection system $d\Omega$ (Figure 1.1) of the inelastically scattered x-rays with high spectral resolution.

Additional limitations of XRS signal detection apply when targeting on the characterization of heterogeneous systems. When the sample consists of organic and inorganic phases, signal detection of the XRS signal coming from light elements can be hindered due to absorption of the photons by heavier elements present. Furthermore, since XRS is a non-resonant scattering process, the measured signal will have contributions from all electrons; i.e. the more electrons there are in the sample compared to the targeted core electrons under study (two 1s electrons in the case of carbon K-edge), the more difficult it is to measure the XRS signal.

1.4 Experimental section

Given the low cross section of the XRS process, the brightness of the x-ray source is a vital parameter to perform a successful XRS experiment. Brightness is defined as the number of photons in a certain bandwidth per second and per mm^2 and mrad^2 . A synchrotron source is 10^9 to 10^{15} times brighter than an x-ray tube source (with a brightness of 10^8 photon/s/ $\text{mm}^2/\text{mrad}^2$). Synchrotron radiation covers the x-ray energy region with a brightness between 10^{17} and 10^{23} photon/s/ $\text{mm}^2/\text{mrad}^2$ [172, 173]. Since the wide availability of synchrotron radiation and the first XRS spectroscopic applications [174, 175], a number of cutting-edge end-stations have been developed dedicated to inelastic scattering from core electrons. A list of worldwide hard x-ray beamlines located in various synchrotron facilities, equipped with end-stations dedicated for XRS experiments are summarized in Table 1.4.

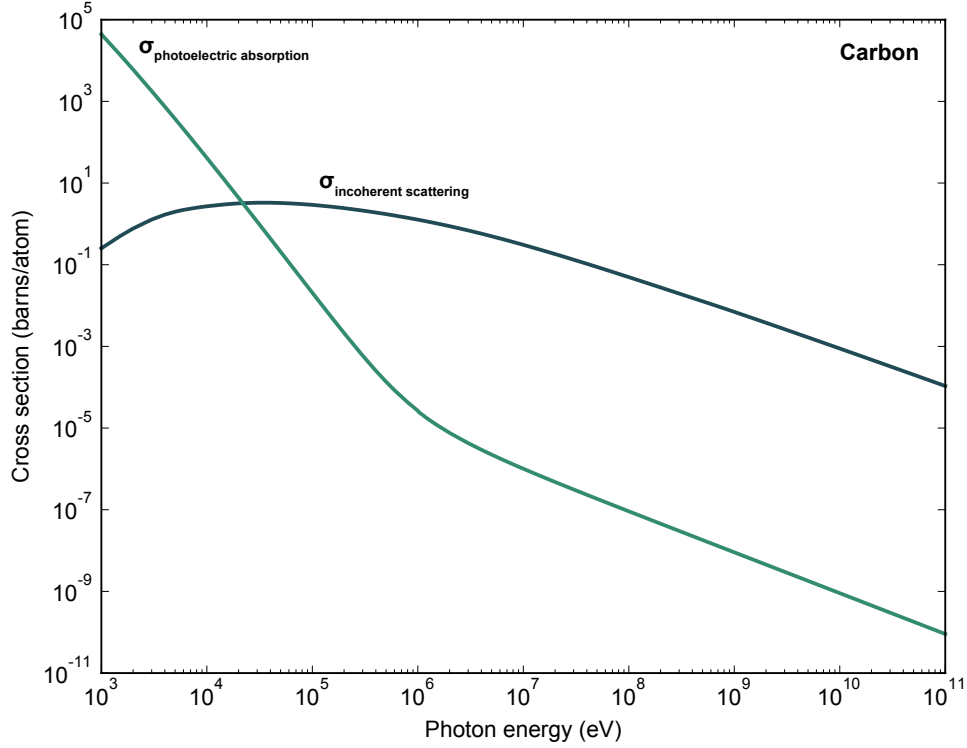


Figure 1.8: Cross section of incoherent scattering and photoelectric absorption in carbon as a function of energy. Data from Berger et al. [171], XCOM: Photon Cross Section Database.

| Synchrotron facility | Beamline | Energy range (keV) | Resolving power $(\Delta E/E)_m$ | Monochromators | Beam size $V \times H$ (μm^2) |
|----------------------|----------------|--------------------|--|--|--|
| SSRL | 6-2b [176] | 4–18.2 | 1×10^{-4} 3×10^{-5} | Si(111) ^a Si(311) ^a | 150 × 400 |
| APS | 16-ID-D [177] | 4.5–37 | 1×10^{-4} | Si(111) ^a | 3 × 5 [*] |
| SPring8 | BL12XU [178] | 4.5–30 | 1.4×10^{-4} 1.5×10^{-5} 5×10^{-6} | Si(111) ^a Si(400) ^c Si(333) ^c | 80 × 120 |
| SOLEIL | GALAXIES [179] | 2.3–12 | 1×10^{-4} 5×10^{-5} 1×10^{-5} | Si(111) ^a Si(220) ^c Si(220) ^d , $\alpha = 9^\circ$ | 30 × 80 10 × 10 [*] |
| ESRF | ID-20[180] | 4–20 | 1.1×10^{-4} 2.8×10^{-5} 1.6×10^{-6} 8.7×10^{-6} | Si(111) ^a Si(311) ^b Si(NN0) ^d , $\alpha = 4^\circ$ Si(NNN) ^d , $\alpha = 5^\circ$ | 50 × 300 8 × 7 [*] |
| PETRA III | P01[181] | 2.5–80 | 1.5×10^{-4} 6.7×10^{-5} | Si(111) ^a Si(311) ^b | 100 × 200 13 × 15 [*] |

Table 1.4: Hard x-ray beamlines equipped with end-stations dedicated for XRS experiments. ^a2-bounce fixed-exit monochromator, ^b2-bounce channel-cut post monochromator, ^c4-bounce high resolution symmetric channel-cut post monochromator, ^d4-bounce high resolution asymmetric channel-cut post monochromator, ^{*} Kirkpatrick-Baez (KB) configuration

We collect an XRS spectrum by varying the energy transfer $\Delta E = E_i - E_f$ in the range of the absorption edge of interest (Figure 1.9). To obtain the energy transfer measurements, one can either change the incident energy E_i at fixed scattered energy E_f or change the scattered energy E_f at fixed E_i . In a standard procedure widely adopted for XRS experiments, the beamline monochromator (thus scanning the incident energy E_i) is scanned in the range of the absorption edge of interest, while the spectrometers are kept at a fixed analyzing energy (E_f). This approach, known as ‘inverse geometry’, is the most practical one, as it is easier to scan the beamline monochromator than an analyzer. Its downside is that momentum transfer varies as a function of incident energy.

The spectrometers in the various beamlines end-stations dedicated for XRS studies are built based on multiple Bragg crystal analyzers positioned in back-scattering angles close to 90° . This approach allows the high-resolution monochromatization of the incident and of the scattered photons and ensures a large solid angle of detection and high efficiency over the whole energy range [182].

1.4.1 Energy resolution

The overall energy broadening of the experimental data can be discussed under two headings: the instrumental broadening (i.e. the energy bandwidth of the monochromatized incident x-ray beam $(\Delta E/E)_m$ and of the spectrometer resolution, which includes the analyzer crystals’ contribution $(\Delta E/E)_a$) and the lifetime broadening. The excitation of a core electron during the XRS process implies the formation of a core-hole with a finite lifetime. Subsequently, the system will respond by filling the core hole with an electron from an upper level while the excess of energy is released through emission of Auger electrons or fluorescence photons. Heisenberg uncertainty principle implies

$$\Gamma \approx \hbar/\tau \quad (1.28)$$

where τ is the lifetime of the final state and Γ is the full width of the resonance that contributes to the energy resolution. The finite lifetime corresponds to an uncertainty in energy, which limits the energy resolution of the XRS spectra. The larger the atomic number Z and the deeper the core hole, the larger is the number of higher energy level electrons that are available to drop

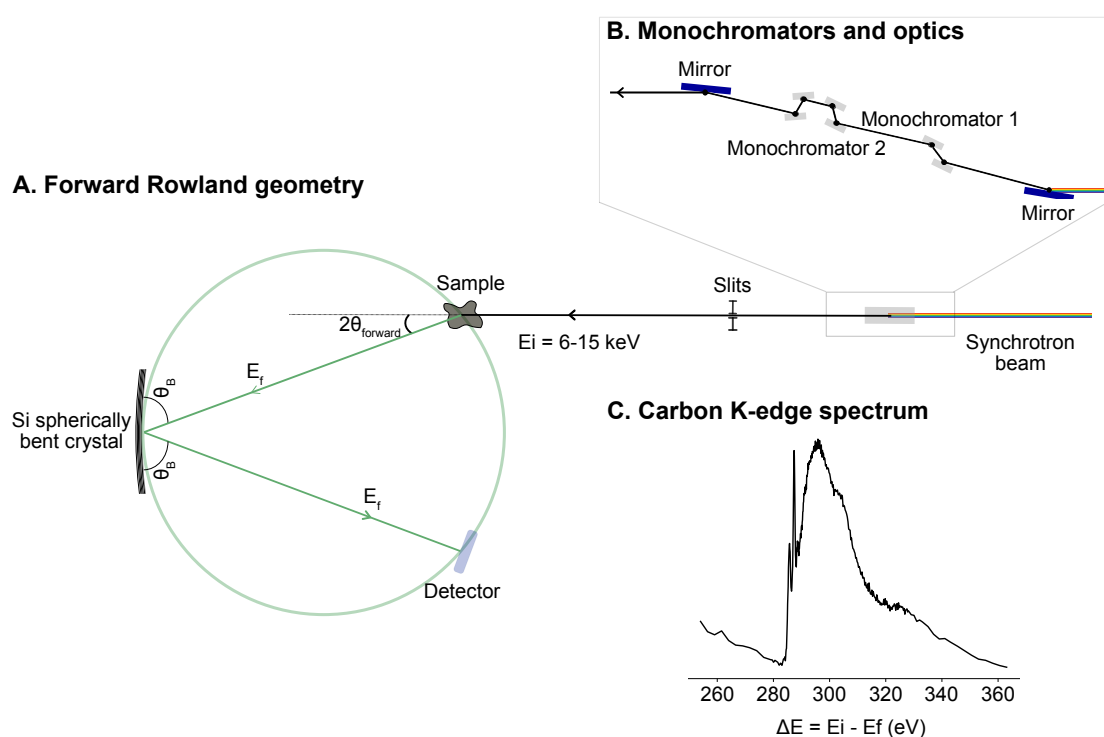


Figure 1.9: Schematic representation of the XRS experimental set-up. A tunable monochromatic x-ray beam with incident energy E_i interacts with the sample. The x-rays scattered off the sample at a lower energy E_f are detected to determine the energy transfer $E_i - E_f$. The XRS spectrum is obtained when the energy transfer $E_i - E_f$ is varied over the absorption edge of interest (e.g. 280–320 eV for the carbon K-edge). The detection system consists of spherically bent crystal analyzers and a detector placed in a Rowland circle geometry.

and fill the core hole, thus the shorter is the core-hole lifetime τ , which results in larger energy uncertainty. The lifetime broadening can be represented by a contribution of Lorentzian shape. If the instrumental resolution is large compared to the lifetime broadening the lineshapes of the core excitation spectra peaks are described by a Gaussian function. The overall resolution is represented by a Voigt function, which is the convolution of a Gaussian (G) and a Lorentzian (L):

$$\left(\frac{\Delta E}{E}\right) = G * L. \quad (1.29)$$

While the broadening of the energy width due to the nature of the process (i.e. lifetime of the core-hole) is intrinsic and cannot be adjusted, the instrumental broadening can be minimized to obtain the most advantageous overall energy resolution for the experiment.

To optimize the instrumental energy resolution given by:

$$\left(\frac{\Delta E}{E}\right)_{ins} = \left[\left(\frac{\Delta E}{E}\right)_m^2 + \left(\frac{\Delta E}{E}\right)_a^2 \right]^{1/2} \quad (1.30)$$

the incident beam's $((\Delta E/E)_m)$ and the analyzers' $((\Delta E/E)_a)$ energy resolution should be comparable. The selection of incident beam and scattered photons' wavelengths is obtained through crystal diffraction following Bragg's law:

$$2d \sin \theta_B = n\lambda \quad (1.31)$$

where θ_B is the Bragg angle of the crystal planes, the integer n corresponds to the order of reflection, λ is the wavelength of the photons, and d is the lattice spacing of crystallographic planes. For a cubic crystal (such as silicon), it is given by:

$$d = \alpha / (h^2 + k^2 + l^2)^{1/2} \quad (1.32)$$

where α is the lattice parameter and h, k, l are the Miller indices. To monochromatize the x-ray beam at a given energy value E , the Bragg angle, θ_B , should be set such as:

$$\theta_B = \arcsin \frac{\lambda}{2d} = \arcsin \left(\frac{hc}{2dE} \right). \quad (1.33)$$

The energy resolution $(\Delta E/E)$ of a Bragg crystal is given by the derivative of Equation 1.31:

$$\left| \frac{\Delta E}{E} \right| = \left| \frac{\Delta \lambda}{\lambda} \right| = \Delta \theta_B \cot \theta_B. \quad (1.34)$$

It is therefore determined by the angular spread $\Delta \theta_B$ and the Bragg angle θ_B . Honkanen and Huotari [183] and Honkanen et al. [184] provide an accurate description of the analyzers resolution considering the dynamical theory of diffraction.

1.4.1.1 Monochromators

X-ray monochromators are devices based on crystals diffraction expressed by Bragg's law (Equation 1.31) and are used to select a range of energies, thus making the synchrotron beam monochromatic to a certain bandwidth. The design of the monochromator may vary for each beamline and the energy range is selected based on the combination of crystals used, their orientation and geometrical considerations (Table 1.4). Monochromator's x-ray diffraction has an intrinsic angular width known as the Darwin width [185]. Monochromators are usually designed in combination of two crystals and monochromator's broadening (below the Darwin width) can be reduced by slightly misaligning the two successive x-ray crystal diffractions [186].

All XRS-dedicated beamlines are equipped with a Si(111) monochromator ($a_{\text{Si}}=5.43\text{\AA}$ at 77 K, $d=a_{\text{Si}}/\sqrt{3}$ for $h = k = l = 1$) with an energy resolution of $\approx 10^{-4}$, corresponding to $\Delta E \approx 1.2$ eV at $E \approx 10$ keV. To improve energy resolution, additional monochromatization stages are often introduced in beamline's design (Figure 1.9). The overall energy resolution obtained by the addition of post-monochromators in various beamlines performing XRS experiments is summarized at Table 1.4.

1.4.1.2 Crystal analyzers

A practical way to perform experiments in a Rowland circle is the Johann approximation. In the Johann geometry, the analyzer surface is spherically bent with a bending radius equal to the Rowland circle diameter [187]. The keystone of Johann-type spectrometers developed for inelastic scattering experiments are the spherically bent crystal analyzers which are combined to collect the scattered photons from a large solid angle, while selecting a specific photon energy ($\hbar\omega_2$) and focusing the scattered beam onto the detector. To sufficiently select a band of

energies of the radiation scattered-off the sample, the analyzer crystals are positioned at Bragg angles θ_B close to 90° . In such case, the angular divergence $\Delta\theta_B$ has the smallest contribution to the energy resolution ($\cot\theta_B \rightarrow 0$) (Equation 1.34). Bergmann and Cramer [182] describe in detail other geometrical contributions to the instrumental energy resolution, which are minimized when Bragg angle is close to 90° .

Given that the analyzers are positioned at back-scattering Bragg angles (slightly lower than 90°), the main contribution to the analyzer resolution is the angular compression [183, 184, 188]. Bending a crystal analyzer induces a stress (i.e. angular strain) perpendicular to its surface, which causes a lattice deformation and results in broadening of reflectivity curve's bandwidth. The theoretical background provided by Takagi and Taupin [189, 190] describes the diffraction properties of bent analyzer crystals while neglecting the angular compression contribution. This approach usually predicts higher resolving power of the analyzer compared to the experiment. Honkanen et al. [184] successfully modeled the analyzers' reflectivity curves by taking into account the angular compression and visualized the angular stress, which has a radial-like dispersion over the surface of the crystal analyzer. The reflectivity curve (i.e. quasi-elastic line) is measured by scanning the incident photon energy across the range of the analyzer energy (given by Equation 1.31). In practice, improving the energy resolution of the experiment can be achieved by increasing the bending radius or decreasing the analyzer area. Introducing mask apertures in front of the analyzers efficiently reduces the strain-induced contributions to the energy resolution which is larger from the outer radial part of the analyzer crystal [191]. The theoretical background to calculate the internal stress and strain fields of spherically bent crystals is provided by Honkanen and Huotari [183]. An alternative to the conventional spherically bent crystals is the use of bent-diced crystals. For bent-diced crystals, a grid of stress-relief cuts are introduced to minimize lattice deformation and achieve higher energy resolution performance [192].

1.4.2 *Signal-to-noise ratio*

We define *noise* as the random, unbiased signal in a measurement. The irreducible minimum level of noise present in the experiments is the so-called *shot noise* arising from the counting statistics. *Shot noise* describes any random uncertainty in a physical quantity caused by counting statistics of the discrete events that underlie the phenomenon. If the number of photons

received per second (i.e. counts) has an average value N and the photons are randomly spaced, the probability to detect k photons per second is given by the Poisson distribution

$$P(k) = \frac{N^k e^{-N}}{N!}. \quad (1.35)$$

For a large number of photons, the Poisson distribution tends towards a Gaussian distribution and the probability of detecting k photons per second is given by

$$P(k) = \frac{1}{\sqrt{2\pi}\sigma} e^{-(k-N)^2/2\sigma^2} \quad (1.36)$$

with a mean of N and standard deviation of $\sigma = \sqrt{N}$, the signal-to-noise ratio (SNR) ratio is given by

$$\text{SNR} = N/\sqrt{N} = \sqrt{N}. \quad (1.37)$$

Overall, to improve the statistical accuracy of a measurement (i.e. increase the SNR) by one order of magnitude, one should increase the number of counts by two orders of magnitude. The basic approach currently being adopted to optimize the *signal-to noise* ratio for XRS experiments is the use of a single point detector for multiple crystal analyzers [191, 192], although the drawback of such configuration is that the data recorded averages over a range of scattering angles. Considering that XRS spectra depend on the momentum transfer, and thus on the scattering angle, ideally we should interpret separately the signal of each crystal analyzer. However, given the large number of crystals used in most of state-of-the-art spectrometers, such approach can complicate data analysis.

Noise is also generated from the electronics used to amplify and process the detector signal. Additional sources of noise can be due to rapid fluctuations during data collection such as rapid changes affecting detectors (temperature or pressure of the gas in an ion chamber) and effects linked to variations in electrons' orbit in the storage ring.

1.4.3 Optimization of *signal-to-background* ratio

Every XRS spectrum shows a background signal arising from other physical processes not directly related to the XRS process. The main physical processes introducing an additional signal during an XRS experiment can be divided into two categories: (a) additional contribu-

tions from inelastic scattering, in particular Compton scattering, and (b) background arising from the sample and its environment (e.g. stray scattering, fluorescence).

1.4.3.1 Contribution from Compton scattering

A careful selection of the momentum transfer will help minimizing the contribution from Compton scattering [193]. During an XRS experiment, the Compton energy shift ΔE_C (Equation 1.18) can fall in the energy range of the XRS signal, the Compton signal therefore produce a background as well as corresponding counting noise. The Compton profiles can be predicted before the experiment using the tabulated Hartree-Fock (HF) atomic Compton profiles, which are calculated from the electron ground-state wavefunction in the limit of the impulse approximation [194, 195]. By selecting the momentum transfer in such a way that the energy range of the core edge under study falls away from the Compton peak maximum, we can maximize the *signal-to-background* ratio, thereby simplifying the subtraction of the valence electron contribution from the total spectrum (Figure 1.10 A).

1.4.3.2 Background arising from the sample environment

The following approaches can be implemented to minimize the background arising from stray scattering from the sample environment and/or air and fluorescence signal generated from elements in the sample set-up: (i) x-ray attenuation and scattering by air molecules can be minimized by the use of vacuum chambers (or of helium enclosures or “helium bags”) in the path of the scattered x-rays from the sample to the analyzer and/or then towards the detector [191, 192]. This approach maximizes the signal reaching the detector and reduces the scattering from the atmosphere, while the sample can be kept under atmospheric conditions, (ii) a two-dimensional (2D) pixelated detector can be used to isolate the signal coming from a region of interest (ROI) (Figure 1.11) [191, 195]. X-rays scattered-off the sample at different depths along the incident beam direction will focus in a different area of a two-dimensional detector (Figure 1.11) due to point-to-point focusing properties of the crystal analyzers (Figure 1.12) [196]. Subsequently, the signal coming from the sample can be isolated from the unwanted scattering contribution outside the sample, from the sample environment (air in the beam path, sample holder, etc.), (iii) setting as close as possible the footprints of all the analyzers will help to achieve a tight collimation of the x-rays reflected from the Bragg crystals. In that

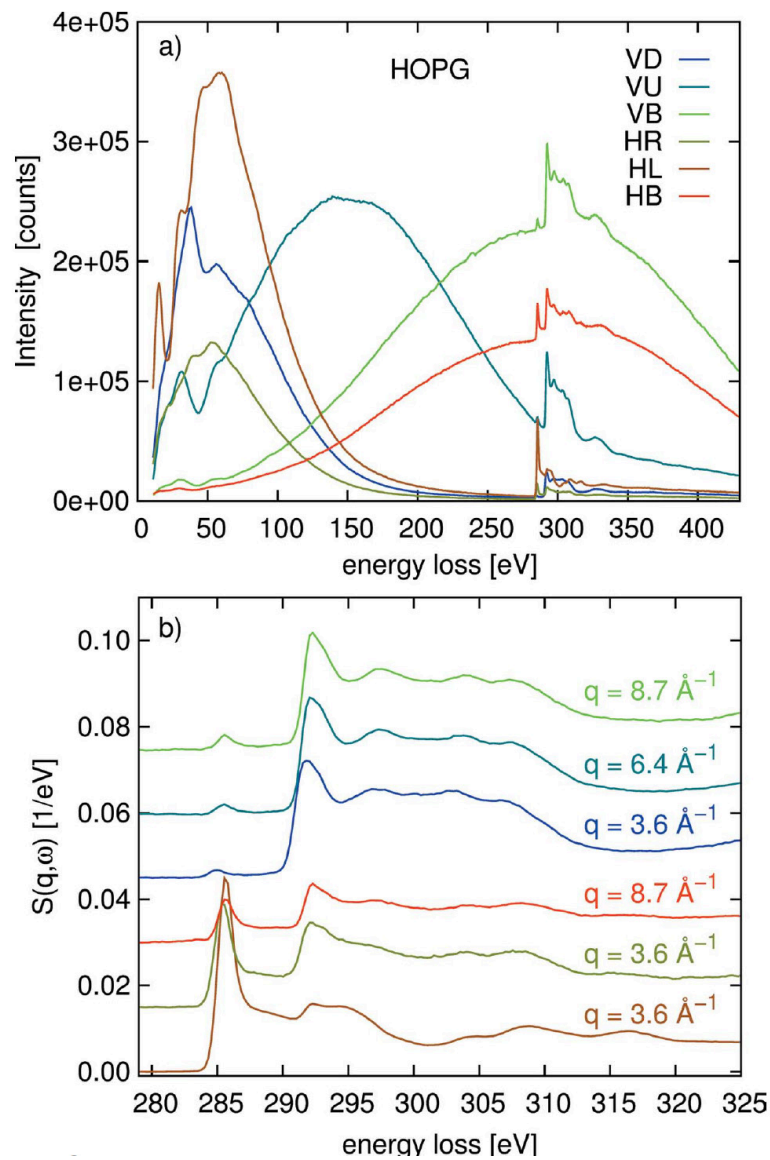


Figure 1.10: Compton dependence on momentum transfer. A. Raw data of highly oriented pyrolytic graphite showing the momentum transfer dependence of Compton scattering. B. Background subtracted and normalized carbon K-edge XRS data of HOPG showing the scattering angle dependence of XRS signal due to the anisotropy of HOPG. Source: Reproduced from Huotari et al. [191].

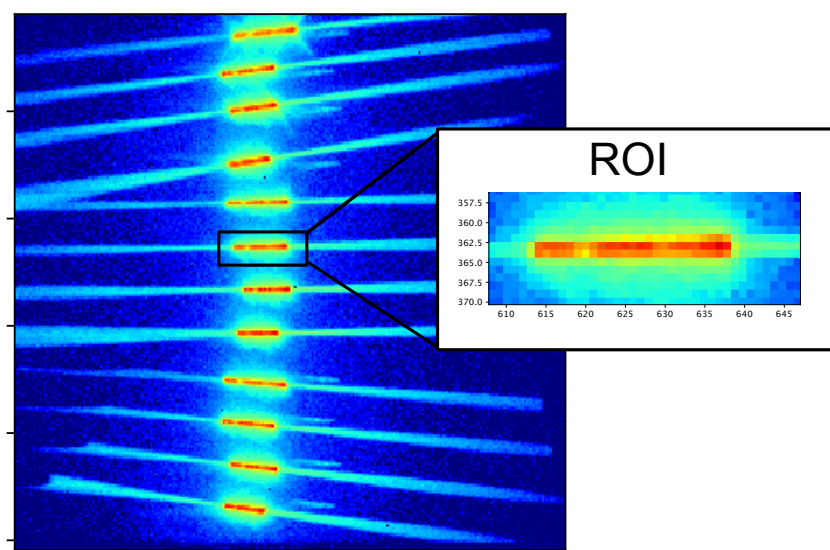


Figure 1.11: 2D detector image showing the signal of 12 crystal analyzers collected at ID20 (ESRF). The image is used to select the region of interest (ROI) corresponding to the signal coming from the sample.

case entrance slits can be used to mask the active surface of the detector to avoid as much as possible the stray scattering [192], (iv) the x-rays scattered-off the sample could be collimated individually for each analyzer; this approach can be implemented when a group of analyzers are kept in a chamber by the use of individual apertures at its entrance [191], (v) fluorescence signal can be minimized by selecting the incident energy below the ionization energy of the elements present, after determination of the fluorescing elements (e.g. elements in the sample holder) are known.

1.4.4 XRS 3D Imaging

XRS imaging utilizing the direct tomography principle introduced by Huotari et al. [197] is a promising additional asset to well-established techniques dedicated to three-dimensional (3D) imaging. Contrary to conventional 3D x-ray imaging methods (i.e. absorption-based 3D x-ray computed tomography (CT)), XRS tomography is based on chemical-bond contrast and does not require any reconstruction algorithm. In organic samples, photons in the hard x-ray regime (5–15 keV) will penetrate the sample from few millimeters to centimeters. X-rays scattered-off the sample at different depths along the incident beam direction will focus on

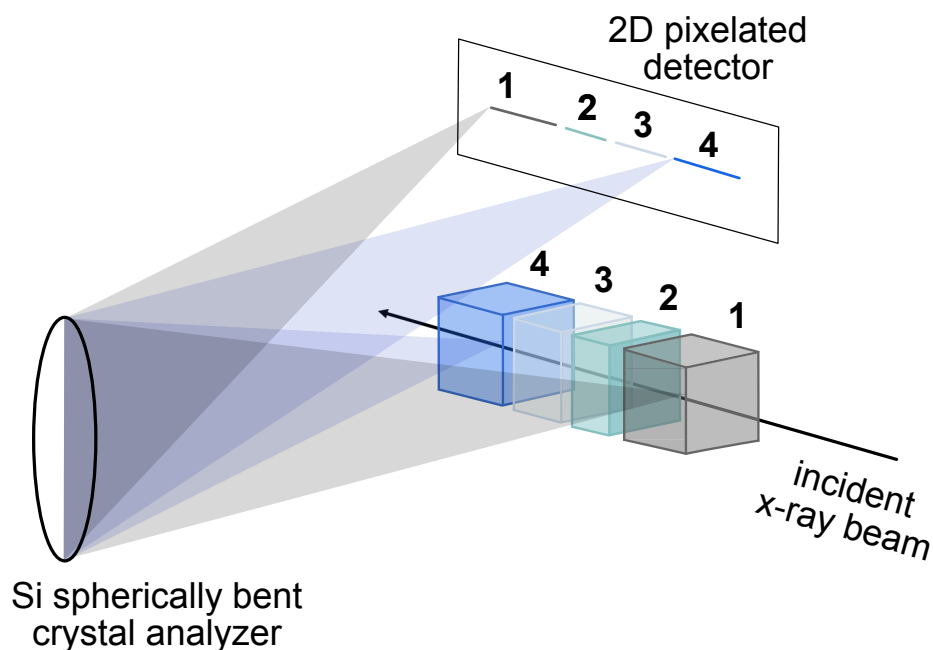


Figure 1.12: Schematic representation of the direct tomography imaging geometry. When the incident hard x-ray beam interact in-depth with a sample of heterogeneous nature, the photons scattered-off the sample will focus onto different positions on a 2D pixelated detector. The spherically bent crystal, not only monochromatizes the scattered radiation, but due to its point-to-point properties acts as a ‘mirror’ for imaging the sample in depth. Source: Adapted from Sahle et al. [196].

a different area of a two-dimensional detector (Figure 1.11) due to point-to-point focusing properties of the crystal analyzers (Figure 1.12) [196]. The successive collection of data laterally by raster scanning the object allows the construction of a 3D tomographic volume. The voxel size is defined by the dimensions of the beam laterally and by the detector pixel size along the beam. For hyperspectral imaging, an XRS spectrum can be collected for each voxel by scanning the incident energy accordingly.

1.4.4.1 Spatial resolution

The main limitation of direct tomography compared to absorption and phase-contrast micro-computed tomography is the limited spatial resolution. The spatial resolution of direct tomography is linked with the bent analyzer crystals’ quality and focusing properties, the size of the incident beam ($\approx 10 \mu\text{m}$) and the detector pixel size ($50\text{--}100 \mu\text{m}$). An algorithm introduced by

Sahle et al. [196] can enhance the spatial resolution through deconvolution of the instrument's optical response function (or *point spread function (PSF)*).

1.5 XRS of complex organic systems

The steps towards a technique's development for the characterization of complex organic systems are targeting the improvement of three *dynamics*: spectral, signal and spatial. XRS is constantly developing, to identify and characterize organic species and discriminate traces. We refer to *complex* systems based on their chemical composition (i.e. consisting of substances' mixtures), difference in relative abundance of their individual components (e.g. organic phases present as a minor component) and multiscale heterogeneity.

1.5.1 Analyzing mixtures of compounds

An XRS spectrum, collected at the carbon K-edge or at the oxygen K-edge, can be exploited to identify the characteristic absorption features of the different chemical groups present in complex materials. The XRS signal can be interpreted by decomposing the spectrum using a combination of Gaussians at diagnostic transition energies (see Section 1.4.1) (Tables 1.2, 1.3). Decomposition of XRS spectra can also be obtained through XRS simulations taking into account the momentum transfer dependence and non-dipolar effects (see Section 1.3.4). The complex chemistry of compounds consisting of substances' mixtures can be better tackled by using set-ups optimized for collecting XRS spectra at high energy resolution that approach the core-hole lifetime of the element under study (see Section 1.4.1).

1.5.1.1 Polycyclic aromatic hydrocarbons in crude oils

The first systematic XRS study of organic systems was reported in early 2000s [21–23, 198, 199]. Bergmann et al. employed XRS to probe the structures of fused aromatic ring systems in asphaltenes, which are a fraction of the substances found in crude oil. Characterizing the molecular structure of the asphaltene fraction provides information of crude oil's phenomenological behaviour (i.e. its function). The open questions when targeting on the characterization of asphaltenes' aromatic ring systems are the mean number of aromatic rings moiety, the width of the distribution and the geometry of the ring linkages. The authors collected XRS spectra

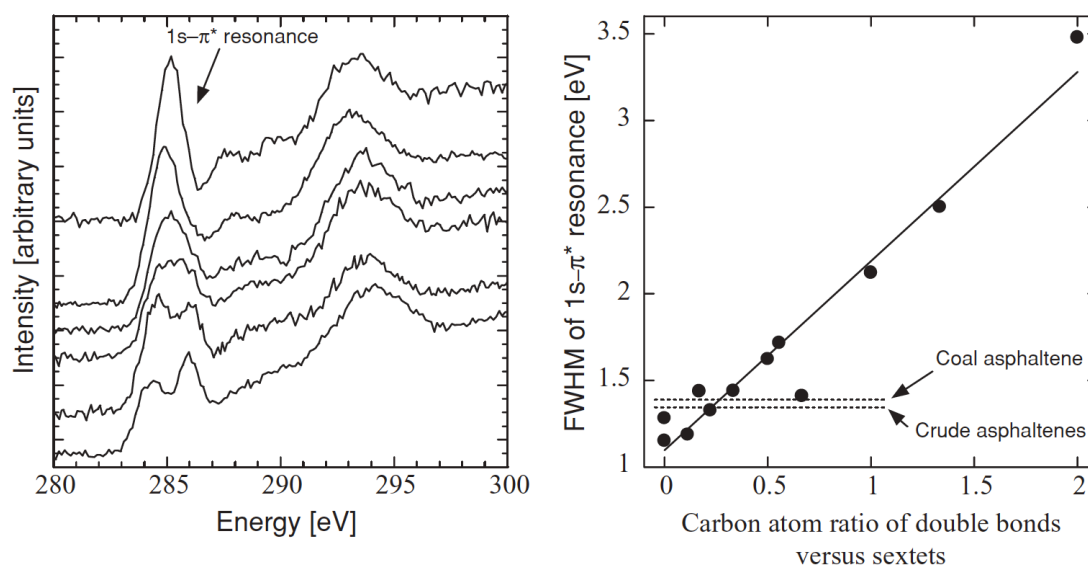


Figure 1.13: Correlation of $1s-\pi^*$ transitions to the ratio of double bonds versus sextets in PAHs model compounds. A. XRS carbon K-edge of PAHs model compounds. From top: triphenylene, benzo[ghi]perylene, benzo[a]pyrene, naphtho[2,3a]pyrene, anthracene, 2,3-benzanthracene. B. Full width half maximum (FWHM) of the $1s-\pi^*$ transition centered at ≈ 285 eV as a function of double bonds versus sextets in PAHs model compounds. The dashed lines represent the measured $1s-\pi^*$ of coal and crude asphaltenes. Source: Reproduced from Bergmann and Mullins [23].

at the carbon K-edge of selected polycyclic aromatic hydrocarbons (PAHs) model compounds and of coals and crude oil asphaltenes. PAHs are composed of fused-ring hydrocarbons (i.e. two aromatic rings that share a pair of carbon atoms). The measured linewidth of the $1s-\pi^*$ resonance at ≈ 285 eV of the PAHs was used to understand the ratio of isolated double bond carbon to aromatic sextet carbon present in the various asphaltenes (Figure 1.13). It was observed that the sharpest the $1s-\pi^*$ resonance of the model PAHs the highest the percentage of sextet carbon. The line broadening was increasing with the increase of isolated double bonds fraction. Given the large degree of sextet carbon present in the asphaltenes, the geometry of the aromatic systems was characterized as pericondensed (i.e. three aromatic rings that share single bridgehead carbon atoms).

1.5.1.2 Polycyclic aromatic hydrocarbon model compounds

Need for higher energy resolution experiments. Recent instrumental developments allowed the collection of high resolution (290 meV) carbon K-edge spectra of a selection of PAHs

model compounds, to better understand the origin of the $1s-\pi^*$ (resonance at ≈ 285 eV) line broadening [200]. The authors observed that the line broadening previously reported with lower-resolution data is a result of a line splitting well defined by the collection of high-resolution data (Figure 1.14). The line splitting is more profound as the percentage of π isolated double bonds (IDB) is increasing. The line splitting was explained based on Clar's description of the electronic structure of fused aromatic systems. According to Clar's model the π bonds in polycyclic aromatic hydrocarbons can consist of aromatic sextet (similar to benzene), which have large highest occupied molecular orbital (HOMO)–lowest unoccupied molecular orbital (LUMO) gaps and isolated double bonds (similar to olefins) which have small HOMO–LUMO gaps [clararomatic]. The XRS experimental spectra result from the summation of core electron transitions to unoccupied molecular orbitals (Figure 1.14). Based on Hückel calculations the high-lying LUMOs for PAHs rich in aromatic sextet cause small gap between LUMO and LUMO+1 which results in sharp $1s-\pi^*$ resonance at ≈ 285 eV (e.g. phenanthrene) (Figure 1.15). PAHs rich in isolated double bonds have a low-lying LUMO and a large LUMO–LUMO+1 gap leading to a spectral split of the $1s-\pi^*$ (e.g. anthracene) (Figure 1.15).

1.5.1.3 Natural-occurring organic systems

Following the high-resolution study of PAHs, Pomerantz et al. [201] collected high-resolution XRS carbon K-edge data of natural-occurring organic systems [e.g. kerogen (i.e. organic matter found in sedimentary rocks), asphaltenes and fresh materials (e.g. algae, fern, rhododendron, peat)] to assess the dominant electronic structures of fused-ring systems. The authors report the abundance of aromatic sextets compared to isolated double bonds attributed to increased stability; aromatic structures with large number of isolated double bonds are less stable thus the possibility to survive in the geological record is far less. Although studying complex organic systems, this study was not targeting on the carbon speciation and chemical intercomparison of the samples. The collected carbon K-edge dataset can be further exploited to provide information on the molecular bonding and heteroatoms' presence in the samples.

The classification of kerogens into types I, II, III is based on the principal source material and the hydrogen/carbon ratio. Type I, II, III kerogens are deposited in lacustrine, marine and terrestrial environments respectively. Prior to the analysis the type I and type II kerogen samples were subjected to acid demineralization using hydrochloric and hydrofluoric acids, to

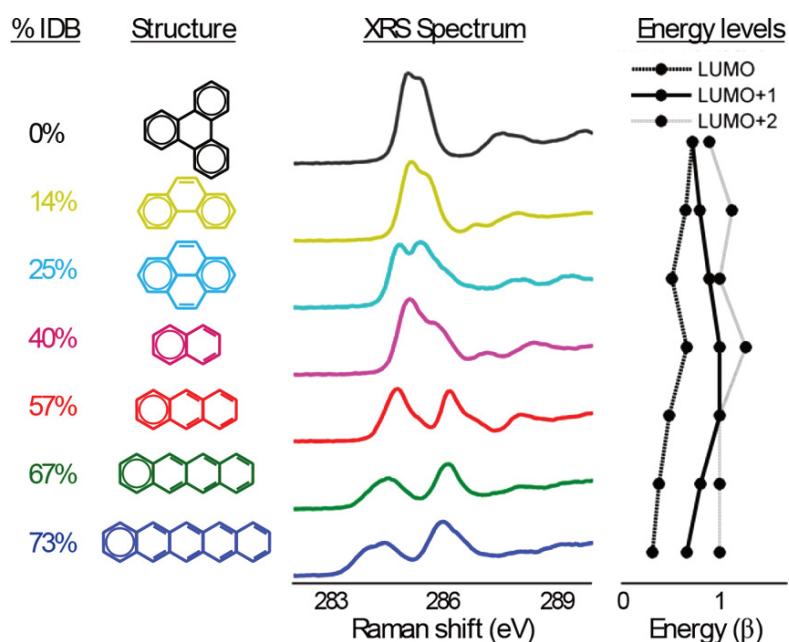


Figure 1.14: XRS spectra of a series of PAHs compounds. From top to bottom the spectra correspond to triphenylene, phenanthrene, pyrene, naphthalene, anthracene, tetracene, and pentacene. % IDB corresponds to the percentage of π isolated double bonds present in the different PAH compounds. Note the profound line splitting at ≈ 285 eV as the % IDB is increasing. The feature corresponds to $1s-\pi^*$ transitions. Source: Reproduced from Pomerantz et al. [200].

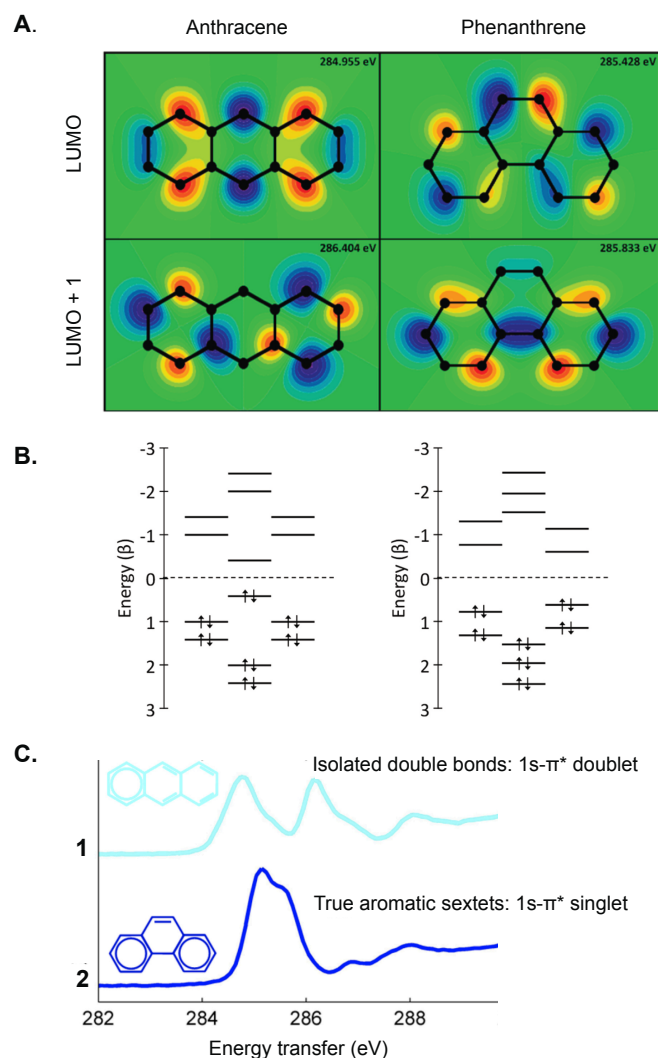


Figure 1.15: Molecular orbitals and XRS spectra of anthracene and phenanthrene. A. LUMO and LUMO+1 ground state wave function contour maps of carbon nuclei in anthracene (left) and phenanthrene (right). Green colour represents the zero amplitude, and red and blue represent opposite phase of maximum amplitudes. B. Plot of the occupied π and unoccupied π^* orbitals energy levels for anthracene (left) and phenanthrene (right) as estimated by Hückel theory. Note the LUMO and LUMO+1 energy gap differences for anthracene (increase of LUMO–LUMO+1 gap and decrease of the HOMO) and phenanthrene (decrease of LUMO–LUMO+1 gap and increase of the HOMO). C. Experimental XRS spectra of anthracene (spectrum 1) and phenanthrene (spectrum 2), resulting from the sum of the transitions to the different π^* unoccupied molecular orbitals at distinct energies. Note the split of the 1s– π^* transition in anthracene due to the large LUMO–LUMO+1 energy gap. Source: Adapted and reproduced from Pomerantz et al. [200].

remove the mineral phase in the sedimentary rocks, aiming on minimizing the impurities and isolating the kerogen to improve *signal-to-noise* ratio.

XRS spectra of immature type I kerogen (fresh outcrop of the Eocene Green River formation), and artificially matured samples (coming from the same outcrop) by semi-opened pyrolysis (samples pyrolyzed for 4h, 6h, 10h, 24h) are shown in Figure 1.16 A. For high maturity samples, the intensity of $1s-\pi^*$ transitions in aromatic carbon (feature at ≈ 285 eV) is increasing while the $1s-\sigma^*$ transitions in aliphatic carbon (feature at ≈ 288 eV) is decreasing. During kerogen artificially-induced maturation a loss of the aliphatic carbon is induced while aromatic carbon is increasing. In type I kerogen, no splitting of the $1s-\pi^*$ peak is observed (during or prior to thermal maturation), indicating the abundance of aromatic sextets rather than isolated double bonds.

Type II kerogen samples, prone to gas and oil generation, collected from the Venezuelan La Luna formation, are characterized by a range of maturity levels from prior to oil formation to overmature. Kerogen levels of maturation is assessed by the reflectance of vitrine maceral (VR_0). The higher the VR_0 the higher the level of maturation of the sample. XRS carbon K-edge spectra of type II kerogen exhibit similar characteristics as type I kerogen. At higher thermal maturities ($VR_0 > 1.6$) the intensity of aliphatic carbon signature ($1s-\sigma^*$ transitions at ≈ 288 eV) is decreasing as the intensity of aromatic carbon ($1s-\pi^*$ transitions at ≈ 285 eV) is increasing (Figure 1.16 B). A similar trend is observed in type III kerogens (coals) (Figure 1.16 C, D).

Asphaltenes, extracted from petroleum and coals, are the fraction of a mixture that dissolves in aromatic solvent (e.g. in toluene) and is insoluble in aliphatic solvent. Coal-derived (CDA) and petroleum (PA) asphaltenes XRS spectra is shown in Figure 1.16 E. The intensity of $1s-\sigma^*$ transitions in aliphatic carbon is more intense in petroleum asphaltenes (PA) compared to coal-derived asphaltenes (CDA). The $1s-\pi^*$ lineshape remains constant for all the samples analyzed, showing the dominance of aromatic sextets over isolated double bonds in asphaltenes, as shown also by Bergmann, Mullins, and Cramer [21, 22, 198].

XRS spectra of algae, a precursor of type I kerogen and fern, rhododendron, and peat, precursors of type III kerogen are shown in Figure 1.16 F. The chemical complexity of fresh materials is evident by the pre-edge XRS features, however, the study doesn't further interpret the chemical composition of the materials.

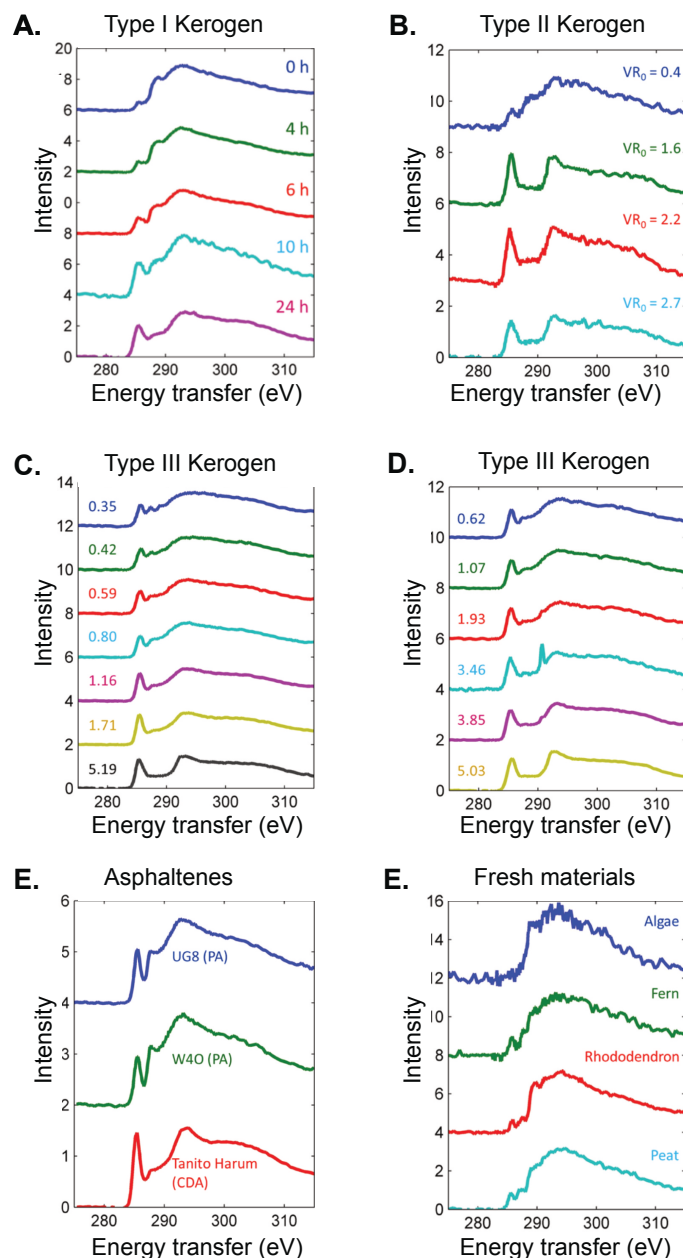


Figure 1.16: X-ray Raman spectra of natural-occurring materials. A. Carbon K-edge XRS spectra of type I kerogen, labeled by their artificially induced thermal maturity; B. Carbon K-edge XRS spectra of type II kerogen, labeled by their thermal maturity; C, D. Carbon K-edge XRS spectra of type III kerogen, labeled by their thermal maturity; E. Carbon K-edge XRS spectra of petroleum (PA) and coal-derived (CDA) asphaltenes; F. Carbon K-edge XRS spectra of fresh materials, precursors of type I kerogen (algae) and type III kerogen (fern, rhododendron, peat). Source: Adapted and reproduced from Pomerantz et al. [201].

1.5.1.4 Biomass-derived pyrolysis and hydrothermal carbon

Higgins et al. [27] report on the use of carbon K-edge spectroscopy via XRS for the study of pyrolysis and hydrothermal carbons (i.e. carbon materials that are thermochemically-produced from renewable sources). Fingerprints of the carbon K-edge confirm structural differences between biomass-derived (Oak, *Quercus Ilex*) pyrolysis and hydrothermal carbon (Figure 1.17). The broader $1s-\pi^*$ transition in aromatics centered at 285 eV and the increased spectroscopic structure at the $1s-\sigma^*$ transitions in aromatic carbon (292–295 eV), observed in the pyrolysis carbon indicated the presence of a continuum of polyaromatic moieties. On the other hand, hydrothermal carbon is characterized by the presence of carboxyl groups ($1s-\pi^*$ transitions, shoulder centered at 288.9 eV). The increased structure and the smaller FWHM of $1s-\pi^*$ transitions (centered at 285 eV) in hydrothermal carbon indicates a more disordered structure and fewer aromatic bonds. Comparison of surface sensitive near edge x-ray absorption fine structure (NEXAFS) and bulk sensitive XRS data, reveals the presence of an enriched aromatic layer on the surface of hydro-thermal carbon. Spectral distortions of soft x-rays NEXAFS possibly arises from the sample thickness. The in-situ investigation of the pyrolysis and/or hydrothermal treatment process seems at hand using XRS.

1.5.1.5 Lithium-ion battery electrolyte solutions

Ketenoglu et al. [202] studied the influence of LiPF_6 , a salt commonly used in lithium-ion battery electrolytes, on the electronic structure of different anhydrous solvents using XRS spectroscopy at the carbon and oxygen K-edge. Increasing the Li-salt concentration in the mixtures of solvents (propylene-carbonates and ethylene-dimethyl-carbonates) increased the energy position of the π^* feature in both the carbon and the oxygen K-edges. Latter was, in agreement with previous x-ray absorption measurements, assigned to an increased Li^+ -dimethyl-carbonate coordination, calling for improved descriptions of electrolyte- Li^+ interactions in numerical simulations that go beyond tetrahedral Li^+ solvation structures. The shift in the carbon K-edge, on the other hand, was attributed to a change of the ionic conductivity of the electrolyte solutions upon the solvation of LiPF_6 . The energy calibration of XRS spectra based on the elastic line energy, independent of the measurement of standards, proved to be a reliable basis for the precise determination of spectral dispersion.

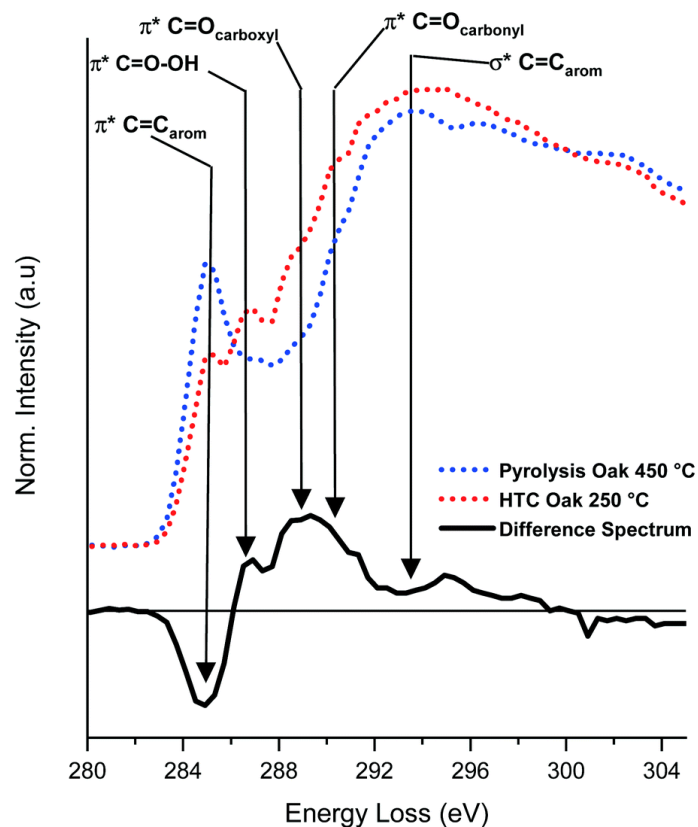


Figure 1.17: X-ray Raman spectra of pyrolysis and hydrothermal carbon. The difference spectrum (in black color) highlights the chemical differences between hydrothermal (HTC-Oak-250 in red color) and pyrolysis (Pyrolysis Oak 450 in blue color) carbon. The core electron transitions in different functional groups are noted. Source: Reproduced from Higgins et al. [27].

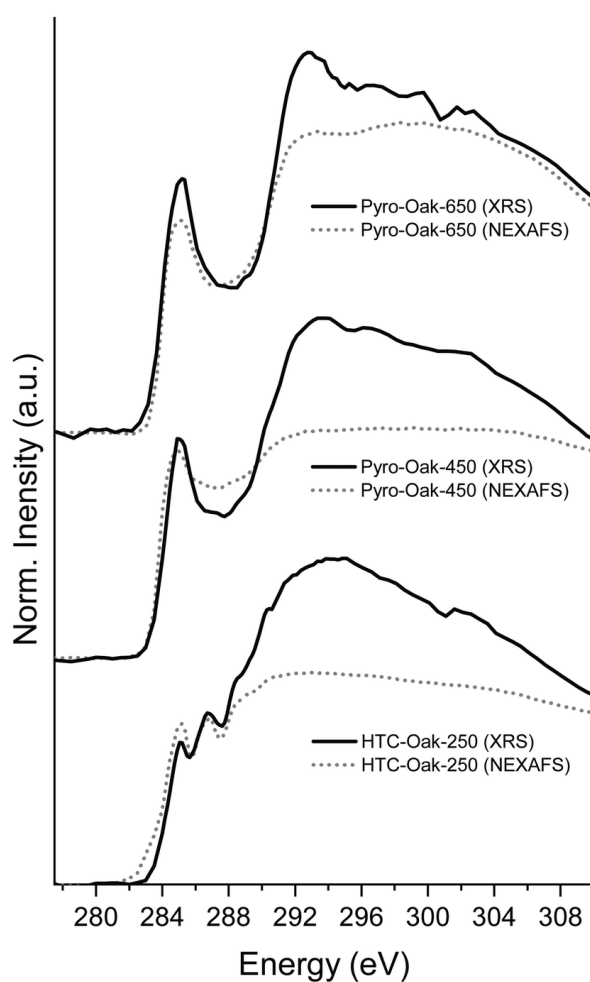


Figure 1.18: Comparison of soft x-ray carbon K-edge spectra, collected in transmission, and x-ray Raman spectra of pyrolysis and hydrothermal carbon. Note the spectral distortions of soft x-ray NEXAFS spectra possibly due to self-absorption, linked to the sample thickness. Source: Reproduced from Higgins et al. [27].

1.5.2 Looking for minor features

The quality of the spectra in terms of energy resolution and *signal-to-noise* ratio is important when targeting on the identification of minor features linked with the presence of heteroatoms and the identification of molecular bonding in heterogeneous samples. Collecting XRS data at the carbon K-edge with moderate energy resolution can complicate the identification of features corresponding to diagnostic transitions. When the *signal-to-noise* ratio is sufficient, a spectral decomposition of moderate energy resolution XRS data can help in the interpretation of XRS spectral features.

1.5.2.1 Paleontological organic specimens

Recently, XRS was exploited in the field of paleontology [25]. The potential of XRS to probe carbon speciation in paleontological specimens belonging to a museum collection was demonstrated through the analysis of a 56 Myr old fossil cocoon, collected from Rivercourt cite (Oise, France) and a 49,000-year-old mammoth dry skin belonging to the Paris National Museum of Natural History. The decomposition of XRS carbon K-edge spectra using a combination of Gaussians at diagnostic transitions allowed the identification of initially unaccounted $1s-\sigma^*$ transitions in C–S bonds from residuals in an iterative process where the discovered spectral features were progressively included in a model and fitted to the data (Figure 1.19). Additionally, the XRS carbon K-edge spectra provided information on the level of aromaticity, presence of oxidized COO groups and turbostraticity. The study introduced XRS in the field of paleontology as an in-situ non-invasive bulk probe which provides information not compromised by surface contamination, thus overcoming common constraints in the characterization of ancient materials.

1.5.2.2 Heteroatoms-containing PAHs

Pomerantz et al. [201] collected XRS carbon K-edge data of oxygen-, sulfur-, and nitrogen-substituted analogs of PAH model compounds. Unlike pure model compounds, naturally occurring organic systems, are often characterized by the presence of heteroatoms. The effect of heteroatoms' presence in the XRS spectra is best understood by comparing the oxygen-, sulfur-, and nitrogen-substituted analogs with pure hydrocarbons XRS spectra (Fig-

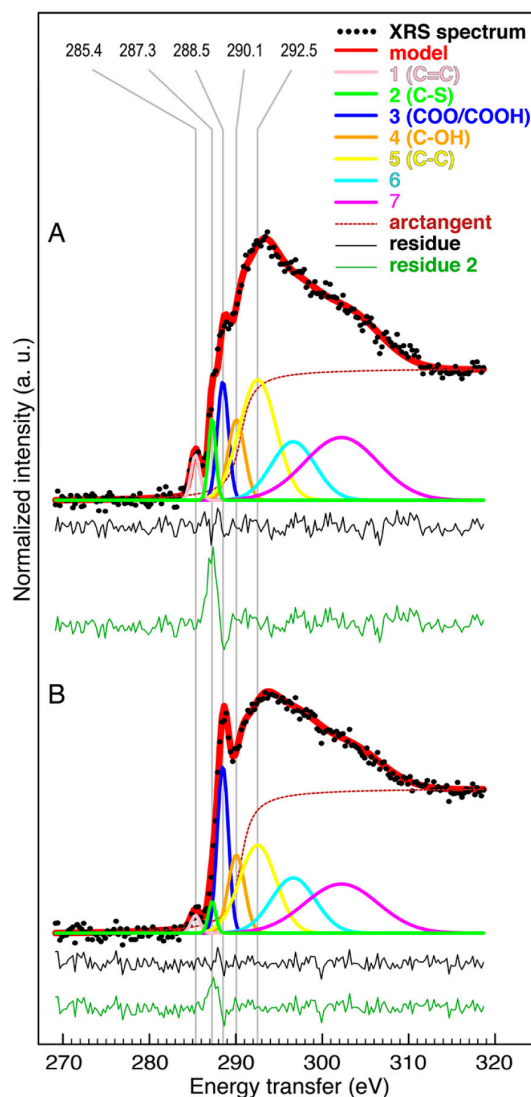


Figure 1.19: Spectral decomposition of XRS spectra of paleontological specimens. A. XRS carbon K-edge of the paleontological cocoon. The fit residue (in green color) is calculated without Gaussian 2 corresponding to C–S $1s-\sigma^*$ transitions indicating the noticeable presence of carbon-bound sulfur in the sample; B. XRS carbon K-edge of the 49,000-year old woolly mammoth dry skin from the Lyakhov Islands (Paris National Museum of Natural History, inv. no. MNHN.F.MAQ 287). The spectra reveal exceptional preservation of the tissue chemistry at the atomic level. Source: Reproduced from Gueriau et al. [25].

ure 1.20). Although heteroatoms have a minor effect, if we examine carefully the XRS spectra of heteroatom-containing PAHs, they contain features characteristic of the functional groups added to the pure system. Note for example, the $1s-\pi^*$ in carboxyl groups centered around 288.6 eV which can be observed in the 2-naphthoic acid (Figure 1.20 A) and 9-anthroic acid (Figure 1.20 C).

1.5.3 Resolving spatially heterogeneous systems

1.5.3.1 First examples of 3D imaging

The two first examples used to demonstrate the capabilities of chemical contrast XRS direct tomography (DT) are: (i) a *phantom* sample prepared by embedding a diamond in graphite powder pressed as pellet (Figure 1.21), and (ii) a layered carbon fiber-reinforced silicon carbide (C/SiC) sample. The carbon K-edge XRS spectral differences between graphite and diamond were used as a source of contrast to image in 3D the diamond embedded several millimeters inside graphite (Figure 1.21 C, D, E). The difference in spectral features of diamond and graphite are based on the nature of the carbon chemical bonding in the allotropes; diamond is solely formed by sp^3 bonds thus it lacks the π^* resonance at 285 eV, while graphite layers are formed by sp^2 bonds. Additionally, for highly oriented pyrolytic graphite, the XRS spectra intensity depends on the orientation of the sample. When $\mathbf{q} \parallel ab$ (sp^2 bonds and \mathbf{q} vector are in the xy plane), the π^* resonance is minimized (Figure 1.21 C).

XRS direct tomography was applied to a C/SiC specimen, a sample that has the unique characteristic to retain its mechanical properties above 2000 K, to determine its carbon bonding and bond orientation. Carbon K-edge XRS spectra of the C/SiC cuboid sample collected along the beam direction provided information on the chemical bonding characteristics within the 7 mm sample thickness (Figure 1.22 B) [197]. The $1s-\pi^*$ transitions observed at ≈ 285 eV is visible along the sample thickness, indicating the sp^2 bond domination. An XRS measurement over the three spatial dimensions was performed to determine the bond orientation variations. The average bond orientation was defined as the angle between \mathbf{q} and the sp^2 plane. The volume is visualized in Figure 1.22 C, D and it is compared with a microtomography (μ CT) volume. Absorption-contrast μ CT allowed the visualization of sample density variations but does not access the chemical bond variations, accessible by XRS direct tomography (Figure 1.22 E).

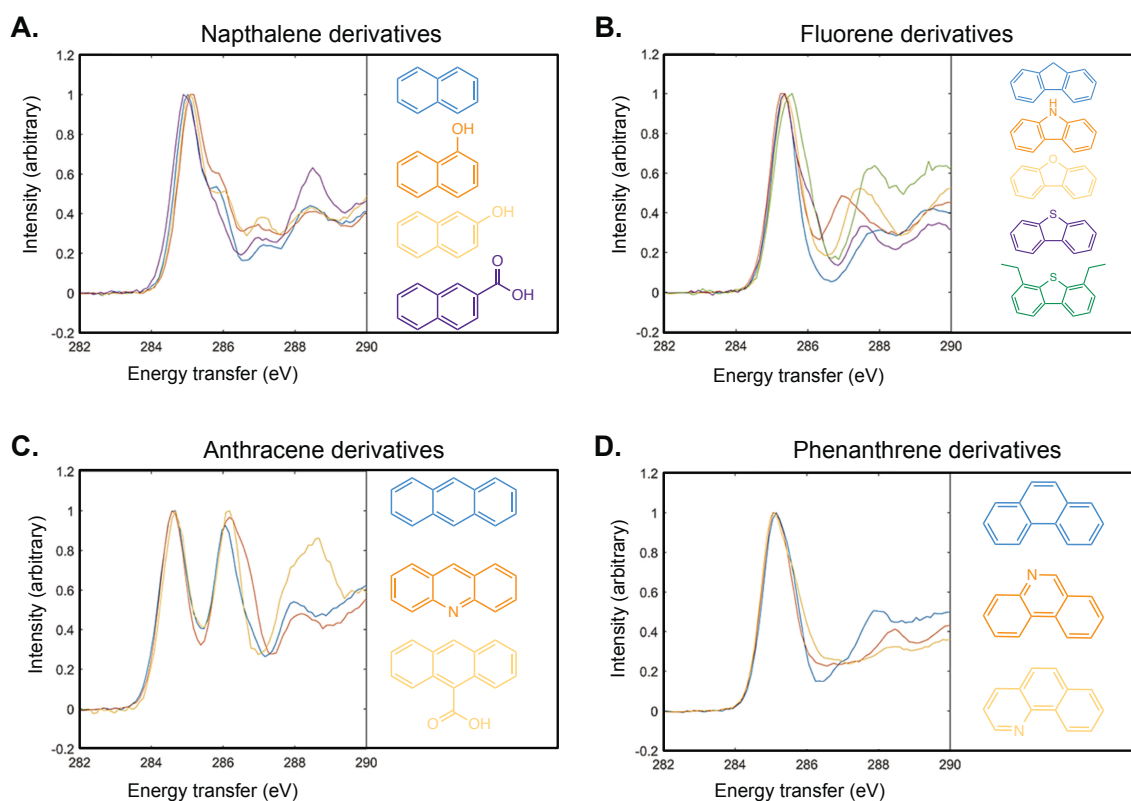


Figure 1.20: XRS spectral features in the presence of heteroatoms. Carbon K-edge XRS spectra of oxygen-, sulfur-, and nitrogen-substituted analogs of PAH model compounds. **A.** XRS spectra of naphthalene derivatives. Spectra correspond to naphthalene (blue), 1-naphthol (orange), 2-naphthol (yellow), 2-naphthoic acid (purple); **B.** XRS spectra of fluorene derivatives. Spectra correspond to fluorene (blue), carbazole (orange), dibenzofuran (yellow), dibenzothiophene (purple), 4,6-diethyldibenzothiophene (purple); **C.** XRS spectra of anthracene derivatives. Spectra correspond to anthracene (blue), acridine (orange), 9-anthroic acid (yellow); **D.** XRS spectra of phenanthrene derivatives. Spectra correspond to phenanthrene (blue), phenanthradine (orange), benzo[h]quinoline (yellow). Source: Adapted and reproduced from Pomerantz et al. [201].

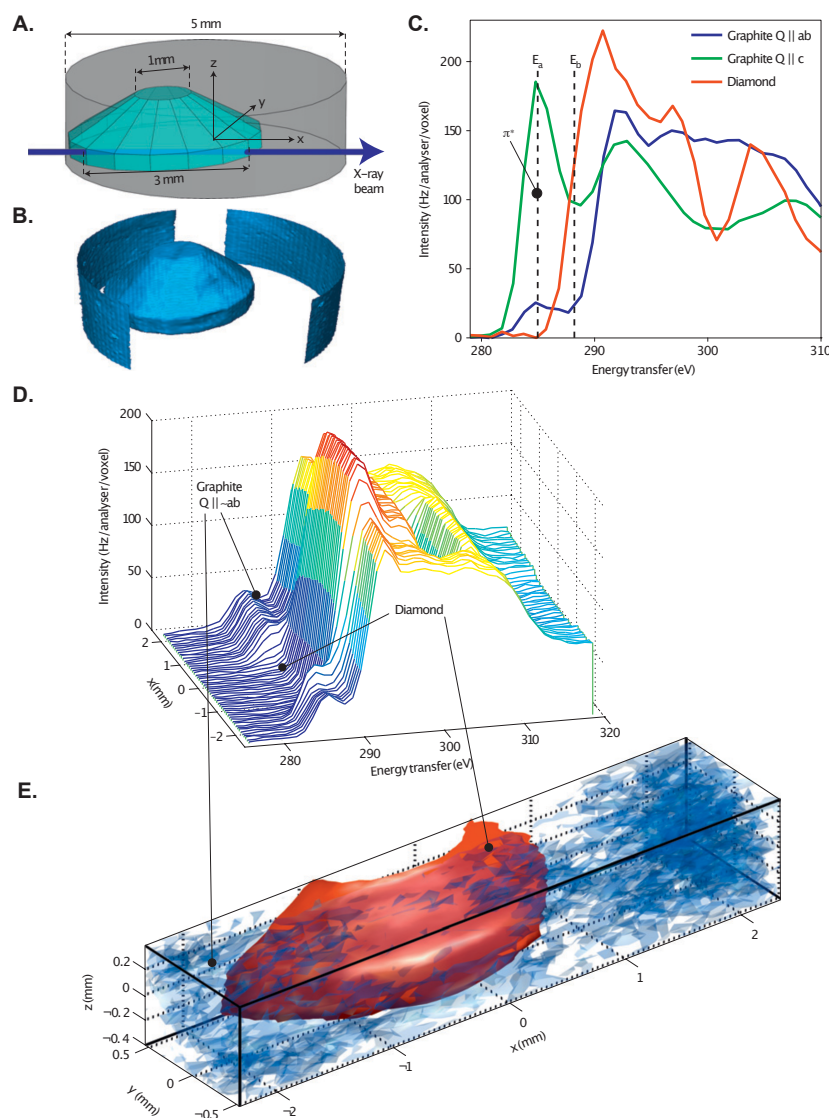


Figure 1.21: XRS direct tomography applied to a diamond-graphite phantom sample. **A.** Schematic representation of diamond embedded in graphite pellet, **B.** 3D volume of the sample based on diffraction contrast, which corresponds to a zero energy transfer measurement (elastic scattering). Graphite and diamond are discriminated due to the difference in crystal structure, **C.** XRS spectra of diamond powder (in red) and highly oriented pyrolytic graphite (in green and blue). Note the lack of $1s-\pi^*$ transitions (≈ 285 eV) in diamond and the angular-dependence of the graphite XRS spectra, **D.** XRS spectra collected along the beam path (x -axis) for the graphite-diamond sample, **E.** 3D volume based on the chemical contrast XRS direct tomography. Isosurfaces in red correspond to the diamond and in blue to graphite with a $\mathbf{q} \parallel ab$ orientation. Source: Reproduced from Huotari et al. [197].

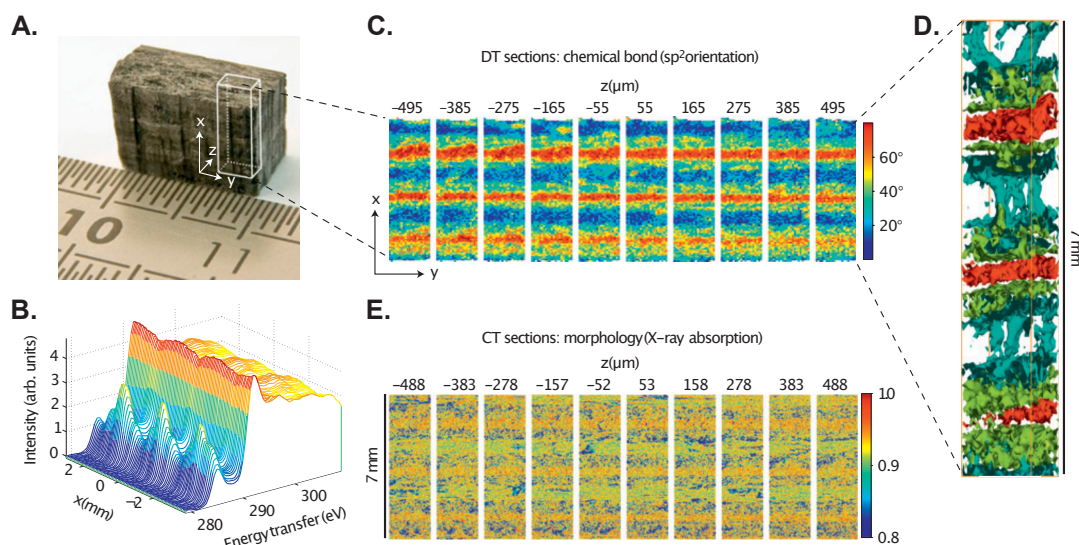


Figure 1.22: XRS direct tomography applied to a C/SiC sample. A. C/SiC sample photograph ($7 \times 10 \times 5 \text{ mm}^3$); B. Carbon K-edge XRS spectra collected along the beam direction; C. 2D direct tomography sections (xy sections for different z) of sp^2 bond plane orientation with respect to q ; D. 3D isosurface plot for selected angles shown in C; E. 2D microtomography (μCT) sections based on absorption contrast showing the sample density variations. Source: Reproduced from Huotari et al. [197].

1.5.3.2 Time-resolved XRS studies of chemical reactions

Inkinen et al. [24] reported a first in-situ time-resolved XRS study on the x-ray-induced dimerization reaction of α -trans-cinnamic (CA) acid to α -truxillic acid (TA) based on rapid carbon K-edge scanning. The time-resolved reference carbon K-edge spectra of α -trans-cinnamic acid and its dimerization product (i.e. α -truxillic acid) were collected to decipher the reactions' kinetics. The long-known UV-induced dimerization reaction was found to likewise be induced by the probe x-ray beam, but the analysis of the time dependence of the reaction led the authors to conclude that the x-ray induced reaction proceeds homogeneously in contrast to the UV-light-induced reaction. Analysis of the carbon K-edge XRS spectral shape time-evolution revealed the effects of two x-ray induced reactions, the dimerization and the disintegration building up on longer time scales. Use of the spatial sensitivity of direct tomography further allowed the authors to analyze the spatial progress of these two reactions throughout the sample (Figure 1.23 C). This study demonstrated that the newest generation of XRS instruments can yield access to speciation kinetics on sub-minute time scales.

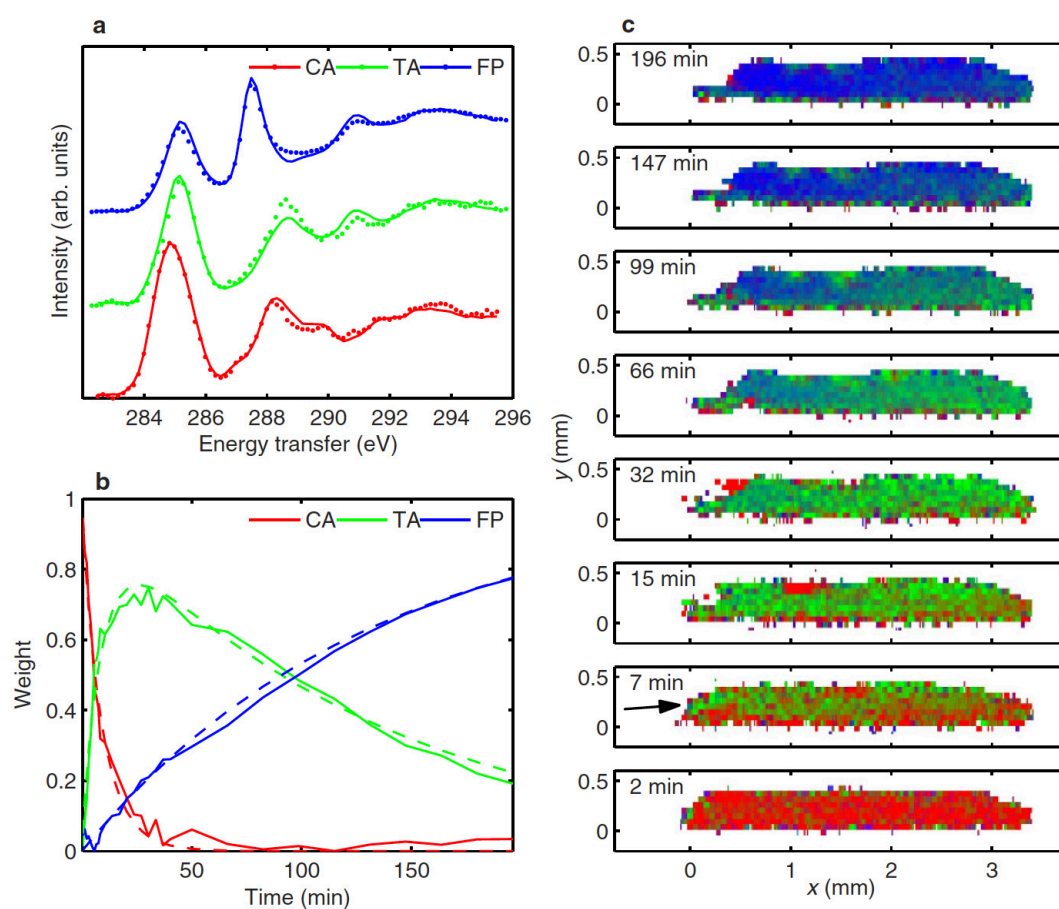


Figure 1.23: Spatial progress of α -trans-cinnamic acid crystal during x-ray induced dimerization. A. Component spectra: α -trans-cinnamic acid (CA), α -truxillic acid (TA), final products (FP); B. Component spectra weights as a function of time; C. Spectral imaging of the chemical composition progress in the α -trans-cinnamic acid crystal. Source: Reproduced from Inkinen et al. [24].

1.6 Current challenges

The remaining challenges of XRS are: (i) the long acquisition times due to the low efficiency of the non-resonant inelastic scattering process. Highly-efficient spectrometers for detecting the scattered x-rays, composed by multiple analyzers, can effectively reduce the acquisition time; (ii) the radiation-induced effects; irradiation of organic materials leads to the formation of new chemical bonds through cross-linking, aggregation, decomposition, oxidation and isomerization [203]. The radiation induced effects can lead to visual damage of the sample, including discoloration and melting, and decomposition. Reducing the irradiation time is vital for collecting meaningful XRS spectra which reflect the chemistry of the organic systems and avoids visual damage of precious samples (e.g. cultural heritage artifacts); (iii) the limited spatial resolution compared to absorption or phase-contrast computed tomography (CT); (iv) the detection of organic traces in a heterogeneous sample may be hampered by the presence of heavy elements; (v) the penetration depth is restricted to the incident beam energy (6–15 keV) and restricts the sample size and composition.

References

- [1] Kepa Ruiz-Mirazo, Carlos Briones, and Andres de la Escosura. “Prebiotic systems chemistry: new perspectives for the origins of life”. In: *Chemical reviews* 114.1 (2014), pp. 285–366.
- [2] John I Hedges et al. “The molecularly-uncharacterized component of nonliving organic matter in natural environments”. In: *Organic Geochemistry* 31.10 (2000), pp. 945–958.
- [3] Michael WI Schmidt and Angela G Noack. “Black carbon in soils and sediments: analysis, distribution, implications, and current challenges”. In: *Global biogeochemical cycles* 14.3 (2000), pp. 777–793.
- [4] Kamil Godula and Dalibor Sames. “CH bond functionalization in complex organic synthesis”. In: *Science* 312.5770 (2006), pp. 67–72.
- [5] Thomas Henning and Farid Salama. “Carbon in the Universe”. In: *Science* 282.5397 (1998), pp. 2204–2210.

- [6] GP Moss, PAS Smith, and D Tavernier. "Glossary of class names of organic compounds and reactivity intermediates based on structure (IUPAC Recommendations 1995)". In: *Pure and applied chemistry* 67.8-9 (1995), pp. 1307–1375.
- [7] Sunghwan Kim, Robert W Kramer, and Patrick G Hatcher. "Graphical method for analysis of ultrahigh-resolution broadband mass spectra of natural organic matter, the van Krevelen diagram". In: *Analytical chemistry* 75.20 (2003), pp. 5336–5344.
- [8] Rebecca J Robbins. "Phenolic acids in foods: an overview of analytical methodology". In: *Journal of agricultural and food chemistry* 51.10 (2003), pp. 2866–2887.
- [9] Dinesh Mohan, Charles U Pittman Jr, and Philip H Steele. "Pyrolysis of wood/biomass for bio-oil: a critical review". In: *Energy & fuels* 20.3 (2006), pp. 848–889.
- [10] Thomas Belin and Florence Epron. "Characterization methods of carbon nanotubes: a review". In: *Materials Science and Engineering: B* 119.2 (2005), pp. 105–118.
- [11] Simon R Kelemen et al. "Direct characterization of kerogen by X-ray and solid-state ^{13}C nuclear magnetic resonance methods". In: *Energy & Fuels* 21.3 (2007), pp. 1548–1561.
- [12] Sylvie Derenne and Thanh Thuy Nguyen Tu. "Characterizing the molecular structure of organic matter from natural environments: An analytical challenge". In: *Comptes Rendus Geoscience* 346.3-4 (2014), pp. 53–63.
- [13] Jevgeni Parshintsev and Tuulia Hyötyläinen. "Methods for characterization of organic compounds in atmospheric aerosol particles". In: *Analytical and bioanalytical chemistry* 407.20 (2015), pp. 5877–5897.
- [14] Ann Newman and Robert Wenslow. "Solid-state Characterization Techniques". In: *Pharmaceutical Crystals: Science and Engineering* (2018), pp. 89–121.
- [15] Scott A Sandford et al. "Organics captured from comet 81P/Wild 2 by the Stardust spacecraft". In: *Science* 314.5806 (2006), pp. 1720–1724.
- [16] Vincent Mazel et al. "Identification of ritual blood in African artifacts using TOF-SIMS and synchrotron radiation microspectroscopies". In: *Analytical chemistry* 79.24 (2007), pp. 9253–9260.

- [17] Chris Jacobsen et al. “Soft X-ray spectroscopy from image sequences with sub-100 nm spatial resolution”. In: *Journal of Microscopy* 197.2 (2000), pp. 173–184.
- [18] Joachim Stöhr. *NEXAFS spectroscopy*. Vol. 25. Springer Science & Business Media, 2013.
- [19] S Bernard et al. “Ultrastructural and chemical study of modern and fossil sporoderms by Scanning Transmission X-ray Microscopy (STXM)”. In: *Review of Palaeobotany and Palynology* 156.1-2 (2009), pp. 248–261.
- [20] Winfried Schülke. *Electron dynamics by inelastic X-ray scattering*. Vol. 7. Oxford University Press, 2007.
- [21] Uwe Bergmann et al. “Carbon K-edge X-ray Raman spectroscopy supports simple, yet powerful description of aromatic hydrocarbons and asphaltenes”. In: *Chemical physics letters* 369.1-2 (2003), pp. 184–191.
- [22] Uwe Bergmann et al. “X-ray Raman spectroscopy—a new tool to study local structure of aromatic hydrocarbons and asphaltenes”. In: *Petroleum science and technology* 22.7-8 (2004), pp. 863–875.
- [23] Uwe Bergmann and Oliver C Mullins. “Carbon X-ray Raman spectroscopy of PAHs and asphaltenes”. In: *Asphaltenes, Heavy Oils, and Petroleomics*. Springer, 2007, pp. 139–155.
- [24] Juho Inkinen et al. “X-ray induced dimerization of cinnamic acid: Time-resolved inelastic x-ray scattering study”. In: *Scientific reports* 5 (2015), p. 15851.
- [25] Pierre Gueriau et al. “Noninvasive Synchrotron-Based X-ray Raman Scattering Discriminates Carbonaceous Compounds in Ancient and Historical Materials”. In: *Analytical Chemistry* 89.20 (2017), pp. 10819–10826.
- [26] Rafaella Georgiou et al. “Carbon speciation in organic fossils using 2D to 3D x-ray Raman multispectral imaging”. In: *Science advances* 5.8 (2019), eaaw5019.
- [27] Luke JR Higgins et al. “X-ray Raman scattering for bulk chemical and structural insight into green carbon”. In: *Physical Chemistry Chemical Physics* 22.33 (2020), pp. 18435–18446.
- [28] Heiko Conrad et al. “Tetrahydrofuran clathrate hydrate formation”. In: *Physical review letters* 103.21 (2009), p. 218301.

- [29] Iina Juurinen et al. "Saturation behavior in X-ray Raman scattering spectra of aqueous LiCl". In: *The Journal of Physical Chemistry B* 117.51 (2013), pp. 16506–16511.
- [30] Iina Juurinen et al. "Effect of the hydrophobic alcohol chain length on the hydrogen-bond network of water". In: *The Journal of Physical Chemistry B* 118.29 (2014), pp. 8750–8755.
- [31] Johannes Niskanen et al. "Protonation dynamics and hydrogen bonding in aqueous sulfuric acid". In: *The Journal of Physical Chemistry B* 119.35 (2015), pp. 11732–11739.
- [32] Laila H Al-Madhagi et al. "X-ray Raman scattering: a new in situ probe of molecular structure during nucleation and crystallization from liquid solutions". In: *CrystEngComm* 20.43 (2018), pp. 6871–6884.
- [33] Philippe Wernet et al. "The structure of the first coordination shell in liquid water". In: *Science* 304.5673 (2004), pp. 995–999.
- [34] Philippe Wernet et al. "Spectroscopic characterization of microscopic hydrogen-bonding disparities in supercritical water". In: *The Journal of chemical physics* 123.15 (2005), p. 154503.
- [35] Yong Q Cai et al. "Ordering of hydrogen bonds in high-pressure low-temperature H₂O". In: *Physical Review Letters* 94.2 (2005), p. 025502.
- [36] Ho Kwang Mao et al. "Electronic structure of crystalline He⁴ at High Pressures". In: *Physical review letters* 105.18 (2010), p. 186404.
- [37] John S Tse et al. "Pressure-induced electron topological transitions in Ba-doped Si clathrate". In: *Physical Review B* 84.18 (2011), p. 184105.
- [38] Hiroshi Fukui et al. "Oxygen K-edge fine structures of water by x-ray Raman scattering spectroscopy under pressure conditions". In: *The Journal of chemical physics* 127.13 (2007), p. 134502.
- [39] Timothy T Fister et al. "Intermediate-range order in water ices: Nonresonant inelastic X-ray scattering measurements and real-space full multiple scattering calculations". In: *Physical Review B* 79.17 (2009), p. 174117.
- [40] Tuomas Pylkkanen et al. "Temperature dependence of the near-edge spectrum of water". In: *The Journal of Physical Chemistry B* 115.49 (2011), pp. 14544–14550.

- [41] D Ishikawa et al. “X-ray Raman scattering of water near the critical point: comparison of an isotherm and isochore”. In: *arXiv preprint arXiv:1210.4274* (2012).
- [42] Christoph J Sahle et al. “Microscopic structure of water at elevated pressures and temperatures”. In: *Proceedings of the National Academy of Sciences* 110.16 (2013), pp. 6301–6306.
- [43] Toshiaki Iitaka et al. “Pressure-induced dissociation of water molecules in ice VII”. In: *Scientific reports* 5 (2015), p. 12551.
- [44] Christoph J Sahle et al. “Influence of TMAO and urea on the structure of water studied by inelastic X-ray scattering”. In: *Physical Chemistry Chemical Physics* 18.24 (2016), pp. 16518–16526.
- [45] Felix Lehmkuhler et al. “Intramolecular structure and energetics in supercooled water down to 255 K”. In: *Physical Chemistry Chemical Physics* 18.9 (2016), pp. 6925–6930.
- [46] Christoph J Sahle et al. “Cation hydration in supercritical NaOH and HCl aqueous solutions”. In: *The Journal of Physical Chemistry B* 121.50 (2017), pp. 11383–11389.
- [47] Christoph J Sahle et al. “Hydration in aqueous solutions of ectoine and hydroxyectoine”. In: *Physical Chemistry Chemical Physics* 20.44 (2018), pp. 27917–27923.
- [48] Johannes Niskanen et al. “Compatibility of quantitative X-ray spectroscopy with continuous distribution models of water at ambient conditions”. In: *Proceedings of the National Academy of Sciences* 116.10 (2019), pp. 4058–4063.
- [49] Christoph J Sahle et al. “Hydration in aqueous osmolyte solutions: the case of TMAO and urea”. In: *Physical Chemistry Chemical Physics* 22.20 (2020), pp. 11614–11624.
- [50] Arto Sakko et al. “Inelastic X-ray scattering and vibrational effects at the K-edges of gaseous N₂, N₂O, and CO₂”. In: *Physical Chemistry Chemical Physics* 13.24 (2011), pp. 11678–11685.
- [51] Juho Inkinen et al. “Temperature dependence of CO₂ and N₂ core-electron excitation spectra at high pressure”. In: *Physical Chemistry Chemical Physics* 15.23 (2013), pp. 9231–9238.
- [52] Lin-Fan Zhu et al. “Inelastic x-ray scattering study on the single excitations of helium”. In: *Journal of Physics B: Atomic, Molecular and Optical Physics* 44.2 (2011), p. 025203.

- [53] Aleksi Mattila et al. "Local electronic structure of MgB_2 by x-Ray Raman scattering at the Boron K Edge". In: *Physical review letters* 94.24 (2005), p. 247003.
- [54] Szabolcs Galambosi et al. "X-ray Raman scattering study of aligned polyfluorene". In: *Macromolecules* 39.26 (2006), pp. 9261–9266.
- [55] Christian Sternemann et al. "The barium giant dipole resonance in barite: a study of soft x-ray absorption edges using hard x-rays". In: *Journal of Analytical Atomic Spectrometry* 23.6 (2008), pp. 807–813.
- [56] Tuomas Pylkkanen et al. "Role of non-hydrogen-bonded molecules in the oxygen K-edge spectrum of ice". In: *The Journal of Physical Chemistry B* 114.11 (2010), pp. 3804–3808.
- [57] Alexander Nyrow et al. "Pressure induced spin transition revealed by iron $\text{M}_{2,3}$ -edge spectroscopy". In: *Applied Physics Letters* 104.26 (2014), p. 262408.
- [58] John S Tse et al. "Pressure-induced changes on the electronic structure and electron topology in the direct FCC \rightarrow SH transformation of silicon". In: *The Journal of Physical Chemistry C* 118.2 (2014), pp. 1161–1166.
- [59] Christoph J Sahle et al. "The Ba 4d–4f giant dipole resonance in complex Ba/Si compounds". In: *Journal of Physics B: Atomic, Molecular and Optical Physics* 47.4 (2014), p. 045102.
- [60] Tod A Pascal et al. "Finite temperature effects on the x-ray absorption spectra of lithium compounds: First-principles interpretation of x-ray Raman measurements". In: *The Journal of chemical physics* 140.3 (2014), p. 034107.
- [61] Simo Huotari et al. "X-ray-Raman-scattering-based EXAFS beyond the dipole limit". In: *Journal of synchrotron radiation* 19.1 (2012), pp. 106–113.
- [62] Alexander Nyrow et al. "Iron speciation in minerals and glasses probed by $\text{M}_{2/3}$ -edge X-ray Raman scattering spectroscopy". In: *Contributions to Mineralogy and Petrology* 167.5 (2014), p. 1012.
- [63] Gérald Lelong et al. "Detecting non-bridging oxygens: non-resonant inelastic x-ray scattering in crystalline lithium borates". In: *Inorganic chemistry* 53.20 (2014), pp. 10903–10908.

- [64] Christopher Weis et al. “Pressure driven spin transition in siderite and magnesiosiderite single crystals”. In: *Scientific reports* 7.1 (2017), pp. 1–10.
- [65] Sylvain Petitgirard et al. “Magma properties at deep Earth’s conditions from electronic structure of silica”. In: *Geochem. Perspect. Lett* 9 (2019), pp. 32–37.
- [66] Emmanuelle de Clermont Gallerande et al. “Quantification of non-bridging oxygens in silicates using x-ray Raman scattering”. In: *Journal of Non-Crystalline Solids* 528 (2020), p. 119715.
- [67] Yejun Feng et al. “Role of inversion symmetry and multipole effects in nonresonant x-ray Raman scattering from icosahedral B_4C ”. In: *Physical Review B* 69.12 (2004), p. 125402.
- [68] Michael Krisch et al. “Momentum transfer dependence of inelastic x-ray scattering from the Li K edge”. In: *Physical review letters* 78.14 (1997), p. 2843.
- [69] C Sternemann et al. “Momentum-transfer dependence of x-ray Raman scattering at the Be K-edge”. In: *Physical Review B* 68.3 (2003), p. 035111.
- [70] Keijo Hämäläinen et al. “Momentum dependence of fluorine K-edge core exciton in LiF ”. In: *Physical Review B* 65.15 (2002), p. 155111.
- [71] Yves Joly et al. “Full-potential simulation of x-ray Raman scattering spectroscopy”. In: *Journal of chemical theory and computation* 13.5 (2017), pp. 2172–2177.
- [72] Robert A Gordon et al. “High multipole transitions in NIXS: Valence and hybridization in 4f systems”. In: *EPL (Europhysics Letters)* 81.2 (2007), p. 26004.
- [73] Joe A Bradley et al. “Core and shallow-core d-to f-shell excitations in rare-earth metals”. In: *Physical Review B* 84.20 (2011), p. 205105.
- [74] Martin Sundermann et al. “The quartet ground state in CeB_6 : An inelastic x-ray scattering study”. In: *EPL (Europhysics Letters)* 117.1 (2017), p. 17003.
- [75] Martin Sundermann et al. “4f Crystal Field Ground State of the Strongly Correlated Topological Insulator SmB_6 ”. In: *Physical review letters* 120.1 (2018), p. 016402.
- [76] Roberto Caciuffo et al. “Uranium 5d-5f electric-multipole transitions probed by non-resonant inelastic x-ray scattering”. In: *Physical Review B* 81.19 (2010), p. 195104.

- [77] Joe A Bradley et al. “Probing electronic correlations in actinide materials using multipolar transitions”. In: *Physical Review B* 81.19 (2010), p. 193104.
- [78] Subhra Sen Gupta et al. “Coexistence of bound and virtual-bound states in shallow-core to valence x-ray spectroscopies”. In: *Physical Review B* 84.7 (2011), p. 075134.
- [79] Martin Sundermann et al. “Direct bulk-sensitive probe of 5f symmetry in URu₂Si₂”. In: *Proceedings of the National Academy of Sciences* 113.49 (2016), pp. 13989–13994.
- [80] Martin Sundermann et al. “Crystal-field states of UO₂ probed by directional dependence of nonresonant inelastic x-ray scattering”. In: *Physical Review B* 98.20 (2018), p. 205108.
- [81] Wendy L Mao et al. “Bonding changes in compressed superhard graphite”. In: *Science* 302.5644 (2003), pp. 425–427.
- [82] Sung Keun Lee et al. “Structure of alkali borate glasses at high pressure: B and Li K-edge inelastic X-ray scattering study”. In: *Physical review letters* 98.10 (2007), p. 105502.
- [83] Yue Meng et al. “The formation of sp³ bonding in compressed BN”. In: *Nature materials* 3.2 (2004), pp. 111–114.
- [84] Sung Keun Lee et al. “Probing of bonding changes in B₂ O₃ glasses at high pressure with inelastic x-ray scattering”. In: *Nature Materials* 4.11 (2005), pp. 851–854.
- [85] Sung Keun Lee et al. “Probing and modeling of pressure-induced coordination transformation in borate glasses: Inelastic x-ray scattering study at high pressure”. In: *Physical Review B* 78.21 (2008), p. 214203.
- [86] Ravhi S Kumar et al. “Inelastic x-ray scattering experiments on B₄C under high static pressures”. In: *Diamond and related materials* 19.5-6 (2010), pp. 530–532.
- [87] Michael Pravica et al. “X-ray Raman spectroscopic study of benzene at high pressure”. In: *The Journal of Physical Chemistry B* 111.40 (2007), pp. 11635–11637.
- [88] Ravhi S Kumar et al. “X-ray Raman scattering studies on C₆₀ fullerenes and multi-walled carbon nanotubes under pressure”. In: *Diamond and related materials* 16.4-7 (2007), pp. 1250–1253.

- [89] Lin Wang et al. “Application of a new composite cubic-boron nitride gasket assembly for high pressure inelastic x-ray scattering studies of carbon related materials”. In: *Review of Scientific Instruments* 82.7 (2011), p. 073902.
- [90] Yu Lin et al. “Amorphous diamond: a high-pressure superhard carbon allotrope”. In: *Physical Review Letters* 107.17 (2011), p. 175504.
- [91] Sean R Shieh et al. “Electronic structure of carbon dioxide under pressure and insights into the molecular-to-nonmolecular transition”. In: *Proceedings of the National Academy of Sciences* 110.46 (2013), pp. 18402–18406.
- [92] Amy Lazicki et al. “New cubic phase of Li_3N : stability of the N_3^- ion to 200 GPa”. In: *Physical review letters* 95.16 (2005), p. 165503.
- [93] Amy Lazicki et al. “Pressure-induced loss of electronic interlayer state and metallization in the ionic solid Li_3N : Experiment and theory”. In: *Physical Review B* 78.15 (2008), p. 155133.
- [94] Michael Pravica et al. “High-pressure studies of melamine”. In: *High Pressure Research* 30.1 (2010), pp. 65–71.
- [95] Michael Pravica et al. “High pressure infrared and x-ray Raman studies of aluminum nitride”. In: *physica status solidi (b)* 250.4 (2013), pp. 726–731.
- [96] Wendy L Mao et al. “X-ray-induced dissociation of H_2O and formation of an $\text{O}_2\text{--H}_2$ alloy at high pressure”. In: *science* 314.5799 (2006), pp. 636–638.
- [97] Jung-Fu Lin et al. “Electronic bonding transition in compressed SiO_2 glass”. In: *Physical Review B* 75.1 (2007), p. 012201.
- [98] Sung Keun Lee et al. “X-ray Raman scattering study of MgSiO_3 glass at high pressure: Implication for triclustered MgSiO_3 melt in Earth’s mantle”. In: *Proceedings of the National Academy of Sciences* 105.23 (2008), pp. 7925–7929.
- [99] Yue Meng et al. “Inelastic x-ray scattering of dense solid oxygen: Evidence for intermolecular bonding”. In: *Proceedings of the National Academy of Sciences* 105.33 (2008), pp. 11640–11644.
- [100] G Lelong et al. “Evidence of fivefold-coordinated Ge atoms in amorphous GeO_2 under pressure using inelastic x-ray scattering”. In: *Physical Review B* 85.13 (2012), p. 134202.

- [101] Benjamin JA Moulton et al. “In situ structural changes of amorphous diopside ($\text{CaMgSi}_2\text{O}_6$) up to 20 GPa: A Raman and O K-edge X-ray Raman spectroscopic study”. In: *Geochimica et Cosmochimica Acta* 178 (2016), pp. 41–61.
- [102] N Hiraoka, H Fukui, and Takuo Okuchi. “EXAFS studies under high pressure by x-ray Raman scattering”. In: *High Pressure Research* 36.3 (2016), pp. 250–261.
- [103] Sung Keun Lee et al. “Oxygen quadclusters in SiO_2 glass above megabar pressures up to 160 GPa revealed by x-Ray Raman scattering”. In: *Physical Review Letters* 123.23 (2019), p. 235701.
- [104] Sung Keun Lee, Peter J Eng, and Ho-kwang Mao. “Probing of pressure-induced bonding transitions in crystalline and amorphous earth materials: insights from x-ray Raman scattering at high pressure”. In: *Reviews in Mineralogy and Geochemistry* 78.1 (2014), pp. 139–174.
- [105] Hiroshi Fukui et al. “Coordination environment of silicon in silica glass up to 74 GPa: An x-ray Raman scattering study at the silicon L edge”. In: *Physical Review B* 78.1 (2008), p. 012203.
- [106] Alexander Nyrow et al. “Bulk sensitive determination of the $\text{Fe}^{3+}/\text{Fe}_{\text{Tot}}$ -ratio in minerals by Fe $\text{L}_{2/3}$ -edge X-ray Raman scattering”. In: *Journal of Analytical Atomic Spectrometry* 31.3 (2016), pp. 815–820.
- [107] Christopher Weis et al. “Combining X-ray $\text{K}\beta$ 1, 3, valence-to-core, and X-ray Raman spectroscopy for studying Earth materials at high pressure and temperature: the case of siderite”. In: *Journal of analytical atomic spectrometry* 34.2 (2019), pp. 384–393.
- [108] Yang Ding et al. “Novel high-pressure monoclinic metallic phase of V_2O_3 ”. In: *Physical review letters* 112.5 (2014), p. 056401.
- [109] Jean-Pascal Rueff and Abhay Shukla. “Inelastic x-ray scattering by electronic excitations under high pressure”. In: *Reviews of Modern Physics* 82.1 (2010), p. 847.
- [110] Christian Sternemann and Max Wilke. “Spectroscopy of low and intermediate Z elements at extreme conditions: in situ studies of Earth materials at pressure and temperature via X-ray Raman scattering”. In: *High Pressure Research* 36.3 (2016), pp. 275–292.

- [111] Piter S Miedema et al. “In situ X-ray Raman spectroscopy of LiBH_4 ”. In: *Physical Chemistry Chemical Physics* 14.16 (2012), pp. 5581–5587.
- [112] Piter S Miedema et al. “In situ x-ray Raman spectroscopy study of the hydrogen sorption properties of lithium borohydride nanocomposites”. In: *Physical Chemistry Chemical Physics* 16.41 (2014), pp. 22651–22658.
- [113] Christoph J Sahle et al. “In situ characterization of the decomposition behavior of $\text{Mg}(\text{BH}_4)_2$ by x-ray Raman scattering spectroscopy”. In: *Physical Chemistry Chemical Physics* 18.7 (2016), pp. 5397–5403.
- [114] Christoph J Sahle et al. “Formation of CaB_6 in the thermal decomposition of the hydrogen storage material $\text{Ca}(\text{BH}_4)_2$ ”. In: *Physical Chemistry Chemical Physics* 18.29 (2016), pp. 19866–19872.
- [115] Oscar Ariel Paredes-Mellone et al. “Li 1s core exciton in LiH studied by x-ray Raman scattering spectroscopy”. In: *Journal of Physics: Condensed Matter* 31.5 (2018), p. 055501.
- [116] Ulrike Boesenberg et al. “Electronic structure changes upon lithium intercalation into graphite—Insights from ex situ and operando x-ray Raman spectroscopy”. In: *Carbon* 143 (2019), pp. 371–377.
- [117] Takamasa Nonaka et al. “In situ x-ray Raman scattering spectroscopy of a graphite electrode for lithium-ion batteries”. In: *Journal of Power Sources* 419 (2019), pp. 203–207.
- [118] Kazuhiko Mukai et al. “In situ X-ray Raman spectroscopy and magnetic susceptibility study on Li $[\text{Li}_{0.15}\text{Mn}_{1.85}]\text{O}_4$ oxygen anion redox reaction”. In: *Chemical Communications* (2020).
- [119] Nienke J Firet et al. “Chemisorption of anionic species from the electrolyte alters the surface electronic structure and composition of photocharged BiVO_4 ”. In: *Chemistry of Materials* 31.18 (2019), pp. 7453–7462.
- [120] Alessandro Longo et al. “What makes Fe-modified MgAl_2O_4 an active catalyst support? Insight from X-ray Raman Scattering”. In: *ACS Catalysis* 10.12 (2020), pp. 6613–6622.

- [121] Marcus Fehse et al. “Bulk-Sensitive Soft X-ray Edge Probing for Elucidation of Charge Compensation in Battery Electrodes”. In: *The Journal of Physical Chemistry C* 123.40 (2019), pp. 24396–24403.
- [122] Keijo Hämäläinen and S Manninen. “Resonant and non-resonant inelastic x-ray scattering”. In: *Journal of Physics: Condensed Matter* 13.34 (2001), p. 7539.
- [123] Sunil K Sinha. “Theory of inelastic x-ray scattering from condensed matter”. In: *Journal of Physics: Condensed Matter* 13.34 (2001), p. 7511.
- [124] Michael Krisch and Francesco Sette. “X-ray Raman scattering from low Z materials”. In: *Surface Review and Letters* 9.02 (2002), pp. 969–976.
- [125] Uwe Bergmann, Pieter Glatzel, and Stephen P Cramer. “Bulk-sensitive XAS characterization of light elements: from X-ray Raman scattering to X-ray Raman spectroscopy”. In: *Microchemical Journal* 71.2-3 (2002), pp. 221–230.
- [126] Adolf Smekal. “Zur quantentheorie der dispersion”. In: *Naturwissenschaften* 11.43 (1923), pp. 873–875.
- [127] Chandrasekhara Venkata Raman. “A new radiation”. In: (1928).
- [128] Bergen Davis and Dana P Mitchell. “Fine structure of the scattered radiation from graphite”. In: *Physical Review* 32.3 (1928), p. 331.
- [129] W Ehrenberg. “Über die Streuung von Röntgenstrahlen an Graphit”. In: *Zeitschrift für Physik* 53.3-4 (1929), pp. 234–236.
- [130] D Coster, I Nitta, and WJ Thijssen. “The Raman effect for X-rays”. In: *Nature* 124.3119 (1929), pp. 230–230.
- [131] BB Ray. “Teilabsorption von Röntgenstrahlen”. In: *Zeitschrift fuer Physik* 66.3-4 (1930), pp. 261–268.
- [132] A Sommerfeld. “Concerning the shape of the Compton lines (From a Letter to AH Compton)”. In: *Physical Review* 50.1 (1936), p. 38.
- [133] K Das Gupta. “A new type of x-ray scattering”. In: *Nature* 166.4222 (1950), pp. 563–564.
- [134] K Das Gupta. “Smekal-raman type modified x-ray scattering”. In: *Physical Review Letters* 3.1 (1959), p. 38.

- [135] K Das Gupta. “Characteristic modified x-ray scattering”. In: *Physical Review* 128.5 (1962), p. 2181.
- [136] K Das Gupta. “Recoil electron resonance in crystals and the Stokes and Anti-Stokes modified lines in x-Ray scattering”. In: *Physical Review Letters* 13.10 (1964), p. 338.
- [137] Yukio Mizuno and Yoshihiro Ohmura. “Theory of X-ray Raman scattering”. In: *Journal of the Physical Society of Japan* 22.2 (1967), pp. 445–449.
- [138] Tadasu Suzuki. “X-ray Raman scattering experiment. I”. In: *Journal of the Physical Society of Japan* 22.5 (1967), pp. 1139–1150.
- [139] Tadasu Suzuki and Hisao Nagasawa. “X-Ray Raman scattering. III. The angular dependence of the scattering intensity”. In: *Journal of the Physical Society of Japan* 39.6 (1975), pp. 1579–1585.
- [140] J Aleksi Soininen, AL Ankudinov, and JJ Rehr. “Inelastic scattering from core electrons: A multiple scattering approach”. In: *Physical Review B* 72.4 (2005), p. 045136.
- [141] Malcom J Cooper. “Compton scattering and electron momentum determination”. In: *Reports on Progress in Physics* 48.4 (1985), p. 415.
- [142] P Eisenberger and PM Platzman. “Compton scattering of x-rays from bound electrons”. In: *Physical Review A* 2.2 (1970), p. 415.
- [143] Ian Fleming. *Molecular orbitals and organic chemical reactions*. John Wiley & Sons, 2011.
- [144] Adam P Hitchcock and DC Mancini. “Bibliography and database of inner shell excitation spectra of gas phase atoms and molecules”. In: *Journal of Electron Spectroscopy and Related Phenomena* 67.1 (1994), p. vii.
- [145] Dawit Solomon et al. “Carbon (1s) NEXAFS spectroscopy of biogeochemically relevant reference organic compounds”. In: *Soil Science Society of America Journal* 73.6 (2009), pp. 1817–1830.
- [146] Corentin Le Guillou et al. “XANES-based quantification of carbon functional group concentrations”. In: *Analytical Chemistry* 90.14 (2018), pp. 8379–8386.
- [147] Karen Heymann et al. “C 1s K-edge near edge X-ray absorption fine structure (NEXAFS) spectroscopy for characterizing functional group chemistry of black carbon”. In: *Organic Geochemistry* 42.9 (2011), pp. 1055–1064.

- [148] Véronique Rouchon and Sylvain Bernard. “Mapping iron gall ink penetration within paper fibres using scanning transmission X-ray microscopy”. In: *Journal of Analytical Atomic Spectrometry* 30.3 (2015), pp. 635–641.
- [149] Julien Alleon et al. “Organic molecular heterogeneities can withstand diagenesis”. In: *Scientific reports* 7.1 (2017), pp. 1–9.
- [150] George D Cody et al. “Determination of chemical-structural changes in vitrinite accompanying luminescence alteration using C-NEXAFS analysis”. In: *Organic Geochemistry* 28.7-8 (1998), pp. 441–455.
- [151] Sylvain Bernard et al. “Geochemical evolution of organic-rich shales with increasing maturity: A STXM and TEM study of the Posidonia Shale (Lower Toarcian, northern Germany)”. In: *Marine and Petroleum Geology* 31.1 (2012), pp. 70–89.
- [152] Adam P. Hitchcock and Chris E. Brion. “Inner-shell excitation of formaldehyde, acetaldehyde and acetone studied by electron impact”. In: *Journal of Electron Spectroscopy and Related Phenomena* 19.2 (1980), pp. 231–250.
- [153] I Ishii and Adam P Hitchcock. “A quantitative experimental study of the core excited electronic states of formamide, formic acid, and formyl fluoride”. In: *The Journal of chemical physics* 87.2 (1987), pp. 830–839.
- [154] MB Robin et al. “Fluorination effects on the inner-shell spectra of unsaturated molecules”. In: *Journal of Electron Spectroscopy and Related Phenomena* 47 (1988), pp. 53–92.
- [155] KL Harding et al. “Inner-shell excitation spectroscopy of peroxides”. In: *Chemical Physics* 461 (2015), pp. 117–124.
- [156] I Ishii and Adam P Hitchcock. “The oscillator strengths for C1s and O1s excitation of some saturated and unsaturated organic alcohols, acids and esters”. In: *Journal of Electron Spectroscopy and Related Phenomena* 46.1 (1988), pp. 55–84.
- [157] JT Francis and Adam P Hitchcock. “Inner-shell spectroscopy of p-benzoquinone, hydroquinone, and phenol: distinguishing quinoid and benzenoid structures”. In: *The Journal of Physical Chemistry* 96.16 (1992), pp. 6598–6610.

- [158] Jussi Lehtola et al. “ERKALE—A flexible program package for X-ray properties of atoms and molecules”. In: *Journal of Computational Chemistry* 33.18 (2012), pp. 1572–1585. DOI: 10.1002/jcc.22987.
- [159] K Hermann et al. “StoBe-DeMon, version 3.0”. In: *STOBE software* (2002).
- [160] Arto Sakko et al. “Density functional study of x-ray Raman scattering from aromatic hydrocarbons and polyfluorene”. In: *Physical Review B* 76.20 (2007), p. 205115.
- [161] Mathieu Taillefumier et al. “X-ray absorption near-edge structure calculations with the pseudopotentials: Application to the K edge in diamond and α -quartz”. In: *Phys. Rev. B* 66 (19 2002), p. 195107. DOI: 10.1103/PhysRevB.66.195107. URL: <https://link.aps.org/doi/10.1103/PhysRevB.66.195107>.
- [162] Paolo Giannozzi et al. “QUANTUM ESPRESSO: a modular and open-source software project for quantum simulations of materials”. In: *Journal of Physics: Condensed Matter* 21.39 (2009), p. 395502.
- [163] Emmanuelle de Clermont Gallerande et al. “First-principles modeling of x-ray Raman scattering spectra”. In: *Physical Review B* 98.21 (2018), p. 214104.
- [164] John Vinson et al. “Bethe-Salpeter equation calculations of core excitation spectra”. In: *Physical Review B* 83.11 (2011), p. 115106.
- [165] Keith Gilmore et al. “Efficient implementation of core-excitation Bethe–Salpeter equation calculations”. In: *Computer Physics Communications* 197 (2015), pp. 109–117. ISSN: 0010-4655.
- [166] Robert D Cowan. *The theory of atomic structure and spectra*. 3. Univ of California Press, 1981.
- [167] M. W. Haverkort, M. Zwierzycki, and O. K. Andersen. “Multiplet ligand-field theory using Wannier orbitals”. In: *Phys. Rev. B* 85 (16 2012), p. 165113. DOI: 10.1103/PhysRevB.85.165113. URL: <https://link.aps.org/doi/10.1103/PhysRevB.85.165113>.

- [168] J. T. Francis and Adam P Hitchcock. “Inner-shell spectroscopy of p-benzoquinone, hydroquinone, and phenol: distinguishing quinoid and benzenoid structures”. In: *The Journal of Physical Chemistry* 96.16 (1992), pp. 6598–6610. doi: 10 . 1021 / j100195a018.
- [169] RA Rosenberg, PJ Love, and Victor Rehn. “Polarization-dependent C (K) near-edge x-ray-absorption fine structure of graphite”. In: *Physical Review B* 33.6 (1986), p. 4034.
- [170] J Aleksi Soininen et al. “Experimental determination of the core-excited electron density of states”. In: *Journal of Physics: Condensed Matter* 18.31 (2006), p. 7327.
- [171] MJ Berger et al. “Xcom: Photon cross sections database, nist standard reference database 8 (xgam)”. In: <http://physics.nist.gov/PhysRefData/Xcom/Text/XCOM.html> (2010).
- [172] Chamseddine Benabderrahmane et al. “Development and operation of a $\text{Pr}_2\text{Fe}_{14}\text{B}$ based cryogenic permanent magnet undulator for a high spatial resolution x-ray beam line”. In: *Physical Review Accelerators and Beams* 20.3 (2017), p. 033201.
- [173] Rainer Wanzenberg et al. “Design status of the ultra-low emittance synchrotron facility PETRA IV”. In: *AIP Conference Proceedings*. Vol. 2054. 1. AIP Publishing LLC. 2019, p. 030002.
- [174] Kazuyuki Tohji and Yasuo Udagawa. “X-ray Raman scattering as a substitute for soft-x-ray extended x-ray-absorption fine structure”. In: *Physical Review B* 39.11 (1989), p. 7590.
- [175] Kazuyuki Tohji and Yasuo Udagawa. “Novel approach for structure analysis by x-ray Raman scattering”. In: *Physical Review B* 36.17 (1987), p. 9410.
- [176] *Experimental Station 6-2b, Stanford Synchrotron Radiation Lightsource, Accessed Aug. 01, 2021*. URL: <https://www-ssrl.slac.stanford.edu/content/beam-lines/bl6-2b>.
- [177] Yuming M Xiao et al. “New developments in high pressure X-ray spectroscopy beam-line at High Pressure Collaborative Access Team”. In: *Review of scientific instruments* 86.7 (2015), p. 072206.

- [178] Yong Q Cai et al. “Optical Design and Performance of the Taiwan Inelastic X-Ray Scattering Beamline (BL12XU) at SPring-8”. In: *AIP Conference proceedings*. Vol. 705. 1. American Institute of Physics. 2004, pp. 340–343.
- [179] James Michael Ablett et al. “The GALAXIES inelastic hard x-ray scattering end-station at Synchrotron SOLEIL”. In: *Journal of synchrotron radiation* 26.1 (2019), pp. 263–271.
- [180] *ID20-Inelastic Scattering I, ESRF*, Accessed Aug. 01, 2021. URL: <https://www.esrf.eu/home/UsersAndScience/Experiments/EMD/ID20/beamline-characteristics.html>.
- [181] *P01 Dynamics, Inelastic X-ray Scattering Station, PETRAIII*, Accessed Aug. 01, 2021. URL: https://photon-science.desy.de/facilities/petra_iii/beamlines/p01_dynamics/inelastic_x_ray_scattering_station/xrs_spectrometer/index_eng.html.
- [182] Uwe Bergmann and Stephen P Cramer. “High-resolution large-acceptance analyzer for x-ray fluorescence and Raman spectroscopy”. In: *Crystal and Multilayer Optics*. Vol. 3448. International Society for Optics and Photonics. 1998, pp. 198–209.
- [183] Ari-Pekka Honkanen and Simo Huotari. “General method to calculate the elastic deformation and X-ray diffraction properties of bent crystal wafers”. In: *IUCrJ* 8.1 (2021).
- [184] Ari-Pekka Honkanen et al. “Study on the reflectivity properties of spherically bent analyser crystals”. In: *Journal of synchrotron radiation* 21.1 (2014), pp. 104–110.
- [185] Charles Galton Darwin. “The theory of x-ray reflexion. Part 2”. In: *Phil. Mag* 27 (1914), pp. 675–690.
- [186] Jesse WM DuMond. “Theory of the use of more than two successive x-ray crystal reflections to obtain increased resolving power”. In: *Physical Review* 52.8 (1937), p. 872.
- [187] Hans Heinrich Johann. “Die erzeugung lichtstarker röntgenspektren mit hilfe von konkavkristallen”. In: *Zeitschrift für Physik* 69.3-4 (1931), pp. 185–206.
- [188] Ari-Pekka Honkanen et al. “Improving the energy resolution of bent crystal x-ray spectrometers with position-sensitive detectors”. In: *Journal of synchrotron radiation* 21.4 (2014), pp. 762–767.

- [189] Satio Takagi. “Dynamical theory of diffraction applicable to crystals with any kind of small distortion”. In: *Acta Crystallographica* 15.12 (1962), pp. 1311–1312.
- [190] Daniel Taupin. “Théorie dynamique de la diffraction des rayons X par les cristaux déformés”. In: *Bulletin de Minéralogie* 87.4 (1964), pp. 469–511.
- [191] Simo Huotari et al. “A large-solid-angle X-ray Raman scattering spectrometer at ID20 of the European Synchrotron Radiation Facility”. In: *Journal of Synchrotron Radiation* 24.2 (2017), pp. 521–530.
- [192] Dimosthenis Sokaras et al. “A high resolution and large solid angle x-ray Raman spectroscopy end-station at the Stanford Synchrotron Radiation Lightsource”. In: *Review of Scientific Instruments* 83.4 (2012), p. 043112.
- [193] Timothy T Fister et al. “Background proportional enhancement of the extended fine structure in nonresonant inelastic x-ray scattering”. In: *Physical Review B* 74.21 (2006), p. 214117.
- [194] Frank Biggs, Lawrence B. Mendelsohn, and Joseph B Mann. “Hartree-Fock Compton profiles for the elements”. In: *Atomic data and nuclear data tables* 16.3 (1975), pp. 201–309.
- [195] Christoph J Sahle et al. “Planning, performing and analyzing X-ray Raman scattering experiments”. In: *Journal of Synchrotron Radiation* 22.2 (2015), pp. 400–409.
- [196] Christoph J Sahle et al. “Improving the spatial and statistical accuracy in X-ray Raman scattering based direct tomography”. In: *Journal of Synchrotron Radiation* 24.2 (2017), pp. 476–481.
- [197] Simo Huotari et al. “Direct tomography with chemical-bond contrast”. In: *Nature Materials* 10.7 (2011), pp. 489–493.
- [198] Uwe Bergmann, Oliver C Mullins, and SP Cramer. “X-ray Raman spectroscopy of carbon in asphaltene: light element characterization with bulk sensitivity”. In: *Analytical Chemistry* 72.11 (2000), pp. 2609–2612.
- [199] Michelle L Gordon et al. “Inner-shell excitation spectroscopy of the peptide bond: Comparison of the C 1s, N 1s, and O 1s spectra of glycine, glycyl-glycine, and glycyl-glycyl-glycine”. In: *The Journal of Physical Chemistry A* 107.32 (2003), pp. 6144–6159.

- [200] Andrew E Pomerantz et al. “Carbon core electron spectra of polycyclic aromatic hydrocarbons”. In: *The Journal of Physical Chemistry A* 122.26 (2018), pp. 5730–5734.
- [201] Andrew E Pomerantz et al. “Electronic Structure of Naturally Occurring Aromatic Carbon”. In: *Energy & fuels* 33.3 (2019), pp. 2099–2105.
- [202] Didem Ketenoglu et al. “X-ray Raman spectroscopy of lithium-ion battery electrolyte solutions in a flow cell”. In: *Journal of synchrotron radiation* 25.2 (2018), pp. 537–542.
- [203] Loïc Bertrand et al. “Mitigation strategies for radiation damage in the analysis of ancient materials”. In: *TrAC Trends in Analytical Chemistry* 66 (2015), pp. 128–145.

Disentangling the chemistry of Australian plant exudates from a unique historical collection

For millennia, the unique physicochemical properties of plant exudates have defined practical applications in material culture and cultural use. Native Australian plant exudates, including resins, kinos, and gums, have been used and continue to be used by Aboriginal Australians for numerous technical and cultural purposes. Especially in the area of analysis of material cultural heritage, there has not been a comprehensive analytical approach to native Australian plant exudates. A historic collection of well-preserved native Australian plant exudates, assembled a century ago by plant naturalists, gives a rare window into the history and chemical composition of these materials. We report here the study of four genera from this collection, Xanthorrhoea, Callitris, Eucalyptus and Acacia, using a multimodal approach based on XRS, FT-IR and inductively coupled plasma mass spectrometry (ICP-MS). Combining the analysis of characteristic features in the XRS and FT-IR spectra provides detailed chemical information about these complex natural species. We use this characterization towards their broader categorization into chemical classes, including terpenoid, aromatic, phenolic and polysaccharide compounds. The study exemplifies the potential of XRS, a synchrotron-based hard x-ray method recently introduced into heritage sciences, to interrogate carbon and oxygen speciation in aged organic systems of complex chemistry, without the limitation of invasive and/or surface specific methods. Our findings provide fundamental understanding of the chemistry of these natural materials long used by Aboriginal Australian peoples.

2.1 Introduction

For millennia, societies have empirically utilized the physicochemical properties of plant exudates and implemented them in practical applications and cultural expression [1–3]. Native Australian plant exudates, including the commonly named resins, kinos and gums, have been

used by Aboriginal Australians over thousands of years across the continent for a variety of purposes. Besides the practical use for examples such as adhesives and binders, they have been employed in a diversity of cultural heritage objects [4–7].

Native plant exudates have an important role in Aboriginal Australian heritage and technological uses. Indigenous Australians across the continent used plant materials from different sources as hafting adhesives (e.g. hafting stone tools to handles), paint binders, priming layers for bark paintings (such as orchid leaf juice), and for medical and narcotic purposes [5, 6, 8–13]. Aboriginal Australians developed technologies for processing the naturally occurring organic materials, maximizing their effective use for each purpose [14]. To change or enhance their properties, specific formulations were often mixed with ocher and other materials, including dried and powdered polysaccharide gums and fibers [6, 15–17].

Plant exudates continue to be incorporated in a variety of cultural contexts in Aboriginal Australian communities [4]. For example, contemporary Australian Aboriginal artists may choose to use traditional binders over synthetic materials such as acrylic or oil paints [4]. Artists go through the time-consuming preparations of paints using traditional binders and pigments, to intentionally connect their artworks to their local landscape, tradition and culture [4, 15].

Only a few characterization studies of the complex chemistry of natural Australian plant exudates have been reported in the context of raw exudates, and similarly on cultural heritage materials. Blee et al. [8] have examined samples including *Xanthorrhoea tateana*, *Xanthorrhoea semiplana* and an *Acacia* gum of an unknown species belonging to the ethnobotany collection of the South Australian Museum (SAM) by FT-IR and chemometric techniques. The authors were able to differentiate native Australian resins and identified probable candidates used for hafted stone knives. Reeves, Popelka-Filcoff, and Lenehan [11] analyzed the same three samples from the SAM collection and also characterized known Australian and European materials of different chemical classes by pyrolysis gas chromatography mass spectrometry (py-GC-MS) with subsequent multivariate statistical analysis. Analysis of the same materials by different methods demonstrated consistent results, e.g. the identification of the C–C ring stretching by FT-IR and the identification of phenolic groups by py-GC-MS for the *Xanthorrhoea* genera. Both papers find that the *Acacia* and *Xanthorrhoea* samples can be distinguished from the other samples by key characteristics in each genera. Bradshaw [13] employed GC-MS to chemically

characterize six ethnographic resins belonging to the Pitt Rivers Museum collected a hundred years ago. Matheson and McCollum [6] analyzed a collection of both raw plant materials and resins from Queensland Museum objects, by FT-IR and GC-MS. While not identifying the major components of the species examined from the raw plant materials and artefacts, the authors were able to assign *Xanthorrhoea*, *Triodia* and *Erythrophleum chlorostahys* resins on archaeological objects to their plant resin counterparts by matching elution times in GC-MS and spectral features in attenuated total reflectance (ATR) FT-IR [6].

At the turn of the 20th century, a group of unknown naturalists assembled an extensive and comprehensive collection of plant exudates sampled across Australia, carefully annotating location information, with most collected from about 1876–1905 (Table 2.1). These samples have been stored up to the present in labeled brown glass jars. Further details and storage conditions of the collection are lost to time, however it is assumed that the individual jars have been kept together and therefore experienced the same conditions over the decades. The first documentation of the collection was in the laboratories at the Art Gallery of South Australia. When these laboratories were closed in the late 1980s, the collection was transferred and held in the South Australian state forensic laboratory (Forensic Science South Australia–FSSA) until the early 2000s. Subsequently, the collection was bequeathed to Flinders University by former scientists at FSSA, Professor Paul Kirkbride and Dr Paul Pigou, with the intention for further research about this unique time capsule of samples. This exceptional collection offers a rare glimpse into well-preserved plant exudates of major cultural and technological interest used both by Aboriginal Australian and European Australian peoples.

Here, we report a detailed characterization of the chemical speciation of native Australian plant exudates from four distinct genera (*Xanthorrhoea*, *Callitris*, *Eucalyptus*, *Acacia*) preserved in the historic collection. While some genera are uniquely from Australia or Oceania and have properties that are not seen in other parts of the globe (*Xanthorrhoea*, *Callitris*, *Eucalyptus*), species of *Acacia* are found worldwide [18]. Although from distinct geographical origins, exudates from *Callitris* have been noted for their chemical similarities to sandarac resin from the *Tetraclinis articulata* tree from northern Africa [19]. Similarly, exudates from Australian *Acacia* have parallels from other *Acacia* species that produce gum Arabic (*Acacia senegal* now known as *Senegalia senegal*) [20]. However, despite extensive characterization of gum Arabic, the vast majority of over a thousand *Acacia* (wattle) species worldwide are found in Australia,

| Samples | Species | Genus | Clade | Location |
|---------|-----------------------------------|--------------|-------------|---|
| 1 | <i>X. arborea</i> | Xanthorrhoea | Angiosperms | Helensburgh, Australia, 29 May 1905 |
| 2 | <i>X. semiplana ssp. tateana</i> | Xanthorrhoea | Angiosperms | Munston, Kangaroo Island, South Australia [SAM No. A66781] |
| 3 | <i>X. semiplana</i> | Xanthorrhoea | Angiosperms | West of Clarendon, South Australia [SAM No. A66782] |
| 4 | <i>C. calcarata</i> | Callitris | Gymnosperms | Quiedong, near Bombala, New South Wales, Australia, 03 March 1887 |
| 5 | <i>C. glauca</i> | Callitris | Gymnosperms | Deniliquin, New South Wales, Australia |
| 6 | <i>C. preissii ssp. verrucosa</i> | Callitris | Gymnosperms | Shuttleton, New South Wales, Australia |
| 7 | White Mallee | Eucalyptus | Angiosperms | Not recorded, 06 May 1911 |
| 8 | <i>E. largiflores</i> | Eucalyptus | Angiosperms | Gunbar, New South Wales, Australia, December 1900 |
| 9 | Not recorded | Acacia | Angiosperms | Coopers Creek [SAM No. A2182] |
| 10 | <i>A. bakeri</i> | Acacia | Angiosperms | Tubulgum, Australia, February 1899 |

Table 2.1: Native Australian plant exudates. The raw materials from the historical collection are approximately 100+ years old. Samples from the South Australian Museum (SAM) (denoted by SAM number) are raw plant materials also stored for decades with the exact collection dates unknown.

remain less studied by analytical approaches. These genera represent many of the general classes of plants that produce exudates in Australia [1], as well as those used in cultural and scientific practices [6, 15].

We analyzed and classified these natural products using chemical characterization by a multimodal approach that includes synchrotron-based x-ray Raman scattering and lab-based analytical methods (FT-IR and ICP-MS). We combined XRS and FT-IR, which provided molecular specificity from identification of major functional groups (approximately proportional to their concentration). We showed that straightforward and sensitive characterization and discrimination of the complex organic compounds is attained using XRS in a non-invasive manner. The work is the first in-depth XRS-based statistical inter-comparison of complex historical samples. Our application of XRS provides an atomic-level understanding of the chemical speciation of the plant exudates in this rare collection. XRS can be applied in a routine way for the chemical characterization of samples without being invasive, and can be considered as a powerful tool for the chemical characterization and fine spectroscopic analysis of solid organic materials.

2.2 Results

2.2.1 Main spectroscopic properties of plant exudates

XRS carbon K-edge (Figure 2.1) and oxygen K-edge (Figure 2.2) spectra were collected for a variety of plant species and genera. The XRS process is based on the inelastic scattering of a high-energy incident photon, $\hbar\omega_1$, which excites a core electron to a vacant higher-energy molecular orbital, while the excess of energy is released with a scattered photon, $\hbar\omega_2$ [21–23]. Spectral decomposition of the normalized background-corrected XRS signal was performed as described (see XRS Data Reduction). XRS is able to provide a unique chemical fingerprint for each of the plant genera under study, thus it can be considered as a reliable non-invasive tool for their discrimination. XRS data interpretation was based on an important corpus of work on carbon K-edge XANES and EELS. A database of inner shell excitation spectra obtained by EELS, gathering a large number of carbon and oxygen K-edge spectra is provided by Hitchcock and Mancini [24]. FT-IR assignments were based in handbooks [25–27] and specific studies cited along the text. FT-IR (Figure 2.3) assisted on the interpretation of the XRS features and the accurate assignment of the core electron transitions in various functional groups. Solution-based ICP-MS was employed for the elemental characterization of all of the samples (*SI Appendix*, Figure A.2).

2.2.1.1 *Xanthorrhoea* resins

Compared to all other plant exudates studied, *Xanthorrhoea* species exhibit the highest amount of aromatic and/or olefinic carbon, which can be considered as a defining feature of the species (Figure 2.1A, *SI Appendix* Table A.5). The XRS carbon K-edge spectra are dominated by the presence of an intense peak at 285.5 eV attributed to the $1s-\pi^*$ transitions in aromatic / olefinic groups (Figure 2.1A). The presence of aromatic groups is confirmed by the FT-IR high intensity sharp peaks centered at 1602 cm^{-1} , 1513 cm^{-1} and 1444 cm^{-1} attributed to C=C stretching (Figure 2.3C). The FT-IR band centered at 1636 cm^{-1} is attributed to C=C stretching of non-aromatic C=C bonds [28]. Its presence is higher in *X. arborea*, while for *X. semiplana* and *X. semiplana ssp. tateana* the feature is less noticeable. The weak intensity FT-IR peak observed at 3023 cm^{-1} is attributed to the CH stretching in alkene groups (Figure 2.3B).

The XRS feature at 287.3–287.4 eV (center of fitted Gaussian 4 varies among the species, *SI*

Appendix Table A.2) is attributed to the $1s-\pi^*$ transitions in phenols ($\text{Ar}-\text{OH}$) and to a lesser extent to $1s-3p/\sigma^*$ transitions in aliphatic groups (C_xH_y) [29] (Figure 2.1A), confirmed by the weak FT-IR bands in the 3000–2800 region corresponding to C–H antisymmetric and symmetric stretch of CH_3 and CH_2 groups (Figure 2.3B). The FT-IR bands centered at 1337 cm^{-1} and 1205 cm^{-1} , linked to the O–H deformation/C–OH stretching, are observable in all *Xanthorrhoea* species (Figure 2.3C). The broad signal in the $3550\text{--}3250\text{ cm}^{-1}$ region is attributed to –OH stretching (Figure 2.3A). The Gaussian 3 fitted at 286.6–286.7 eV (the center varies among *Xanthorrhoea* species, SI Appendix Table A.2) is tentatively assigned to $1s-\pi^*$ transitions in ketones ($\text{R}_2\text{C}=\text{O}$) (Figure 2.1A). Oxygen $1s-\pi^*$ excitations in carbonyl groups ($\text{C}=\text{O}$) (Gaussian 1 centered at 531.1–531.5 eV) are observed at the XRS oxygen K-edge spectra (Figure 2.2A). FT-IR spectra exhibit a small shoulder around 1670 cm^{-1} that could be related to the $\text{C}=\text{O}$ of aromatic ketones, which appears at lower wavelengths than aliphatic ketones due to the conjugation (Figure 2.3C) [30]. The XRS feature centered at 289.2 eV, is attributed to the $1s-3p/\sigma^*$ electronic transitions in hydroxyl groups ($\text{R}-\text{OH}$) (Figure 2.1A, SI Appendix Table A.5) [29].

2.2.1.2 *Callitris* resins

The XRS carbon K-edge spectrum of *C. calcarata* is characterized by a main peak at 288.7 eV assigned to the $1s-\pi^*$ electronic transitions in carboxyl groups ($-\text{COOH}$) (Figure 2.1B). The presence of carboxyls in the sample are confirmed by the strong broad feature of the FT-IR spectrum centered at 1695 cm^{-1} attributed to $\text{C}=\text{O}$ stretching of carboxylic acids (Figure 2.3A), the band around 3450 cm^{-1} related to O–H stretching and the peak at 1236 cm^{-1} linked to the C–OH stretching / O–H deformation of the OH groups (Figure 2.3C). The XRS oxygen K-edge spectra of *Callitris* species confirm as well the abundance of carboxylic acids. Compared to all the other genera, the spectra exhibit a higher intensity peak centered at 532.1 assigned to the oxygen $\text{C}=\text{O}$ $1s-\pi^*$ transitions in carboxyls ($-\text{COOH}$) while the feature centered at 535.2 eV is attributed to the oxygen O–H $1s-\pi^*$ transitions in carboxyl groups ($-\text{COOH}$) [31] (Figure 2.2B).

The XRS peak at 285.4 eV corresponds to $1s-\pi^*$ transitions in aromatic or olefinic groups ($\text{C}=\text{C}$) (Figure 2.1B). The presence of low intensity bands at 1610 cm^{-1} and 1497 cm^{-1} attributed to the $\text{C}=\text{C}$ stretching in aromatic compounds indicates the low aromaticity of the *Callitris* species (Figure 2.3C), linked to the ageing process of the resin [32]. The FT-IR band cen-

tered at 1644 cm^{-1} attributed to the C=C stretching is linked to the presence of non-aromatic C=C bonds. The band at 3080 cm^{-1} linked to the C–H stretching from the C=C moieties confirms the existence of these structures (Figure 2.3B). The low intensity XRS feature centered at 286.7 eV is possibly attributed to $1s-\pi^*$ electronic transitions in ketone groups (Figure 2.1B). The FT-IR shoulder around 1726 cm^{-1} is attributed to the C=O stretching in ketones and the 1236 cm^{-1} band to the O–H bending in alcohols (Figure 2.3C).

The broad XRS feature in the region 287.3–288 eV, centered at 287.6 eV is attributed to the $1s-3p/\sigma^*$ of aliphatic groups (Figure 2.1B); their presence is confirmed by the strong intensity peaks of CH_2 and CH_3 antisymmetric and symmetric stretch in the $3000-2800\text{ cm}^{-1}$ region of the FT-IR spectrum (Figure 2.3B). The presence of these groups is confirmed by the bands around 1467 cm^{-1} ($-\text{CH}_2-$) and around 1384 cm^{-1} (deformation of CH_3 and CH_2 groups) (Figure 2.3C).

2.2.1.3 *Eucalyptus kino*

The XRS carbon K-edge spectra of *Eucalyptus* exudates exhibit an intense peak centered at 287.4 eV assigned to $1s-\pi^*$ transitions in phenolic groups (Ar–OH) [29] (Figure 2.1C, *SI Appendix* Table A.5). The presence of OH groups is confirmed by the FT-IR band at 3326 cm^{-1} (O–H stretching) (Figure 2.3A) and by the bands centered at 1340 cm^{-1} and 1200 cm^{-1} attributed to the OH deformation / C–OH stretching in O–H (Figure 2.3C). The presence of aromatic groups is noticeable by the bands at 1612 , 1534 and 1447 cm^{-1} (C=C stretching in aromatic groups) (Figure 2.3C). The electronic transitions at 287.4 eV could have been as well attributed to $1s-3p/\sigma^*$ transitions in aliphatic (C_xH_y) groups, however the lack of intense FT-IR bands in the region $3000-2800\text{ cm}^{-1}$ confirms the absence of CH_2 and CH_3 groups (only a weak aliphatic signal can be seen for *E. largiflorens*) (Figure 2.3B). The FWHM of the fitted Gaussian 4 centered at 287.4 eV is narrower compared to other genera which indicates the absence of transitions' overlap (*SI Appendix* Table A.2).

White Mallee and *E. Largiflorens* spectra are characterized by the presence of $1s-\pi^*$ transitions in aromatic rather than olefinic carbon (centered at 285.5 and 285.6 eV respectively) (Figure 2.1C) confirmed by the presence of FT-IR bands at 1612 cm^{-1} , 1534 cm^{-1} and 1447 cm^{-1} attributed to the C=C stretching in aromatic compounds (Figure 2.3C). The main differences between *Eucalyptus* species is the intensity of the XRS features corresponding to the presence

of carboxyls ($-\text{COOH}$) and aliphatic alcohols ($\text{R}-\text{OH}$) (Figure 2.1C). The $1s-\pi^*$ transitions in carboxyls centered at 288.5 eV are higher for the *White Mallee* species, which agrees with the higher intensity of the band at 1700 cm^{-1} in the FT-IR spectra attributed to $\text{C}=\text{O}$ stretching (Figure 2.3A). At the XRS oxygen K-edge, *White Mallee* exhibit a higher intensity π^* resonance centered at 532.1 eV attributed to oxygen $1s-\pi^*$ transitions in carboxyls ($-\text{COOH}$) (Figure 2.2C). The feature at 535.2 eV is attributed to the $\text{O}-\text{H}$ oxygen $1s-\pi^*$ transitions in carboxyl groups.

The XRS feature centered at 289.4 eV, attributed to the $1s-3p/\sigma^*$ electronic transitions in aliphatic alcohols ($\text{R}-\text{OH}$), is more intense for *E. Largifloreus* species (Figure 2.1C, *SI Appendix Table A.5*). Both *Eucalyptus* species lack of intense bands around 2900 cm^{-1} ; only weak intensity peaks at 2977 cm^{-1} and 2934 cm^{-1} are present in the spectra of *E. Largifloreus* (Figure 2.3B). This suggests a low proportion of $\text{C}-\text{H}$ bonds compared to $\text{C}-\text{C}/\text{C}=\text{C}/\text{C}\equiv\text{C}$ bonds (substituted or fused cycloalkanes and unsaturations). In addition, FT-IR data suggests a higher proportion of carbohydrates in *E. largifloreus*.

2.2.1.4 *Acacia* gums

The XRS spectra of *Acacia* exhibit significant spectral differences among the two species (Figure 2.1D, *SI Appendix Table A.5*); the abundance of the various peaks is different and the varied center of the fitted Gaussians in the same energy transfer region indicates the differences in chemical composition (*SI Appendix Table A.2*). The sample of unknown *Acacia* species lacks the aromatic and/or olefinic carbon (no feature around 285.4 eV) and exhibits an intense feature centered at 289.6 eV which corresponds to the $1s-3p/\sigma^*$ transitions in hydroxyls ($\text{R}-\text{OH}$) (Figure 2.1D). The intense FT-IR band centered at 3410 cm^{-1} , present in both samples, is attributed to the $\text{O}-\text{H}$ stretching (Figure 2.3A).

Acacia unknown species exhibits a small feature in the XRS carbon K-edge spectrum centered at 286.8 eV attributed to the $1s-\pi^*$ transitions in ether groups ($\text{R}-\text{O}-\text{R}'$) (Figure 2.1D) [33, 34]. The shoulder centered at 288.6 eV is attributed to the $1s-\pi^*$ in acetal carbons ($\text{R}_2\text{C}(\text{OR}')_2$) [33–35]. Compared to *Acacia unknown species*, *A. bakeri* exhibits higher intensity peaks centered at 286.8 eV attributed to the $1s-\pi^*$ transitions in ether groups ($\text{R}-\text{O}-\text{R}'$) (Figure 2.1D, *SI Appendix Table A.5*) [33, 34] and at 288.6 eV attributed to the $1s-\pi^*$ of acetal carbons ($\text{R}_2\text{C}(\text{OR}')_2$) (Figure 2.1D, *SI Appendix Table A.5: Gaussians 3,5*) [33–35]. $\text{O}-\text{C}-\text{O}$ carbon is

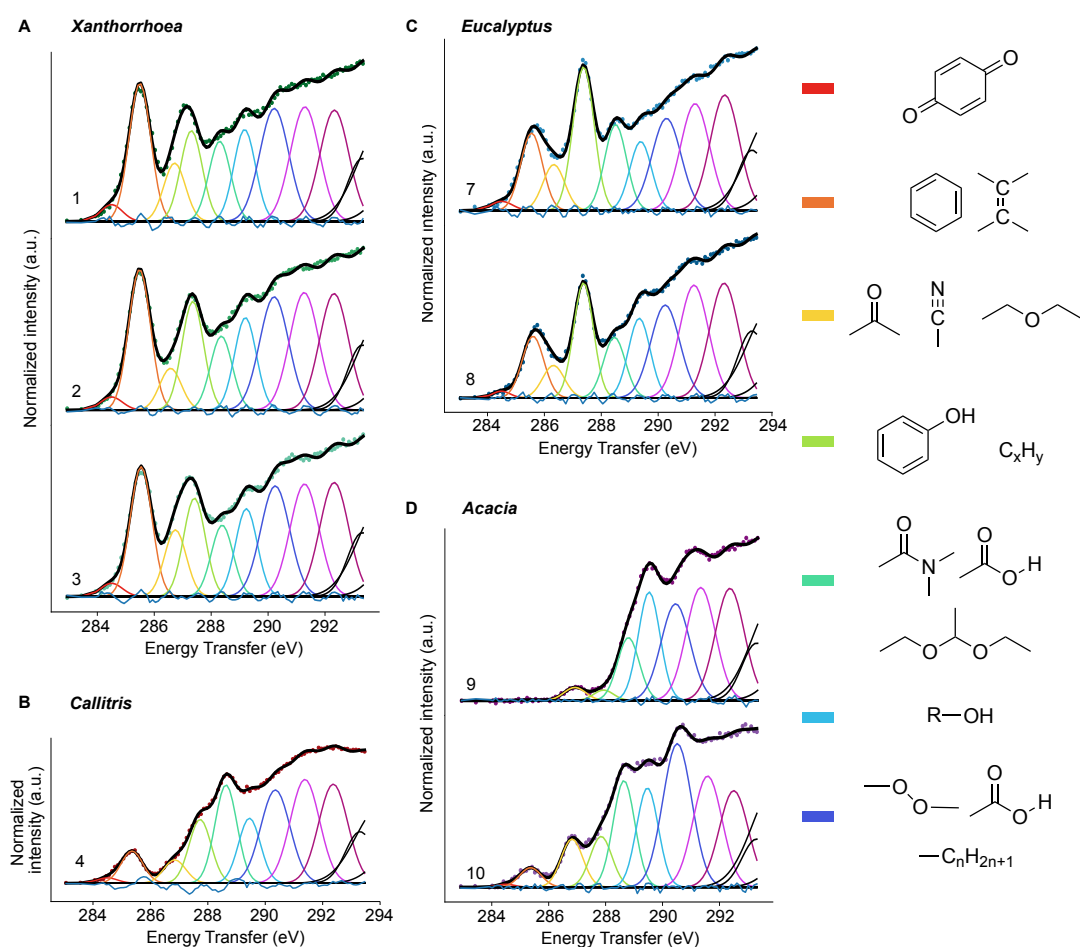


Figure 2.1: XRS carbon K-edge spectra decomposition. A. 1, *X. arborea*; 2, *X. semiplana* ssp. *tateana*; 3, *X. semiplana*; B. 4, *C. calcarata*; C. 7, White Mallee; 8, *E. largiflores*; D. 9, Acacia, unknown species, 10, *A. bakeri*. The centers of Gaussians correspond to core electron transitions at specific functional groups as reported in the literature of soft x-rays absorption and/or EELS studies (see *S.I Appendix Table A.1*).

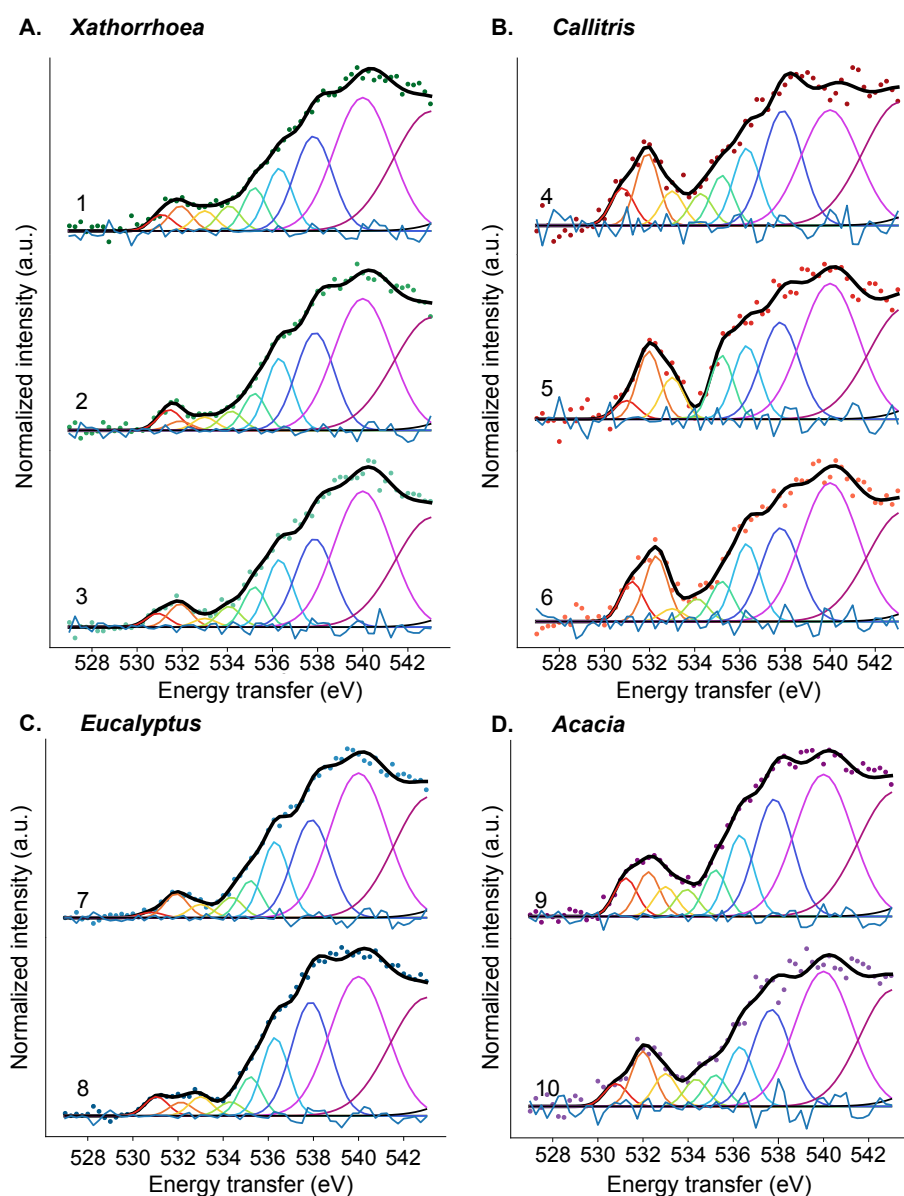


Figure 2.2: XRS oxygen K-edge spectra decomposition. A. 1, *X. arborea*; 2, *X. semiplana* ssp. *tateana*; 3, *X. semiplana*; B. 4, *C. calcarata*; 5, *C. glauca*; 6, *C. preissii* ssp. *verrucosa*; C. 7, White Mallee; 8, *E. largiflorens*; D. 9, Acacia, unknown species, 10, *A. bakeri*. The centers of Gaussians correspond to core electron transitions at specific functional groups as reported in the literature of soft x-rays absorption and/or EELS studies (see *S.I Appendix Table 2.2*).

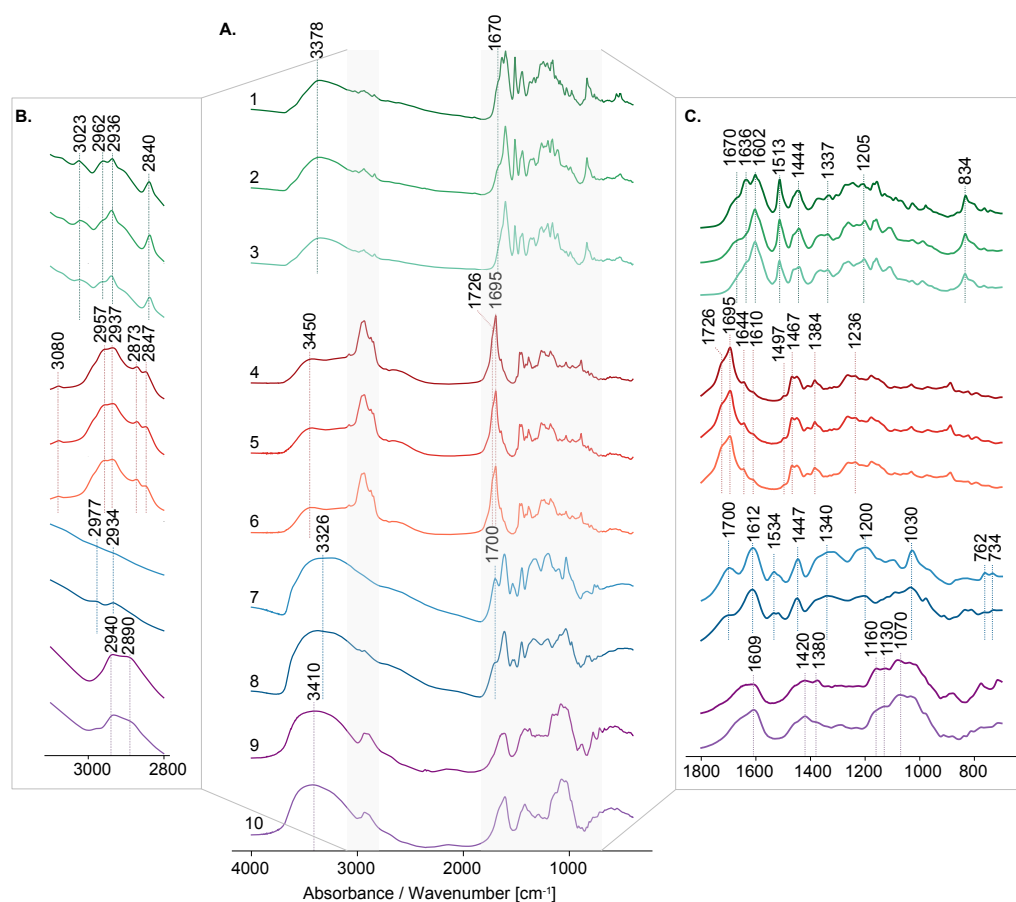


Figure 2.3: FT-IR spectra of native Australian plant exudates. 1, *X. arborea*; 2, *X. semiplana* ssp. *tateana*; 3, *X. semiplana*; 4, *C. calcarata*; 5, *C. glauca*; 6, *C. preissii* ssp. *verrucosa*; 7, White Mallee; 8, *E. largiflores*; 9, Acacia, unknown species, 10, *A. bakeri*

considered highly diagnostic for sugars since it can be found in a limited number of organic compounds [36]. For *A. bakeri*, the XRS feature centered at 290.6 eV, possibly indicates the presence of alkyl groups (Figure 2.1D). The XRS carbon K-edge spectrum of *A. bakeri* exhibits a peak at 285.3 eV attributed to $1s-\pi^*$ transitions in aromatic and/or olefinic carbon.

The FT-IR spectra of Acacia species (*A. bakeri*, *unknown species*) exhibit the following features (Figure 2.3): (a) an intense broad band in the $3600-3000\text{ cm}^{-1}$ range attributed to O–H stretching, (b) a peak centered at 2940 cm^{-1} attributed to the CH_2 antisymmetric stretching, and a band at 2890 cm^{-1} linked to the CH stretching, (c) a broad asymmetrical band centered at 1609 cm^{-1} possibly linked with the presence of absorbed water, (d) two intense bands at 1420 cm^{-1} and at 1380 cm^{-1} possibly attributed to the deformation of CH_3 and CH_2 groups, (e) a broad band centered around 1070 cm^{-1} and two bands centered at 1160 cm^{-1} and 1130 cm^{-1} linked to the skeletal vibrations of polysaccharides. The differences in intensity among the two species are possibly related to the proportion of monosaccharides or their organization in the polysaccharide chain.

2.3 Discussion

2.3.1 X-ray Raman spectroscopy as an unconventional complement to lab-based techniques

This work demonstrates the advantage of XRS in the characterization of inherently complex natural materials, composed of a variety of organic molecule classes. The historical collection provides an opportunity to understand the chemical nature of the plant exudates that have undergone simultaneously ageing processes for over a century; samples within the collection kept at simultaneous, yet unknown conditions. The conditions experienced by this historical collection demarcate the samples from fresh materials and defines the collection as an appropriate reference for understanding aged samples. Further analysis of fresh materials and data comparison will help identify the aging mechanisms of the samples. We suggest that before XRS is applied for the identification of organic materials in complex aged heritage artifacts, aging experiments of fresh materials should be carried out to establish a greater degree of detection accuracy.

XRS is a very powerful element-specific hard x-ray technique [23, 37] that provides atomic-level chemical speciation information for light elements such as carbon and oxygen, equivalent

to XANES spectroscopy (also known as near-edge x-ray absorption fine structure, NEXAFS) [38]. The technique overcomes the limitations of conventional XANES for the study of these organic samples related to the short penetration depth of soft x-rays. As XRS is a hard x-ray bulk-sensitive probe, it does not require special sample treatment and/or environment. It can be applied in a non-invasive manner to probe bulk carbon speciation (millimeter scale) in complex organic systems, including valuable heritage samples [39, 40]. XRS has also been successfully employed as a three-dimensional imaging probe to study natural heritage organic samples to determine organic signatures and trace their evolution through time [40].

The name “x-ray Raman scattering” comes from the analogue of inelastic scattering in the optical region, introduced by Raman in 1928. While optical Raman spectroscopy probes vibrational excitations in the meV range using photons in the eV range, x-ray Raman scattering probes electronic excitations in the tens to hundreds eV range using photons in the hard x-ray range (6–15 keV). This work demonstrates the advantages of XRS for studying organic natural plant products. In combination with the established method, FT-IR, XRS successfully provided a full characterization of signature chemical features between the genera. FT-IR spectroscopy is a widely used technique to provide complementary detailed molecular information to optical Raman spectroscopy of cultural heritage materials [41–44]. The probe depth of both techniques is three orders of magnitude shorter than that of XRS ($\approx \mu\text{m}$). A limitation of optical Raman analysis of organic compounds arises from the fact that high energy sources may activate electronic transitions which produce fluorescence phenomena that decrease signal sensitivity. Surface-enhanced Raman scattering (SERS) is able to quench fluorescence and increase Raman signal, but requires invasive sample treatment [45]. ATR-FT-IR is a non-invasive technique that can be performed directly on the heritage object. However, it requires contact of the crystal with the sample which may cause deformation. Py-GC-MS is a powerful technique which allows the separation and identification of characteristic marker compounds in complex organic matrices with a high degree of sensitivity and specificity [46, 47]. Py-GC-MS requires removing sample from the object, of at least few tens of micrograms (bulk analysis), which is always a constraint when dealing with the study of important cultural and historical samples. Py-GC-MS usually requires relatively short run times, yet, derivatization of the sample is necessary. XRS is a non-invasive technique, however, access to a synchrotron and an XRS spectrometer is prerequisite.

2.3.2 Classification of compounds into chemical classes

Among the objectives of the study was to provide a spectral signature for each exudate, which carries information on its bonding structure. We have applied Fisher's linear discriminant analysis (LDA), a supervised statistical learning algorithm, to examine if the multivariate decomposition of the XRS signal (*SI Appendix* Table A.5) carries enough information to discriminate between the various genera. LDA was applied to the data consisting of the integrated area of the fitted Gaussian distributions in the energy transfer region 283.0–290.5 eV.

For a sample set consisting of k classes (here $k = 4$), LDA is proposing $K - 1$ orthogonal projections such that the *between-group scatter* is maximal with respect to the *within-group scatter*. Following this criteria, the first projection, also termed first component of the LDA, is best discriminating each of the K classes, the second projection is optimal when the data is projected on the hyper plane orthogonal to first projection, and so on. Figure 2.4A represent the results of the LDA applied to the XRS data. In this graph, there is a clear separation between the datapoints of each genera, supporting the capacity of the XRS data to discriminate the genera of sample of unknown origin. To further assess the discriminating power of the XRS decomposed spectra, we tested the hypothesis that the separation seen on the LDA is obtained by mere chance through overfitting of the data; a not so unlikely possibility since we are analyzing only 8 samples for $k = 4$ classes and $N = 7$ variables. This hypothesis is rejected with a $p\text{-value} = 1.31\%$, below the standard 5% threshold (Figure 2.4B).

The present multi-analytical study classifies the plant exudates deriving from different native Australian genera in broader chemical classes: phenolic and aromatic compounds (*Eucalyptus*, *Xanthorrhoea*), polysaccharides (*Acacia*), terpenoids (*Callitris*). The chemical characterization of these genera, can inform on the cultural uses of the plant exudates. The chemical similarity of plant exudates unique of the ecosystem of Australia (e.g. *Callitris*) with plant exudates widely used in Europe (e.g. African sandarac (*Tetraclinis*)) highlights how cultures across the world converged towards similar solutions and the parallel uses of materials deriving from distinct plant genera. The plant exudates this study analyzed fall into the categories of two examples of resins, one of kino and one of gum, by the chemical classification.

The Australian grass tree *Xanthorrhoea* produces a resinous material dominated by aromatic and phenolic hydrocarbons including aromatic and/or olefinic carbon, consistent with

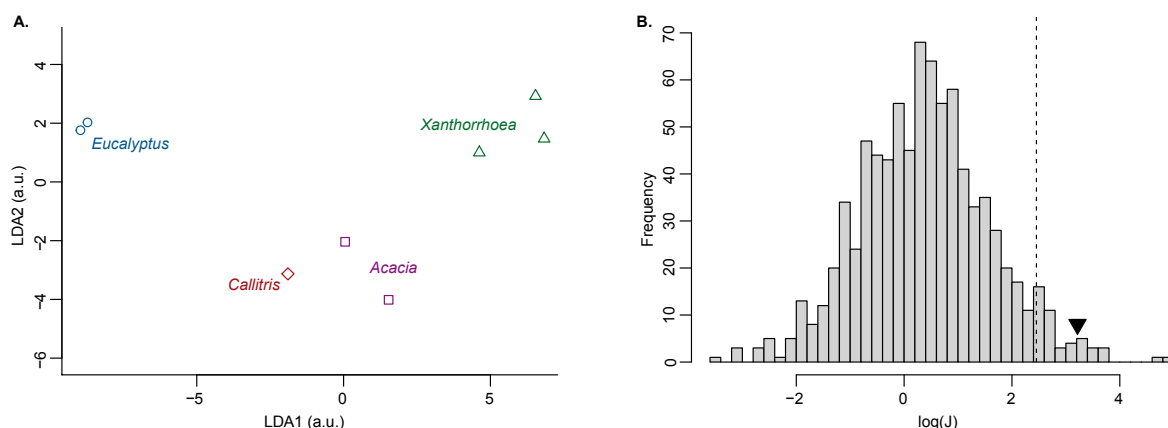


Figure 2.4: Fischer’s linear discriminant analysis (LDA). **A.** Fischer’s linear discriminant analysis applied to the Gaussian decomposition of the XRS spectra of 8 samples of known genera. Projection on the first 2 (out of 3) best directions found by LDA. **B.** The histogram of $\log(J)$, where J is the metric of the LDA, for all the possible non-equivalent groupings with groups of respectively 3, 2, 2 and 1 samples. The vertical dashed line represents the 5% p -value threshold of this statistics, and the black triangle the value of $\log(J)$ obtained for the grouping based on the genera of the samples.

their categorization as plant resins and their physical properties and use in hafting. The *Xanthorrhoea* species are unique to Australia, and the genera name *Xanthorrhoea* means “yellow flow”, denoting the color of their exudates, however when dried, the color of the brittle resin can range from yellow to red. Given their low solubility in water, Aboriginal Australians use *Xanthorrhoea* for practical purposes including hafting, waterproofing or repair of bark containers and canoes and artistic purposes (e.g. attaching elements to objects) [48–50]. *Xanthorrhoea* species are geographically well-defined; thus they can be valuable for tracing the source of the object and the trade between communities [13]. Recent Aboriginal Australian artists including Lindsay Harris, Christopher Pease and Rover Thomas have used *Xanthorrhoea* resins in their artworks as pigment binders [4]; as a choice linked to country and culture.

Callitris, a genus prominent and unique in Australian ecosystems, belongs in the chemical class of diterpenoid resins with a substantial presence of carboxylic acids, characterized by callitrisic and communic acid. There is not extensive literature on the chemistry of *Callitris* plant exudates, perhaps due to its specific geographic location. One exception is Simoneit et al. [51] who documented that the general chemistry and color of *Callitris* exudates are similar to others in the Cupressaceae (cypress) family including their ability to polymerize similar to exudates from other conifer tree species [51]. The results of this study demonstrate that the

Australian *Callitris* species can be directly compared in terms of chemistry with the African sandarac (*Tetraclinis*), a well-studied resin widely used as varnish in European artworks [19, 52]. African sandarac — a labdane type diterpenic resin — is characterized by the presence of communic acid, a diterpenic acid similar to abietic acid which polymerizes. Similarly to the *Xanthorrhoea* exudates, *Callitris* are also resins and therefore can be used as adhesives and in binding [6]. Many European historical manuscripts describe recipes of varnishes made with sandarac and highlight its use as a high quality material [53–56]. Although *Callitris* was also used as a varnish it has not been extensively exported from Australia [19].

Eucalyptus exudates are primarily dominated by phenolic and other aromatic constituents. In the literature, exudates from *Eucalyptus* species are often described as gums or resins (e.g. “gum tree”). This terminology can be misleading since they are neither polysaccharide or polyterpenoid, rather they are more accurately described as kino, which is chemically defined by Lambert et al. as dominated by phenolic and other aromatic constituents [57, 58]. Kino composition is based on the polymerization of phenolic and flavan compounds which create the significant tannin composition, which forms the characteristic astringent properties. In general the liquid exudate hardens in air, and the kinos can be categorized generally into groups based on their solubilities in alcohol and water. Colors of *Eucalyptus* kino range from dark red-brown to yellow and range from very friable to breaking into large fragments [59]. Kino was used by Aboriginal Australian peoples for medical applications including treating wounds and tooth decay and as an astringent as well as internally for infections, colds and influenza, and continue to have applications today [12, 59].

Acacia exhibit characteristic features of polysaccharides; thus they belong to the wide category of gums. As such, they are water-soluble materials that contain polysaccharide-protein complexes and is a biopolymer which can act as an emulsifier that occur in a range of colors [60]. Stretching back 70,000 years ago, *Acacia* has found many applications in arts, cosmetics, medicines and food and continues to be a significantly traded commodity worldwide [60]. Aboriginal Australian peoples use acacia (wattle gum) in a variety of food preparations, either by mixing the gum in water or mixing with other native foods such as eugenia apples, as well as in medicinal preparations for treating colds and coughs [12, 61–63]. In arts, acacia gums are found as binders across several cultures for various painting and ink media (e.g. watercolors, gouache) [60, 64, 65]. Gum Arabic, one of the most notable gums historically used as bind-

ing media in artworks across Africa, the Mediterranean region and Asia, derives from *Acacia senegal* and *Acacia seyal* (recently named genera *Senegalia*) and it is harvested commercially mainly in Sudan (80%) [1]. Although the majority of the species of *Acacia* are in Australia, the majority of the analyses have focused on the commercial species *Acacia/Senegalia senegal* and *Acacia/Senegalia seyal*.

2.3.3 Cultural uses and limitation of extant data

Cultural heritage conservators often face the challenge of treating an object while respecting the artistic intent and cultural factors, thus avoiding interventions with modern synthetic materials where possible [66]. The accurate characterization and understanding of the natural binders' chemical and physical properties and stability are important for the treatment decisions as well as understanding the intent of the artist. There is extensive literature on the analysis of European artists' binder materials across several categories including resins, polysaccharides, terpenoids, waxes, and oils [11]; however the characterization of native Australian materials is significantly understudied as compared to European-style materials. In addition, there are not complete or comprehensive datasets for Australian raw materials, as there are for European materials (see for instance the IRUG database [67]). Therefore this work contributes to our fundamental understanding of Australian plant exudates, and crucially, a reliable method for identification and differentiation of traditional binders in museum, art gallery and cultural collections [4].

Indigenous and western scientific knowledge towards the development of sustainable, and environmentally friendly applications of biomaterials, using locally available materials. The promotion of 'green', local materials fits into global trends towards developing functional, sustainable uses of resources and novel approaches to extant technologies that recognize traditional and non-traditional uses of materials [68–72].

2.4 Conclusions

We have demonstrated the complementary use of XRS and FT-IR to successfully identify critical chemical features specific to each genera for native Australian plant exudates from a unique historical collection. XRS provides the fundamental bonding information of light elements, FT-

IR provides the functional group information. The combination of these techniques delivers a novel and powerful characterization and chemical classification of bulk plant exudates and their properties with further potential for identification in artworks, cultural heritage items and museum collections. The fascinating parallels between various uses of plant exudates across cultures illustrates the chemical similarity of the plant exudates unique of the ecosystem of Australia (e.g. *Callitris*) with plant exudates found around the world (e.g. African sandarac (*Tetraclinis*)). While many native species are unique to Australia, they can be classified in similar fundamental chemical typologies as other species around the globe, exemplified by *Acacia* and *Eucalyptus*. Interestingly, comparing the chemical compositions of *Callitris* from Australia with that of *Tetraclinis* from Europe, shows key similarities, despite being geographically isolated genera. In turn, the fundamental chemistry of the material also often dictates the cultural use, whether it has ideal properties for a pigment binder or hafting agent. While many of these material properties are utilized on the bulk scale, it is the fundamental compositional and functional group chemistry that determines the desirable properties for cultural and other applications. It is therefore no surprise that natural materials discovered and manipulated over thousands of years of tradition, continue to inspire their present and future uses.

2.5 Materials and methods

2.5.1 Materials

A sample-set of native Australian plant genera (*Eucalyptus*, *Callitris*, *Xanthorrhoea*, *Acacia*), summarized in Table 2.1 were analyzed. The samples were selected from South Australian Museum (SAM) collections and a historical biological collection gathered from diverse locations across Australia and held for years in the South Australia state forensic laboratory (Forensic Sciences South Australia-FSSA) and now located at Flinders University. Unfortunately the collectors of this exceptional comprehensive collection are unknown and the original data notebooks no longer exist; however, samples in the historical biological collection are over a century old where each amber jar is clearly labeled with the collection location and date and offer an unprecedented study set. While the exact storage conditions are unknown across

time, they are consistent within the collection, which minimizes the effects of variables such as temperature and humidity.

2.5.2 XRS spectroscopy

X-ray Raman measurements (carbon K-edge and oxygen K-edge) were performed using the high-resolution X-ray Raman spectrometer operated at beamline 6-2 at the Stanford Synchrotron Radiation Laboratory [73]. The instrument consists of 40 crystal Si(440) analyzers arranged on overlapping Rowland circles of 1000 mm and at a fixed Bragg angle of 88° , resulting in a fixed detection energy at 6462 eV and an overall energy resolution of 0.29 eV. Spectra are recorded using an inverse scanning approach, wherein the detection energy is held constant at 6462 eV while the incident energy is scanned through a Si(311) double-crystal monochromator. The average momentum transfer is $q \approx 0.65 \text{ \AA}^{-1}$, which ensures that dipole transitions dominate the spectra and therefore the X-ray Raman spectra are formally equivalent to conventional soft X-ray absorption spectra.

For each sample, the mean carbon K-edge spectrum shown in Figure 2.1 was obtained from a collection of multiple consecutive spectra on numerous sample regions to ensure sufficient signal-to-noise ratio and high data quality. No visual damage was observed on the samples under study. The experimental conditions were optimized to minimize radiation damage. We were measuring the samples at a grazing geometry ($\approx 6^\circ\text{--}7^\circ$) and therefore the projected beam footprint on the sample was quite long ($>5 \text{ mm}$) in the horizontal direction. Vertically the beam FWHM was $\approx 150 \mu\text{m}$. Mean spectra were energy-calibrated using the average center of the elastic scattering peaks collected before and between XRS measurements, to take into account the energy drift of the monochromator with time. Using the empirical formula $y = a/(x - b)$ [74], we performed a non-linear fit to the pre-edge region and subtracted the background. The background-corrected spectra were then normalized to the post-edge region with no significant oscillation.

XRS oxygen K-edge experiments were performed at GALAXIES beamline (Synchrotron SOLEIL, France) with an energy resolution of 1.2 eV [75]. The spectrometer is equipped with 4 spherically bent Si(444) analyzer crystals [76]. For the XRS spectrum acquisition, we scanned the beamline energy along the absorption edge of interest, at a fixed analyzer energy. Experiments were performed at a Si(444) analyzer energy of $\approx 8.0 \text{ keV}$ operated at a Bragg angle

of 86° . The data was collected at backscattered geometry (scattering angle of $2\theta \approx 130^\circ$) to maximize the XRS signal. The momentum transfer is $q \approx 7.5 \text{ \AA}^{-1}$. The beamline is equipped with a cryogenically cooled Si(111) double-crystal monochromator. The monochromatized X-ray beam is focused by a toroidal mirror to a spot size ($V \times H$) of approximately $30 \times 80 \mu\text{m}^2$. We collected energy transfer measurements along the oxygen K-edge around 530 eV energy transfer with an energy step of 0.5 eV and dwell time of 400 ms per energy step. For the sake of comparison, oxygen K-edge data was collected at beamline 6-2 (SSRL) at low momentum transfer ($q \approx 0.65 \text{ \AA}^{-1}$) for four samples (*X. semiplana* ssp. *tateana*, *C. calcarata*, White Mallee, *E. largiflorens*). Comparison of the oxygen K-edge XRS spectra collected at high and low momentum transfer do not exhibit any spectral differences (see *SI Appendix* Figure A.1).

2.5.3 FTIR spectroscopy

FT-IR spectra were collected with a spectrometer Bruker Alpha II equipped with a DTGS detector. Measurements were performed in transmission mode using KBr pellets (Sigma Aldrich, FT-IR grade, ref. 221864). A total of 128 scans have been accumulated in each sample, using a resolution of 4 cm^{-1} in the range between 4000 to 400 cm^{-1} . All spectra showed have not been corrected in order to avoid any kind of distortion.

2.5.4 XRS data reduction

The spectral decomposition of the XRS signal in the region of interest 283.0–292.5 eV and 530.8–538.5 eV was performed using a linear combination of Gaussians. The parameters of the model to be fitted are the intensity, the full width half maximum (FWHM) and the center of each Gaussian. The FWHM has a lower (FWHM of the elastic line) and an upper bound (selected in such a way to minimize the post-fit residual). The center of each Gaussian is allowed to vary slightly during the fit in a constrained energy transfer region that corresponds to electronic transitions in specific oxygen-containing functional groups expected for these families of compounds. The shift of the center and the width of the fitted Gaussian provides information on the overlap of functional groups of which their transitions are expected to be in the same energy transfer region. Post-fit residuals were calculated to check for possible missing features as Ref. [39]. The intensity, FWHM and center of each Gaussian are fitted

using a nonlinear least squares regression implemented in Python. All the parameters are summarized in *SI Annex* Table S1, S3.

2.5.5 Statistical testing of XRS data classification

Fischer linear discrimination is finding the projections which maximizes the ratio J of the *between-group scatter* divided by the *within-group scatter*. Formally, for a given set of projections defined by their matrix \mathbf{W} , noting \mathbf{S}_B and \mathbf{S}_W respectively the *between-group* and *within-group* scatter matrices and for any square matrix \mathbf{M} noting $|\mathbf{M}|$ its determinant, J is defined by:

$$J(\mathbf{W}) = \frac{|\mathbf{W}^t \mathbf{S}_B \mathbf{W}|}{|\mathbf{W}^t \mathbf{S}_W \mathbf{W}|}$$

Once the LDA is performed, the maximum J can also be computed as the product of the singular values attached to each of the proposed projections. Whilst J is a good metric of the ability of the set of projection to separate the dataset into predefined groups, its scale is too dependent upon the number of samples, the number of groups and the number of variables. Hence the value of J can not be used alone to judge if a given LDA is producing a meaningful discrimination. To assess the quality of the discrimination obtained based on the genera of the samples, we compared the value of J with the one obtained for all other possible (random) grouping of the samples with the same group sizes, that is with respectively 3, 2, 2 and 1 members. From the $8! = 40320$ possible permutations of the samples, we kept a single representative from all equivalent groupings: two groupings are equivalent if they differ only by the order of the samples within each groups (leading to $6 \times 2 \times 2 = 24$ equivalents) or by swapping the two groups made of exactly 2 samples (leading to 2 equivalents). This way, we obtained all the 840 non-equivalent groupings of the samples. For each of these (random) grouping, the LDA is performed and the corresponding value of J is recorded and reported on a histogram of possible $\log(J)$ values, Figure 2.4B. Using the grouping based on the genera of the samples, we obtained $J = 24.91$ from the LDA, this being the eleventh highest value of the J computed for all (840) possible groupings. In regard of this rank, the null hypothesis “this value of J is obtained by pure chance” can be rejected with a p -value of $11/840 = 1.31\%$. Note that in this test the lowest possible p -value would have been $1/840 = 0.12\%$ and that the standard threshold ($p = 5\%$) corresponds to a value of $J = 11.62$. All statistical computations

were performed using the R Language and Environment for Statistical Computing [77]. LDA was performed using the `lda` function from the MASS package [78].

References

- [1] Amos Nussinovitch. *Plant gum exudates of the world: sources, distribution, properties, and applications*. Boca Raton, FL, US: CRC Press, 2010.
- [2] Amélia Pilar Rauter et al. *Natural products in the new millennium: prospects and industrial application*. Vol. 47. Springer Science & Business Media, 2013.
- [3] CL Mantell. “The natural hard resins—their botany, sources and utilization”. In: *Economic Botany* 4.3 (1950), pp. 203–242.
- [4] Sharon Alcock. “Painting Country: Australian Aboriginal artists’ approach to traditional materials in a modern context”. In: *AICCM Bulletin* 34.1 (2013), pp. 66–74.
- [5] Owen Powell, Roderick J Fensham, and Paul Memmott. “Indigenous use of spinifex resin for hafting in north-eastern Australia”. In: *Economic botany* 67.3 (2013), pp. 210–224.
- [6] Carney D Matheson and AJ McCollum. “Characterising native plant resins from Australian Aboriginal artefacts using ATR-FTIR and GC/MS”. In: *Journal of archaeological science* 52 (2014), pp. 116–128.
- [7] Tim Maloney et al. “Direct dating of resin hafted point technology in Australia”. In: *Australian Archaeology* 81.1 (2015), pp. 35–43.
- [8] Alisa J Blee et al. “Towards the identification of plant and animal binders on Australian stone knives”. In: *Talanta* 82.2 (2010), pp. 745–750.
- [9] Jeffrey F Parr. “The identification of Xanthorrhoea resins by starch morphology: Prospects for archaeological and taxonomic applications”. In: *Economic Botany* 56.3 (2002), pp. 260–270.
- [10] Jeff Parr. “Once, twice maybe, but not three times: Reheating Xanthorrhoea australis resin”. In: *Australian Archaeology* 49.1 (1999), pp. 23–27.

- [11] Tiffany Reeves, Rachel S Popelka-Filcoff, and Claire E Lenehan. “Towards identification of traditional European and indigenous Australian paint binders using pyrolysis gas chromatography mass spectrometry”. In: *Analytica chimica acta* 803 (2013), pp. 194–203.
- [12] Philip A Clarke. *Aboriginal people and their plants*. Rosenberg Publishing, 2011.
- [13] Fiona Bradshaw. “Chemical characterisation of museum-curated ethnographic resins from Australia and New Guinea used as adhesives, medicines and narcotics”. In: *Heritage Science* 1.1 (2013), p. 36.
- [14] Zena Cumpston. *Food, tools and medicine: 5 native plants that illuminate deep Aboriginal knowledge*. en. URL: <http://theconversation.com/food-tools-and-medicine-5-native-plants-that-illuminate-deep-aboriginal-knowledge-145240> (visited on 04/10/2021).
- [15] Nicholas Mark Smith. “Ethnobotanical field notes from the Northern Territory, Australia”. In: *Journal of the Adelaide Botanic Garden* 14.1 (1991), pp. 1–65.
- [16] *Bark Paintings | Development Services*. URL: <https://manual.museum.wa.gov.au/conservation-and-care-collections-2017/ethnographic-material/bark-paintings> (visited on 04/10/2021).
- [17] *Conservation*. URL: <https://nga.gov.au/conservation/objects/bark.cfm> (visited on 04/10/2021).
- [18] Andrew H. Thornhill et al. “A dated molecular perspective of eucalypt taxonomy, evolution and diversification”. en. In: *Australian Systematic Botany* 32 (1 2019), pp. 29–48. ISSN: 1030-1887. DOI: 10.1071/SB18015. URL: <http://www.publish.csiro.au/?paper=SB18015> (visited on 04/10/2021).
- [19] Jean H Langenheim. *Plant resins: chemistry, evolution, ecology, and ethnobotany*. Oregon, US: Timber Press, 2003.
- [20] Gideon F Smith and Estrela Figueiredo. “Conserving Acacia Mill. with a conserved type: what happened in Melbourne?” In: *Taxon* 60.5 (2011), pp. 1504–1506.
- [21] Yukio Mizuno and Yoshihiro Ohmura. “Theory of X-ray Raman scattering”. In: *Journal of the Physical Society of Japan* 22.2 (1967), pp. 445–449.

- [22] Tadasu Suzuki. “X-ray Raman scattering experiment. I”. In: *Journal of the Physical Society of Japan* 22.5 (1967), pp. 1139–1150.
- [23] Winfried Schülke. *Electron dynamics by inelastic X-ray scattering*. Vol. 7. Oxford University Press, 2007.
- [24] Adam P. Hitchcock and Chris E. Brion. “Inner-shell excitation of formaldehyde, acetaldehyde and acetone studied by electron impact”. In: *Journal of Electron Spectroscopy and Related Phenomena* 19.2 (1980), pp. 231–250.
- [25] Joseph B Lambert. *Organic structural spectroscopy*. Pearson College Division, 1998.
- [26] LJFC Bellamy. *The infrared spectra of complex molecules*. Springer Science & Business Media, 2013.
- [27] Daimay Lin-Vien et al. *The handbook of infrared and Raman characteristic frequencies of organic molecules*. Elsevier, 1991.
- [28] Calvin J. Brett et al. “Revealing structural evolution occurring from photo-initiated polymer network formation”. In: *Communications Chemistry* 3.1 (2020), pp. 1–7.
- [29] Julien Alleon et al. “Organic molecular heterogeneities can withstand diagenesis”. In: *Scientific reports* 7.1 (2017), pp. 1–9.
- [30] Tsonko Kolev. “Vibrational assignment of in-and out-of-plane modes of some aromatic and arylaliphatic ketones”. In: *Journal of Molecular Structure* 349 (1995), pp. 381–384.
- [31] Yan Zubavichus et al. “Innershell absorption spectroscopy of amino acids at all relevant absorption edges”. In: *The Journal of Physical Chemistry A* 109.32 (2005), pp. 6998–7000.
- [32] Victoria Beltran et al. “Markers, reactions, and interactions during the aging of Pinus resin assessed by Raman spectroscopy”. In: *Journal of Natural Products* 80.4 (2017), pp. 854–863.
- [33] Leena-Sisko Johansson and JM Campbell. “Reproducible XPS on biopolymers: cellulose studies”. In: *Surface and Interface Analysis: An International Journal devoted to the development and application of techniques for the analysis of surfaces, interfaces and thin films* 36.8 (2004), pp. 1018–1022.

- [34] Véronique Rouchon and Sylvain Bernard. “Mapping iron gall ink penetration within paper fibres using scanning transmission X-ray microscopy”. In: *Journal of Analytical Atomic Spectrometry* 30.3 (2015), pp. 635–641.
- [35] Corentin Le Guillou et al. “XANES-based quantification of carbon functional group concentrations”. In: *Analytical Chemistry* 90.14 (2018), pp. 8379–8386.
- [36] Joseph B Lambert, Yuyang Wu, and Jorge A Santiago-Blay. “Taxonomic and chemical relationships revealed by nuclear magnetic resonance spectra of plant exudates”. In: *Journal of natural products* 68.5 (2005), pp. 635–648.
- [37] Uwe Bergmann, Pieter Glatzel, and Stephen P Cramer. “Bulk-sensitive XAS characterization of light elements: from X-ray Raman scattering to X-ray Raman spectroscopy”. In: *Microchemical Journal* 71.2-3 (2002), pp. 221–230.
- [38] Joachim Stöhr. *NEXAFS spectroscopy*. Vol. 25. Springer Science & Business Media, 2013.
- [39] Pierre Gueriau et al. “Noninvasive Synchrotron-Based X-ray Raman Scattering Discriminates Carbonaceous Compounds in Ancient and Historical Materials”. In: *Analytical Chemistry* 89.20 (2017), pp. 10819–10826.
- [40] Rafaella Georgiou et al. “Carbon speciation in organic fossils using 2D to 3D x-ray Raman multispectral imaging”. In: *Science advances* 5.8 (2019), eaaw5019.
- [41] Silvia Prati et al. “New frontiers in application of FTIR microscopy for characterization of cultural heritage materials”. In: *Topics in Current Chemistry* 374.3 (2016), p. 26.
- [42] Marika Spring et al. “ATR-FTIR imaging for the analysis of organic materials in paint cross sections: case studies on paint samples from the National Gallery, London”. In: *Analytical and Bioanalytical Chemistry* 392.1-2 (2008), pp. 37–45.
- [43] Peter Vandenabeele, Howell GM Edwards, and Luc Moens. “A decade of Raman spectroscopy in art and archaeology”. In: *Chemical Reviews* 107.3 (2007), pp. 675–686.
- [44] Marco Leona, Jens Stenger, and Elena Ferloni. “Application of surface-enhanced Raman scattering techniques to the ultrasensitive identification of natural dyes in works of art”. In: *Journal of Raman Spectroscopy: An International Journal for Original Work in all Aspects of Raman Spectroscopy, Including Higher Order Processes, and also Brillouin and Rayleigh Scattering* 37.10 (2006), pp. 981–992.

- [45] Norman Colthup. *Introduction to infrared and Raman spectroscopy*. Elsevier, 2012.
- [46] Maria Perla Colombini et al. “Analytical strategies for characterizing organic paint media using gas chromatography/mass spectrometry”. In: *Accounts of chemical research* 43.6 (2010), pp. 715–727.
- [47] Francesco Caruso et al. “Micro-analytical identification of the components of varnishes from South Italian historical musical instruments by PLM, ESEM–EDX, microFTIR, GC–MS, and Py–GC–MS”. In: *Microchemical Journal* 116 (2014), pp. 31–40.
- [48] Susan Valis. “Investigation into the distortion of Triodia and Xanthorrhoea resins on Australian Aboriginal artefacts in museum collections”. In: *AICCM Bulletin* 17.1-2 (1991), pp. 61–74.
- [49] Veerle Rots et al. “Hafted Tool-use Experiments with Australian Aboriginal Plant Adhesives: Triodia Spinifex, Xanthorrhoea Grass Tree and Lechenaultia divaricata Min-drie”. In: *EXARC Journal* 1 (2020).
- [50] *Hard Yakka! Grass Tree Resin (Xanthorrhoea)*. en-AU. Mar. 2016. URL: <https://koorihistory.com/grass-tree-resin/> (visited on 04/10/2021).
- [51] Bernd RT Simoneit et al. “Terpenoid compositions of resins from Callitris species (Cupressaceae)”. In: *Molecules* 23.12 (2018), p. 3384.
- [52] Dominique Scalarone, Massimo Lazzari, and Oscar Chiantore. “Ageing behaviour and analytical pyrolysis characterisation of diterpenic resins used as art materials: Manila copal and sandarac”. In: *Journal of analytical and applied pyrolysis* 68 (2003), pp. 115–136.
- [53] Daniel Varney Thompson. *The craftsman’s handbook: Il libro dell’arte by Cennino d’Andrea Cennini*. 1954.
- [54] Donald C Fels et al. *Lost secrets of Flemish painting, including the first complete English translation of the De Mayerne Manuscript, BM Sloane 2052*. Eijsden, the Netherlands: Alchemist, 2004.
- [55] Charles Lock Eastlake. *Methods and materials of painting of the great schools and masters*. Courier Corporation, 2001.

- [56] Mrs Mary P Merrifield. *Medieval and Renaissance treatises on the arts of painting: original texts with English translations*. Courier Corporation, 1999.
- [57] Joseph B Lambert et al. “Characterization of Eucalyptus and chemically related exudates by nuclear magnetic resonance spectroscopy”. In: *Australian Journal of Chemistry* 60.11 (2007), pp. 862–870.
- [58] Joseph B Lambert et al. “Characterization of plant exudates by principal-component and cluster analyses with nuclear magnetic resonance variables”. In: *Journal of natural products* 73.10 (2010), pp. 1643–1648.
- [59] Cornelia Locher and Laura Currie. “Revisiting kinos—an Australian perspective”. In: *Journal of Ethnopharmacology* 128.2 (2010), pp. 259–267.
- [60] Christian Sanchez et al. “Acacia gum: History of the future”. In: *Food Hydrocolloids* 78 (2018), pp. 140–160.
- [61] Diana Jæger et al. “Isolation and structural characterization of echinocystic acid triterpenoid saponins from the Australian medicinal and food plant *Acacia ligulata*”. In: *Journal of Natural Products* 80.10 (2017), pp. 2692–2698.
- [62] *Wattle (Acacia) and its many uses*. en-AU. Sept. 2017. URL: [http : / / koorihistory . com / wattle /](http://koorihistory.com/wattle/) (visited on 04/10/2021).
- [63] Philip A Clarke. “Australian ethnobotany: an overview”. In: *Australian Aboriginal Studies* 2 (2003), pp. 21–38.
- [64] Clara Granzotto et al. “Plant gum identification in historic artworks”. In: *Scientific reports* 7 (2017), p. 44538.
- [65] Maria Perla Colombini, Alessio Ceccarini, and Alessia Carmignani. “Ion chromatography characterization of polysaccharides in ancient wall paintings”. In: *Journal of Chromatography A* 968.1-2 (2002), pp. 79–88.
- [66] AICCM. *Code of ethics and code of practice*. 2000.
- [67] Beth A Price and P Boris. *Infrared and Raman Users Group Spectral Database. 2007 ed. Vol. 1 & 2. Philadelphia: IRUG, 2009. Infrared and Raman Users Group Spectral Database. Web. 20 June 2014. 2007.*

- [68] Subrata Mondal, Paul Memmott, and Darren Martin. "Preparation and characterization of polyurethanes from spinifex resin based bio-polymer". In: *Journal of Polymers and the Environment* 20.2 (2012), pp. 326–334.
- [69] Subrata Mondal, Paul Memmott, and Darren Martin. "Preparation and characterization of spinifex resin-based bio-polyurethane/thermoplastic polyurethane blends". In: *Polymer-Plastics Technology and Engineering* 52.15 (2013), pp. 1535–1541.
- [70] Subrata Mondal et al. "Physico-thermal properties of spinifex resin bio-polymer". In: *Materials Chemistry and Physics* 133.2-3 (2012), pp. 692–699.
- [71] Harshi K Gamage et al. "Indigenous and modern biomaterials derived from Triodia ('spinifex') grasslands in Australia". In: *Australian Journal of Botany* 60.2 (2012), pp. 114–127.
- [72] Loïc Bertrand et al. "Paleo-inspired systems: Durability, Sustainability and Remarkable Properties". In: *Angew. Chem. Int. Ed.* 57.25 (2018), pp. 7288–7295.
- [73] Dimosthenis Sokaras et al. "A high resolution and large solid angle x-ray Raman spectroscopy end-station at the Stanford Synchrotron Radiation Lightsource". In: *Review of Scientific Instruments* 83.4 (2012), p. 043112.
- [74] Uwe Bergmann et al. "Carbon K-edge X-ray Raman spectroscopy supports simple, yet powerful description of aromatic hydrocarbons and asphaltenes". In: *Chemical physics letters* 369.1-2 (2003), pp. 184–191.
- [75] Jean-Pascal Rueff et al. "The GALAXIES beamline at the SOLEIL synchrotron: inelastic X-ray scattering and photoelectron spectroscopy in the hard X-ray range". In: *Journal of synchrotron radiation* 22.1 (2015), pp. 175–179.
- [76] James Michael Ablett et al. "The GALAXIES inelastic hard X-ray scattering end-station at Synchrotron SOLEIL". In: *Journal of Synchrotron Radiation* 26.1 (2019), pp. 263–271.
- [77] R Core Team. *R: A Language and Environment for Statistical Computing*. R Foundation for Statistical Computing. Vienna, Austria, 2020. URL: <https://www.R-project.org/>.

- [78] W. N. Venables and B. D. Ripley. *Modern Applied Statistics with S*. Fourth. ISBN 0-387-95457-0. New York: Springer, 2002. URL: <http://www.stats.ox.ac.uk/pub/MASS4>.

Carbon speciation in organic fossils using 2D to 3D x-ray Raman multispectral imaging

The in-situ 2D and 3D imaging of the chemical speciation of organic fossils is an unsolved problem in paleontology and cultural heritage. Here, we use x-ray Raman scattering (XRS) based imaging at the carbon K-edge to form 2D and 3D images of the carbon chemistry in two exceptionally preserved specimens, a fossil plant dating back from the Carboniferous, and an ancient insect entrapped in 53 million-year-old amber. The 2D XRS imaging of the plant fossil reveals a homogeneous chemical composition with micrometric ‘pockets’ of preservation, likely inherited from its geological history. The 3D XRS imaging of the insect cuticle displays an exceptionally well preserved remaining chemical signature typical of polysaccharides such as chitin around a largely hollowed out inclusion. Our results open up new perspectives for in-situ chemical speciation imaging of fossilized organic materials, with the potential to enhance our understanding of organic specimens and their paleobiology.

3.1 Introduction

The chemistry of ancient organic materials carries information of their original nature. Because this information is difficult to decode and limited by degradation, the depiction of chemical signatures preserved in the fossil record constitutes one of the essential challenges for paleontologists.

In some rare cases, organic structures can be preserved in rocks. Emblematic cases of organic preservation include mammoths entombed in the permafrost [1, 2], insects trapped in amber ([3–6]), colored dinosaur feathers [7], and charcolified or lignitic fossil plants from the Carboniferous used as the main source for coal. Although fascinating, the search for ancient biomolecules imposes stringent interpretational and analytical challenges as (i) taphonomic and diagenetic processes may strongly affect original chemistry, (ii) contaminants are likely

present at the surface of the samples, and (iii) carbon-based compounds can be preserved as traces.

Most fossil biogenic organic compounds have been detected in their native form using invasive analysis such as gas chromatography/mass spectrometry (GC/MS; e.g., [8, 9]) or amplified by polymerase chain reaction (PCR; e.g., [1, 2, 4]). However, such measurements are performed on extracts and therefore only represent averaged information over the sampling volume and do not yield the spatial complexity of the chemistry of such specimens for which imaging is a requisite. The development of new analytical tools and/or technical improvements towards higher sensitivity or resolution have recently pushed forward the search for traces of ancient biomolecules in the fossil record [10].

For instance, Fourier transform infrared (FT-IR) mapping revealed the preservation of amide and thiol groups of the β -keratin molecule in ca. 50-million-year-old reptile skin from Utah (USA) [11]. Time-of-flight secondary ion mass spectrometry (ToF-SIMS) data provided identification of hemoglobin-derived porphyrin molecules in a ca. 46-million-year-old blood-engorged mosquito from Montana (USA) [12]. In conjunction with immunohistochemical staining and FT-IR imaging, ToF-SIMS identified endogenous proteinaceous and lipid constituents, keratinocytes and branched melanophores, which evidence for homeothermy and crypsis in a ca. 180-million-year-old ichthyosaur from Germany [13]. One of the most promising experimental approaches is scanning transmission x-ray microscopy (STXM), a synchrotron-based soft x-ray technique which can probe speciation of light elements in micro-metric samples at a spatial resolution of few tens of nanometers [14]. Carbon K-edge spectra obtained on carbonaceous systems consist of spectral features that can differentiate organic compounds [15]. Applied to paleontology, STXM identified partially degraded sporopollenin molecules within a ca. 230-million-year-old lycopphyte megaspore from France [16], and partially preserved chitin–protein complexes within the cuticles of a ca. 310-million-year-old scorpion from Illinois (USA) and of a ca. 420-million-year-old eurypterid from Canada [17]. This technique even allowed documenting the chemical nature of ancient (several billion years old) organic microfossils [18].

However, these techniques present some limitations, the main one being the lack of bulk sensitivity. In fact, STXM-based x-ray absorption near edge structure (XANES) spectroscopy only allows probing thin samples (i.e. samples transparent to x-rays at the transition energy

of the element of interest). FT-IR, Raman and ToF-SIMS imaging also only provide surface sensitivity. Thus, any contamination of the surface by exogenous organic matter, but also sample roughness, can compromise data acquisition and interpretation. This ‘black and white’ situation where organic compounds either absorb too much or too little (hard x-rays) to allow meaningful imaging, depending on the nature of the probe, still poses numerous challenges to the depiction of the 3D chemical speciation of primarily organic systems. A method providing spatially-resolved information of organic carbon speciation in 3D and over large areas appears critically required to overcome these limitations.

Here, we report the unprecedented use of a hard x-ray probe for the element-specific chemical bulk imaging of ancient materials. Taking advantage of the capability of non-resonant x-ray Raman scattering (XRS) for direct tomography with chemical-bond contrast [19], we develop 2D and 3D x-ray Raman scattering spectral imaging for cultural heritage and geosciences. The large penetrative power of hard x-rays enables the measurement to be done in a non-invasive way, with no particular preparation nor specific experimental conditions, in air, and provides information that is not compromised by surface contamination by ensuring that the dominant signal contribution is from the bulk of the probed material [20]. XRS 2D and 3D imaging are demonstrated against a fragment of *Lepidodendron* trunk from the Upper Carboniferous (ca. 305 Mya) of Pas-de-Calais (France), and an Eocene ant (ca. 53 Mya) entrapped in amber from Oise (France), respectively. The present results reveals local “pockets” of preservation in the chemical composition of the plant fossil, likely inherited from its geological history, while they acquaint the exceptional preservation of the insect cuticle by showing chemical signatures of polysaccharides such as chitin.

3.2 Results and discussion

We collected XRS carbon K-edge intensities using *mapping* (or *raster-scanning*) by moving sequentially objects across the photon beam at a given incident energy while measuring the scattered intensity. Several such maps are acquired at different energy losses through the carbon K-edge to produce a hyperspectral datacube.

Illuminating a sample with an incident energy E and setting a (fixed) analyzer energy E_f , the energy loss $\Delta E = E - E_f$ can create electronic excitations. If ΔE is tuned to a transition

involving a bound electron, the resulting spectroscopy is called x-ray Raman scattering spectroscopy. Beside a q -dependent background which is dominated, at high momentum transfer (q), by Compton scattering and, at low q , by collective valence electron excitations such as plasmons, the XRS spectrum contains in general non-dispersive features which are generated when a fraction of incident photon energy is transferred to the sample inner shell electrons, promoting them into unoccupied states[21]. XRS therefore enables the measurement of the near-edge excitation spectrum in the energy loss domain. It combines the chemical sensitivity of x-ray absorption spectroscopy (XAS) for the study of the speciation of light elements such as carbon with the benefit of high photon energy (of 6–13 keV range), discarding the significant experimental constraints of XAS at the low energy of the carbon K-edge (280–350 eV). XRS has demonstrated a great potential to probe carbon speciation in homogeneous liquid or solid carbon-based samples that are poor in heavier elements (absorption of x-ray from the latter represents the main limitation of this technique). XRS has been shown a promising means to identify the chemical speciation of light elements in a range of systems from oil cuts to artists' pigments [20–22]. The proof of concept of imaging has been established on a model object [19], yet XRS imaging of real-to-life materials has never been studied.

3.2.1 Micro-scale 2D imaging of carbon on centimetric Carboniferous plants

We used XRS imaging (XRI) to study a fragment of *Lepidodendron* trunk collected on a Upper Carboniferous (ca. 305 Mya) coal slag heap in Noyelles-lez-Lens, France (Figure 3.1A–C). The fossil fragment, easily recognizable by its characteristic diamond-shaped pattern, is ca. 6 cm long and 2.5 cm wide and lies on a black shale, yellowish in places, which also includes other plant fragments. Most of the *Lepidodendron* trunk has the same appearance and color as the shale, but it also contains a thicker, vitreous material black to very shiny (extremely similar to vitrinite) distributed along the edges of most diamond-shaped leaf scars. A few beige patches are irregularly distributed over the fossil.

XRI produces carbon maps with a micrometric spatial resolution (down to a few micrometers as defined by the beam size) over large *pluri-centimetric* objects. In contrast to carbon mapping using scanning electron microscopy with energy dispersive X-ray spectroscopy (SEM-EDX), 2D-XRI provides bulk mapping such that the carbon signal is not (or minimally) hampered by contamination or surface roughness. Collecting a map before and after the K-

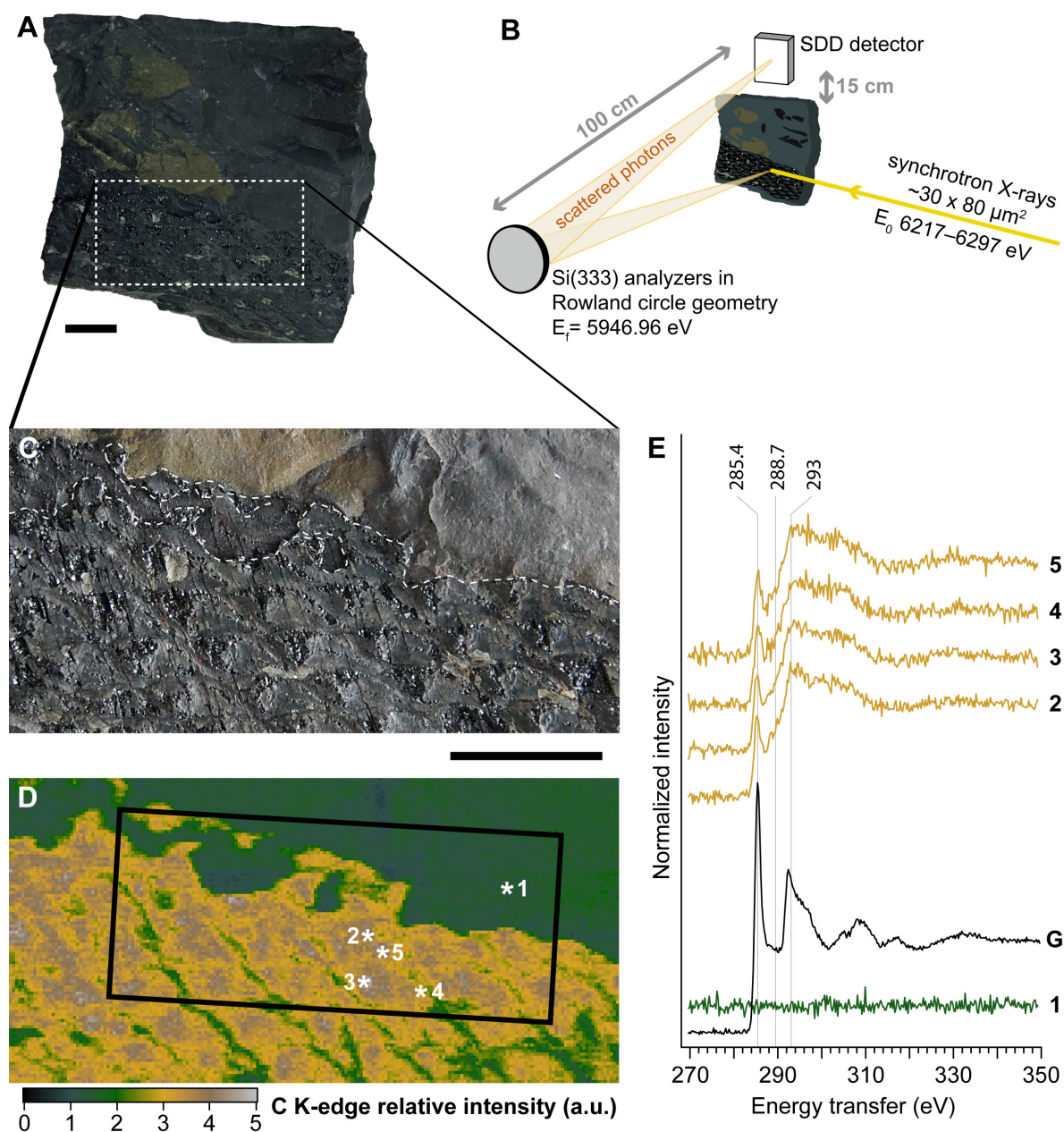


Figure 3.1: Carbon x-ray Raman scattering mapping and spectroscopy of a fragment of *Lepidodendron* trunk from the Upper Carboniferous (ca. 305 Mya) of Noyelles-lez-Lens, France. (A) Optical photograph of the studied object. (B) Schematic view of the experimental XRS setup. (C) Close up on the studied area. The dashed line represents the boundaries identified in D. (D) Carbon map from the dotted box area in A (scan area: $40 \times 20 \text{ mm}^2$, 20,000 pixels, scan step: $200 \times 200 \mu\text{m}^2$, beam size: $15 \times 15 \mu\text{m}^2$). The box corresponds to the area analyzed in Figure 3.2. (E) Normalized background-corrected carbon K-edge XRS spectra from the locations indicated by stars in D (sum of 4 spectra; 500 ms per energy step; beam size: $15 \times 15 \mu\text{m}^2$), and pure graphite (G) for energy calibration and reference; spectra were vertically shifted for increased readability. Scale bars represent 1 cm.

edge allows reconstructing an edge-jump map, a map of carbon concentration within the sample. The map obtained appears surprisingly contrasted considering the above description of the sample: despite their similar appearance and color, the fossil is clearly enriched in carbon, and no contrast is observed between the vitreous material, the beige patches and the rest of the fossil (Figure 3.1C,D). The carbon distribution can be used to pinpoint interesting areas for spectroscopy. We collected five full XRS-based carbon K-edge XANES spectra (Figure 3.1E), one from the shale and four from the plant, targeting at the different materials observed (at the edge and inside of the diamond-shaped leaf scars) and at the different carbon amounts revealed by the map. The black shale matrix does not contain significant amounts of organic carbon. Surprisingly again, all four spectra from the fossil appear very similar after background-corrected normalization. The spectra reveal two main absorption features at 285.4 and 293.0 eV attributed to $1s-\pi^*$ and $1s-\sigma^*$ electronic transitions in aromatic or olefinic C=C carbons, respectively [23]. In contrast to usual low-energy C-XANES spectroscopy, bulk probing of the expected random-oriented polycrystalline material allows comparing the intensity of these spectroscopic features.

With a $(1s-\pi^*)/(1s-\sigma^*)$ ratio (that is, $1s-\pi^*/(1s-\sigma^* + \arctangent)$, where the arctangent function models the edge jump in the C-XANES spectra) of 0.45, these spectra reveal that the graphitic macromolecular organic carbon composing the *Lepidodendron* trunk is not highly ordered but rather similar to bituminous coals[24]. In contrast to lignite, the spectra of the *Lepidodendron* trunk do not exhibit any clear absorption feature at 288.7 eV attributed to carboxylic functional groups ($1s-\pi^*$ transition).

There is only a limited number of characteristic resonances at the carbon K-edge [20, 25], and the spectra at this edge from the *Lepidodendron* trunk are well explained by a combination of two Gaussians centered at the $1s-\pi^*$ and $1s-\sigma^*$ energies and of an arctangent-shaped contribution to account for transitions to the continuum (Figure 3.2A). To further test the homogeneity of the carbon speciation over a very large sample area, we collected maps at different characteristic energies (270, 280, 285, 288, 293 and 350 eV). The spectral decomposition of the reduced XRS-based XANES spectra obtained for each pixel using the same Gaussians and arctangent, plus a linear fit of the Compton background fits very well to the experimental data (Figure 3.2C). The decomposition gives a $(1s-\pi^*)/(1s-\sigma^*)$ ratio of 0.58, well comparable to that obtained for the full XRS-based XANES spectrum collected at the same location (0.45).

The Gaussian distributions clearly highlight two classes of pixels, those belonging to the fossil (high contribution) and those from the shale matrix (low contribution, reflecting the lower carbon content of the shale; Figure 3.1E, spectrum 1). The distribution of the $(1s-\pi^*)/(1s-\sigma^*)$ ratio within the fossil appears quite homogeneous, with a mean ratio of 0.56 (Figure 3.2D). This chemical map does not reveal any contrast matching the optical morphology of the sample either, as the vitreous material surrounding the diamond-shaped leaf scars remains spectroscopically indistinguishable from the rest of the fossil.

Very interestingly, a few pixels yield significantly different ratios: less than 5% and 2% of the pixels record ratios <0.35 and >1 , respectively, suggesting a complex preservation history with local chemical heterogeneity. Pixels with lower ratios may indicate micrometric “pockets” of preservation where the plant material has not been turned into coal, but only as lignite or even show the presence of less degraded plant compounds, such as cellulose or lignin, whereas pixels at high ratio indicate the local presence of much more thermally altered compounds.

These results demonstrate the strong potential of 2D-XRI to evaluate carbon speciation in heterogeneous fossils. Observation of micrometric “pockets” of preservation appears particularly promising for further molecular identification.

3.2.2 Revisiting the 3D preservation of insect in amber

In dense samples such as rocks, 6–15 keV x-rays penetrate a few tens to hundreds of micrometers. In contrast, they will penetrate from millimeters to centimeters in organic matter. X-rays scattered off the object at different depths along the incident beam direction will focus on different areas of the pixelated detector due to the point-to-point focusing properties of the bent analyzer crystals (Figure 3.3A). The collection of data along the beam direction thereby provides a 1D image where the contrast is governed by the inelastic scattering signal after proper integration; similar to confocal imaging. The collection of successive sections by raster-scanning the object then makes it possible to construct a 3D tomographic volume at a resolution defined by the dimensions of the projected beam laterally and by the detector projected pixel size along the beam (direct tomography [19, 26]).

We performed 3D-XRI of a block of Eocene amber containing a morphologically well-preserved ant worker, without wings (Oise, France, ca 53 Mya; Figure 3.3B). Experimental

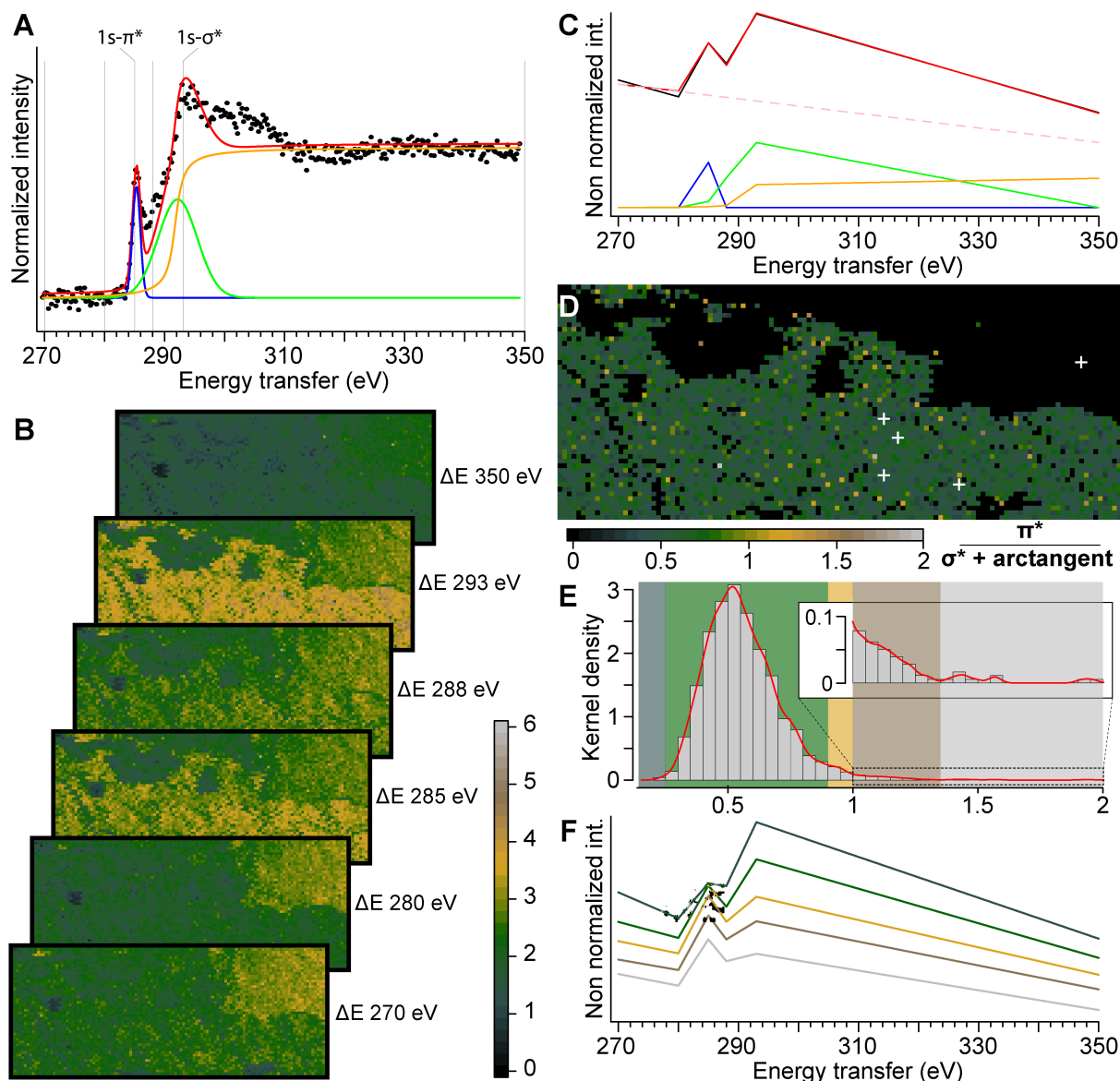


Figure 3.2: 2d XRS carbon K-edge speciation mapping of a fragment of *Lepidodendron* trunk from the Upper Carboniferous (ca. 305 Mya) of Noyelles-lez-Lens, France. (A) Spectral decomposition in 2 Gaussians and an arctangent of edge features of the background-corrected normalized XRS carbon K-edge XANES spectrum from the location indicated as point “2” in Figure 3.1D. (B) Carbon intensity maps collected at 270, 280, 285, 288, 293 and 350 eV from the dotted box area in Figure 3.1D (scan step: $300 \times 300 \mu\text{m}^2$, 6000 pixels, beam size: $15 \times 15 \mu\text{m}^2$). Note how accurately the intensities in the fossils match the full spectra collected, and how the intensities decrease following the Compton scattering background in the shale. (C) Spectral decomposition of the reduced spectrum collected at the exact same location as spectrum point “2” in A and Figure 3.1D. (D) Distribution of the $(1s-\pi^*)/(1s-\sigma^* + \arctangent)$ ratio within the *Lepidodendron* trunk (calculated from the spectral decomposition of the reduced spectrum at each pixel). The white crosses indicate the location of the full spectra shown in Figure 3.1E. (E) Histogram and kernel density of the ratio, allowing to pinpoint a few pixels with speciation different from the full spectra collected. (F) Mean (reduced) spectra from the different classes of ratio identified by their respective color boxes in E.

conditions were selected to yield a voxel size of $50 \times 50 \times 50 \mu\text{m}^3$, each voxel being associated to its own XRS-based XANES spectrum.

The image of the total signal intensity leads to direct observation of most of the morphology of the fossil (Figs. 3.3C and 3.4A). The three tegma are visible (head, mesosoma, metasoma including the petiole but not showing segment details), the mandibles, maxillary palps, and remnants of three legs, confirming that the hyperspectral dataset contains enough information to contrast different parts of the fossils. A mean spectrum from 150 pixels in the bulk amber (Figure 3.4D) exhibits a feature at 285.4 eV attributed to $1s-\pi^*$ transitions of aromatic-olefinic carbons, a broad feature in the 287.3–289.0 eV energy range, and a feature at 292.4 eV related to C–C $1s-\sigma^*$ contributions [23]. Ambers form during the polymerization of non-volatile terpenoids, major components of the resins produced as a protective metabolism by many angiosperms and gymnosperms, while the volatile terpenoids escape to the atmosphere. The Eocene Oise amber, an Ic type resin typical of angiosperms derived from *Fabaceae* sp. [27], is characterized by the presence of aromatic-olefinic carbons, attributed to terpenoids, biomarkers of the botanical origin of the resins [28]. The broad feature likely corresponds to the superimposition of the $1s-\sigma^*$ electronic transitions of aliphatic carbons (287.3–288.0 eV) [25], formed during polymerization [28], and the $1s-\pi^*$ transitions of carbonyl groups.

Contrasts observed in the specimen indicate the presence of different chemical compounds. Spectra from the perimeter of the insect show features markedly different from the bulk amber. The XRS spectrum $I(\Delta E, X)$ at a given voxel of coordinates $X = (x, y, z)$ is a linear combination of the spectra of the different compounds present plus a background signal from valence electron background and Compton scattering:

$$I(\Delta E, X) = \sum_{n=1}^N A_n(X) I_n^{\text{ref, norm}}(\Delta E) + C_1(X) + C_2(X) \Delta E \quad (3.1)$$

where ΔE is the energy transfer with respect to the K-edge of the element under study. When the model is complete (all reference compounds identified), the A_n parameters reflect the quantity of each species n of normalized XRS spectrum $I_n^{\text{ref, norm}}(\Delta E)$ in the voxel probed. In the restricted ΔE range used, the tail of the background in the XRS spectrum is expected to be quasi affine in energy and is modelled as $C_1(X) + C_2(X) \Delta E$.

The decomposition of the XRS data was performed as described in Material and Methods, using as initial guess the averaged spectrum of amber measured in the bulk amber (Fig-

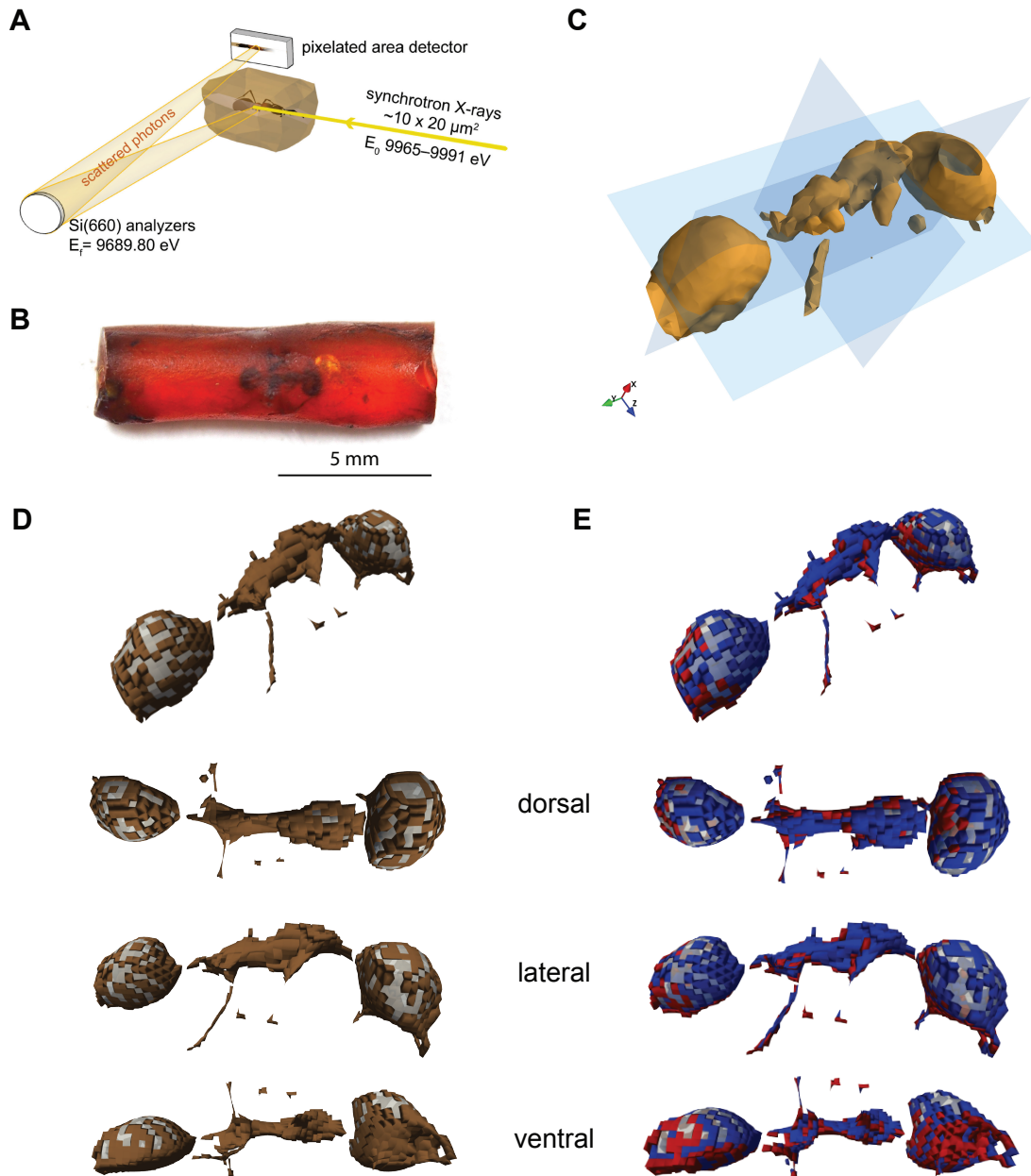


Figure 3.3: XRS 3d carbon K-edge speciation mapping of an Eocene (ca. 53 Mya) ant entrapped in amber from Oise, France (A) Schematic view of the experimental XRS setup. (B) Optical photograph of the specimen. (C) Isosurface of the raw, energy integrated, intensity data. (D) 3D rendering of the ant cuticle (brown) and internal void (transparent grey) classes of voxels based on the total signal intensity, image with interpolation (voxel size: $50 \mu\text{m}^3$, 23,409 voxels (amber voxels not shown), beam size: $10 \times 20 \mu\text{m}^2$). Oblique, dorsal, lateral right and ventral views of the 3D rendering after smoothing (averaged voxel-distance interpolation) (E) Clustering of the ant cuticle voxels (brown voxels shown in D) based on the A_{chit} parameter allows chemically distinguishing two classes of voxels: one in dorso-right position (negative A_{chit} values in blue), the other in ventro-left position (positive A_{chit} values in red), here shown in oblique, dorsal, lateral right and ventral 3D views (after smoothing).

ure 3.4D). As shown on the map of the quadratic error of the fit, the spectral data differ considerably from the amber for a line one pixel wide at the location of the insect's former cuticle (Figure 3.4B). Spectra from these pixels show significantly different characteristics compared to those of the amber matrix. In particular, some show a more intense feature at 288.3 eV attributed to $1s-\pi^*$ transitions from amide groups, while others are characterized by the absence of spectral feature at 285.4 eV which points to the absence of aromatic-olefin carbons.

Arthropods' cuticle is a hierarchically structured material composed by the external thin epicuticle layer, rich in lipids and proteins, and the exocuticle and endocuticle composed mainly by chitin-protein complexes. Chitin $((C_8H_{13}O_5N)_n)$, a linear polymer of β -1,4-linked N-acetyl glucosamine, unlike most carbohydrate compounds, is not water soluble and is known to be quite decay-resistant[17, 29, 30]. We therefore compared the latter spectra to a reference chitin sample measured with XRS spectroscopy under identical conditions. Since both show similar features, we added a chitin reference spectrum to our fitting model. The parameters A_{amb} and A_{chit} predicted from linear least square fitting reflect the possible presence of the compounds in each voxel. Positive values of A_{chit} ($A_{chit} > 0.007$) are observed in the ventral exoskeleton (indicated by arrow *ExV*, Figure 3.4C). In contrast, significantly different values ($A_{chit} < -0.007$) are observed for pixels denoted by arrow *ExD* which leads to a second spectrum when segmented (Figure 3.4C). We speculate that the negative A_{chit} values in the least squares regression indicate the presence of an additional chemical compound not included in the model.

The clustering of the data based on A_{chit} allows discussing the chemistry of the arthropods' cuticle. The spectrum *ExV* is characterised by the presence of $1s-\pi^*$ transitions due to the presence of aromatic and/or olefinic carbons (Figure 3.4D). Both spectra *ExV* and from the chitin reference are dominated by a broad complex feature centered at 288.3 eV, which has been attributed to the presence of carbonyl associated with the amidyl group of the glycosyl ring [17]. The complex feature centered at 289.2 eV of the XRS spectrum of the chitin standard is attributed to the $1s-3p/\sigma^*$ transition of O-alkyl (C-OH) moieties [15]. The feature at 286.6 eV, present in the chitin standard, is assigned to the presence of vinyl ketone moieties, a possible result of radiation-induced changes [31]. The feature at 285.4 eV, assigned to the presence of $1s-\pi^*$ transition of olefinic moieties, may either be indicative of the specimen chemistry

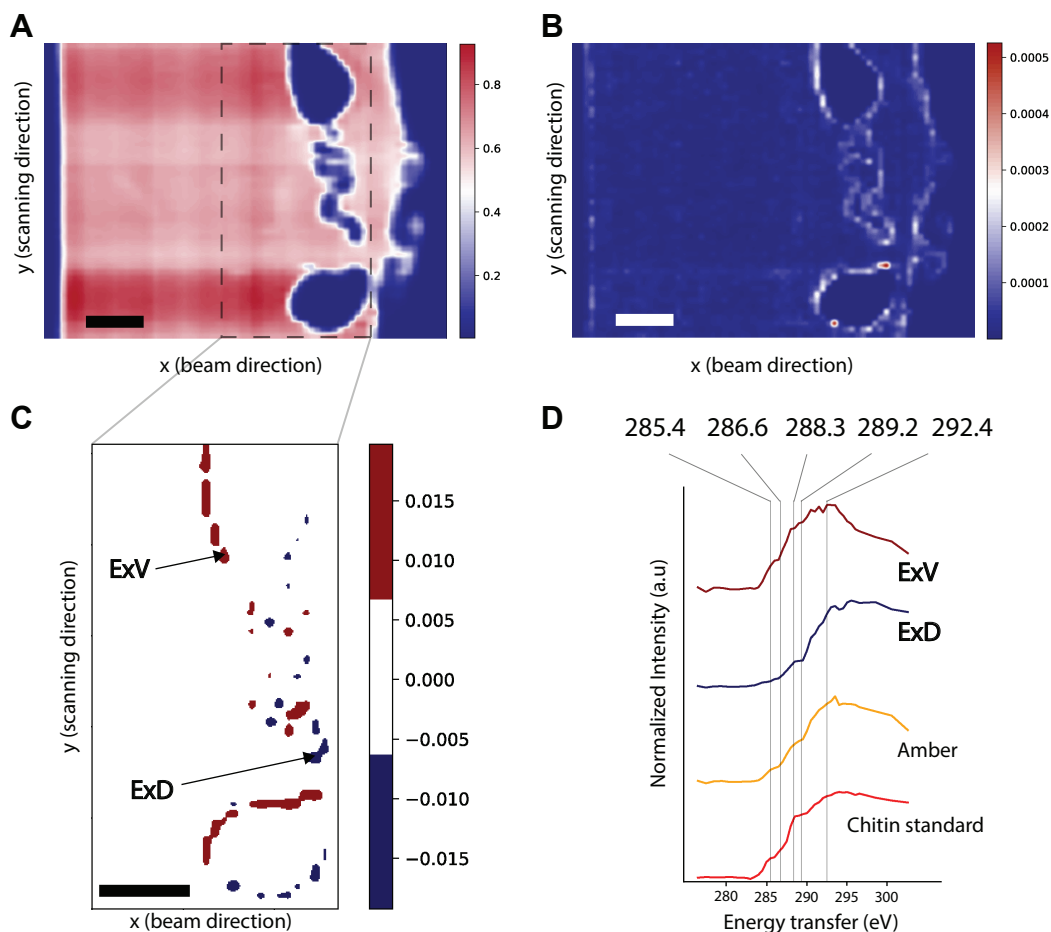


Figure 3.4: XRS virtual cross section and spectra of an Eocene ant entrapped in amber from Oise (France, ca. 53 Mya). (A) Total intensity virtual cross section image (pixel size: $50 \mu\text{m}^2$, beam size: $10 \times 20 \mu\text{m}^2$) of the ant entrapped in the Eocene amber (image with interpolation). (B) Spatial distribution of the quadratic error showing the diverse chemical regions of the sample when performing a fit based on the amber reference (image with interpolation). (C) Spatial distribution of A_{chit} when performing a fit based on the reference compounds Amber and Chitin (image with interpolation). (D) From top to bottom, distinctive normalized mean XRS spectral profiles corresponding to the ventral ($A_{\text{chit}} > 0.007$, ExV) and the dorsal ($A_{\text{chit}} < -0.007$, ExD) areas of the exoskeleton, as indicated with the arrows in C, Oise amber collected from the bulk specimen (*Amber*); chitin standard used as a reference material (*Chitin standard*). Scale bars represent $500 \mu\text{m}$.

and/or result from the elimination of hydroxyl groups from polysaccharides during irradiation as reported by Cody et al. [31].

In contrast, $1s-\pi^*$ transitions are totally absent from the arthropod's cuticle close to the specimen dorsal-right surface (spectrum *ExD*, Figure 3.4C and D). The less intense feature of this spectrum, centered at 288.3 eV, is attributed to the overlapping contribution of $1s-\pi^*$ transitions in amide groups[15] and the possible presence of $1s-\sigma^*$ transitions of aliphatic groups in the energy region 287.3–288.0 eV [25]. The presence of aliphatic carbons is consistent with the seminal work of Stankiewicz et al.[32] which identifies through invasive means aliphatic geopolymers in amber inclusions' exoskeleton, attributed to burial diagenetic transformation of the original chemistry of the organism. Chitin and ligno-cellulose could be identified using Py-GC/MS in sub-fossil (2–20 ka) insect and plant specimens entrapped in resins from Kenya, yet no trace of these macromolecules could be identified in Dominican amber inclusions (>25 Ma), instead aliphatic polymers and sulphur-containing moieties were identified [32]. Aliphatic signatures were also identified in fossil arthropods preserved in sediments (e.g.Gupta et al. [30]). In all the previous examples mentioned, Py-GC/MS was used at a semi quantitative level; selective sampling does not ensure that the sampling area is representative of the whole specimen. Here, the identification of two distinct chemical fingerprints in the exoskeleton (dorso-right vs. ventral-left distributions, Figure 3.3E) points the importance of discriminating the spatial distribution of organic compounds in 3D, at a global scale, in order to provide complete information about the specimens' biochemistry, physiology, molecular evolution or function, or chemical interactions between the organism and the depositional setting. Inclusions in amber occur in several flow sequences and often form multiple inclusions, or syn-inclusions. Each flow leads to a preservation mode that depends on several unknown factors including time. Cody et al. highlighted the need for a 3D approach of taphonomy to constrain paleobiological interpretations [33]. Their CT-scan tomography of multiple inclusions in the same sample revealed different levels of preservation depending on the resin layer and on the type of organism.

Although amber and copal (fossil tree resin) preserve three-dimensionally and in superb detail numerous organisms (insects, feathers, plants, etc.) as a result of entrapment that rapidly dehydrates the inclusions and protects them from water and microbial decay[3], many localities only preserve cuticle or hollow moulds (such as the ant we studied herein), or no fossils

at all, and the processes that control this range in preservation (nature of the resin producer and of the inclusions, environmental conditions, maturation, reworking) remains essentially unknown[34, 35].

The clustering of the data based on the total intensity allows the discrimination of the inclusion from the surrounding organic substrate. Further decomposition of the cuticle voxels (brown voxels in Figure 3.3D) based on the A_{chit} parameter allows the identification of chitin traces distributed in the cuticle (Figure 3.3E). This wealth of information allows us to report the first ever full non-invasive 3D speciation of carbonaceous compounds inside a paleontological specimen (Figure 3.3). Cuticle voxels with A_{chit} positive values are represented in red and A_{chit} negative values in blue color. The lack of carbon signal in the internal part of the abdomen and the head (transparent grey voxels in Figure 3.3D–E) points to the poor preservation state of the internal soft tissue structures, while the voxels with chitin affinities (positive A_{chit} values, red voxels in Figure 3.3E) confirm the preservation of the cuticular anatomy in the ventral surface of the insect. Until now, chemical characterization has mainly focused on the amber and very few studies have investigated the inclusions due to the following challenges[36]: spectral features from the inclusions are predicted to be very close in wavenumber to those of the resin, and because components of the resin have largely penetrated the inclusions [32], sampling and/or spectroscopy techniques only provide average information, which involve destructive sample preparation, restricting their use for rare specimens.

The fact that we were able to detect polysaccharide traces and distinguish the preserved insect's exoskeleton from its encasing amber and hollow parts in 3D with reasonable resolution, opens entire new avenues for the chemical characterization of organisms preserved in amber.

3.3 Conclusions and implications

Over the last two decades, XRS spectroscopy has been successfully applied for chemical speciation of light element systems and conditions not suited for a soft x-ray probe. Our results shown here extend this capability to the hyperspectral 2D and 3D imaging of organic-rich paleontological specimens and geological objects. The possibility to work on such samples without any specific preparation and under ambient conditions is the critical advantage of

this hard x-ray probe. While other imaging methods, most notably x-ray phase contrast tomography, provides better spatial resolution and is less restricted in terms of sample size and composition, the XRS method shown here uniquely complements such information by providing unprecedented insights into 3D carbon speciation. Given the small cross section and resulting weak signal strength, XRS based speciation characterization and imaging poses some restrictions for sample size and composition. For 2D imaging, the main restriction is the presence of heavy elements in the sample, which reduce the scattering volume. As current XRS setups operate in the 6–15 keV range, 3D imaging is furthermore restricted to sample sizes and compositions that permit the penetration at such x-ray energies. Further work will aim at minimizing the source of potential radiation-induced damage [37]. Several directions can be pursued: use of cryogenic and anaerobic conditions for some samples; increase in x-ray energy to reduce the photoelectric cross section while increasing the XRS intensity and penetration length; defocusing the beam in the vertical direction using the so-called 2D sectioning mode [19].

In addition to ancient fossils, the development of this approach to the study of organic-rich heterogeneous materials shows promise for numerous fields of research, including geosciences, life sciences, materials sciences, and cultural heritage.

3.4 Materials and methods

3.4.1 Paleontological samples

Two paleontological samples were examined: (i) a fragment of *Lepidodendron* trunk collected by one of us (PG) on a Upper Carboniferous (*ca.* 305 Mya) coal slag heap in Noyelles-lez-Lens, France, on April 15th, 2012; (ii) an insect (inv. no. PA-xxx, Hymenoptera, Formicidae) entrapped in amber, an Ic type resin typical of angiosperms and derived from a Fabaceae. The amber deposit of Oise, discovered in 1996 at the Quesnoy locality in the Oise River area of Paris basin in France, have been dated as earliest Eocene (approximately 53 million-years-old) [38]. The specimen belongs to the paleontological collections of the Natural History Museum of Paris.

For comparison, we collected data on purified powder of chitin from shrimp shells (C9752, CAS: 1398-61-4, Sigma-Aldrich, St. Louis, USA).

3.4.2 X-ray Raman-based spectral imaging

All experiments were performed at the GALAXIES and ID20 beamlines at the SOLEIL and the ESRF synchrotrons, respectively. The spectrometer at the GALAXIES beamline was equipped with 4 spherically bent Si(444) analyzer crystals operated at a Bragg angle of 86° [39]. The ESRF spectrometer is equipped to house 72 spherically bent Si(660) analyzer crystals, 36 of which were used in the forward scattering geometry (median scattering angle: 30°) and 36 in the backscattering geometry (median scattering angle: 122°) [40] resulting in average momentum transfers of $2.6 \pm 0.6 \text{ \AA}^{-1}$ and $8.8 \pm 0.6 \text{ \AA}^{-1}$, respectively.

On both beamlines, the incident x-ray beam was monochromatized using a cryogenically cooled Si(111) double-crystal monochromator and focused by Kirkpatrick-Baez mirrors to a spot size (V×H) of approximately $10 \times 20 \text{ }\mu\text{m}^2$ at ID20 and $15 \times 15 \text{ }\mu\text{m}^2$ at GALAXIES. The overall energy resolution was 1.2 eV.

XRI was performed on the specimens without any prior sampling. Four dimensional volumes were taken at ID20 by scanning the x-ray beam across the sample horizontally and parametrically varying the sample in the vertical position and the x-ray beam energy to create energy losses in the vicinity of the carbon K-edge (280–310 eV). The used step sizes were $50 \text{ }\mu\text{m}$ in the horizontal and vertical direction. The energy step was 1 eV over the pre-edge region (276.4–282.4 eV), 0.5 eV over the carbon K-edge region (282.4–296.4 eV) and 2 eV up to 302.4 eV.

This is an early stage development of the technique and we have tested several configurations at the beamlines including to survey radiation damage that can occur. The Lepidodendron XRS data was collected by continuously scanning the sample in the beam at fixed energy, thus reducing the exposure time. No visible radiation induced damage was observed in this sample which is known to be stable under irradiation. In contrast, amber is known to be a very sensitive material under irradiation. The 3D amber volume presented here was collected in high-flux mode (10^{13} ph/s) resulting in darkening of the exposed area after two minutes dwell time. Nevertheless the spectra still carry chemical information of the sample original chemistry and none of the samples show signal corresponding to a significantly altered material [20]. Optimisation to further reduce the impact of irradiation is beyond the scope of this PhD manuscript, however we did carry out tests in a low-flux mode (20 times less) and higher

energy resolution which shows promise to mitigate radiation damage. Further efficient ways to avoid damage are discussed in the conclusions.

3.4.3 3D reconstruction of the XRI data

All data was analyzed using the XRStools program package [26] and 3D volumes were created for each energy loss step as described recently [41]. Finally, data from different analyzer crystals were interpolated onto a common energy loss scale to account for the slightly different elastic line energies of the different analyzer crystals and data from the 36 low-momentum-transfer analyzer crystals was averaged over.

3.4.4 Statistical processing of the 3D XRI data

Decomposition of the XRS spectrum $I(\Delta E, X)$ was performed according to equation 3.1, using a non-linear least squares fitting procedure implemented in Python. Normalized spectra were used as reference spectra, $I_n^{\text{ref, norm}}(\Delta E)$ (see main text for description of the references used at each processing step). The goodness of fit was evaluated on the basis of the residual (quadratic) sum of squares, $RSS = \sum_{i=1}^n \left(I_i^{\text{exp}} - I_i^{\text{predicted}} \right)^2$.

References

- [1] Matthias Hoss, Svante Paabo, and NK Vereshchagin. “Mammoth DNA sequences”. In: *Nature* 370.6488 (1994), pp. 333–334.
- [2] Hendrik N Poinar et al. “Metagenomics to paleogenomics: large-scale sequencing of mammoth DNA”. In: *Science* 311.5759 (2006), pp. 392–394.
- [3] George O Poinar and Roberta Hess. “Ultrastructure of 40-million-year-old insect tissue”. In: *Science* 215.4537 (1982), pp. 1241–1242.
- [4] Rob DeSalle et al. “DNA sequences from a fossil termite in Oligo-Miocene amber and their phylogenetic implications”. In: *Science* 257.5078 (1992), pp. 1933–1936.
- [5] Raúl J Cano et al. “Amplification and sequencing of DNA from a 120–135-million-year-old weevil”. In: *Nature* 363.6429 (1993), pp. 536–538.

- [6] David Penney et al. “Absence of ancient DNA in sub-fossil insect inclusions preserved in ‘Anthropocene’ Colombian copal”. In: *PloS one* 8.9 (2013), e73150.
- [7] Jakob Vinther et al. “The colour of fossil feathers”. In: *Biology Letters* 4.5 (2008), pp. 522–525.
- [8] Jochen J Brocks et al. “Archean molecular fossils and the early rise of eukaryotes”. In: *Science* 285.5430 (1999), pp. 1033–1036.
- [9] Gordon D Love et al. “Fossil steroids record the appearance of Demospongiae during the Cryogenian period”. In: *Nature* 457.7230 (2009), pp. 718–721.
- [10] Derek EG Briggs and Roger E Summons. “Ancient biomolecules: their origins, fossilization, and role in revealing the history of life”. In: *BioEssays* 36.5 (2014), pp. 482–490.
- [11] Nicholas P. Edwards et al. “Infrared mapping resolves soft tissue preservation in 50 million year-old reptile skin”. In: *Proceedings of the Royal Society of London B: Biological Sciences* 278.1722 (2011), pp. 3209–3218.
- [12] Dale E Greenwalt et al. “Hemoglobin-derived porphyrins preserved in a Middle Eocene blood-engorged mosquito”. In: *Proceedings of the National Academy of Sciences* 110 (2013), pp. 18496–18500.
- [13] Johan Lindgren et al. “Soft-tissue evidence for homeothermy and crypsis in a Jurassic ichthyosaur”. In: *Nature* 564 (2018), pp. 359–365.
- [14] Chris Jacobsen et al. “Soft X-ray spectroscopy from image sequences with sub-100 nm spatial resolution”. In: *Journal of Microscopy* 197.2 (2000), pp. 173–184.
- [15] Dawit Solomon et al. “Carbon (1s) NEXAFS spectroscopy of biogeochemically relevant reference organic compounds”. In: *Soil Science Society of America Journal* 73.6 (2009), pp. 1817–1830.
- [16] Sylvain Bernard et al. “Exceptional preservation of fossil plant spores in high-pressure metamorphic rocks”. In: *Earth and Planetary Science Letters* 262.1-2 (2007), pp. 257–272.
- [17] George D Cody et al. “Molecular signature of chitin-protein complex in Paleozoic arthropods”. In: *Geology* 39.3 (2011), pp. 255–258.

- [18] Julien Alleon et al. "Molecular preservation of 1.88 Ga Gunflint organic microfossils as a function of temperature and mineralogy". In: *Nature Communications* 7 (2016), p. 11977.
- [19] Simo Huotari et al. "Direct tomography with chemical-bond contrast". In: *Nature Materials* 10.7 (2011), pp. 489–493.
- [20] Pierre Gueriau et al. "Noninvasive Synchrotron-Based X-ray Raman Scattering Discriminates Carbonaceous Compounds in Ancient and Historical Materials". In: *Analytical Chemistry* 89.20 (2017), pp. 10819–10826.
- [21] Winfried Schülke. *Electron dynamics by inelastic X-ray scattering*. Vol. 7. Oxford University Press, 2007.
- [22] Uwe Bergmann and Oliver C Mullins. "Carbon X-ray Raman spectroscopy of PAHs and asphaltenes". In: *Asphaltenes, Heavy Oils, and Petroleomics*. Springer, 2007, pp. 139–155.
- [23] Serge Bernard et al. "XANES, Raman and XRD study of anthracene-based cokes and saccharose-based chars submitted to high-temperature pyrolysis". In: *Carbon* 48.9 (2010), pp. 2506–2516.
- [24] Karen Heymann et al. "C 1s K-edge near edge X-ray absorption fine structure (NEXAFS) spectroscopy for characterizing functional group chemistry of black carbon". In: *Organic Geochemistry* 42.9 (2011), pp. 1055–1064.
- [25] Corentin Le Guillou et al. "XANES-based quantification of carbon functional group concentrations". In: *Analytical Chemistry* 90.14 (2018), pp. 8379–8386.
- [26] Christoph J Sahle et al. "Planning, performing and analyzing X-ray Raman scattering experiments". In: *Journal of Synchrotron Radiation* 22.2 (2015), pp. 400–409.
- [27] Jean Jossang et al. "Quesnoin, a novel pentacyclic ent-diterpene from 55 million years old Oise amber". In: *The Journal of organic chemistry* 73.2 (2008), pp. 412–417.
- [28] Youssef A Nohra et al. "Chemical characterization and botanical origin of French ambers". In: *Journal of Natural Products* 78.6 (2015), pp. 1284–1293.
- [29] B Artur Stankiewicz et al. "Preservation of chitin in 25-million-year-old fossils". In: *Science* 276.5318 (1997), pp. 1541–1543.

- [30] Neal S Gupta et al. “The fossilization of eurypterids: a result of molecular transformation”. In: *Palaaios* 22.4 (2007), pp. 439–447.
- [31] George D Cody et al. “Soft X-ray induced chemical modification of polysaccharides in vascular plant cell walls”. In: *Journal of Electron Spectroscopy and Related Phenomena* 170.1-3 (2009), pp. 57–64.
- [32] B Artur Stankiewicz et al. “Chemical preservation of plants and insects in natural resins”. In: *Proceedings of the Royal Society of London. Series B: Biological Sciences* 265.1397 (1998), pp. 641–647.
- [33] David Coty et al. “The first ant-termite syninclusion in amber with CT-scan analysis of taphonomy”. In: *PloS one* 9.8 (2014), e104410.
- [34] Xavier Martinez-Delclòs, Derek EG Briggs, and Enrique Peñalver. “Taphonomy of insects in carbonates and amber”. In: *Palaeogeography, Palaeoclimatology, Palaeoecology* 203.1-2 (2004), pp. 19–64.
- [35] Victoria E McCoy, Carmen Soriano, and Sarah E Gabbott. “A review of preservational variation of fossil inclusions in amber of different chemical groups”. In: *Earth and Environmental Science Transactions of The Royal Society of Edinburgh* 107.2-3 (2018), pp. 203–211.
- [36] Howell GM Edwards, Dennis W Farwell, and Susana E Jorge Villar. “Raman microspectroscopic studies of amber resins with insect inclusions”. In: *Spectrochimica Acta Part A: Molecular and Biomolecular Spectroscopy* 68.4 (2007), pp. 1089–1095.
- [37] Loïc Bertrand et al. “Mitigation strategies for radiation damage in the analysis of ancient materials”. In: *Trends Anal. Chem.* 66 (2015), pp. 128–145.
- [38] André Nél et al. “Un gisement sparnacien exceptionnel à plantes, arthropodes et vertébrés (Éocène basal, MP7): Le Quesnoy (Oise, France)”. In: *Comptes Rendus de l’Académie des Sciences - Séries IIA - Earth and Planetary Science* 329 (1999), pp. 65–72.
- [39] James Michael Ablett et al. “The GALAXIES inelastic hard X-ray scattering end-station at Synchrotron SOLEIL”. In: *Journal of Synchrotron Radiation* 26.1 (2019), pp. 263–271.

-
- [40] Simo Huotari et al. “A large-solid-angle X-ray Raman scattering spectrometer at ID20 of the European Synchrotron Radiation Facility”. In: *Journal of Synchrotron Radiation* 24.2 (2017), pp. 521–530.
- [41] Christoph J Sahle et al. “Improving the spatial and statistical accuracy in X-ray Raman scattering based direct tomography”. In: *Journal of Synchrotron Radiation* 24.2 (2017), pp. 476–481.

Nanoscale characterization of organic dark-coloured pigments

Nanoscale chemical characterization provides new insights into the carbon chemistry of organic dark-coloured pigments. Scanning transmission x-ray microscopy (STXM) demonstrates the complexity of artistic pigments based on carbon that can be addressed at the nanometric spatial resolution. We show that x-ray absorption spectroscopy, in the soft x-ray range, complements the XRS approach when its spatial limit is reached. We analyze dark colored pigments documented in Mayern's manuscript (date stone, peach stone, sticklac, bone black), a candle fume black, a wood soot (bistre), a commercially available vine black (Kremer), and a carbon black. The nanoscale chemical heterogeneity observed in the analysed pigments indicates a non-homogeneous transformation of the precursor materials during pyrolysis or combustion of the sample.

4.1 Introduction

Organic dark-coloured pigments are available to the artists in a variety of forms [1]. Winter and FitzHugh documented and classified artists' pigments based on carbon either according to their manufacture process (i.e. graphite, charred materials, flame carbons, cokes) or their source material (i.e. pigments of vegetable origin, animal origin, soots and smokes, graphitic pigments, black earths') [1–3]. The wide range of carbon-based materials used as dark-coloured pigments in diverse cultural and historical contexts make their identification complex and incomplete [1]. Identification and documentation of the raw materials is often crucial to understand the artists' methodology, to attribute the work of art to a workshop or an artist and to define proper restoration and conservation practices.

Researchers attempted to chemically characterize and set up criteria for the organic dark-coloured pigments' discrimination. Research on commercial carbon-based pigments (e.g. graphite, lampblack, vine black, ivory and bone black, asphaltum, Van Dyck brown

and cassel earth, etc) has been carried out by means of various techniques. Fourier transform infrared spectroscopy (FT-IR) has been employed for their molecular characterization [4, 5]. Tomasini, Siracusano, and Maier [4] proposed two flow charts for the commercial organic pigments' discrimination: (i) one based on the presence of characteristic FT-IR bands (e.g. hydrocarbon bands at the $3000\text{--}2800\text{ cm}^{-1}$ spectral region), and (ii) one based on the percentage of the carbon content and the presence of heteroatoms, such as sulfur, potassium, phosphorous, calcium and sodium; information extracted from scanning electron microscopy (SEM) coupled with energy dispersive x-ray spectroscopy (EDS) [4].

The distinct morphology of the pigments' particles, linked with the raw starting material and the manufacture process of the pigments can be used for their identification in complex heritage samples [4, 6]. In a study of ancient Egyptian papyri, the black pigment found in the ink was identified as a flame carbon through its specific morphology consisting of spheroidal particles of $\approx 85\text{ nm}$ in diameter observed by SEM image, although its specific source material (lampblack or soot) was not identified [6]. Autran et al. isolated the diffraction signal of these flame carbons through synchrotron-based x-ray diffraction computed tomography (XRD-CT) [6].

Optical Raman spectroscopy provided information on the degree of structural order of commercial black pigments [7, 8]. The organic pigments studied, being highly disordered materials, showed similar Raman spectra, exhibiting two characteristic broad Raman bands, one around 1580 cm^{-1} known as G band ('graphite' band) and an additional band around 1350 cm^{-1} known as D band ('disorder' band). The intensity ratio of the D and G band indicated the graphitization level of the pigments [5, 7]. The general classification of a black pigment as a carbonaceous material is easy to achieve, yet, the specific source of the material is hard to be discriminated due to close similarities in the spectra; only slight differences in band position, intensities and bandwidths may be observed [5, 7, 9].

Destructive thermoanalytical analysis, including differential scanning calorimetry (DSC) and thermogravimetry coupled with FT-IR under nitrogen flow (TG-FT-IR) has been employed for studying the thermal stability of commercially available vine blacks, bone blacks and lamp-blacks, their inorganic/organic ratio and their decomposition products [5]. Organic residues of vine plants (lignin and cellulose) were identified in vine black purchased from Kremer; the absence of lignin and cellulose pyrolysis products in the Zecchi vine black indicated a dif-

ferent production process (i.e. produced at higher temperature or with prolonged heating) [5]. Both Tomasini, Siracusano, and Maier and Lluveras-Tenorio et al. in individual studies reported adulteration in a commercial samples [4, 5].

In this work, we analyzed a range of dark colored organic pigments, summarized in Table 4.1 (see *Materials* subsection). Four pigments were prepared by University of Amsterdam students using organic materials (sticklac, date and peach stone, bones) following recipes and instructions documented in the *Mayerne manuscript* (Table 4.1, samples 1–4). Between 1620 and 1646, Theodore de Mayerne (1573-1655), an influential physician of the time, created an exemplary art-technological text source containing handwritten records on artistic techniques. Through in-situ observations, artists' interviews and his own experimentation, Mayerne gathered artisanal know-how, from textual sources and living artists [10]. The 17th century *manuscript*, entitled "*Pictoria, sculptoria et quae subalternarum artium*" (Figure B.1) comprises historical recipes and technical practises on the preparation of pigments – including organic pigments (Figures B.2, B.4, B.5, B.6, B.3, B.7). The retrospective use of the manuscript by artists in the early 20th century and its study by conservators and technical art historians today, highlights the importance of transferring scientific knowledge on art processes and materials [11].

This study set out to investigate the chemical heterogeneity of the organic pigments (summarized in Table 4.1) at the nanoscale. By employing scanning transmission x-ray microscopy (STXM), we collected carbon K-edge x-ray absorption near edge structure (XANES) data with nanometric spatial resolution to investigate the carbon bonding of the samples. For comparison, x-ray Raman scattering (XRS) was employed to collect carbon K-edge XANES data in the energy loss domain. XRS utilises hard x-rays to provide bulk-sensitive speciation information primarily to light elements, such as carbon, whose binding energy falls in the soft x-ray region [12]. We showed that STXM nanoscale images provided new insights into the carbon chemistry of the dark-coloured organic pigments and demonstrated their chemical complexity and inhomogeneity that cannot be tackled when the spatial limit of XRS is reached.

4.2 Materials and methods

4.2.1 Materials

We analyzed a sample-set of dark-coloured organic pigments, summarized in Table 4.1: (i) the samples 1–5 were manufactured at University of Amsterdam by Liz Hebert, Noah van der Meer, Nikita Shah, Momoko Okuyama, Jessie Carter, Camille Dullaart, and Paul Kisner, based on historical references found in the *Mayerne manuscript* [13]. The sample preparation was supervised by Maartje Stols-Witlox and Jenny Boulboulé; (ii) a bister (sample 6) manufactured by Birgit Reissland (the samples 1–6 were provided to us by Leila Sauvage); (iii) two commercially available pigments supplied by Kremer Inc were analyzed: a bister [12100] (sample 7) and a vine black [47000] (sample 9); (iv) a carbon black [NBS311] (sample 8) supplied by National Bureau of Standards (NBS, today NIST).

Winter and FitzHugh [1] documented and classified the artists' pigments based on carbon either according to their manufacture process (i.e. graphite, charred materials, flame carbons, cokes) or their source material (i.e. pigments of vegetable origin, animal origin, soots and smokes, graphitic pigments, black earths') [1, 2]. Date stone, peach stone, and vine black belong to the wide category of vegetable chars. Their names denote the diversity of starting materials [1]. Bister, also referred as bistre, is an impure wood soot which contains brownish tarry impurities, responsible of the dark brown colour of the pigment [1]. The amount of tarry materials depends on the distance of soot collection; the closer to the place of combustion the larger the amount of tarry materials, which affects the chemical composition of the pigment. In the 16th century, Boltz describes how soot produces a shiny deposit after the combustion of hardwoods in an oven or chimney [14]. Parry and Coste suggests the preparation of bister from beechwood [15], as documented earlier by Hochheimer [16]. Bister is mentioned in the preparation of bistre glazes [17], inks and watercolors [18]. Bister was also identified on medieval oil paintings [19].

Bone is a composite, hierarchical biomaterial which consists of closely associated organic (≈ 20 wt%), inorganic phase (≈ 70 wt%), and water (≈ 10 wt%) [20]. Organic phase primarily consists of type I fibrillar collagen ($\approx 90\%$), characterized by a triple helical structure formed by polypeptides [21, 22]. Carbon may also derive from fats. Inorganic phase of bone consists of a highly disordered apatite, distinct from geological hydroxylapatite ($\text{Ca}_{10}(\text{PO}_4)_6(\text{OH})_2$), depleted

in hydroxyl ions (OH^-), containing carbonate substitutions (3–8 %) and water in its apatite structure $(\text{Ca}_{10-x}[(\text{PO}_4)_{6-x}(\text{CO}_3, \text{HPO}_4)_x](\text{OH})_{2-x} \cdot n\text{H}_2\text{O})$ [21, 23, 24]. Identification of the non-carbon constituent (i.e. the bone mineral) has been in many heritage studies the source of identification of bone and ivory black [7, 25].

The production of a black pigment by burning sticklac is proposed in Mayerne manuscript in Folio 29 in which a conversation between Mayerne and John Hoskins (an English miniature painter) taking place on the 14th of March 1634 is documented (see Folio 29, Figure B.4). Stick lac (*"La Laque qui vient des Indes Orientales"*) is known in arts for the production of a red pigment, however, according to Hoskins the lac can be burned to create a black pigment. Beside Mayern manuscript sticklac black and its manufacture method is not mentioned in any modern publication regarding historical pigments, even in sections referring to Indian lake and lac (raw material) [26]. Sticklac is a complex substance secreted on twigs of native Indian and South-East Asian trees by scale insects (*Kerria lacca*). The main constituents of sticklac (i.e. raw lac) are: (i) resins ($\approx 68\%$), a polyester complex of long-chain hydroxy fatty acids and sesquiterpenic acids, (ii) dyes ($\approx 10\%$), consisting of anthraquinone derivatives (i.e. laccaic acids) and (iii) waxes ($\approx 6\%$), consisting of mixtures of long-chain acids, alcohols, esters and hydrocarbons [27]. Non-purified lac may also contain insect body, bark of host trees and other impurities [28].

4.2.2 Scanning transmission x-ray microscopy

Scanning transmission x-ray microscopy (STXM), a synchrotron-based technique, allows nanometric scale observations of x-ray absorption measurements at the soft x-ray energy region. A STXM microscope consists of a Fresnel zone plate, an order sorting aperture (OSA), the sample holder (samples are mounted on piezo stages) and an x-ray detector, enclosed in an aluminum chamber that can be evacuated to 10^{-6} torr. For increased thermal stability and reduce of interferometer drifts helium is added [29]. X-ray absorption near edge structure (XANES) spectra are obtained through successive collection of 2D images (*image stacks*) at fixed photon energies over the edge of interest (Figure 4.1). The x-ray beam is focused on the sample using a zone plate and a two dimensional (2D) image is collected by scanning the sample at a specific energy with a nanometric spatial resolution (of minimum 20 nm) and a dwell

| Samples | Description | Source material | Manufacturer | Historical reference |
|---------|-------------------|---|--|---|
| 1 | Date stone black | date pits charred | University of Amsterdam, 2019 | <i>Mayerne manuscript</i> , folio 95r (Fig. B.5) |
| 2 | Peach stone black | peach pits charred | University of Amsterdam, 2019 | <i>Mayerne manuscript</i> , folios 18r, 84r (Fig. B.2, B.3) |
| 3 | Sticklac | organic substance secreted by <i>Tacchanlia lacca</i> scale insects | University of Amsterdam, 2019 | <i>Mayerne manuscript</i> , folio 29r (Fig. B.4) |
| 4 | Bone black | lamp feet bones charred | University of Amsterdam, 2019 | <i>Mayerne manuscript</i> , folio 93r (Fig. B.7) |
| 5 | Candle fume black | candle, unknown composition | University of Amsterdam, 2019 | |
| 6 | Bister | wood | prepared by Birgit Reissland, Dresden, Germany, 2020 | |
| 7 | Bister | beechwood | Kremer Inc., 2018 [12100] | |
| 8 | Carbon black | natural gas | National Bureau of Standards [NBS311] | |
| 9 | Vine black | plant waste | Kremer Inc., 2018 [47000] | |

Table 4.1: Organic pigments analysed at the nanoscale via STXM

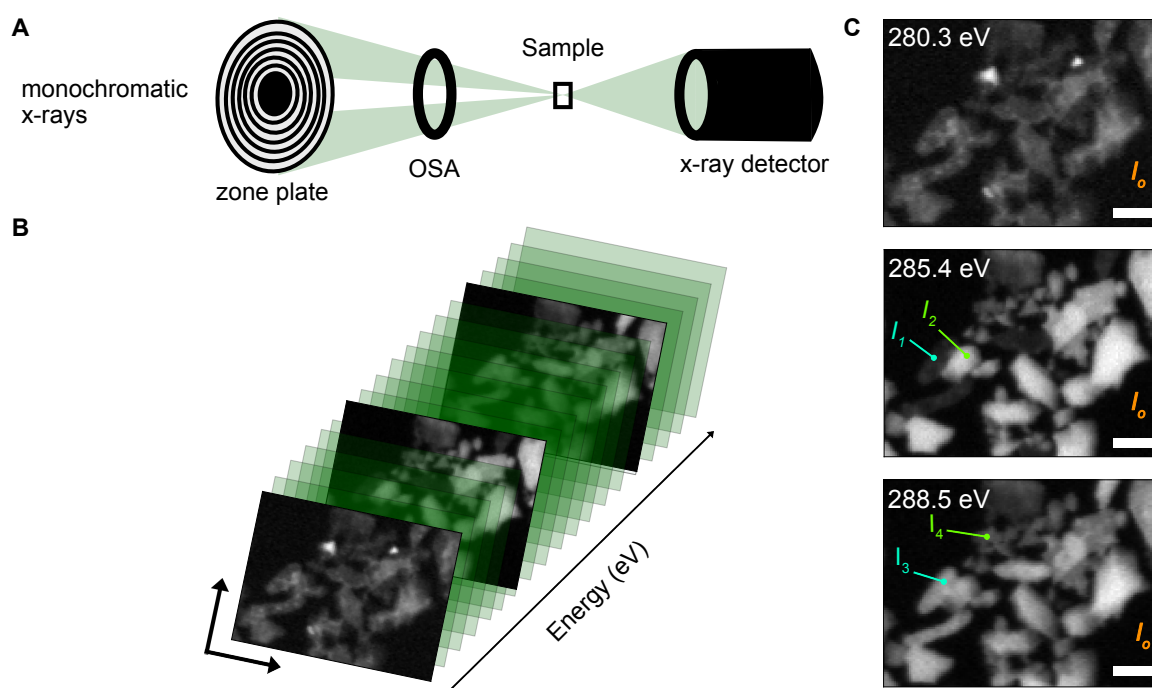


Figure 4.1: Scanning transmission x-ray microscopy. A. Schematic representation of a STXM microscope, consisting of a Fresnel zone plate, an order sorting aperture (OSA), the sample holder and an x-ray detector; B. Each image is scanned at a specific energy (e.g. 280.3 eV); for an image stack acquisition a series of images is acquired at successive energies; C. Aligned and optical density (OD) corrected STXM images of charred date pits sample acquired at specific energies (280.3 eV, 285.4 eV and 288.6 eV). Areas where there is no sample present are defined as I_0 areas. Intensity variations (e.g. I_1 and I_2 (at 285.4 eV) or I_3 and I_4 (at 288.5 eV)) in the images collected at specific diagnostic energies correspond to speciation variations in the sample.

time of few milliseconds per pixel. The collected datacube consists of a XANES spectrum for each pixel with a minimum size of $20 \text{ nm} \times 20 \text{ nm}$.

Carbon K-edge XANES spectra of the present study have been collected on HERMES beamline at the synchrotron SOLEIL. HERMES beamline, dedicated to soft x-ray microscopy, generates photons in the energy range from 70 eV to 2500 eV [30]. For samples 1–7 image stacks have been collected with an energy step of 1 eV over the 270–282 eV energy range, 0.1 eV over the 282.1–294.9 eV energy range, 1 eV over 295–315 eV energy range and 5 eV over 320–390 eV energy range with a dwell time of two milliseconds per pixel. For samples 8,9 image stacks have been collected with an energy step of 1 eV over the 270–282 eV energy range, 0.1 eV over the 282.1–294.9 eV energy range, 1 eV over 295–315 eV energy range and 2.5 eV over 370–397.5 eV energy range with a dwell time of two milliseconds per pixel.

4.2.2.1 Sample preparation

Carbon K-edge XANES data collected via STXM requires preparation of ultrathin samples (thickness of ca. 100 nm). To achieve the required thickness, for the STXM analysis, samples were finely powdered and suspended in pure H₂O. A droplet of 5 μ L was deposited in silicon nitride (SiN) membranes and let to dry under vacuum.

4.2.2.2 Data processing

Hyperspectral data obtained via STXM was first processed with aXis2000 software [31]. In STXM experiments the data recorded corresponds to the intensity of the transmitted x-rays. Using aXis2000 the recorded data was converted to optical density (OD) by $-\ln(I/I_o)$, where I is the intensity of the x-rays transmitted through the sample and I_o is the intensity of the x-rays in a pre-selected region without the sample present. Intrinsic mechanical and thermal drifts during the acquisition of images at a sequence of energies (i.e. recorded stacks) are causing misalignment of the recorded images. Stacks were aligned using Jacobsen's alignment routine available via aXis2000.

The aligned and OD-converted image stacks collected for each sample were generated as .mrc extensions and undergone further processing procedures within the Python environment. For each pixel we calculated the total intensity (i.e. the sum of the intensities at a sequence of energies) and the signal-to-noise ratio (i.e. the maximum signal divided by the standard deviation of the absorption signal in the energy range 270.3–281.3 eV). A pre-selection of spectra based on the total intensity histogram and a signal-to-noise threshold (>20) was performed aiming at identification of regions with no sample or noisy pixels, which were set to zero. The pre-selected spectra were normalised by the integrated area of each spectrum.

The pre-selected and normalized spectra (by the integrated area of each spectrum) were classified through hierarchical clustering analysis (*sklearn.cluster.AgglomerativeClustering*) [32] using the Ward variance minimization algorithm as a linkage method and the Euclidean distance as a metric of pairwise distances between observations. The number of clusters was selected using the graph of the Euclidean distance (calculated via *scipy.cluster.hierarchy.linkage* [33]) as a function of the number of classes (see graph 4.2); the objective function is decreas-

ing as the number of classes is increasing. An acceptable choice of classes corresponds to an objective function which does not change drastically if one or more classes are added [34].

For each spectra cluster an average spectrum is calculated by accessing the aligned and OD-converted intensities. A linear background was calculated and subtracted from the average spectra. The background-corrected average spectra were then normalized to the post-edge region with no significant oscillation.

4.2.3 X-ray Raman scattering spectroscopy

We collected XRS carbon K-edge data with an energy resolution of 1.2 eV (calculated as the FWHM of the elastic line) for the commercially available bister (Kremer) (Table 4.1 sample 7), carbon black (Table 4.1 sample 8) and commercially available vine black (Kremer) (Table 4.1 sample 9). The experiments were performed at GALAXIES beamline (Synchrotron SOLEIL, France) [35], equipped with 4 spherically bent Si(444) analyzer crystals [36]. Experiments were performed at a Si(444) analyzer energy of ≈ 7.9 keV operated at a Bragg angle of 86° . The data was collected at backscattered geometry (scattering angle of $2\theta \approx 130^\circ$) to maximize the XRS signal. The momentum transfer is $q \approx 7.5 \text{ \AA}^{-1}$. The beamline is equipped with a cryogenically cooled Si(111) double-crystal monochromator. The monochromatized X-ray beam is focused by a toroidal mirror to a spot size ($V \times H$) of approximately $30 \times 80 \mu\text{m}^2$. We collected energy transfer measurements along the carbon K-edge (275–320 eV) energy transfer with an energy step of 0.25 eV.

4.3 Results

4.3.1 Hierarchical clustering of STXM nanoscale images

Hierarchical clustering analysis was employed as a means to discriminate carbon signatures in each STXM energy stack (see *Data processing* subsection). For each sample analyzed, the number of classes was chosen based on the step-like features observed at the plot of Euclidean distance (objective function) as a function of the number of classes. Graph 4.2, which corresponds to the hierarchical clustering of date pits charred pigment, illustrates this point clearly. The clustering objective function is decreasing as the number of classes is increasing. Potential options of the number of classes are marked in red. In Figure 4.3 and Figure 4.4 two examples

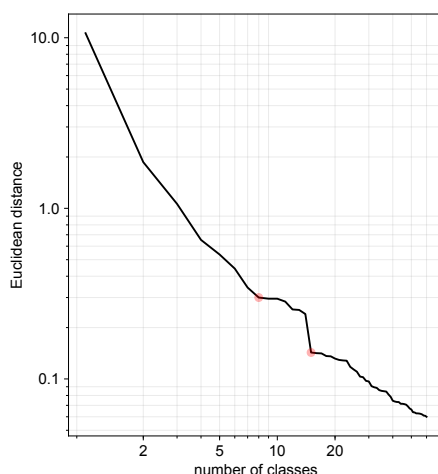


Figure 4.2: Hierarchical clustering analysis of the 7463 carbon K-edge XANES spectra obtained via STXM of the charred date pits. The graph presents the clustering objective function (Euclidean distance) as a function of the number of classes. In red are marked potentials options of the number of classes (8,15 classes). Eight or fifteen classes are considered an acceptable choices since adding few extra classes does not change significantly the objective function [34]. The clustering images corresponding to the chosen number of classes (8, 15) are shown in Figures 4.3,4.4, respectively.

of pixels' grouping (8 and 15 classes) of date pits charred pigment, are shown respectively. The higher the number of classes chosen, the more detailed is the characterization of the sample; spectral signatures present at lower percentage are made visible. For each sample the average spectra of the pixel classes and their percentage are displayed. This approach allowed us to decipher samples' areas characterized by chemical heterogeneity.

4.3.2 Charred date pits sample

The hierarchical clustering analysis of the charred date pits sample (Table 4.1 sample 1) hyperspectral data obtained via STXM illustrated the presence of distinct organic signatures. The normalized average carbon K-edge XANES spectra for each class, in the case of the 8 and 15 classes, are displayed in Figure 4.3 and Figure 4.4, respectively.

The average spectrum of the *pixel class A* (Figure 4.3 A) points out the presence of quinonic compounds in the sample; the shoulder centered at 284.6 eV present in the corresponding average spectrum is attributed to the $1s-\pi^*$ transition in $C=C$ in quinones [37]. *Pixel class B* and *pixel class C*, shown in Figure 4.3 B and Figure 4.3 C which represent the higher percentage

of pixels (28% and 34.9%, respectively), indicate intense aromaticity in the charred date pits sample; the peak centered at 285.5 eV is attributed to the $1s-\pi^*$ transitions in aromatic and/or alkene carbon ($C=C$) [38]. The peak centered at 292.5 is associated to the $1s-\sigma^*$ transitions in aromatics ($C=C$). The average and normalized spectra of *pixel class B* and *pixel class C* exhibit different ratio of $1s-\pi^*/1s-\sigma^*$ transitions. The peak at 290.4 eV is tentatively attributed to the $1s-\pi^*$ transition in carbonates and/or the $1s-4p$ transitions in alkyl carbon (C_nH_{2n+1}) [39]. The spectral feature centered at 288.5 eV is assigned to the $1s-\pi^*$ transitions in carboxyls ($-COOH$).

The average spectra of *pixel class D* (Figure 4.3 D) and *pixel class E* (Figure 4.3 E) are characterized by an intense feature centered at 290.4 eV attributed to the $1s-\pi^*$ transition in carbonates (CO_3). The absorption band centered at 285.5 eV corresponds to $1s-\pi^*$ transitions in aromatic and/or alkene groups ($C=C$). The absorption band centered at 287.3 eV is attributed to the overlap of $1s-\pi^*$ transitions in phenols ($Ar-OH$) and $1s-3p/\sigma^*$ transitions in aliphatic groups (C_xH_y). The peak at 288.5 eV is assigned to the $1s-\pi^*$ transitions in carboxyls ($COOH$). *Pixel class D* is characterized by the intense features centered at 297.4 eV and 299.4 eV, attributed to the potassium (K) L_3 and L_2 edges, respectively [40].

Pixel class F (Figure 4.3 F) and *pixel class G* (Figure 4.3 G) have a notably distinct chemical fingerprint. In the normalized average spectrum of *pixel class G* the dominant peak at 288.5 eV is tentatively attributed to the overlap of $1s-\pi^*$ in carboxyl groups ($-COOH$) and amide ($-C(=O)-N$) groups. The feature is shifted to 288.3 eV for *pixel class F* indicating the presence of solely amides ($-C(=O)-N$). The feature centered at 285.1 eV corresponds to the $1s-\pi^*$ transitions of carbon linked to another carbon ($C-C$). The peak at 290.4 eV is tentatively attributed to $1s-\pi^*$ transitions in carbonates (CO_3). The shoulder centered at 287.3 eV is attributed to the $1s-3p/\sigma^*$ in aliphatic carbon (C_xH_y) and/or the $1s-\pi^*$ transitions in phenols ($Ar-OH$) [41]. The peak at 286.7 eV is attributed to the $1s-\pi^*$ transitions in carbonyl groups ($C=O$) [42].

4.3.3 Charred peach stone sample

The hierarchical clustering analysis of the charred peach stone sample (Table 4.1 sample 2) hyperspectral data obtained via STXM and the normalized average carbon K-edge XANES spectra for each class, in the case of 15 classes, are displayed in Figure 4.5. Overall, all the pixel classes of the peach stone black sample analyzed are characterized by increased aromaticity;

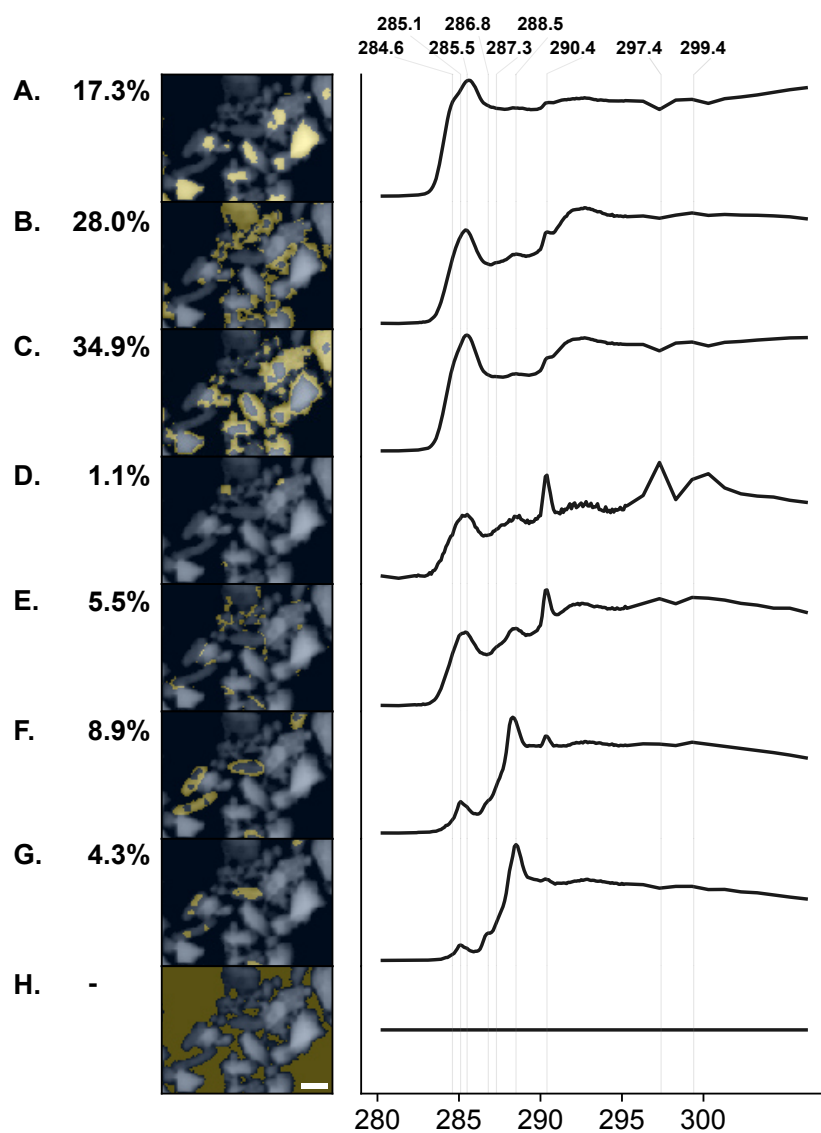


Figure 4.3: Hierarchical clustering analysis of the 7463 pre-selected carbon K-edge XANES spectra (as described in Data processing 4.2.2.2) obtained via STXM analysis of the charred date pits. Each image, A–H, represents the pixels (in yellow) belonging to the same class (chosen number of classes: eight classes) and the corresponding average carbon K-edge XANES spectra on the right. The percentage of pixels belonging to each class is calculated out of the pre-selected non-zero pixels. Scale bar, 1 μm .

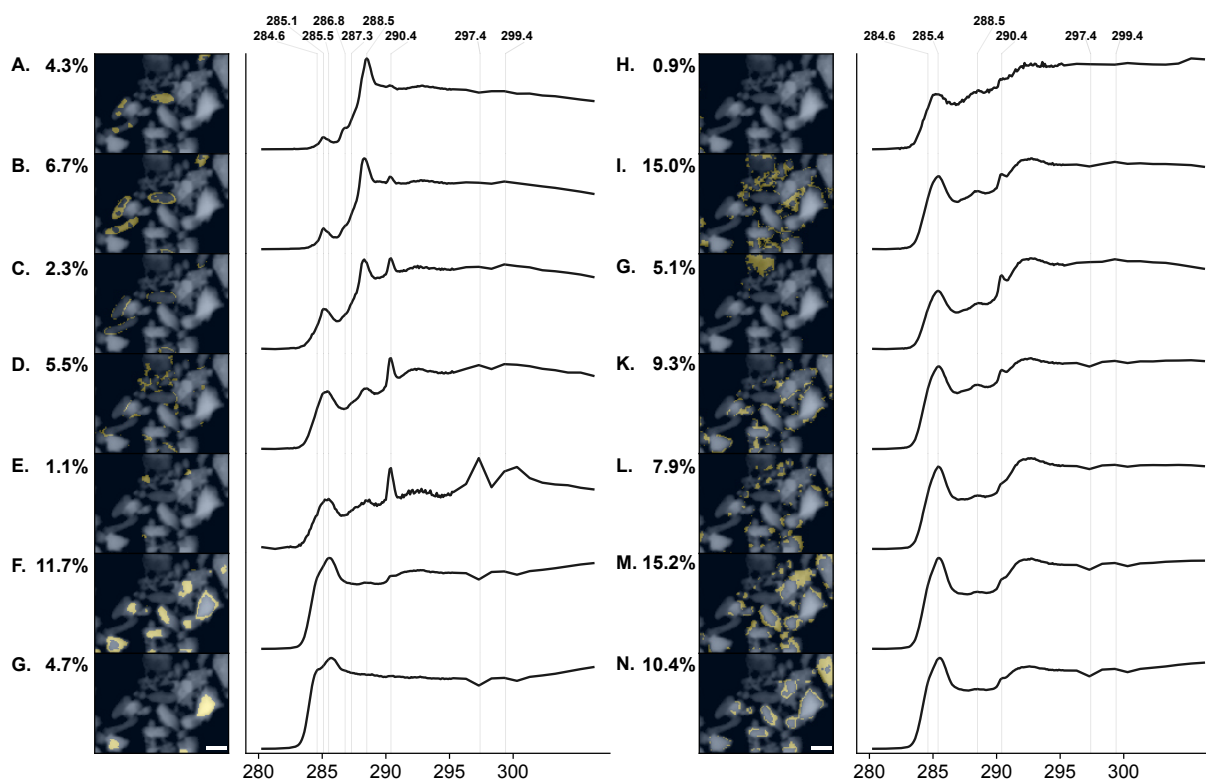


Figure 4.4: Hierarchical clustering analysis of the 7463 pre-selected carbon K-edge XANES spectra (as described in Data processing 4.2.2.2) obtained via STXM analysis of the charred date pits. Each image (A–N) represents the pixels (in yellow) belonging to the same class (chosen number of classes: fifteen classes) and the corresponding average carbon K-edge XANES spectra on the right. The class corresponding to the pre-selected pixels set to zero is not shown. The percentage of pixels belonging to each class is calculated out of the pre-selected non-zero pixels. Scale bar, 1 μm .

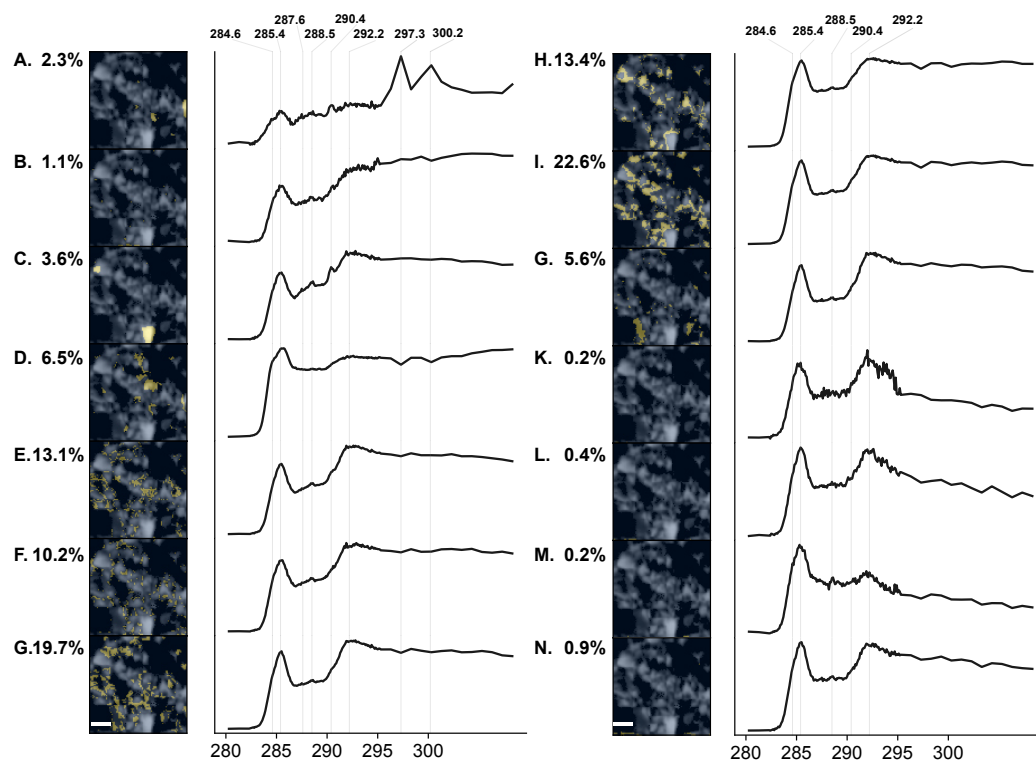


Figure 4.5: Hierarchical clustering analysis of the 6247 pre-selected carbon K-edge XANES spectra (as described in Data processing 4.2.2.2) obtained via STXM analysis of the charred peach stone. Each image (A–N) represents the pixels (in yellow) belonging to the same class (chosen number of classes: fifteen classes) and the corresponding average carbon K-edge XANES spectra on the right. The class corresponding to the pre-selected pixels set to zero is not shown. The percentage of pixels belonging to each class is calculated out of the pre-selected non-zero pixels. Scale bar, 1 μm .

the absorption band at 285.4 eV attributed to the $1s-\pi^*$ transitions in aromatic groups ($\text{C}=\text{C}$) is dominant [38]. For the majority of the pixel classes (Figure 4.5 C, E–N) the average carbon K-edge XANES spectra exhibit an increased structure at the $1s-\sigma^*$ transition in aromatic carbon ($\text{C}=\text{C}$) (292 to 295 eV), indicative of structural ordered polyaromatic structures [43]. *Pixel class C* (Figure 4.5 C) exhibit a peak at 290.4 eV assigned to the $1s-\pi^*$ transition in carbonates (CO_3) and/or the $1s-4p^*$ in alkyl carbon ($\text{C}_n\text{H}_{2n+1}$). An absorption band at 288.5 eV is attributed to $1s-\pi^*$ transitions in carboxyls ($-\text{COOH}$). The intensity of the bands assigned to carbonates and/or alkyl carbon and to carboxyls is decreasing in *pixel classes E–G* (Figure 4.5 E–G). The absorption band at 284.6 eV in the average spectrum of *pixel class D* (Figure 4.5 D) is attributed to $1s-\pi^*$ transitions in $\text{C}=\text{C}$ quinonic compounds [37]. The absorption band at 297.3 eV characteristic of *pixel class A*, is attributed to potassium L_3 edge [40].

4.3.4 Sticklac black sample

The hierarchical clustering analysis of the sticklac black (Table 4.1 sample 3) hyperspectral data obtained via STXM and the normalized average carbon K-edge XANES spectra for each class, in the case of 15 classes, are displayed in Figure 4.6. The presence of aromatic carbon ($1s-\pi^*$ transition at 285.3 eV) is notable for the sticklac black sample analyzed (Figure 4.6). The broadening of the band extending towards 284 indicates the presence of $1s-\pi^*$ transitions in quinonic compounds, which have lower energy π^* states [37, 42]. The broad absorption band at the energy range 286–288.7 eV present in *pixel classes A–D* (Figure 4.6 A–D) is possibly associated with oxygen containing and aliphatic groups; which are gradually decreasing in *pixel class E* (Figure 4.6 E) and *pixel class F* (Figure 4.6 F). The high percentage of inorganic phase, (*pixel classes A, G–N*) (Figure 4.6 A, G–N) is noteworthy. The presence of potassium is prominent in *pixel class A* and *pixel classes G–N* ($L_{3,2}$ edges at 297.3 eV and 299.4 eV respectively) [40]. The absorption band at 290.4 eV is attributed to the $1s-\pi^*$ transitions in carbonates (CO_3).

4.3.5 Bone black sample

The hierarchical clustering analysis of the bone black sample (Table 4.1 sample 4) hyperspectral data obtained via STXM and the normalized average carbon K-edge XANES spectra for each class, in the case of 15 classes, are displayed in Figure 4.7. A high percentage of the bone black pigment analyzed is characterized by the spectra C–F shown in Figure 4.7. The sharp peak at 290.3 eV is indicative of the $1s-\pi^*$ transitions in carbonate groups [40]. The feature centered around 350 eV, which corresponds to the Ca $L_{2,3}$ edge, is linked with the apatite structure in the bone. We expect that an energy scan with a finer step at the Ca $L_{2,3}$ -edge XANES region would exhibit two main features centered at 349.3 eV and 352.6 eV corresponding to the L_3 and L_2 edges of Ca [40, 44]. The feature centered at 288.5 eV is attributed to the overlap of $1s-\pi^*$ transitions in amide groups ($-C(=O)-N$) (e.g. peptide groups in proteins) and $1s-\pi^*$ in carboxyl groups ($-COOH$). The shoulder centered at 287.6 eV is attributed to the $1s-3p/\sigma^*$ transitions in aliphatic groups ($CxHy$). The small absorption band at 285.1 eV indicates the presence of aromatic and/or olefinic carbon ($1s-\pi^*$ transitions).

A small percentage (1%) of the analyzed bone black pigment (*pixel class A* shown in Figure 4.7 A) shows a chemical distinct spectral signature characterized by increased aromaticity.

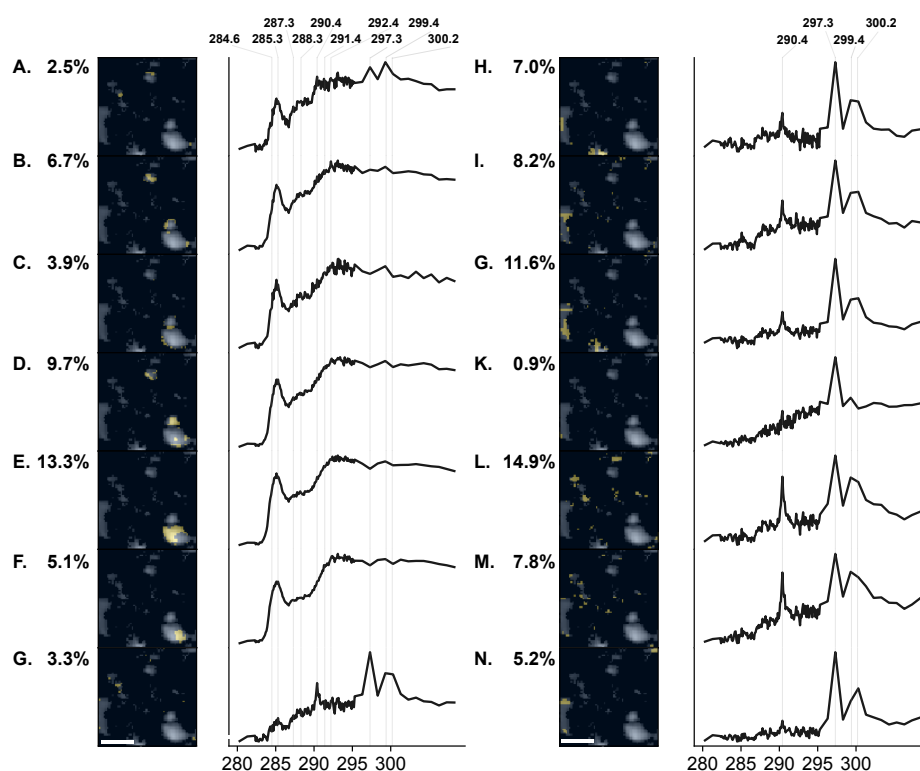


Figure 4.6: Hierarchical clustering analysis of the 632 pre-selected carbon K-edge XANES spectra (as described in Data processing 4.2.2.2) obtained via STXM analysis of the charred stick lac. Each image (A–N) represents the pixels (in yellow) belonging to the same class (chosen number of classes: fifteen classes) and the corresponding average carbon K-edge XANES spectra on the right. The class corresponding to the pre-selected pixels set to zero is not shown. The percentage of pixels belonging to each class is calculated out of the pre-selected non-zero pixels. Scale bar, 1 μm .

The dominant peak centered at 285.3 eV corresponds to $1s-\pi^*$ transitions in aromatic carbon. The increased structure of the feature at 292.4 eV attributed to the $1s-\sigma^*$ transition in aromatic carbon ($C=C$) indicates the presence of structural ordered polyaromatic structures [43]. The peak centered at 288.5 eV is attributed to the $1s-\pi^*$ transitions in amide ($-C(=O)-N$) and carboxyl ($-\text{COOH}$) groups [38]. The shoulder centered at 287.5 eV is attributed to the $1s-3p/\sigma^*$ transitions in aliphatic groups (C_xH_y). The peak at 290.3 eV indicates the presence of carbonates. The presence of the Ca edge is observed at ca. 350 eV.

The chemical distinct *pixel class B* shown in Figure 4.7 B, representing only the 0.2% of the analyzed area, is characterized by the mean spectrum 2. The $1s-\pi^*$ transitions ($C=C$) centered at 285.3 eV and the $1s-\sigma^*$ ($C=C$) at 292.4 eV reflect the aromatic nature of the region. The peak at 288.5 eV likely corresponds to joint contribution of $1s-\pi^*$ transitions in amide ($-C(=O)-N$) and carboxyl ($-\text{COOH}$) groups. The absence of a feature at 290.3 eV suggests the absence of carbonate minerals in the specific region.

4.3.6 Candle fume black sample

The hierarchical clustering analysis of the bone black sample (Table 4.1 sample 5) hyperspectral data obtained via STXM and the normalized average carbon K-edge XANES spectra for each class, in the case of 4 classes, are displayed in Figure 4.8. The candle fume black pigment analyzed is characterized by the intense feature at 290.4 eV attributed to the $1s-\pi^*$ in carbonates and/or the $1s-4p^*$ transitions in alkyl carbon. The intensity of the peak varies in the three *pixel classes A–C* of the sample shown in Figure 4.8. The higher the intensity of the absorption band at 290.4 eV (carbonates) the higher the absorption bands at 297.4 eV and 299.4 eV, attributed to the potassium (K) L_3 and L_2 edges, respectively. The average carbon K-edge XANES spectra of the three pixel classes of candle fume black are also characterized by the presence of $1s-\pi^*$ transitions in aromatic/alkene carbon ($C=C$) at 285.4 eV and the $1s-\pi^*$ transitions in carboxyl groups ($-\text{COOH}$) at 288.6 eV. A small shoulder centered at ≈ 287.4 eV is associated with the presence of $1s-\pi^*$ transitions in phenols ($\text{Ar}-\text{OH}$) [41] and/or the $1s-3p/\sigma^*$ transitions in aliphatic groups (C_xH_y).

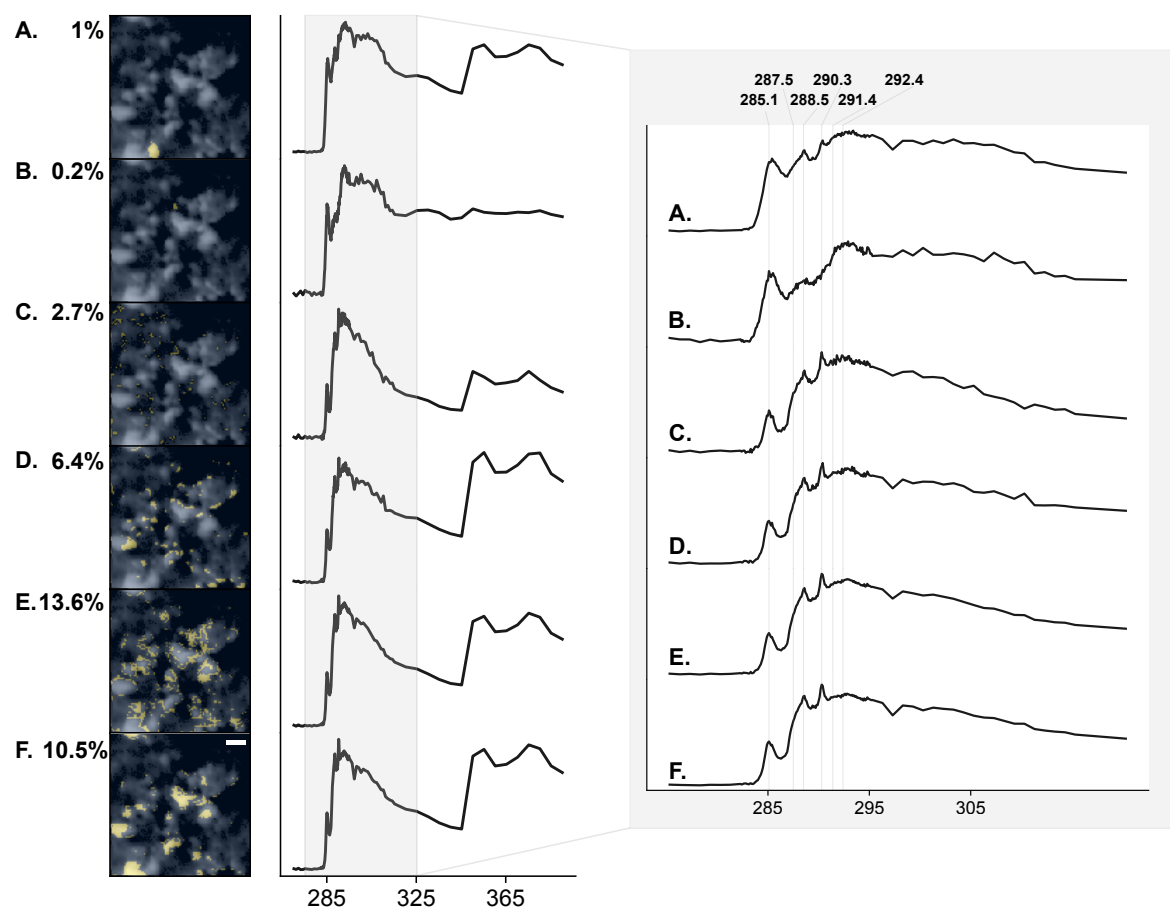


Figure 4.7: Hierarchical clustering analysis of the 11619 pre-selected carbon K-edge XANES spectra (as described in Data processing 4.2.2.2) obtained via STXM analysis of the bone black. Each image (A–F) represents the pixels (in yellow) belonging to the same class (chosen number of classes: fifteen classes) and the corresponding average carbon K-edge XANES spectra on the right. Only six out of the fifteen chosen classes are shown due to chemical similarity with the classes A–F. The percentage of pixels belonging to each class is calculated out of the pre-selected non-zero pixels. Scale bar, 1 μm .

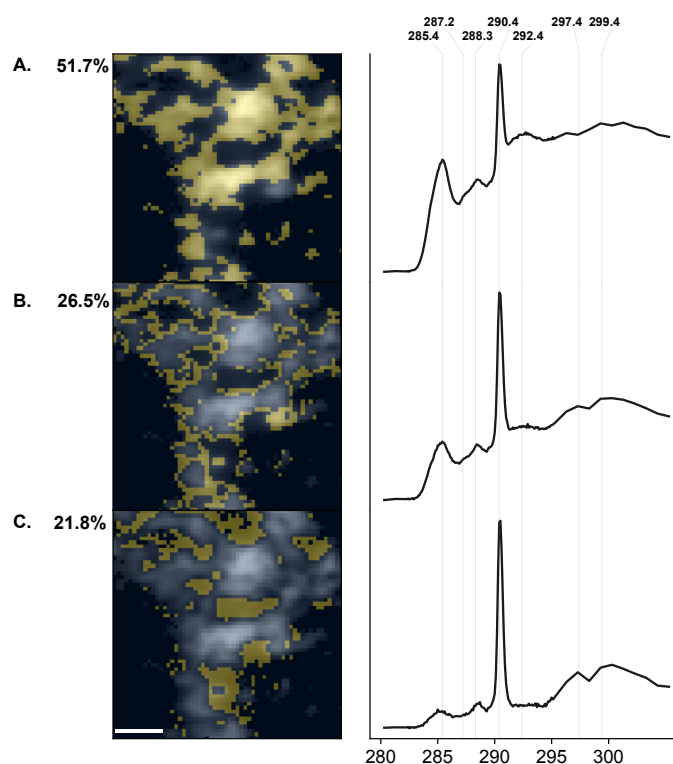


Figure 4.8: Hierarchical clustering analysis of the 2278 pre-selected carbon K-edge XANES spectra (as described in Data processing 4.2.2.2) obtained via STXM analysis of the candle fume black. Each image (A–C) represents the pixels (in yellow) belonging to the same class (chosen number of classes: four classes) and the corresponding average carbon K-edge XANES spectra on the right. The class corresponding to the pre-selected pixels set to zero is not shown. The percentage of pixels belonging to each class is calculated out of the pre-selected non-zero pixels. Scale bar, 1 μm .

4.3.7 Bister samples

The hierarchical clustering analysis of the bister sample (Table 4.1 sample 6) hyperspectral data obtained via STXM and the normalized average carbon K-edge XANES spectra for each class, in the case of 15 classes, are displayed in Figure 4.9. The average carbon K-edge XANES spectra of the *pixel classes* A–M (Figure 4.10 A–M) are characterized by the dominant peak at 288.6 eV attributed to the $1s-\pi^*$ transitions in carboxyl groups ($-\text{COOH}$), possibly linked with the decomposition products of lignin, such as vanillic acid (3-methoxy-4-hydroxybenzoic acid) and syringic acid (3,5-dimethoxy-4-hydroxybenzoic acid) [17]). The small absorption band at 285.2 eV is attributed to the $1s-\pi^*$ transitions in aromatic and/or alkene carbon ($\text{C}=\text{C}$) [38]. The shoulder centered at 287.4 eV is attributed to joint contribution of $1s-3p/\sigma^*$ transitions in aliphatic groups (C_xH_y) and $1s-\pi^*$ transitions in phenols ($\text{Ar}-\text{OH}$) [41], possible marker of methoxyphenols deriving from lignin. Lignin decomposes into guaiacol (2-methoxyphenol) and syringol (1,3-dimethoxyphenol) derivatives [17]. The absorption band at 286.5 eV is attributed to the $1s-\pi^*$ in furan derivatives (α -carbon $\text{C}-\text{O}$) [43, 45]. Furanose isomers and levoglucosan (1,6-anhydro- β -D-glucopyranose) are combustion/decomposition products of cellulose and hemicellulose and are considered accountable for the stickiness and hygroscopicity of bister [17, 46]. The intensity of the absorption bands at 286.5 eV varies in different pixel classes (see Figure 4.10). The sharp absorption band centered at 290.5 eV prominent at the average spectra of *pixel classes* A–D (Figure 4.10 A–D) is attributed to the $1s-4p$ transitions in alkyl carbon (C_nH_{n+1}) [39, 47]. The absorption band at 289.6 eV is assigned to the $1s-3p/\sigma^*$ in alcohols $\text{C}-\text{OH}$ [39].

The spectral differences between the bister sample prepared by Birgit Reissland (Table 4.1 sample 6) and the commercial pigment supplied from Kremer (Table 4.1 sample 7) are significant (Figure 4.12: *spectra* 6, 7), which indicates differences in the preparation procedure and/or the raw material used.

4.3.8 Carbon black sample

The carbon chemistry of the flame carbon pigment examined (Table 4.1 sample 8) appears quite homogeneous (hierarchical clustering analysis of the STXM energy stack is not shown). The average carbon K-edge XANES spectra of carbon black (see Figures 4.12, 4.13 spectrum 8)

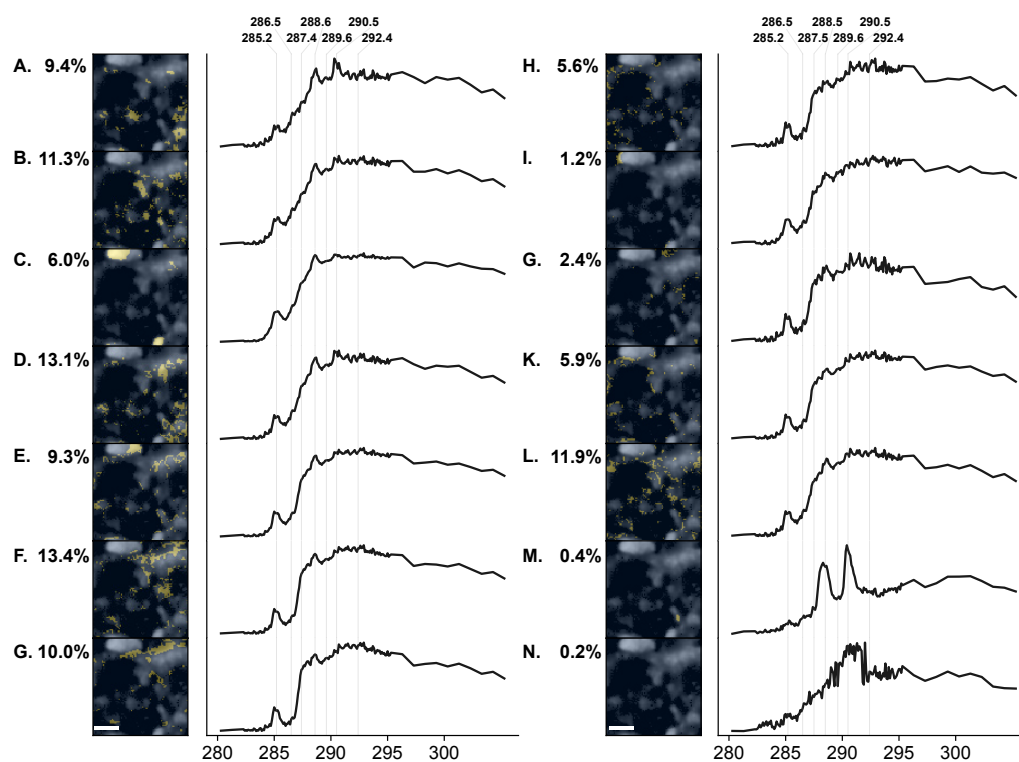


Figure 4.9: Hierarchical clustering analysis of the 3604 pre-selected carbon K-edge XANES spectra (as described in Data processing 4.2.2.2) obtained via STXM analysis of the bister. Each image (A–N) represents the pixels (in yellow) belonging to the same class (chosen number of classes: fifteen classes) and the corresponding average carbon K-edge XANES spectra on the right. The class corresponding to the pre-selected pixels set to zero is not shown. The percentage of pixels belonging to each class is calculated out of the pre-selected non-zero pixels. Scale bar, 1 μm .

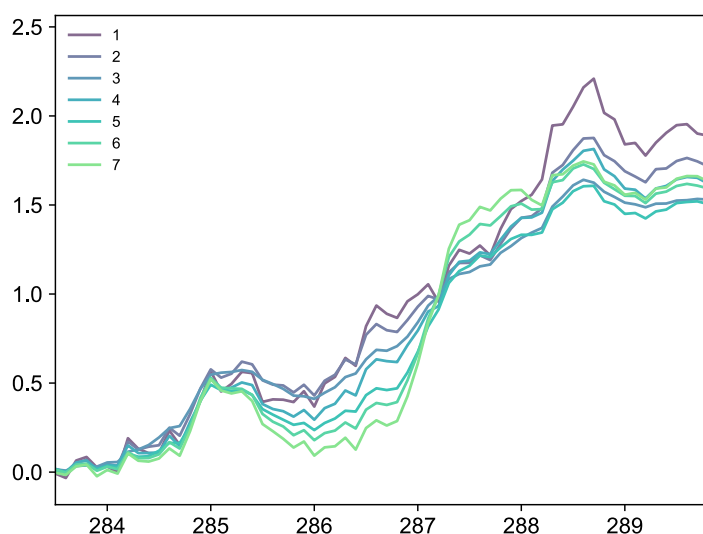


Figure 4.10: Comparison of the average spectra 1–7 obtained via hierarchical clustering analysis of the STXM data of bister sample as presented in Figure 4.9. Note the decrease of the absorption band at 286.5 eV attributed to the $1s-\pi^*$ in furan derivative compounds (α -carbon C–O)[45], markers of cellulose/hemicellulose degradation [17, 43].

is characterized by the $1s-\pi^*$ transitions in aromatics centered at 285.3 eV. The increased structure of the $1s-\sigma^*$ transitions in the 292–295 eV region suggests the presence of polyaromatic moieties [43]. The presence of aromatic carboxylic acids is implied by the peak centered at 288.4 eV which is attributed to $1s-\pi^*$ transitions in carboxyl groups bonded to unsaturated carbon [48]. The shoulders centered at 287.3 eV and 290.5 eV are attributed to the $1s-3p/\sigma^*$ transitions in aliphatic groups (C_xH_y) and/or the $1s-4p$ transitions in alkyl carbon (C_nH_{2n+1}) respectively [39, 47].

4.3.9 Vine black sample

The hierarchical clustering analysis of the vine black sample (Table 4.1 sample 9) hyperspectral data obtained via STXM and the normalized average carbon K-edge XANES spectra for each class, in the case of 15 classes, are displayed in Figure 4.11. The absorption band at 284 eV in the chemical distinct *pixel class A* is indicating the presence of quinonic compounds [49]. The band at 288.5 eV, characteristic of the *classes A–C* and *class F*, is attributed to the $1s-\pi^*$ transitions in carboxyl ($-\text{COOH}$) groups. The absorption band at 286.6 eV associated with carbonyl groups, possibly attributed to the $1s-\pi^*$ in furan derivatives (α -carbon C–O) [43, 45]

(combustion/decomposition products of cellulose and hemicellulose) is present only in *classes A–C*. In *classes B,C* the band centered at 285.2 eV is attributed to $1s-\pi^*$ in aromatic and/or alkene carbon ($C=C$). In *class G* the broad $1s-\pi^*$ transition band at 285.2 eV, extending towards 284 eV and 286 eV indicate the presence of quinone-like compounds [42, 49].

Classes H–N are characterized by an intense feature at 285.1 eV attributed to $1s-\pi^*$ transitions in aromatic carbon. The distinct structure of the band at 292.4 eV which arises from the $1s-\sigma^*$ transitions indicates the presence of polyaromatic compounds ($C=C$) [42, 43]. The lack of a sharp $1s-\sigma^*$ exciton peak between 291–292 eV indicate the presence of smaller graphene sheets [42]. The notable feature at 287.6 eV is attributed to the $1s-3p/\sigma^*$ transitions in aliphatic groups (C_xH_y). FT-IR data collected by Lluveras-Tenorio et al. [5] confirm the presence of aromatics (1595 cm^{-1} , 1430 cm^{-1} ; $\nu C-C$) and aliphatics (2980 cm^{-1} , 2920 cm^{-1} , 2850 cm^{-1} ; $\nu C-H$) in the vine black Kremer commercial pigment originating from the pyrolysis of cellulose and lignin [5].

4.4 Discussion

4.4.1 Nano-scale heterogeneity of the dark-coloured organic pigments

For each dark-coloured organic pigment, STXM analysis provides meaningful, interpretable spatially resolved spectroscopic data at the carbon K-edge. STXM nanoscale mapping of the analysed pigments reveals an heterogeneous carbon signature at the nanoscale, a behaviour that cannot be observed at the microscale, neither via bulk XRS speciation analysis nor by averaging the STXM signal. The hierarchical clustering analysis of the hyperspectral STXM data successfully identifies the distribution of different organic phases in the analysed samples, possibly a result of the non-homogeneous transformation of the precursor materials during the manufacture process.

4.4.2 The importance of the precursor material and manufacture process in the pigment's final chemistry

Each pigment results from the pyrolysis or combustion of precursor organic materials and the manufacture process leads to their heat-induced transformation. Understanding the physico-chemical processes that take place during the precursor materials' transformation, retrieving

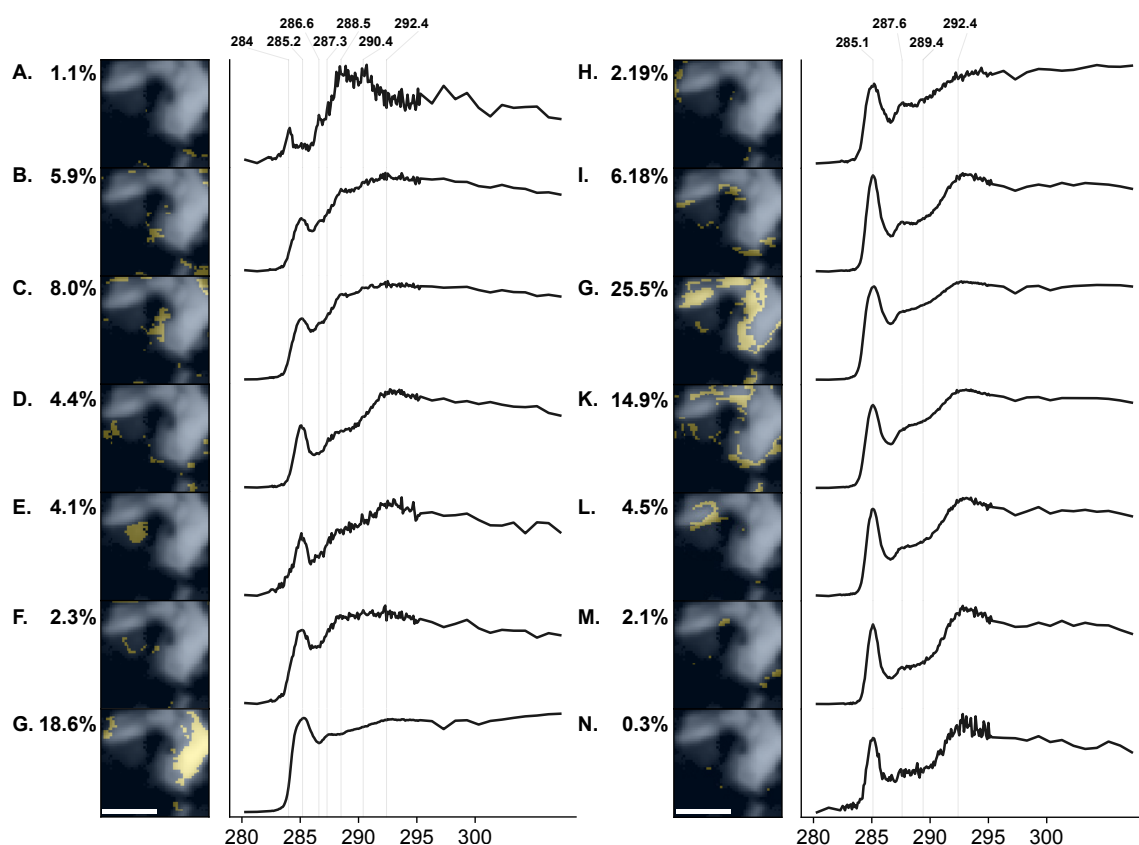


Figure 4.11: Hierarchical clustering analysis of the 1505 pre-selected carbon K-edge XANES spectra (as described in Data processing 4.2.2.2) obtained via STXM analysis of the vine black. Each image (A–N) represents the pixels (in yellow) belonging to the same class (chosen number of classes: fifteen classes) and the corresponding average carbon K-edge XANES spectra on the right. The class corresponding to the pre-selected pixels set to zero is not shown. The percentage of pixels belonging to each class is calculated out of the pre-selected non-zero pixels. Scale bar, 1 μm .

information on precursor materials' chemistry, and documenting the final chemistry of the pigment is important if aiming in the identification of the pigments in complex heritage artworks.

Our results show that for each pigment the degree of heterogeneity (i.e. the percentage of pixels having distinct chemical signatures) varied and it is possibly linked with the pigments' manufacture conditions, indicating a non-homogeneous transformation of the precursor materials during pyrolysis or combustion of the sample. Various studies report the connection between the temperature and the chemical transformation of the precursor organic material during pyrolysis or combustion [5, 20, 42, 50]. The heating temperature applied may obstruct the identification of the resulting pigment in more complex heritage artifacts. Prolongated heating or high temperature results in the complete transformation of the pigment's chemistry into polyaromatic structures which makes their discrimination based on the chemistry of the precursor materials impossible. The lower the temperature applied the higher the possibility to trace the original chemistry of the precursor material.

Winter and FitzHugh [1] documented and classified the artists' pigments based on carbon either according to their manufacture process (i.e. graphite, charred materials, flame carbons, cokes) or their source/precursor material (i.e. pigments of vegetable origin, animal origin, soots and smokes, graphitic pigments, black earths') [1, 2]. Date stone, peach stone, and vine black belong to the wide category of vegetable chars. Their names denote the diversity of starting materials [1]. Chemically complex biomass-derived chars are the solid residues of incomplete combustion [42]. The chemical transformation of charred biomass is highly linked to the charring temperature. Increasing the temperature leads to the formation of aromatic ring structures followed by the condensation of aromatic units into larger conjugated sheets; thus an increased aromaticity is observed. The breakdown of the raw material appearing at different temperatures depends on its composition; the relative quantities of biopolymers (precursor materials) in the raw plant material determines the charring conditions to yield *transition chars* [42].

Keiluweit et al. suggests the categorization of chars according to their unique physico-chemical states [42]: (i) the *transition chars* in which the native crystalline entity of the plant biopolymers (i.e precursor materials: cellulose, hemicellulose, lignin) is preserved, (ii) the *amorphous chars* in which the heat-induced altered materials co-exist with the developing aro-

matic polycondensates, (iii) the *composite chars* consisting of poorly ordered graphene layers embedded in amorphous phases, and (iv) the *turbostratic chars* characterized by the presence of disordered graphitic crystallites. FT-IR analysis of wood and grass chars evolution as a function of temperature indicate that no chemical changes occur in the range between 100–200 °C, the dehydration of cellulose and lignin starts at 300 °C, the transformation of precursor materials (lignin/cellulose) occurs at 400 °C and the degree of condensation is increasing at 500 °C and beyond [42].

According to Reidsma et al. thermal degradation of collagen (in bone) under reducing conditions initiates at 200°C and results in its conversion into alkylated benzenes, phenols and condensed aromatic compounds (300-340°C). However, the complete transformation of collagen into polyaromatic compounds occurs at higher temperatures [20, 50]. The low percentage of polyaromatic signatures in the carbon K-edge average spectra (only in *pixel clusters A,B*) of the bone black analyzed is an indicator of the low heating temperature of the sample. The heat-induced alteration under reducing conditions of both proteins (i.e. bone) and polysaccharides (i.e. wood constituent) results into solid residues of aromatic nature. Increasing temperature (>400°C) results in increased ordering and formation of polyaromatic planar sheets in both charred bone and charred wood which can make their discrimination challenging, if based only in the organic phase of the charred bone.

4.4.3 Comparison of soft-XAS and XRS carbon K-edge spectra

XRS is a hard x-ray probe which, to first approximation, has the same spectral information as XANES (see *Chapter 1*). Figure 4.12 presents the average carbon K-edge XANES data of the organic pigments summarized at Table 4.1, collected via scanning transmission x-ray microscopy (STXM) (in black color) and x-ray Raman spectroscopy (in red color). Figure 4.13 compares the spectroscopic XRS and STXM data of commercial bister (Kremer), carbon black (national bureau of standards) and commercial vine black (Kremer). The spectral differences observed are mainly attributed to the lower energy resolution of the XRS data acquired at GALAXIES beamline in 2018. The bulk-sensitive XRS data are collected with lower energy resolution (≈ 1.2 eV, due to instrumental constraints at the GALAXIES beamline at the time when the experiments were performed) compared to STXM data (≈ 0.3 eV) which results in averaging of the spectral features and makes their chemical characterization harder. With the

availability of powerful synchrotron sources and efficient new x-ray spectrometers [35, 51–53], the application of XRS as a bulk-sensitive probe of light elements has burgeoned [54–57] and an energy resolution comparable with STXM can now be achieved (see Chapter 2).

As hard x-rays penetrate deep into the sample, XRS overcomes several difficulties related to the soft x-ray probe of conventional low-Z XAS techniques, where the samples have to be either specifically prepared or altered (i.e. samples transparent to x-rays at the transition energy of the element of interest), often in an invasive manner which may be risky to the sample, or studied in a vacuum chamber. XRS spectral shape is not affected by self-absorption processes, contrary to soft x-rays studies in which spectral saturation can be observed due to self-absorption.

While the bulk sensitivity of the hard x-ray probe has practical advantages, by averaging the signal over larger volume, XRS is not sensitive to spatially resolve nanoscale heterogeneity. The nanometric lateral resolution of STMX cannot be reached. The co-existence of heterogeneous organic phases observed at the nanoscale could not be resolved with the micrometric (\approx tens of microns) resolution of the 2D or 3D XRS imaging. STXM allowed nanoscale characterization of the dark-coloured organic samples which shed light to their chemical complexity. Overall, STXM consists of a powerful and complementary probe for the characterization of complex organic systems.

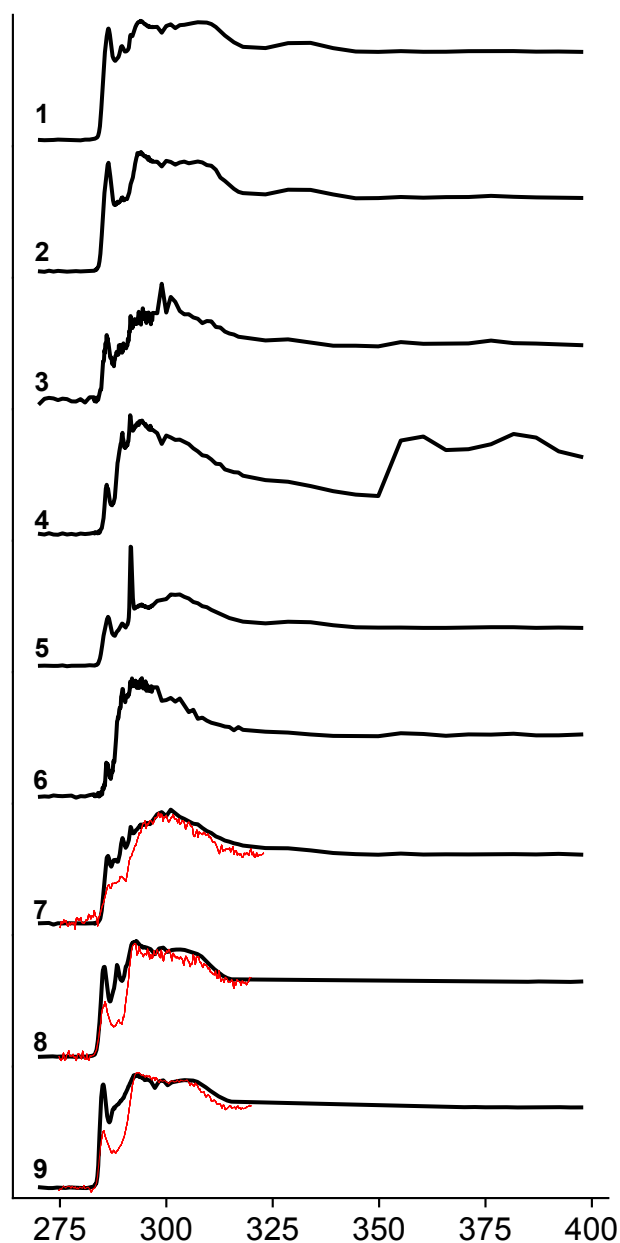


Figure 4.12: Normalized average STXM spectra of organic pigments. 1, Date pits charred; 2, Peach pits charred; 3, Stick lac charred; 4, Lamp feet bones charred; 5, Candle fume black; 6, Bister; 7, Commercial bister (Kremer); 8, Carbon black (National bureau of standards); 9, Commercial vine black (Kremer). In red color are the bulk XRS carbon K-edge spectra (spectra 7,8,9) collected with lower energy resolution (1.2 eV).

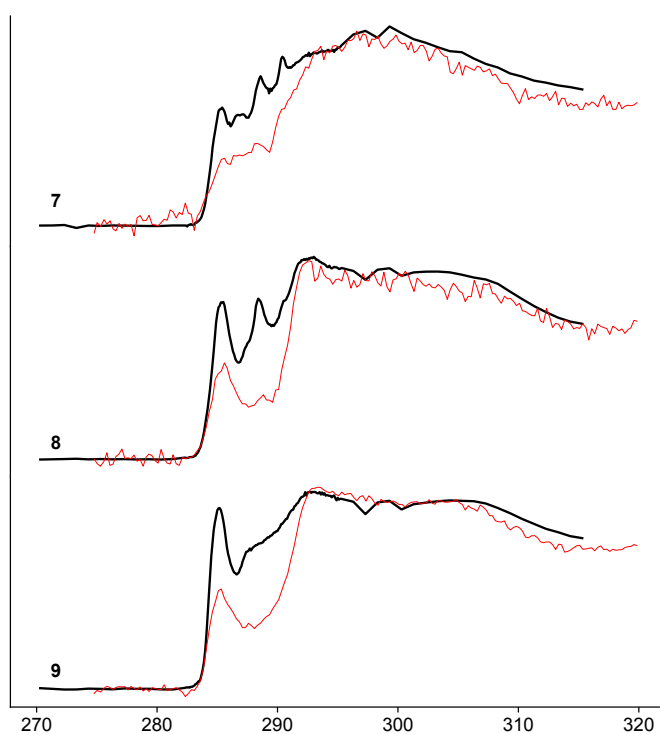


Figure 4.13: Comparison of STXM (black) and XRS (red) carbon K-edge spectra of organic pigments. 7, Commercial bistar (Kremer); 8, Carbon black (National bureau of standards); 9, Commercial vine black (Kremer). Note the averaging of the spectral features in the low energy resolution XRS spectra (1.2 eV).

References

- [1] John Winter and E West FitzHugh. "Pigments based on carbon". In: *Artists' pigments 4* (2007), pp. 1–37.
- [2] John Winter. "The characterization of pigments based on carbon". In: *Studies in Conservation* 28.2 (1983), pp. 49–66.
- [3] Marika Spring, Rachel Grout, and Raymond White. "'Black Earths': A Study of Unusual Black and Dark Grey Pigments used by Artists in the Sixteenth Century". In: *National Gallery Technical Bulletin* 24 (2003), pp. 96–114.
- [4] Eugenia Tomasini, Gabriela Siracusano, and Marta Silvia Maier. "Spectroscopic, morphological and chemical characterization of historic pigments based on carbon. Paths for the identification of an artistic pigment". In: *Microchemical Journal* 102 (2012), pp. 28–37.
- [5] Anna Lluveras-Tenorio et al. "A multi-analytical characterization of artists' carbon-based black pigments". In: *Journal of Thermal Analysis and Calorimetry* 138.5 (2019), pp. 3287–3299.
- [6] Pierre-Olivier Autran et al. "Revealing the Nature of Black Pigments Used on Ancient Egyptian Papyri from Champollion Collection". In: *Analytical Chemistry* (2020).
- [7] Eugenia P Tomasini et al. "Micro-Raman spectroscopy of carbon-based black pigments". In: *Journal of Raman Spectroscopy* 43.11 (2012), pp. 1671–1675.
- [8] Anna Lluveras-Tenorio et al. "The development of a new analytical model for the identification of saccharide binders in paint samples". In: *PLoS One* 7.11 (2012).
- [9] Nathan S Daly et al. "Multivariate analysis of Raman spectra of carbonaceous black drawing media for the in situ identification of historic artist materials". In: *Journal of Raman Spectroscopy* 49.9 (2018), pp. 1497–1506.
- [10] Donald C. Fels et al. *Lost Secrets of Flemish Painting: Including the First Complete English Translation of the De Mayerne Manuscript, B.M. Sloane 2052*. Alchemist, 2010.

- [11] Jenny Boulboulle. “Drawn up by a learned physician from the mouths of artisans: The Mayerne manuscript revisited”. In: *Netherlands Yearbook for History of Art/Nederlands Kunsthistorisch Jaarboek Online* 68.1 (2019), pp. 204–249.
- [12] Winfried Schülke. *Electron dynamics by inelastic X-ray scattering*. Vol. 7. Oxford University Press, 2007.
- [13] Donald C Fels et al. *Lost secrets of Flemish painting, including the first complete English translation of the De Mayerne Manuscript, BM Sloane 2052*. Eijsden, the Netherlands: Alchemist, 2004.
- [14] Valentin Boltz. *Illuminierbuch: wie man allerlei Farben bereiten, mischen und auftragen soll: allen jungen angehenden Malern und Illuministen nützlich und förderlich*. Sändig, 1913.
- [15] Ernest John Parry and John Henry Coste. *The chemistry of pigments*. Scott, Greenwood, 1902.
- [16] Carl Friedrich August Hochheimer. *Chemische Farben-Lehre oder ausführlicher Unterricht von Bereitung der Farben zu allen Arten der Malerey*. Vol. 1. Gräff, 1803.
- [17] Ursula Baumer et al. “On the Use of Bistre in Transparent Wood Varnishes: Analysis, Application and Reconstruction”. In: *Studies in Conservation* 64.sup1 (2019), S115–S125.
- [18] Rosamond Drusilla Harley. “Artists’ pigments, c. 1600-1835; a study in English documentary sources”. In: (1982).
- [19] Janine Walcher, Heike Stege, Bayerische Staatsgemäldesammlung, et al. *Let the material talk: technology of late-medieval Cologne panel painting*. 2014.
- [20] Femke H Reidsma et al. “Charred bone: Physical and chemical changes during laboratory simulated heating under reducing conditions and its relevance for the study of fire use in archaeology”. In: *Journal of Archaeological Science: Reports* 10 (2016), pp. 282–292.
- [21] Adele L Boskey. “Mineralization of bones and teeth”. In: *Elements* 3.6 (2007), pp. 385–391.
- [22] Stephen Weiner. *Microarchaeology: beyond the visible archaeological record*. Cambridge University Press, 2010.

- [23] Jill Dill Pasteris, Claude H Yoder, and Brigitte Wopenka. “Molecular water in nominally unhydrated carbonated hydroxylapatite: The key to a better understanding of bone mineral”. In: *American Mineralogist* 99.1 (2014), pp. 16–27.
- [24] Brigitte Wopenka and Jill D Pasteris. “A mineralogical perspective on the apatite in bone”. In: *Materials Science and Engineering: C* 25.2 (2005), pp. 131–143.
- [25] David Buti et al. “Picasso’s Acrobat Family in focus: an investigation of materials and techniques of an iconic work in the collection of the Gothenburg Museum of Art”. In: *SN Applied Sciences* 2.8 (2020), pp. 1–9.
- [26] Nicholas Eastaugh, ed. *Pigment compendium: a dictionary and optical microscopy of historical pigments*. eng. New ed. OCLC: 845288553. Amsterdam: Elsevier, Butterworth-Heinemann, 2008. ISBN: 9780750689809.
- [27] Purnendu Kumar Bose. “Chemistry of lac”. In: *J. Inst. Chem. India* 25 (1963), pp. 83–98.
- [28] KK Sharma, A Roy Chowdhury, and S Srivastava. “Chemistry and Applications of Lac and Its By-Product”. In: *Natural Materials and Products from Insects: Chemistry and Applications*. Springer, 2020, pp. 21–37.
- [29] Julie Cosmidis and Karim Benzerara. “Soft X-ray scanning transmission spectro-microscopy”. In: *Biom mineralization sourcebook: Characterization of biominerals and biomimetic materials* (2014), pp. 115–133.
- [30] Rachid Belkhou et al. “HERMES: a soft X-ray beamline dedicated to X-ray microscopy”. In: *Journal of Synchrotron Radiation* 22.4 (2015), pp. 968–979.
- [31] Adam Hitchcock. *aXis 2000 – Analysis of X-ray Images and Spectra*. URL: <http://unicorn.mcmaster.ca/aXis2000.html> (visited on 04/22/2021).
- [32] F. Pedregosa et al. “Scikit-learn: Machine Learning in Python”. In: *Journal of Machine Learning Research* 12 (2011), pp. 2825–2830.
- [33] Pauli Virtanen et al. “SciPy 1.0: Fundamental Algorithms for Scientific Computing in Python”. In: *Nature Methods* 17 (2020), pp. 261–272. DOI: 10.1038/s41592-019-0686-2.

- [34] Loïc Bertrand et al. "Identification of the finishing technique of an early eighteenth century musical instrument using FTIR spectromicroscopy". In: *Analytical and bioanalytical chemistry* 399.9 (2011), pp. 3025–3032.
- [35] Jean-Pascal Rueff et al. "The GALAXIES beamline at the SOLEIL synchrotron: inelastic X-ray scattering and photoelectron spectroscopy in the hard X-ray range". In: *Journal of synchrotron radiation* 22.1 (2015), pp. 175–179.
- [36] James Michael Ablett et al. "The GALAXIES inelastic hard X-ray scattering end-station at Synchrotron SOLEIL". In: *Journal of Synchrotron Radiation* 26.1 (2019), pp. 263–271.
- [37] JT Francis and Adam P Hitchcock. "Inner-shell spectroscopy of p-benzoquinone, hydroquinone, and phenol: distinguishing quinoid and benzenoid structures". In: *The Journal of Physical Chemistry* 96.16 (1992), pp. 6598–6610.
- [38] Corentin Le Guillou et al. "XANES-based quantification of carbon functional group concentrations". In: *Analytical Chemistry* 90.14 (2018), pp. 8379–8386.
- [39] Sylvain Bernard et al. "Geochemical evolution of organic-rich shales with increasing maturity: A STXM and TEM study of the Posidonia Shale (Lower Toarcian, northern Germany)". In: *Marine and Petroleum Geology* 31.1 (2012), pp. 70–89.
- [40] Karim Benzerara et al. "Scanning transmission X-ray microscopy study of microbial calcification". In: *Geobiology* 2.4 (2004), pp. 249–259.
- [41] JL Solomon, Robert J Madix, and Joachim Stöhr. "Orientation and absolute coverage of benzene, aniline, and phenol on Ag (110) determined by NEXAFS and XPS". In: *Surface Science* 255.1-2 (1991), pp. 12–30.
- [42] Marco Keiluweit et al. "Dynamic molecular structure of plant biomass-derived black carbon (biochar)". In: *Environmental science & technology* 44.4 (2010), pp. 1247–1253.
- [43] Luke JR Higgins et al. "X-ray Raman scattering for bulk chemical and structural insight into green carbon". In: *Physical Chemistry Chemical Physics* 22.33 (2020), pp. 18435–18446.
- [44] Julie Cosmidis et al. "Characterization of Ca-phosphate biological materials by scanning transmission X-ray microscopy (STXM) at the Ca L_{2, 3}, P L_{2, 3}-and C K-edges". In: *Acta biomaterialia* 12 (2015), pp. 260–269.

- [45] M Mauerer et al. “Resonant excitation and decay of core holes in condensed layers of furan and pyrrole”. In: *The Journal of chemical physics* 99.5 (1993), pp. 3343–3352.
- [46] Bernd RT Simoneit et al. “Levoglucosan, a tracer for cellulose in biomass burning and atmospheric particles”. In: *Atmospheric Environment* 33.2 (1999), pp. 173–182.
- [47] George D Cody et al. “Determination of chemical-structural changes in vitrinite accompanying luminescence alteration using C-NEXAFS analysis”. In: *Organic Geochemistry* 28.7-8 (1998), pp. 441–455.
- [48] Dawit Solomon et al. “Carbon (1s) NEXAFS spectroscopy of biogeochemically relevant reference organic compounds”. In: *Soil Science Society of America Journal* 73.6 (2009), pp. 1817–1830.
- [49] J. T. Francis and Adam P Hitchcock. “Inner-shell spectroscopy of p-benzoquinone, hydroquinone, and phenol: distinguishing quinoid and benzenoid structures”. In: *The Journal of Physical Chemistry* 96.16 (1992), pp. 6598–6610. doi: 10 . 1021 / j100195a018.
- [50] Annelies van Hoesel et al. “Combusted bone: Physical and chemical changes of bone during laboratory simulated heating under oxidising conditions and their relevance for the study of ancient fire use”. In: *Journal of Archaeological Science: Reports* 28 (2019), p. 102033.
- [51] Dimosthenis Sokaras et al. “A high resolution and large solid angle x-ray Raman spectroscopy end-station at the Stanford Synchrotron Radiation Lightsource”. In: *Review of Scientific Instruments* 83.4 (2012), p. 043112.
- [52] Simo Huotari et al. “A large-solid-angle X-ray Raman scattering spectrometer at ID20 of the European Synchrotron Radiation Facility”. In: *Journal of Synchrotron Radiation* 24.2 (2017), pp. 521–530.
- [53] Christopher Weis et al. “Combining X-ray $K\beta$ 1, 3, valence-to-core, and X-ray Raman spectroscopy for studying Earth materials at high pressure and temperature: the case of siderite”. In: *Journal of analytical atomic spectrometry* 34.2 (2019), pp. 384–393.

- [54] Uwe Bergmann et al. “Carbon K-edge X-ray Raman spectroscopy supports simple, yet powerful description of aromatic hydrocarbons and asphaltenes”. In: *Chemical physics letters* 369.1-2 (2003), pp. 184–191.
- [55] Uwe Bergmann and Oliver C Mullins. “Carbon X-ray Raman spectroscopy of PAHs and asphaltenes”. In: *Asphaltenes, Heavy Oils, and Petroleomics*. Springer, 2007, pp. 139–155.
- [56] Ulrike Boesenberg et al. “Electronic structure changes upon lithium intercalation into graphite—Insights from ex situ and operando x-ray Raman spectroscopy”. In: *Carbon* 143 (2019), pp. 371–377.
- [57] Andrew E Pomerantz et al. “Electronic Structure of Naturally Occurring Aromatic Carbon”. In: *Energy & fuels* 33.3 (2019), pp. 2099–2105.

Conclusions and Perspectives

The present study has been one of the first attempts to thoroughly examine the prospects of x-ray Raman scattering as a non-invasive probe for the study of heritage materials. We focus on complex organic systems, which present multi-scale heterogeneity due to chemical composition spatial variations, difference in relative abundance of their individual components (e.g. organic phases present as a minor component), or complex chemical composition (consisting of differing chemical groups) in the volume probed. The investigation of organic heritage materials via XRS uncloaks their chemical complexity and multi-scale heterogeneity. XRS interrogates carbon and oxygen speciation in complex organic systems, without invasive and/or surface limited methods. A historic collection of well-preserved native Australian plant exudates, assembled a century ago by plant naturalists, is studied using a two-modal approach. The combined analysis of the XRS and FT-IR spectral features provides a fundamental understanding of the bonding and the functional group information, thus it favours the chemical characterization of the natural materials long used by Aboriginal Australian peoples. XRS operating as a non-invasive 3D imaging technique is prove useful in expanding our understanding of organic-rich heterogeneous heritage materials. XRS carbon K-edge tomographic images of an exceptionally preserved specimen, a 53 million-year old insect entrapped in amber, determine organic signatures and trace their evolution through time. Contrasts observed in the specimen indicate the presence of different chemical species, a result of diagenesis over time. When the limitation of XRS spatial resolution is reached, STXM is an alternative soft x-ray probe for the nanometric carbon speciation of chemically complex materials. Organic dark-coloured art pigments studied via STXM showed a non-homogeneous nanoscale distribution of organic phases, possibly a result of their manufacture process.

Providing insights into the organic chemistry of precious samples without specific preparation and under ambient conditions, via spot or three-dimensional analysis, is a critical advantage of this hard x-ray bulk probe. Yet, the long acquisition times due to low efficiency of the non-resonant inelastic scattering process, can obstruct the acquisition of meaningful spectra. The development of highly-efficient spectrometers, consisting of multiple analyzers, can effectively reduce acquisition time. Prolonged radiation exposure induces side effects that cause

damage to the sample (e.g. discoloration, melting, decomposition, formation of new chemical bonds). The precise conditions for minimizing the radiation-induced damage in precious heritage samples remain to be elucidated. A further study could assess the benefits of using cryogenic and anaerobic conditions, and defocusing the beam in the vertical direction using the so-called 2D sectioning mode. The increase in the x-ray incident energy (6-15 keV) has a double benefit: the reduce of the photoelectric cross section while increasing the penetration depth and the XRS signal intensity. The incident beam intensity restricts the penetration length, the sample size and composition. In point analysis or 2D imaging, the detection of organic traces in an heterogeneous sample may be hampered by the presence of heavy elements, which reduce the scattering volume due to absorption. XRS has limited spatial resolution compared to other imaging techniques, such as absorption or phase-contrast computed tomography (CT) and scanning transmission x-ray microscopy. Notwithstanding this limitations, XRS yields 3D bonding information of light elements, in a non-invasive manner.

Overcoming the existing challenges and advance future developments in XRS methodology and instrumentation, will facilitate the study of organic heterogeneous materials in numerous fields of research, including geosciences, life sciences, materials science and heritage science.

Supplementary information for Chapter 2

A.1 Materials and Methods

A.1.1 Materials

A sample-set of native Australian plant genera (*Eucalyptus*, *Callitris*, *Xanthorrhoea*, *Acacia*), summarized in Table 1 were analyzed. The samples were selected from South Australian Museum (SAM) collections and a historical biological collection gathered from diverse locations across Australia and held for years in the South Australia state forensic laboratory (Forensic Sciences South Australia-FSSA) and now located at Flinders University. Unfortunately the collectors of this exceptional comprehensive collection are unknown and the original data notebooks no longer exist; however, each amber jar is clearly labeled with the collection location and date. Many of these samples in the historical biological collection are over a century old and have been stored in amber glass bottles under ambient conditions and offer an unprecedented study set. By keeping the storage conditions consistent within the collection, it minimizes the effects of temperature and humidity as a variable across the collection.

A.1.2 XRS spectroscopy

X-ray Raman measurements (carbon K-edge and oxygen K-edge) were performed using the high-resolution X-ray Raman spectrometer operated at beamline 6-2 at the Stanford Synchrotron Radiation Laboratory [1]. The instrument consists of 40 crystal Si(440) analyzers arranged on overlapping Rowland circles of 1000 mm and at a fixed Bragg angle of 88° , resulting in a fixed detection energy at 6462 eV and an overall energy resolution of 0.29 eV. Spectra are recorded using an inverse scanning approach, wherein the detection energy is held constant at 6462 eV while the incident energy is scanned through a Si(311) double-crystal monochromator. The average momentum transfer is $q \approx 1.23$ a.u., which ensures that dipole transitions

A.1. MATERIALS AND METHODS

dominate the spectra and therefore the X-ray Raman spectra are formally equivalent to conventional soft X-ray absorption spectra.

XRS oxygen K-edge experiments were performed at GALAXIES beamline (Synchrotron SOLEIL, France) with an energy resolution of 1.2 eV. The spectrometer is equipped with 4 spherically bent Si(444) analyzer crystals [2]. For the XRS spectrum acquisition, we scanned the beamline energy along the absorption edge of interest, at a fixed analyzer energy. Experiments were performed at a Si(444) analyzer energy of ≈ 8.0 keV operated at a Bragg angle of 86° . The data was collected at backscattered geometry (scattering angle of $2\theta \approx 130^\circ$) to maximize the XRS signal. The momentum transfer q is $\approx 7.5 \text{ \AA}^{-1}$. The beamline is equipped with a cryogenically cooled Si(111) double-crystal monochromator. The monochromatized X-ray beam is focused by a toroidal mirror to a spot size ($V \times H$) of approximately $30 \times 80 \mu\text{m}^2$. We collected energy transfer measurements along the oxygen K-edge around 530 eV energy transfer with an energy step of 0.5 eV and dwell time of 400 ms per energy step.

A.1.3 FT-IR spectroscopy

FT-IR spectra were collected with a spectrometer Bruker Alpha II equipped with a DTGS detector. Measurements were performed in transmission mode using KBr pellets (Sigma Aldrich, FT-IR grade, ref. 221864). A total of 128 scans have been accumulated in each sample, using a resolution of 4 cm^{-1} in the range between 4000 to 400 cm^{-1} . All spectra showed have not been corrected in order to avoid any kind of distortion.

A.1.3.1 *Xanthorrhoea* resins

The FT-IR absorbance spectra of *Xanthorrhoea* species (*X. arborea*, *X. semiplana* ssp. *tateana*, *X. semiplana*) (Fig.3) are dominated by the following features: (a) a broad signal in the $3550\text{--}3250 \text{ cm}^{-1}$ region attributed to --OH stretching, (b) a weak intensity peak observed at 3023 cm^{-1} attributed to the CH stretching in alkene groups, (c) weak intensity peaks centered at 2962 cm^{-1} , 2936 cm^{-1} , 2840 cm^{-1} , attributed to the CH_3 and CH_2 antisymmetric stretch and CH_2 symmetric stretch respectively, (d) a peak centered at 1636 cm^{-1} (mainly observed at *X. arborea* spectrum) attributed to $\text{C}=\text{C}$ stretching in conjugated $\text{C}=\text{C}$ bonds, (e) high intensity sharp peaks centered at 1602 cm^{-1} , 1513 cm^{-1} and 1444 cm^{-1} attributed to $\text{C}=\text{C}$ stretching indicating the presence of aromatic groups, (f) several sharp bands in the range $1275\text{--}1000 \text{ cm}^{-1}$

A.1. MATERIALS AND METHODS

attributed to in-plane C–H deformation, (g) the bands at 1337 cm^{-1} and 1205 cm^{-1} linked to the OH deformation and the C–OH stretching, and (h) a strong band centered at 832 cm^{-1} attributed to out-of-plane C–H deformation.

A.1.3.2 *Callitris* resins

The FT-IR absorbance spectra of *Callitris* species (*C. glauca*, *C. calcarata*, *C. preissii* ssp. *verrucosa*) (Fig.3) are dominated by the following features: (a) a broad band centered at 3450 cm^{-1} corresponding to the stretching of polymeric O–H, (b) a band at 3080 cm^{-1} corresponding to the stretching vibration of C=C bonds, (c) strong intensity peaks centered at 2957 cm^{-1} , 2937 cm^{-1} , 2873 cm^{-1} , 2845 cm^{-1} attributed to the CH₂ and CH₃ antisymmetric stretch and CH₂ and CH₃ symmetric stretch respectively, the presence of these groups is confirmed by the bands around 1467 cm^{-1} (–CH₂–) and around 1384 cm^{-1} (deformation of CH₃ and CH₂ groups), (d) a strong broad signal centered at 1695 cm^{-1} attributed to C=O stretching from the carboxylic acid; (e) a band centered at 1644 cm^{-1} attributed to the presence of conjugated C=C bonds.

A.1.3.3 *Eucalyptus* kino

The FT-IR spectra of *Eucalyptus* species (White Mallee, *E. largiflorens*) (Fig.3) exhibit the following features: (a) an intense broad band centered at 3326 cm^{-1} corresponding to the stretching of polymeric O–H, (b) a peak at 1700 cm^{-1} attributed to C=O stretching probably from COOH groups, (c) high intensity bands at 1612 cm^{-1} , 1534 cm^{-1} and 1447 cm^{-1} attributed to the C=C stretching from aromatic compounds, (d) two bands centered at 762 and 734 cm^{-1} attributed to the =CH out-of-plane bending vibrations.

A.1.3.4 *Acacia* gums

The FT-IR spectra of *Acacia* species (*A. bakeri*, *unknown species*) exhibit the following features (Fig.3): (a) an intense broad band in the $3600\text{--}3000\text{ cm}^{-1}$ range attributed to O–H stretching, (b) a peak centered at 2940 cm^{-1} attributed to the CH₂ antisymmetric stretching, and a band at 2890 cm^{-1} linked to the CH stretching (c) a broad asymmetrical band centered at 1609 cm^{-1} possibly linked with the presence of absorbed water. (d) two intense bands at 1420 cm^{-1} and at 1380 cm^{-1} possibly attributed to the deformation of CH₃ and CH₂ groups (e) a broad band

A.1. MATERIALS AND METHODS

centered around 1070 cm^{-1} and two bands centered at 1160 cm^{-1} and 1130 cm^{-1} linked to the skeletal vibrations of polysaccharides. The differences in intensity among the two species is possibly related to the proportion of monosaccharides or their organization in the polysaccharide chain.

A.1.4 ICP-MS

Inductively coupled plasma mass spectrometry experiments were performed at Flinders University, using a PerkinElmer NexION 350D inductively coupled plasma mass spectrometer equipped with a PC3 Peltier Cooler Organics Sample Introduction Kit (PerkinElmer, Massachusetts, USA). Sample Preparation involved microwave digestion using an Anton Paar Multiwave Eco (Anton Paar, Gratz, Austria) as follows. 100 mg of sample was placed in the tubes and 5 mL of nitric acid was introduced. The tubes were then sealed and left in the fumehood overnight (17–18 h) as a pre-digestion. The microwave digestion initially ramped the temperature to 100°C over 15 min then was held there for 5 min, second stage ramped the temperature to 180°C over 10 min and held there for 10 min. All temperature increases were linear and monitored as an average across all sample vessels. The 5 mL of digested sample were then made up to 50 mL using Milli-Q ultrapure water (Merck Millipore, Massachusetts, USA) and further diluted 1 in 5 once again with Milli-Q ultrapure water. The prepared samples were then analyzed using the kinetic discrimination (KED) mode which uses helium as the collision gas. The parameters of the analysis were as follows: RF Power of 1600 W, Meinhard glass TR-50-C 0.5 mm I.D nebulizer, quartz glass cyclonic spray chamber with Peltier cooler, 2 mm I.D. quartz injector, demountable quartz torch, nickel/aluminium triple cone interface, plasma gas flow of 18 L min^{-1} , nebulizer gas flow of 0.87 L min^{-1} , helium gas flow of 4.7 mL min^{-1} and a dual detector mode (pulse/analog) reading 10 sweeps with 3 replicates per sample. The standards used contained the elements: Ag, Al, As, B, Ba, Be, Ca, Cd, Co, Cr, Fe, K, Mg, Mn, Mo, Na, Pb, Sb, Se, Si, Sr, Ti, Tl, U, V and Zn. Apart from uranium all other elements ranged from 0.1–100 ppb and uranium ranged from 0.01–10 ppb.

A.1.5 XRS data reduction

The spectral decomposition of the XRS signal in the region of interest 283.0–292.5 eV and 530.8–538.5 eV was performed using a linear combination of Gaussians. The parameters of

A.1. MATERIALS AND METHODS

| | Center (eV) | FWHM (eV) | Assignment | Transitions |
|--------------|-------------|-----------|---|----------------------------------|
| – Gaussian 1 | 283–284.5 | 0.3–0.9 | Aromatic carbonyl (C=O) and/or quinone [4] | 1s– π^* |
| – Gaussian 2 | 285.3–285.6 | 0.3–0.9 | Aromatic and/or olefinic carbon [5] | 1s– π^* |
| – Gaussian 3 | 286–287 | 0.3–0.9 | Ketones ($R_2C=O$)/ nitriles ($C\equiv N$)[5]/ ethers (R-O-R')[6] | 1s– π^* |
| – Gaussian 4 | 287–288 | 0.3–0.9 | Phenols (Ar–OH) (287–287.3 eV) [7]/ aliphatics (C_xH_y) (287.3–288 eV) [5] | 1s– π^* 1s–3p/ σ^* |
| – Gaussian 5 | 288.3–288.8 | 0.3–0.9 | Amides ($R-C(=O)-N(R',R'')$)/ carboxyl ($-C(=O)OH$)/ acetal carbon ($R_2C(OR')_2$, $R'\neq H$)[5] | 1s– π^* |
| – Gaussian 6 | 289–289.6 | 0.3–0.9 | Alcohols (R–OH) [8] | 1s–3p/ σ^* |
| – Gaussian 7 | 290–290.9 | 0.3–1.2 | Additional 1s– π^* transitions of carboxylic or peroxide groups/ alkyl carbon [8, 9] | 1s– π^* 1s–4p |
| Gaussian 8 | 291.2–291.8 | 0.3–1.2 | Graphitic materials display an exciton at 291.5 eV which reflects the electron delocalization over several aromatic units [9] | 1s– σ^* |
| Gaussian 9 | 292.3–292.7 | 0.3–1.2 | Aromatic and/or olefinic carbon and contributions from multiple scattering [9] | 1s– σ^* |

Table A.1: XRS carbon K-edge spectral decomposition

the model to be fitted are the intensity, the full width half maximum (FWHM) and the center of each Gaussian. The FWHM has a lower (FWHM of the elastic line) and an upper bound (selected in such a way to minimize the post-fit residual). The center of each Gaussian is allowed to vary slightly during the fit in a constrained energy transfer region that corresponds to electronic transitions in specific oxygen-containing functional groups expected for these families of compounds. The shift of the center and the width of the fitted Gaussian provides information on the overlap of functional groups of which their transitions are expected to be in the same energy transfer region. Post-fit residuals were calculated to check for possible missing features as Ref. [3]. The intensity, FWHM and center of each Gaussian are fitted using a non-linear least squares regression implemented in Python. All the parameters are summarized in Table A.1, A.3.

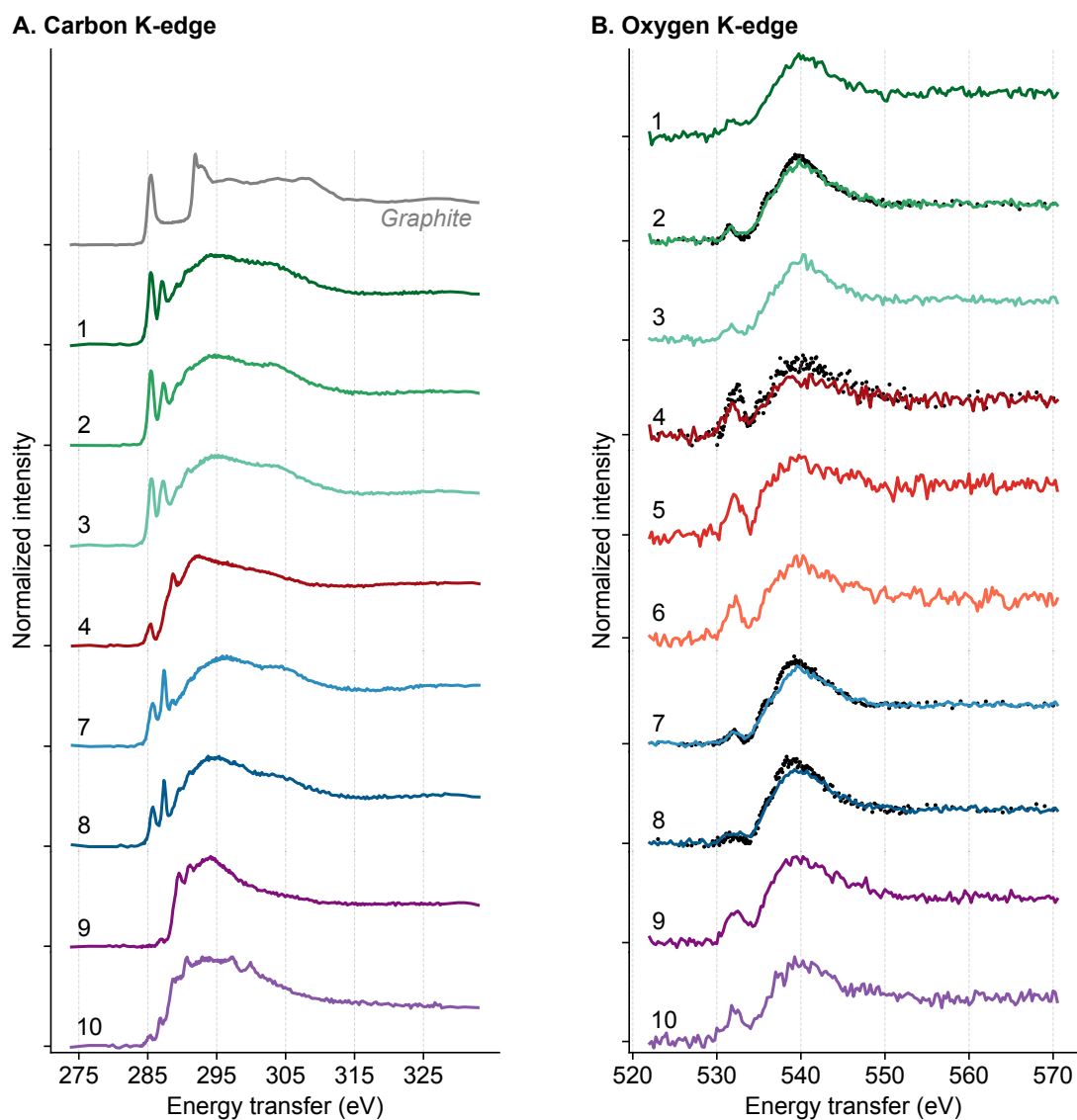


Figure A.1: XRS data of native Australian plant exudates. A. Carbon K-edge (energy resolution: 0.3 eV, SSRL beamline 6-2b). B. Oxygen K-edge (energy resolution: 1.2 eV; SOLEIL beamline GALAXIES). In black color (spectra 2,4,7,8) are higher resolution data for comparison (0.3 eV, SSRL). 1, *X. arborea*; 2, *X. semiplana* ssp. *tateana*; 3, *X. semiplana*; 4, *C. calcarata*; 5, *C. glauca*; 6, *C. preissii* ssp. *verrucosa*; 7, White Mallee; 8, *E. largiflores*; 9, Acacia, unknown species; 10, *A. bakeri*.

A.1. MATERIALS AND METHODS

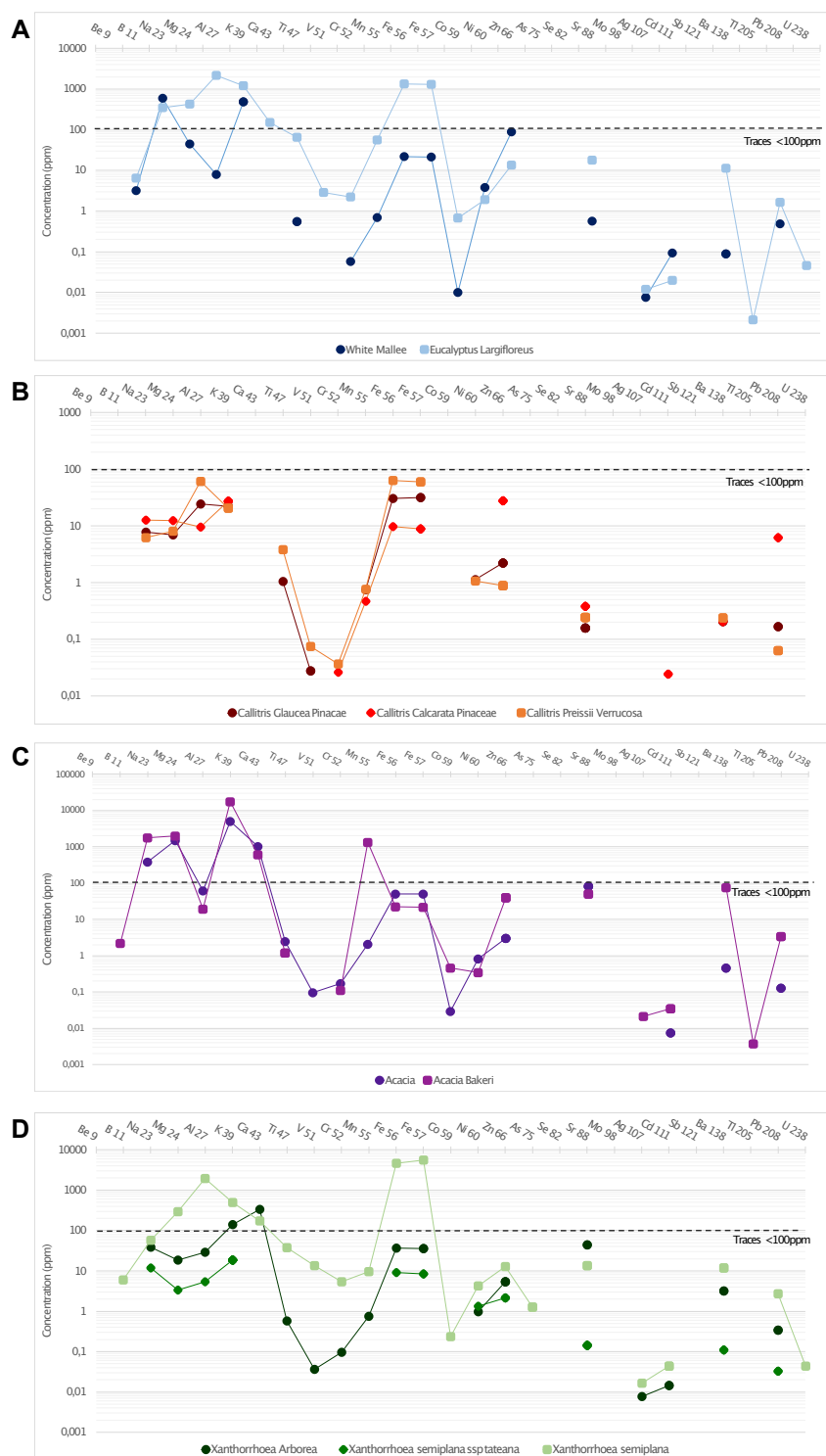


Figure A.2: ICP-MS data of native Australian plant exudates A. *Xanthorrhoea*, B. *Callitris*, C. *Eucalyptus*, D. *Acacia*

| | - Gaussian 1 | | | - Gaussian 2 | | | - Gaussian 3 | | | - Gaussian 4 | | | - Gaussian 5 | | | - Gaussian 6 | | | - Gaussian 7 | | |
|---|--------------------|-----------------------|------------------|--------------------|-----------------------|------------------|--------------------|-----------------------|------------------|--------------------|-----------------------|------------------|--------------------|-----------------------|------------------|--------------------|-----------------------|------------------|--------------------|-----------------------|------------------|
| | μ_{Fit} | σ_{Fit} | I_{Fit} | μ_{Fit} | σ_{Fit} | I_{Fit} | μ_{Fit} | σ_{Fit} | I_{Fit} | μ_{Fit} | σ_{Fit} | I_{Fit} | μ_{Fit} | σ_{Fit} | I_{Fit} | μ_{Fit} | σ_{Fit} | I_{Fit} | μ_{Fit} | σ_{Fit} | I_{Fit} |
| <i>X. arborea</i> | 284.5 | 0.38 | 0.18 | 285.5 | 0.38 | 1.46 | 286.7 | 0.38 | 0.62 | 287.3 | 0.38 | 0.96 | 288.3 | 0.38 | 0.85 | 289.2 | 0.38 | 0.97 | 290.2 | 0.51 | 1.20 |
| <i>X. semiplana</i> ssp. <i>tateana</i> | 284.5 | 0.38 | 0.14 | 285.5 | 0.38 | 1.44 | 286.6 | 0.38 | 0.43 | 287.4 | 0.38 | 1.12 | 288.4 | 0.38 | 0.76 | 289.2 | 0.38 | 0.95 | 290.2 | 0.51 | 1.16 |
| <i>X. semiplana</i> | 284.5 | 0.38 | 0.13 | 285.5 | 0.38 | 1.32 | 286.7 | 0.38 | 0.68 | 287.4 | 0.38 | 0.99 | 288.4 | 0.38 | 0.72 | 289.2 | 0.38 | 0.89 | 290.3 | 0.51 | 1.12 |
| <i>C. calcarata</i> | 284.5 | 0.36 | 0.06 | 285.4 | 0.38 | 0.34 | 286.8 | 0.38 | 0.25 | 287.7 | 0.38 | 0.68 | 288.6 | 0.38 | 1.05 | 289.5 | 0.38 | 0.70 | 290.4 | 0.51 | 0.99 |
| White Mallee | 284.5 | 0.38 | 0.08 | 285.6 | 0.38 | 0.65 | 286.3 | 0.38 | 0.39 | 287.4 | 0.37 | 1.20 | 288.5 | 0.38 | 0.72 | 289.4 | 0.38 | 0.58 | 290.3 | 0.51 | 0.78 |
| <i>E. largiflorens</i> | 284.5 | 0.31 | 0.07 | 285.6 | 0.38 | 0.66 | 286.3 | 0.38 | 0.35 | 287.4 | 0.35 | 1.24 | 288.5 | 0.38 | 0.65 | 289.3 | 0.38 | 0.87 | 290.2 | 0.51 | 0.99 |
| <i>Acacia unknown species</i> | 284.4 | 0.14 | 0.00 | 285.4 | 0.38 | 0.01 | 286.9 | 0.38 | 0.16 | 287.9 | 0.35 | 0.13 | 288.8 | 0.38 | 0.79 | 289.5 | 0.38 | 1.36 | 290.5 | 0.51 | 1.21 |
| <i>A. bakeri</i> | 284.5 | 0.31 | 0.04 | 285.4 | 0.38 | 0.28 | 286.8 | 0.38 | 0.69 | 287.8 | 0.38 | 0.73 | 288.6 | 0.38 | 1.52 | 289.5 | 0.38 | 1.42 | 290.5 | 0.51 | 2.05 |

Table A.2: XRS carbon K-edge spectra decomposition. Center (μ_{Fit}), standard deviation (σ_{Fit}) and Intensity (I_{Fit}) of the fitted Gaussian distributions)

| | Center (eV) | FWHM (eV) | Assignment | Transitions |
|--|-------------|-----------|---|----------------|
| - Gaussian 1 | 530.8–531.6 | 1.2 | C=O (Ketones ($R_2C=O$) (531.3 eV)[10]/ Amides ($R-C(=O)-N(R',R'')$) (531.5 eV)[11]) | 1s- π^* |
| - Gaussian 2 | 531.9–532.3 | 1.2 | C=O (Carboxyls ($-C(=O)OH$))[12] | 1s- π^* |
| - Gaussian 3 | 533–533.5 | 1.2 | O–O (Peroxides (ROOR))[13] | 1s- σ^* |
| - Gaussian 4 | 533.9–534.7 | 1.2 | O–H (Alcohols ($R-OH$))[14] | 1s- σ^* |
| - Gaussian 5 | 535.2–535.7 | 1.2 | O–H (Phenols ($Ar-OH$)[15]/ carboxyls ($-(C=O)OH$))[12] | 1s- π^* |
| - Gaussian 6 | 536.3–537 | 1.2–1.4 | Excitations to Rydberg MO's (Peroxides (ROOR)[13]) | 1s-3s |
| - Gaussian 7 | 537–538.5 | 1.2–2 | C–O (Peroxides (ROOR)[13]/ Alcohols ($R-OH$)[14]) | 1s- σ^* |

Table A.3: XRS oxygen K-edge spectral decomposition

| | - Gaussian 1 | | | - Gaussian 2 | | | - Gaussian 3 | | | - Gaussian 4 | | | - Gaussian 5 | | | - Gaussian 6 | | | - Gaussian 7 | | |
|-----------------------------------|--------------------|-----------------------|------------------|--------------------|-----------------------|------------------|--------------------|-----------------------|------------------|--------------------|-----------------------|------------------|--------------------|-----------------------|------------------|--------------------|-----------------------|------------------|--------------------|-----------------------|------------------|
| | μ_{Fit} | σ_{Fit} | I_{Fit} | μ_{Fit} | σ_{Fit} | I_{Fit} | μ_{Fit} | σ_{Fit} | I_{Fit} | μ_{Fit} | σ_{Fit} | I_{Fit} | μ_{Fit} | σ_{Fit} | I_{Fit} | μ_{Fit} | σ_{Fit} | I_{Fit} | μ_{Fit} | σ_{Fit} | I_{Fit} |
| <i>X. arborea</i> | 531.1 | 0.51 | 0.18 | 531.9 | 0.51 | 0.28 | 533 | 0.51 | 0.23 | 534.1 | 0.51 | 0.29 | 535.2 | 0.51 | 0.49 | 536.3 | 0.59 | 0.71 | 537.8 | 0.85 | 1.07 |
| <i>X. semiplana ssp. tateana</i> | 531.4 | 0.51 | 0.28 | 531.9 | 0.51 | 0.12 | 533 | 0.51 | 0.18 | 534.2 | 0.51 | 0.26 | 535.2 | 0.51 | 0.50 | 536.3 | 0.59 | 0.97 | 537.9 | 0.85 | 1.32 |
| <i>X. semiplana</i> | 530.9 | 0.51 | 0.18 | 531.9 | 0.51 | 0.30 | 533 | 0.51 | 0.11 | 534.1 | 0.51 | 0.27 | 535.2 | 0.51 | 0.53 | 536.3 | 0.59 | 0.89 | 537.9 | 0.85 | 1.16 |
| <i>C. calcarata</i> | 530.8 | 0.51 | 0.40 | 531.9 | 0.51 | 0.78 | 533 | 0.51 | 0.37 | 534.3 | 0.51 | 0.34 | 535.2 | 0.51 | 0.54 | 536.3 | 0.59 | 0.83 | 537.9 | 0.85 | 1.23 |
| <i>C. glauca</i> | 531 | 0.51 | 0.19 | 532 | 0.51 | 0.70 | 533 | 0.51 | 0.43 | 533.9 | 0.51 | 0.02 | 535.2 | 0.51 | 0.65 | 536.3 | 0.59 | 0.75 | 537.8 | 0.85 | 0.99 |
| <i>C. preissii ssp. verrucosa</i> | 531.2 | 0.51 | 0.52 | 532.3 | 0.51 | 0.85 | 533 | 0.51 | 0.17 | 534.1 | 0.51 | 0.30 | 535.2 | 0.51 | 0.52 | 536.3 | 0.59 | 1.01 | 537.8 | 0.85 | 1.21 |
| White Mallee | 530.8 | 0.51 | 0.06 | 531.9 | 0.51 | 0.28 | 533 | 0.51 | 0.16 | 534.4 | 0.51 | 0.24 | 535.2 | 0.51 | 0.43 | 536.3 | 0.59 | 0.89 | 537.9 | 0.85 | 1.15 |
| <i>E. largiflorens</i> | 531 | 0.51 | 0.25 | 532.1 | 0.51 | 0.17 | 533 | 0.51 | 0.25 | 534.3 | 0.51 | 0.18 | 535.2 | 0.51 | 0.50 | 536.3 | 0.59 | 1.00 | 537.9 | 0.85 | 1.47 |
| <i>Acacia unknown species</i> | 531.2 | 0.51 | 0.44 | 532.2 | 0.51 | 0.51 | 533 | 0.51 | 0.34 | 533.9 | 0.51 | 0.31 | 535.2 | 0.51 | 0.54 | 536.3 | 0.59 | 0.93 | 537.8 | 0.85 | 1.35 |
| <i>A. bakeri</i> | 530.8 | 0.51 | 0.27 | 532 | 0.51 | 0.66 | 533 | 0.51 | 0.39 | 534.4 | 0.51 | 0.33 | 535.2 | 0.51 | 0.37 | 536.3 | 0.59 | 0.71 | 537.7 | 0.85 | 1.16 |

Table A.4: XRS oxygen K-edge spectra decomposition. Center (μ_{Fit}), standard deviation (σ_{Fit}) and Intensity (I_{Fit}) of the fitted Gaussian distributions)

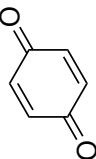
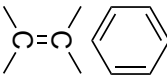
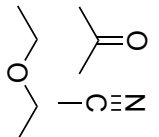
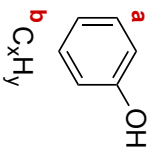
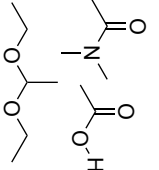
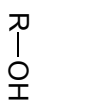
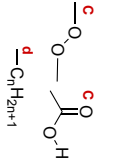
| | - Gaussian 1 | - Gaussian 2 | - Gaussian 3 | - Gaussian 4 | - Gaussian 5 | - Gaussian 6 | - Gaussian 7 |
|--|---|---|---|---|---|---|---|
| |  |  |  |  |  |  |  |
| Energy transfer (eV) | 284.4–284.5 | 285.4–285.6 | 286.3–286.9 | 287.3–287.9 | 288.3–288.8 | 289.2–289.5 | 290.2–290.5 |
| Transitions | 1s- π^* | 1s- π^* | 1s- π^* | ^a 1s- π^* ^b 1s-3p/ σ^* | 1s- π^* | 1s-3p/ σ^* | ^c 1s- π^* ^d 1s-4p * |
| | A_{Fit} (Normalized intensity · eV) | | | | | | |
| <i>X. arborea</i> | 0.17 | 1.4 | 0.59 | 0.92 | 0.81 | 0.93 | 1.53 |
| <i>X. semiplana</i> <i>ssp. lateana</i> | 0.13 | 1.38 | 0.41 | 1.07 | 0.73 | 0.91 | 1.48 |
| <i>X. semiplana</i> | 0.13 | 1.26 | 0.65 | 0.96 | 0.69 | 0.85 | 1.43 |
| <i>C. calcarata</i> | 0.05 | 0.33 | 0.24 | 0.65 | 1.01 | 0.67 | 1.28 |
| White Mallee | 0.07 | 0.62 | 0.37 | 1.11 | 0.69 | 0.55 | 0.9 |
| <i>E. largiflorens</i> | 0.06 | 0.64 | 0.33 | 1.08 | 0.62 | 0.82 | 1.27 |
| <i>Acacia un-</i> <i>known species</i> | 0.00 | 0.01 | 0.16 | 0.12 | 0.76 | 1.31 | 1.55 |
| <i>A. bakeri</i> | 0.03 | 0.27 | 0.66 | 0.69 | 1.46 | 1.36 | 2.62 |

Table A.5: Contribution of functional groups to the XRS carbon K-edge spectra. Integrated area of the fitted Gaussian distributions (A_{Fit} , calculated as $A_{\text{Fit}} = I_{\text{Fit}} \cdot \sigma \cdot \sqrt{2\pi}$)

References

- [1] Dimosthenis Sokaras et al. “A high resolution and large solid angle x-ray Raman spectroscopy end-station at the Stanford Synchrotron Radiation Lightsource”. In: *Review of Scientific Instruments* 83.4 (2012), p. 043112.
- [2] James Michael Ablett et al. “The GALAXIES inelastic hard X-ray scattering end-station at Synchrotron SOLEIL”. In: *Journal of Synchrotron Radiation* 26.1 (2019), pp. 263–271.
- [3] Pierre Gueriau et al. “Noninvasive Synchrotron-Based X-ray Raman Scattering Discriminates Carbonaceous Compounds in Ancient and Historical Materials”. In: *Analytical Chemistry* 89.20 (2017), pp. 10819–10826.
- [4] Karen Heymann et al. “C 1s K-edge near edge X-ray absorption fine structure (NEXAFS) spectroscopy for characterizing functional group chemistry of black carbon”. In: *Organic Geochemistry* 42.9 (2011), pp. 1055–1064.
- [5] Corentin Le Guillou et al. “XANES-based quantification of carbon functional group concentrations”. In: *Analytical Chemistry* 90.14 (2018), pp. 8379–8386.
- [6] Véronique Rouchon and Sylvain Bernard. “Mapping iron gall ink penetration within paper fibres using scanning transmission X-ray microscopy”. In: *Journal of Analytical Atomic Spectrometry* 30.3 (2015), pp. 635–641.
- [7] Julien Alleon et al. “Organic molecular heterogeneities can withstand diagenesis”. In: *Scientific reports* 7.1 (2017), pp. 1–9.
- [8] George D Cody et al. “Determination of chemical-structural changes in vitrinite accompanying luminescence alteration using C-NEXAFS analysis”. In: *Organic Geochemistry* 28.7-8 (1998), pp. 441–455.
- [9] Sylvain Bernard et al. “Geochemical evolution of organic-rich shales with increasing maturity: A STXM and TEM study of the Posidonia Shale (Lower Toarcian, northern Germany)”. In: *Marine and Petroleum Geology* 31.1 (2012), pp. 70–89.
- [10] Adam P. Hitchcock and Chris E. Brion. “Inner-shell excitation of formaldehyde, acetaldehyde and acetone studied by electron impact”. In: *Journal of Electron Spectroscopy and Related Phenomena* 19.2 (1980), pp. 231–250.

REFERENCES

- [11] I Ishii and Adam P Hitchcock. “A quantitative experimental study of the core excited electronic states of formamide, formic acid, and formyl fluoride”. In: *The Journal of chemical physics* 87.2 (1987), pp. 830–839.
- [12] MB Robin et al. “Fluorination effects on the inner-shell spectra of unsaturated molecules”. In: *Journal of Electron Spectroscopy and Related Phenomena* 47 (1988), pp. 53–92.
- [13] KL Harding et al. “Inner-shell excitation spectroscopy of peroxides”. In: *Chemical Physics* 461 (2015), pp. 117–124.
- [14] I Ishii and Adam P Hitchcock. “The oscillator strengths for C1s and O1s excitation of some saturated and unsaturated organic alcohols, acids and esters”. In: *Journal of Electron Spectroscopy and Related Phenomena* 46.1 (1988), pp. 55–84.
- [15] JT Francis and Adam P Hitchcock. “Inner-shell spectroscopy of p-benzoquinone, hydroquinone, and phenol: distinguishing quinoid and benzenoid structures”. In: *The Journal of Physical Chemistry* 96.16 (1992), pp. 6598–6610.

Supplementary information for Chapter 4

B.1 Mayerne Manuscript: "*Pictoria, sculptoria et quae subalternarum artium*"

The *Mayerne manuscript* entitled "*Pictoria, sculptoria et quae subalternarum artium*" (Fig. B.1) contains handwritten records on artistic techniques gathered between 1620 and 1646, written or collected by Sir Theodore de Mayerne (1573-1655), an influential physician of the time [1]. Mayerne collected, organized and compiled artisanal know-how from textual sources and living artists, through in-situ observations, artists' interviews and his own experimentation, creating an exemplary art-technological text source. The 17th century manuscript comprises recipes and technical practises on the preparation of pigments – including organic pigments (Fig. B.2, B.4, B.5, B.6, B.3, B.7) – inks, dyes, oils and varnishes, the priming and preparation of painting surfaces and the conservation and restoration of paintings [2]. Pigment preparation techniques were experimented and displayed on folios of colour samples with captions (Fig. B.8).

The manuscript contains 170 heterogeneous folios, bound into a book after Mayerne's death. Today, the manuscript (*Sloane MS 2052*) is preserved at the British library; it was acquired in 1753 by the British Museum as part of Sloane manuscripts' collection. The digitized manuscript is accessible online [3]. Ernst Berger (1847-1919) provided the full transcription and translation of the *Mayerne manuscript* for the first time in 1901 [4]. The retrospective use of the manuscript by artists in the early 20th century and its study by conservators and technical art historians today, highlights the importance of transferring scientific knowledge of art processes and materials.

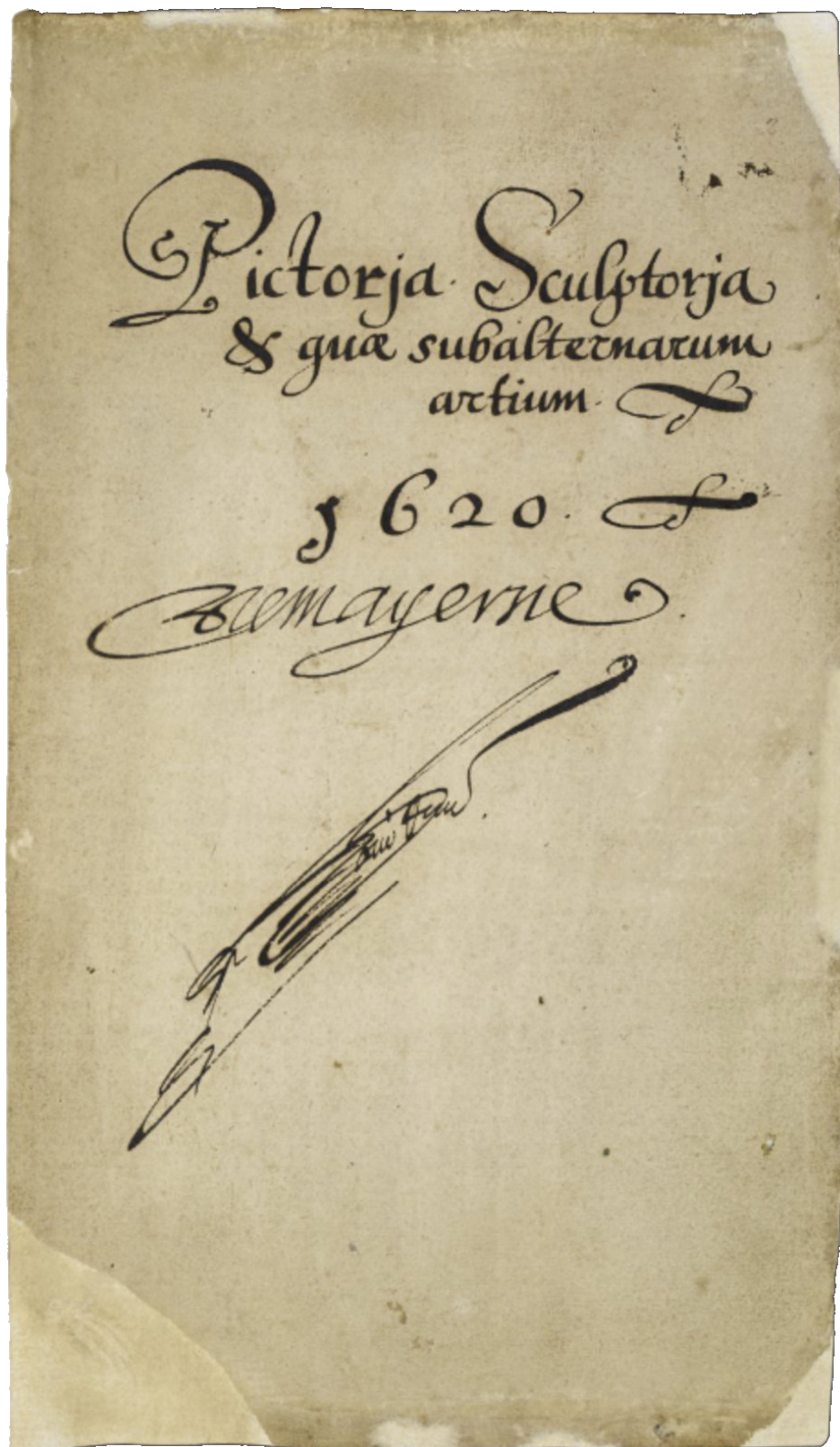


Figure B.1: Sloane MS 2052, folio 2r, London, British Library [3]. Manuscript's title page hand-written by Mayerne (photo: © British Library Board).

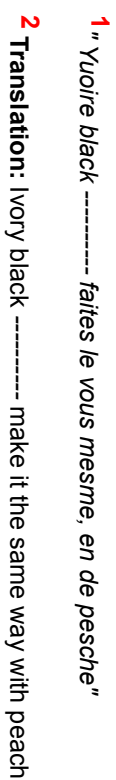
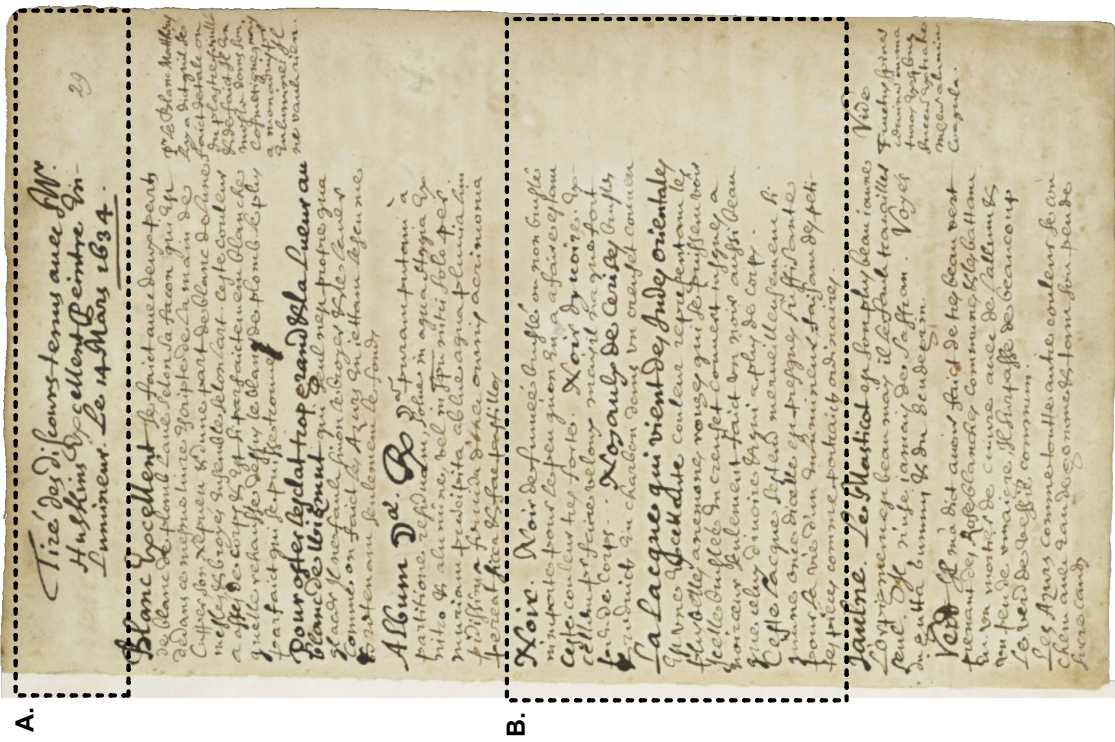


Figure B.3: Sloane MS 2052, folio 84r, London, British Library [3]. The note suggests the preparation of *ivory black* and *peach black* in the same way. ¹ Transcription by Jenny Boulboulé, ² translation from Fels et al. [1] (photo: © British Library Board).



A. ¹ " Tiré des discours tenus avec Mr. Huskins excellent peintre Enlumineur. Le 14 Mars 1634. "

² Translation: Excerpt from a discussion with Mr. Huskins, an excellent illuminator. March 14, 1634.

[...]

B. ¹ " **Noir.** Noir de fumée brulé ou non brulé n'importe pour le peu qu'on en a faire, estant ceste couleur tres forte. **Noir d'ivoire.** Excellent pour faire veloux mais il na que fort peu de corps. **Noyaux de Cerises bruses and reduicts en charbon dans une creuset couuert.**

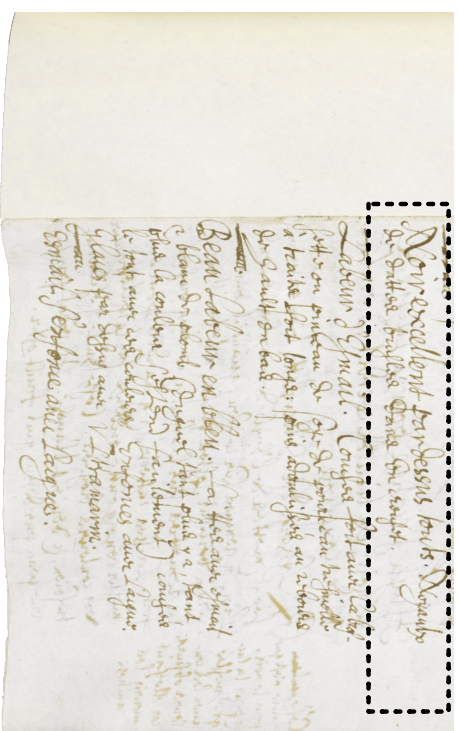
La Lacque qui vient des Indes Orientales est une excellente couleur representant les plus belles anemones rouges qui se puissent voir. Icele brulée en creuset couuert jusques a noircir seulement fait un noir aussi beau que celui d'ivoire & est a plus de corps. Ceste lacque sestend merueilleusement si qu'une once dicelle est presque suffisante pour la vie d'un Enlumineur, faisant des petites pieces comme portraits ordinaires. "

Translation: **Black.** Lampblack, regardless whether burnt or not with the little use that is made of it, is too strong a pigment. **Ivory black.** Excellent for painting velvet, since it has little body. **Cherry stone.** Burned and transformed into charcoal in a covered crucible produces a good black².

The **Lac** (ed. Sticklac, Kerria lacca Kerr) coming from **East India** is of an excellent colour similar to the most beautiful red anemones that can be imagined. Burn it in closed crucible until it darkens and it will be a black as beautiful as ivory black, & with more body. This lac is wonderfully suitable to such extent that an ounce is almost enough for an entire lifetime of an illuminator that makes small works such as normal portraits³.

[...]

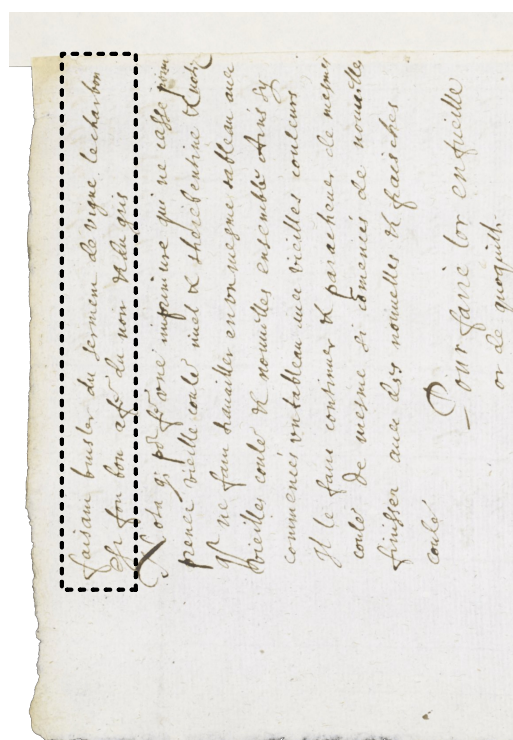
Figure B.4: Sloane MS 2052, folio 29r, London, British Library [3]. Discussion with the artist Huskins, reporting his empirical knowledge on preparation practises and use of organic black pigments, including *lampblack*; *ivory black*, *cherry stone*, *lac*. ¹ Transcription by Jenny Boulboulé, ² translation from Fels et al. [1], ³ translation from Daal and Bul [5] (photo: © British Library Board).



¹"Noir excellent pardessus tous. Noyaux de dattes bruslés dans un creuset."

² Translation: Most excellent than all other blacks. Date pits burnt in a crucible.

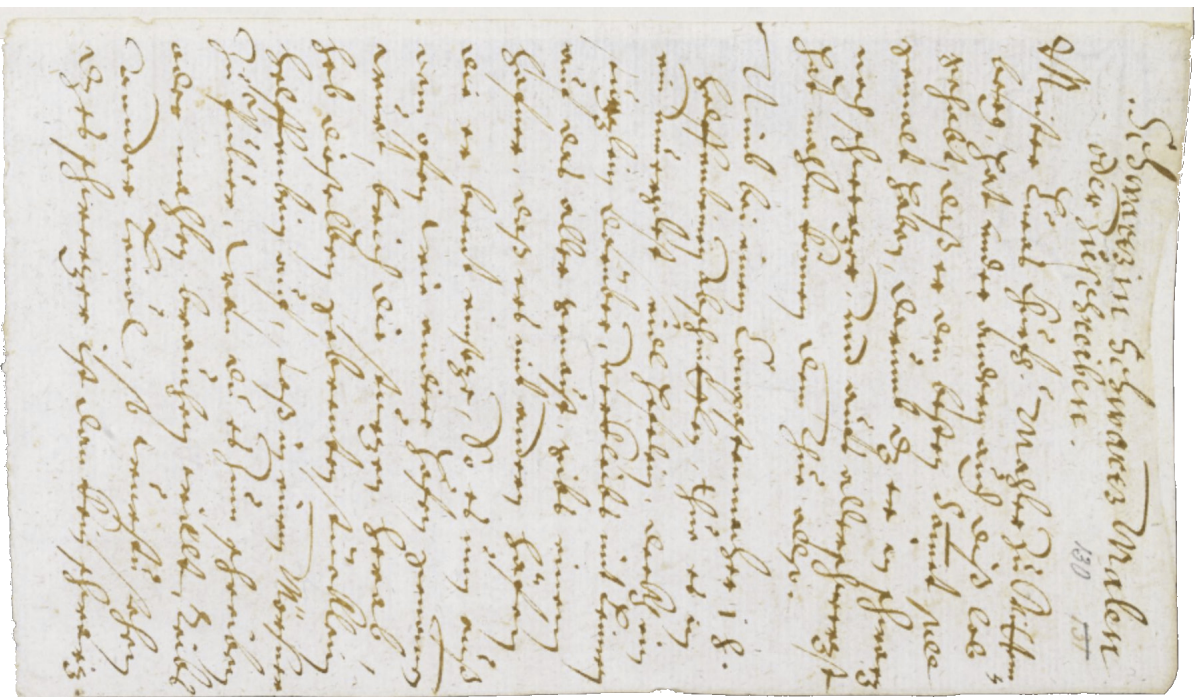
Figure B.5: Sloane MS 2052, folio 95r, London, British Library [3]. The note suggests that *date pits* burned in a crucible results in the preparation of the most excellent of all black pigments. ¹ Transcription by Jenny Boulboulé, ² translation from Fels et al. [1] (photo: © British Library Board).



¹ "[...] faisant brusler du serment de vigne le charbon est fort bon a faire du noir & du gris."

² **Translation:** [...] by burning grape vine pruning a very good charcoal emerges for making black and gray

Figure B.6: Sloane MS 2052, folio 11v, London, British Library [3]. The burning of *grape vine* pruning creates a charcoal that can be used as black or gray color. ¹ Transcription by Jenny Boulboulé, ² translation from Fels et al. [1] (photo: © British Library Board).



"Schwarz in Schwartz malen oder zuschreiben.

Meister Lucas Cheufs, Mahler zu Wittenberg, hat under andern auch diss lob gehabt, dass er den besten Samnit soll gemalt haben, darumb daz er in schwarz noch schwarzer, vnd allerschwarzt hat mahlen können, dem Thue also: Nimb bei einem Compostenmacher 1 h. helfenbeinen Abschnitten, thue es in ein..... glet sovel helfeiben, deckh ein stüzzlein darüber, verkleibs mit Leimen auf das aller genaust, gibs einem hafter, dass ers mit andern hätten die er brent einseze. So es nun auss dem offen wie andere hätten genommen wurt, brich die stützen herab, heb die selben gebranten stücklein helfenbein auf, stoss in einem Mörsner zu Pulver, war du es zum schreiben oder malhen brauchen wilt, reibs under leinöl, so wirstu sehen, daz schwarzer ist dan kein schwarz."

¹ Translation: Painting or writing in black.

Master Lucas Cheufs, painter at Wittenberg, received among others this praise, that he was supposed to have painted the best velvet in that he could paint even the blackest of all in black as follows. Take one h. [handfull] of ivory scraps from a compost maker, put it in a [unreadable] smooth so much ivory, cover with a little bell, seal with glue most carefully, give it to a potter to fire in the klin with other pots. When it is then taken out of the oven with the other pots, break off the bell, take out the burnt pieces of ivory and crush to powder in a mortar. When you want to use it for writing or painting, grind it with linseed oil. So would you see then that no black is blacker.

Figure B.7: Sloane MS 2052, folio 130r, London, British Library. Instructions on the preparation of ivory black pigment by the painter Master Lucas Cheuf. ¹ Translation from Fels et al. [1] (photo: © British Library Board).

B.1. MAYERNE MANUSCRIPT: "PICTORIA, SCULPTORIA ET QUAE SUBALTERNARUM ARTIUM"



Figure B.8: Sloane MS 2052, folio 80v, London, British Library [3]. Color pigment – including black pigments (dotted line) – samples and captions (photo: © British Library Board).

References

- [1] Donald C. Fels et al. *Lost Secrets of Flemish Painting: Including the First Complete English Translation of the De Mayerne Manuscript, B.M. Sloane 2052*. Alchemist, 2010.
- [2] Jenny Boulboulé. “Drawn up by a learned physician from the mouths of artisans: The Mayerne manuscript revisited”. In: *Netherlands Yearbook for History of Art/Nederlands Kunsthistorisch Jaarboek Online* 68.1 (2019), pp. 204–249.
- [3] *Sloane MS 2052, visited on 01 August 2021*. URL: [http : / / www . bl . uk / manuscripts/FullDisplay.aspx?ref=Sloane_MS_2052](http://www.bl.uk/manuscripts/FullDisplay.aspx?ref=Sloane_MS_2052).
- [4] Ernest Berger. “Quellen für Maltechnik während der Renaissance und deren Folgezeit (XVI.–XVIII Jahrhundert) in Italien”. In: *Spanien, den Niederlanden, Deutschland, Frankreich und England nebst dem De Mayerne Manuskript, München* (1901).
- [5] Jan van Daal and Suzanne Bul. “Art Technological Source Research Instructor: Herman den Otter Conservation and Restoration of Cultural Heritage, Technical Art History University of Amsterdam, 29-03-2018”. In: ().

Three XRS-dedicated beamlines

In the following section we introduce the specificities of three end-stations developed at ID-20 beamline of the European Synchrotron Radiation Facility (ESRF), the 6-2 beamline of the Stanford Synchrotron Radiation Lightsource (SSRL) and GALAXIES beamline (Source optimisée de lumière d'énergie intermédiaire du LURE (SOLEIL)); the spectrometers are dedicated for XRS experiments. A list with hard x-ray beamlines located in various synchrotron facilities, equipped with end-stations dedicated for XRS experiments are summarized in Table 1.4.

C.1 ESRF ID20

The ID20 beamline (ESRF) is equipped with a spectrometer dedicated to the study of core electron excitation using non-resonant inelastic scattering for low- Z elements [1]. The ID20 end-station is made of 72 spherically bent Si($nn0$) Johann-type analyzer crystals, separated in six movable units of twelve crystals; three operating in the horizontal and three in the vertical scattering plane. Each crystal analyzers' unit is placed in a carbon fiber vacuum chamber to minimize absorption and unwanted scattering from air. The two features that differentiate this spectrometer compared to other XRS spectrometers are its imaging capabilities and the flexible scattering angles selection for each analyzer chamber allowing a wide range of momentum transfer data collection. The spectrometer is equipped with one pixelated area detector for each movable crystal analyzers' chamber allowing to perform 3D X-ray Raman scattering imaging (XRI) based in the so-called direct tomography technique (Figure 1.12) [2, 3]. The imaging capability of the spectrometer is a valuable tool for the in-situ study of complex heterogeneous samples [4]. The source can be focused down to $8\mu\text{m} \times 16\mu\text{m}$ spot size ($V \times H$). The 2D detection is also used for the optimization of the *signal-to-background* ratio by separating the signal coming from the sample and the unwanted scattering from the sample environment.

Each of analyzers' unit is flexible to move individually for a variety of scattering angles thus allowing to collect data for a range of momentum transfer. The variety of possible config-

urations maximizes the solid angle detection and allows the collection of data in back-scattered and forward geometry simultaneously.

The achievable energy resolution at ID20 varies from 0.3 eV to 2.0 eV depending on the selection of the post-monochromators. The ID20 is equipped with a cryogenically cooled Si(111) monochromator which can be combined with a variety of post-monochromators; a Si(311) channel-cut, a four bounce Si(*nnn*) (*n*=3,4,5), a Si(*nn0*) (*n*=4,6,8) or a highly specialized back-scattering Si(*nnn*) channel-cut monochromator for ultra-high energy-resolution applications (Table 1.4).

To minimize the strain-induced contributions to the energy resolution, three types of circular masks with diameters (40 mm, 60 mm and 80 mm) are available aiming to reduce the illuminated crystal area. To fulfill the condition of operating at Bragg angles close to 90°, and still reserve space for the sample, the detector can be displaced off the Rowland circle by a distance of $2z$ (Figure C.1). At the same time, the analyzers are moved away from the sample by a distance z to keep the focus of the analyzers on the detector [1]. As a result, Bragg angles vary across the analyzer (i.e. dispersive direction) causing a dispersion known as *off-Rowland* contribution to the energy resolution given by

$$\frac{\Delta E}{E} = \frac{zD}{R^2} \cot \theta_B \quad (\text{C.1})$$

where D is the size of the analyzers in the dispersive direction, R is the Rowland circle radius, and θ_B is the Bragg angle of the analyzer reflection. Off-Rowland geometry is a main contributor to the overall resolving power to minimize the off-Rowland contribution, the spectrometer operates at analyzer Bragg angles θ_B close to 90° and the z/R (relative offset) and D/R (individual analyzer opening) are minimized.

C.2 SSRL 6-2b

The end-station of the wiggler beamline 6-2 at SSRL is dedicated to XRS spectroscopy experiments, with an energy resolution (≈ 0.3 eV) comparable to soft x-ray based techniques. It is equipped with two multi-crystal Johann type spectrometers positioned on intersecting Rowland circles of 1 m; the first one consists of 40 spherically bent diced Si(110) crystal analyzers placed in forward geometry (scattering angles centered at 40°) allowing low-momentum

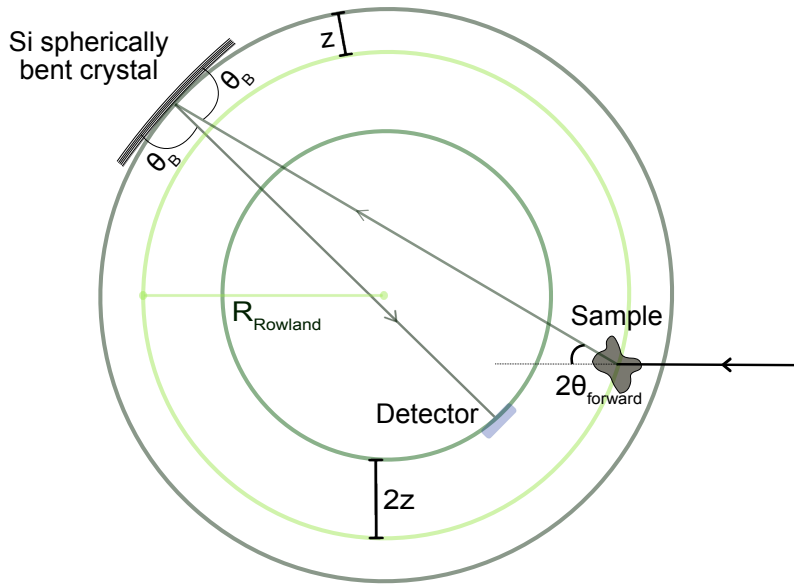


Figure C.1: Schematics of off-Rowland geometry

transfer (low- q) experiments thus enable soft-XAS equivalent studies. The second spectrometer consists of 14 non-diced spherically bent Si(110) crystal analyzers positioned at backward scattering angles (centered at 145°), thus enabling high-momentum transfer (high- q) experiments for the study of dipole-forbidden transitions.

The beamline, operating in an energy range of 4–18 keV, is equipped with two liquid nitrogen cooled double crystal monochromators: a Si(111) and a Si(311). A Rh-coated collimating and focusing mirror is positioned before and after the monochromator. A spot size of $100\ \mu\text{m} \times 400\ \mu\text{m}$ (V \times H) is achieved at the sample position.

To achieve the optimal energy resolution the intrinsic energy resolution of the monochromator should be comparable to the energy resolution of the incident beam (0.18 eV for the Si(311) monochromator). To reduce the lattice deformation (i.e. the stress induced perpendicular to the surface of the spherically bent crystals), which reduces the energy resolution of the analyzers, the spectrometer operating at low- q is equipped with bent-diced crystals. The 75 % of each diced crystal's surface is covered by several thousand of spherically bent packets of $1 \times 1\ \text{mm}^2$ size of 0.3 mm thickness bonded on a glass substrate. With a single diced crystal the overall resolution is within the range of 0.22–0.28 meV (measured for the elastic line scans with the Si(311) monochromator). The calculated crystal contribution (effective Darwin

width) is ≈ 170 meV. On the contrary, the high-q spectrometer is equipped with conventional Si(110) spherically bent crystals. To minimize the geometrical contributions the crystals for both monochromators are operating on a fixed Bragg angle close to 90° .

For optimization of the *signal-to-noise ratio*, one silicon drift detector is used for each spectrometer. A tight collimation of the x-rays is achieved by positioning the footprint of the analyzers as close as possible. To minimize the *signal-to-background ratio* $1 \times 5 \text{ mm}^2$ entrance slits are used as masks for the detector's active surface. During the experiments, an helium polypropylene bag is added to the overall experimental set-up, to minimize the attenuation and diffused scattering of the x-rays in their path from the sample to the analyzers and then toward the detector.

C.3 SOLEIL GALAXIES

When the experimental work of this thesis took place, GALAXIES beamline at synchrotron SOLEIL (France) was equipped with 4 spherically bent Si(111) analyzer crystals positioned at a 2×2 configuration [5]. The analyzers were operating at a Bragg angle close to 90° . For monochromatization of the incident beam a cryogenically cooled Si(111) double-crystal monochromator was used. The inelastic scattering end-station operated in an energy range from 4–12 keV. The overall energy resolution was approximately 1.2 eV (measured at the elastic line scan). Two focusing modes of the monochromatized X-ray beam were available: the KB mirrors which provide a micro-focused beam with spot size $\approx 10 \times 10 \text{ }\mu\text{m}^2$ (V \times H) or a toroidal mirror that provided a higher x-ray intensity with a beam spot size (V \times H) of approximately $\approx 30 \times 80 \text{ }\mu\text{m}^2$.

Since 2021, the GALAXIES undulator beamline at synchrotron SOLEIL (France) is equipped with a new spectrometer for XRS. It comprises of an array of $40 \times$ Si(110) spherically bent analyzers ($R = 1$ m, Bragg angle = 87°) assembled in a compact way on a portion of a sphere as described in Sokaras et al. [6]. The incident photon energy is selected by a cryogenically cooled Si(111) double-crystal monochromator. A second, high resolution post-monochromator (HRM) can be inserted in the beam to improve the energy resolution. It uses two sets of $4 \times$ Si(220) crystals with symmetric and asymmetric reflections ($\alpha = 9^\circ$) in a four-bounce, non dispersive geometry. The HRM yields a resolution between 100 meV (asymmetric case) and

300 meV (symmetric case) over a wide energy range (3.5-12 keV). Two focusing modes of the monochromatized X-ray beam are available: the KB mirrors which provide a micro-focused beam with spot size $\approx 10 \times 10 \mu\text{m}^2$ (V \times H) or a toroidal mirror that provides a higher x-ray intensity with a beam spot size (V \times H) of approximately $\approx 30 \times 80 \mu\text{m}^2$.

References

- [1] Simo Huotari et al. “A large-solid-angle X-ray Raman scattering spectrometer at ID20 of the European Synchrotron Radiation Facility”. In: *Journal of Synchrotron Radiation* 24.2 (2017), pp. 521–530.
- [2] Simo Huotari et al. “Direct tomography with chemical-bond contrast”. In: *Nature Materials* 10.7 (2011), pp. 489–493.
- [3] Christoph J Sahle et al. “Improving the spatial and statistical accuracy in X-ray Raman scattering based direct tomography”. In: *Journal of Synchrotron Radiation* 24.2 (2017), pp. 476–481.
- [4] Rafaella Georgiou et al. “Carbon speciation in organic fossils using 2D to 3D x-ray Raman multispectral imaging”. In: *Science advances* 5.8 (2019), eaaw5019.
- [5] Jean-Pascal Rueff et al. “The GALAXIES beamline at the SOLEIL synchrotron: inelastic X-ray scattering and photoelectron spectroscopy in the hard X-ray range”. In: *Journal of synchrotron radiation* 22.1 (2015), pp. 175–179.
- [6] Dimosthenis Sokaras et al. “A high resolution and large solid angle x-ray Raman spectroscopy end-station at the Stanford Synchrotron Radiation Lightsource”. In: *Review of Scientific Instruments* 83.4 (2012), p. 043112.

Appendix D

Scientific dissemination and synchrotron experiments

D.1 Scientific dissemination

D.1.1 Publications

- **Georgiou, R.**, Gueriau, P., Sahle, C. J., Bernard, S., Mirone, A., Garrouste, R., Bergmann, U., Rueff, J-P., Bertrand, L. (2019). Carbon speciation in organic fossils using 2D to 3D x-ray Raman multispectral imaging. *Science advances*, 5(8), eaaw5019.
- Bergmann, U., **Georgiou, R.**, Gueriau, P., Rueff, J. P., Bertrand, L. (2019). Nouvelles spectroscopies Raman X du carbone pour les matériaux anciens. *Reflets de la physique*, (63), 22-25.
- **Georgiou, R.**, Sahle, C., Sokaras, D., Bernard, S., Bergmann, U., Rueff, J-P., Bertrand, L., (2020). X-ray Raman scattering: A hard x-ray probe of complex organic systems. *In preparation*
- **Georgiou, R.**, Popelka-Filcoff, R. S., Sokaras, D., Beltran, V., Spangler, J., Lehmann, R., Lenehan, C., Bernard, S., Cohen, S., Rueff, J-P., Bergmann, U., and Bertrand L. Disentangling the Chemistry of Australian Plant Exudates from a Unique Historical Collection. *In preparation*

D.1.2 Conferences

- Workshop ‘Cultural and Natural Heritage at ESRF-EBS’, ESRF, Grenoble, France, 22 - 24 January 2020, **Oral**
- Workshop ‘DIMXIMAGE: Advanced training on the analysis of synchrotron-based X-

D.2. SYNCHROTRON EXPERIMENTS

ray images for heritage and ancient materials', Site du Synchrotron SOLEIL, Saint-Aubin, France, October 14-16, 2019, **Oral**

- Journées de la Matière Condensée (JMC), Grenoble, France, August 27-31, 2018, **Oral**
- Gordon research seminar 'Scientific methods in cultural heritage research', Castelldefels, Barcelona, July 21-22, 2018, **Poster**
- GeoRaman2018, Catania, Italy, June 10-14, 2018, **Oral**

D.2 Synchrotron experiments

- Identifying carbonaceous compounds in carbon-black based pigments using a novel X-ray Raman scattering technique, 2018, GALAXIES, SOLEIL, **In House**
- The chemical preservation of insects in amber revisited: Inside from 3D X-ray Raman scattering, October 2018, ID-20, ESRF, **Proposal number: 81599**
- Discrimination of carbon-based artists' pigments using a novel X-ray Raman scattering technique, November 2018, GALAXIES, SOLEIL, **Proposal number: 20180263**
- Disentangling the Chemistry of Australian Plant Exudates from aUnique Historical Collection, 2019, 6-2b, SSRL, **In House**
- Nanoscale characterization of carbon-based artists' pigments through STXM, February 2020, HERMES, SOLEIL, **Proposal number: 20191914**
- 3D X-ray Raman scattering imaging for the investigation of artworks, June 2020, GALAXIES, SOLEIL, **Proposal number: 20191187**

D.2. SYNCHROTRON EXPERIMENTS

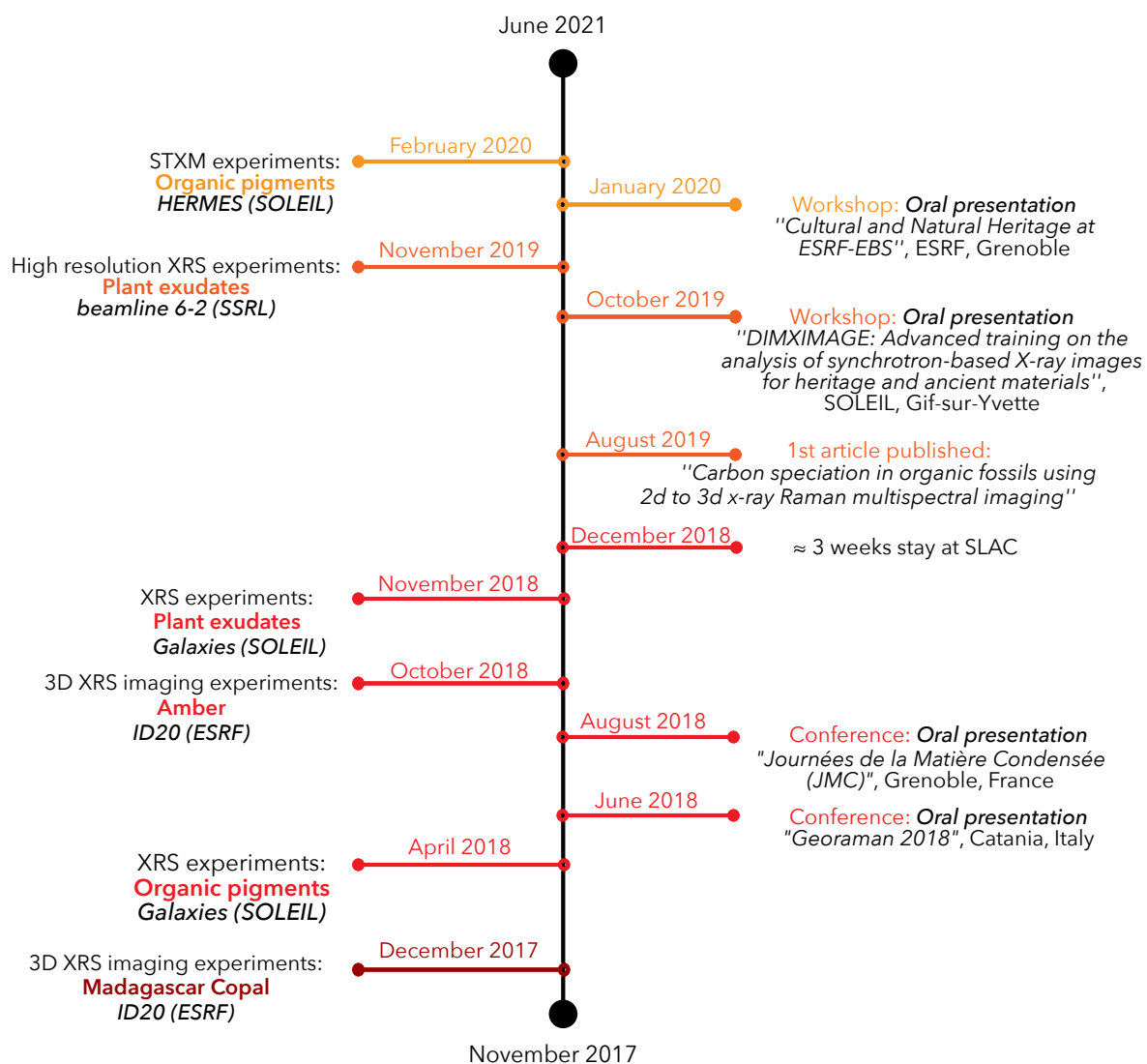


Figure D.1: PhD timeline

Appendix E

Résumé de thèse

Les moyens analytiques permettant d'évaluer la composition organique d'échantillons complexes sont limités et précieux pour les sciences du patrimoine. Ce travail explore le potentiel de la diffusion Raman de rayons X (XRS) comme approche non invasive pour étudier des matériaux paléontologiques, archéologiques et artistiques. Nous optimisons la méthodologie XRS requise pour l'étude d'échantillons complexes, comprenant des spécimens paléontologiques organiques et une collection d'exsudats végétaux à valeur patrimoniale, et explorons sa capacité à accéder aux différents niveaux d'information recherchés. La spectroscopie XRS est employée pour étudier des échantillons organiques anciens en 3D sur des dimensions millimétriques, de façon non invasive, pour déterminer les signatures organiques et retracer leur évolution dans le temps. En exploitant la tomographie directe basée sur le contraste des signaux chimiques, nous introduisons l'imagerie Raman des rayons X en 3D (XRI) dans le domaine du patrimoine naturel. La collecte successive d'images XRI tomographiques d'un spécimen exceptionnellement préservé, un insecte ancien de 53 millions d'années piégé dans l'ambre, permet d'évaluer la distribution spatiale des vestiges biologiques. Les résultats soulignent l'importance d'une imagerie de spéciation des spécimens à l'échelle de l'objet, afin d'en comprendre la biochimie, l'évolution moléculaire et les interactions entre organisme et milieu de dépôt. L'imagerie chimique tridimensionnelle apparaît essentielle à la compréhension de matériaux hétérogènes du patrimoine chimiquement altérés qui, ont subi des processus de diagenèse et de vieillissement au fil du temps. Nous démontrons que la spectroscopie XRS à haute résolution spectrale offre une nouvelle voie d'analyse de matériaux organiques du patrimoine culturel. Nous examinons une collection historique d'exsudats de plantes australiennes utilisées par les peuples aborigènes depuis des milliers d'années. Les peuples aborigènes australiens ont utilisé les extraordinaires propriétés physico-chimiques des exsudats des plantes australiennes (gommes, résines et kinos) dans divers usages, allant des applications pratiques à l'expression culturelle. L'analyse détaillée de la signature spectrale des transitions électroniques à partir des niveaux de coeur des atomes de carbone et d'oxygène permet d'identifier les

liaisons chimiques et de comparer des sécrétions végétales appartenant à des classes chimiques distinctes (terpénoïdes, polysaccharides, composés phénoliques et aromatiques). Nous démontrons par une analyse statistique que la caractérisation et la discrimination directe des composés organiques complexes est atteinte par spectroscopie XRS, avec une bonne sensibilité et de manière non invasive. Des approches statistiques ont été développées pour traiter les données tridimensionnelles XRI et décomposer les spectres obtenus. Nous montrons que la microscopie à transmission des rayons X en balayage (acronyme anglais : “STXM”), dans la gamme des rayons X “mous”, complète les approches XRI quand la limite spatiale de ces dernières est atteinte. Nous avons analysé des pigments organiques documentés dans le manuscrit de De Mayern par STXM. Les images à l’échelle nanométrique fournissent de nouvelles informations sur la chimie du carbone de ces pigments et démontrent leur complexité chimique qui ne peut être abordée qu’à cette résolution spatiale. L’hétérogénéité chimique à l’échelle nanométrique observée dans les pigments analysés indique une transformation non homogène des matériaux précurseurs pendant la pyrolyse ou la combustion. En conclusion, les résultats illustrent la valeur des méthodes XRS en tant que sonde spectroscopique et d’imagerie non invasive in situ de la spéciation des éléments légers dans les matériaux du patrimoine. Avec ce travail, nous fournissons une nouvelle perspective de l’exploitation de données XRS applicable à un grand nombre de systèmes organiques, hétérogènes et chimiquement complexes, et nous discutons des défis restant à surmonter et des perspectives futures de ces approches.

List of Figures

| | | |
|------|---|----|
| 1.1 | Schematic diagram of the inelastic scattering process | 10 |
| 1.2 | Basic kinematics of Compton scattering | 15 |
| 1.3 | X-ray Raman scattering induced transitions of core electron | 19 |
| 1.4 | Carbon core excitation reference spectra of gas phase molecules | 20 |
| 1.5 | Oxygen core excitation reference spectra of gas phase molecules | 21 |
| 1.6 | Calculation of phenol molecule XRS spectrum. | 24 |
| 1.7 | Density functional theory (DFT) calculation of levulinic acid XRS spectrum . . | 25 |
| 1.8 | Cross section of incoherent scattering and photoelectric absorption in carbon as a function of energy | 28 |
| 1.9 | Schematics of the XRS experimental set-up | 30 |
| 1.10 | Compton dependence on momentum transfer | 36 |
| 1.11 | 2D detector image showing the signal of 12 crystal analyzers collected at ID20 (ESRF) | 37 |
| 1.12 | Schematic representation of direct tomography imaging geometry | 38 |
| 1.13 | Correlation of $1s-\pi^*$ transitions to the ratio of double bonds versus sextets in PAHs model compounds. | 40 |
| 1.14 | XRS spectra of a series of PAHs compounds. | 42 |
| 1.15 | Molecular orbitals and XRS spectra of anthracene and phenanthrene. | 43 |
| 1.16 | X-ray Raman spectra of natural-occurring materials | 45 |
| 1.17 | X-ray Raman spectra of pyrolysis and hydrothermal carbon | 47 |
| 1.18 | Comparison of soft x-ray and x-ray Raman carbon K-edge spectra of pyrolysis and hydrothermal carbon | 48 |
| 1.19 | Spectral decomposition of XRS spectra of paleontological specimens | 50 |
| 1.20 | XRS spectral features in the presence of heteroatoms | 52 |
| 1.21 | XRS direct tomography applied to a diamond-graphite phantom sample | 53 |
| 1.22 | XRS direct tomography applied to a C/SiC sample. | 54 |

LIST OF FIGURES

| | | |
|------|--|-----|
| 1.23 | Spatial progress of α -trans-cinnamic acid crystal during x-ray induced dimerization. | 55 |
| 2.1 | XRS carbon K-edge spectra decomposition. | 83 |
| 2.2 | XRS oxygen K-edge spectra decomposition | 84 |
| 2.3 | FT-IR spectra of native Australian plant exudates | 85 |
| 2.4 | Fischer's linear discriminant analysis. | 89 |
| 3.1 | Carbon x-ray Raman scattering mapping and spectroscopy of a fragment of <i>Lepidodendron</i> trunk from the Upper Carboniferous (ca. 305 Mya) of Noyelles-lez-Lens, France | 108 |
| 3.2 | 2d XRS carbon K-edge speciation mapping of a fragment of <i>Lepidodendron</i> trunk from the Upper Carboniferous (ca. 305 Mya) of Noyelles-lez-Lens, France | 111 |
| 3.3 | XRS 3d carbon K-edge speciation mapping of an Eocene (ca. 53 Mya) ant entrapped in amber from Oise, France | 113 |
| 3.4 | XRS virtual cross section and spectra of an Eocene ant entrapped in amber from Oise (France, ca. 53 Mya) | 115 |
| 4.1 | Scanning transmission x-ray microscopy | 131 |
| 4.2 | Clustering objective function as a function of the number of classes for charred date pits | 134 |
| 4.3 | Hierarchical clustering analysis of STXM data of the charred date pits (8 classes) | 136 |
| 4.4 | Hierarchical clustering analysis of STXM data of the charred date pits (15 classes) | 137 |
| 4.5 | Hierarchical clustering analysis of STXM data of the charred peach stone (15 classes) | 138 |
| 4.6 | Hierarchical clustering analysis of STXM data of the charred stick lac (15 classes) | 140 |
| 4.7 | Hierarchical clustering analysis of STXM data of the charred bone black (15 classes) | 142 |
| 4.8 | Hierarchical clustering analysis of STXM data of candle fume black (4 classes) | 143 |
| 4.9 | Hierarchical clustering analysis of STXM data of bister (15 classes) | 145 |
| 4.10 | Presence of furan derivatives in the bister sample | 146 |
| 4.11 | Hierarchical clustering analysis of STXM data of vine black (15 classes) | 148 |
| 4.12 | Normalized average STXM spectra of organic pigments | 152 |

LIST OF FIGURES

| | | |
|------|--|-----|
| 4.13 | Comparison of STXM and XRS carbon K-edge spectra of organic pigments . . | 153 |
| A.1 | XRS data of native Australian plant exudates | 167 |
| A.2 | ICP-MS data of native Australian plant exudates | 168 |
| B.1 | Sloane MS 2052, folio 2r | 176 |
| B.2 | Sloane MS 2052, folio 18r | 177 |
| B.3 | Sloane MS 2052, folio 84r | 178 |
| B.4 | Sloane MS 2052, folio 29r | 179 |
| B.5 | Sloane MS 2052, folio 95r | 180 |
| B.6 | Sloane MS 2052, folio 111v | 181 |
| B.7 | Sloane MS 2052, folio 130r | 182 |
| B.8 | Sloane MS 2052, folio 80v | 183 |
| C.1 | Schematics of off-Rowland geometry | 187 |
| D.1 | PhD timeline | 192 |

List of Tables

| | | |
|-----|---|-----|
| 1.1 | Hybridization of carbon orbitals | 18 |
| 1.2 | Characteristic core electron transitions at the carbon K-edge of simple molecules | 22 |
| 1.3 | Characteristic core electron transitions at the oxygen K-edge of simple molecules | 23 |
| 1.4 | Hard x-ray beamlines equipped with end-stations dedicated for XRS experiments. | 28 |
| 2.1 | Native Australian plant exudates | 78 |
| 4.1 | Organic pigments analysed at the nanoscale via STXM | 130 |
| A.1 | XRS carbon K-edge spectral decomposition | 166 |
| A.2 | Fitted parameters of XRS carbon K-edge spectra decomposition | 169 |
| A.3 | XRS oxygen K-edge spectral decomposition | 170 |
| A.4 | Fitted parameters of XRS oxygen K-edge spectra decomposition | 171 |
| A.5 | Contribution of functional groups to the XRS carbon K-edge spectra | 172 |

Acronyms

ATR attenuated total reflectance

CT computed tomography

DDSCS double differential scattering cross section

DFT density functional theory

DT direct tomography

EELS electron energy loss spectroscopy

ESRF European Synchrotron Radiation Facility

FIB focused ion beam

FT-IR Fourier transform infrared spectroscopy

HF Hartree-Fock

HOMO highest occupied molecular orbital

HOPG highly oriented pyrolytic graphite

ICP-MS inductively coupled plasma mass spectrometry

IDB isolated double bonds

IXS inelastic x-ray scattering

KB Kirkpatrick-Baez

LDA linear discriminant analysis

LUMO lowest unoccupied molecular orbital

NMR nuclear magnetic resonance

NEXAFS near edge x-ray absorption fine structure

NRIXS non-resonant inelastic x-ray scattering

PAHs polycyclic aromatic hydrocarbons

PSF point spread function

py-GC-MS pyrolysis gas chromatography mass spectrometry

ROI region of interest

SERS surface-enhanced Raman scattering

SNR signal-to-noise ratio

SOLEIL Source optimisée de lumière d'énergie intermédiaire du LURE

SSRL Stanford Synchrotron Radiation Lightsource

STXM scanning transmission x-ray microscopy

ToF-SIMS time-of-flight secondary ion mass spectrometry

TXM transmission x-ray microscopy

VR₀ vitrine maceral

XANES x-ray absorption near edge structure

XAS x-ray absorption spectroscopy

XPS x-ray photoelectron spectroscopy

XRI x-ray Raman scattering imaging

XRS x-ray Raman scattering

